Universität Rostock



Traditio et Innovatio

Stability of Island Grids: A Study of Required Grid-Forming Wind Turbines Taking into Account Load Impact

Dissertation

for

obtaining the academic degree of

Doctor of Engineering (Dr.-Ing.)

of the Faculty of Computer Science and Electrical Engineering

of the University of Rostock

submitted by:

M.Eng. Nastaran Hammes (born Fazli)

Rostock, 10.06.2025

https://doi.org/10.18453/rosdok_id00005774


Dieses Werk ist lizenziert unter einer
Creative Commons Namensnennung - Nicht kommerziell - Keine
Bearbeitungen 4.0 International Lizenz.

Reviewers:

1. Reviewer: Prof. Dr.-Ing. Hans-Günter Eckel, Universität Rostock

2. Reviewer: Prof. Dr.-Ing. Dirk Westermann, Technische Universität Ilmenau

3: Reviewer: Dr.-Ing. Hendrik Just, 50Hertz Transmission GmbH, Berlin

Date of submission: 10.06.2025

Date of the defense: 05.03.2026

Acknowledgments

I would like to express my gratitude to my doctoral supervisor, *Prof.Dr.-Ing. Hans-Günter Eckel*, for providing me the opportunity to work on the *Netz-Stabil*[1] and *OffWiPP*[2] projects at his *Chair of Power Electronics and Electrical Drives* at the *University of Rostock*. His guidance, expertise, and critical insights have been instrumental in shaping this thesis and bringing it to completion.

I am also deeply thankful to my colleagues in the department, with whom I had the pleasure of working collaboratively and productively. I am especially grateful to *Dr.-Ing. Sidney Gierschner* for his valuable advice and support during the preparation of this thesis, and to *M.Sc. Christian Neumann* for his helpful suggestions and insights as my project partner. I also thank *Dr.-Ing. Yves Hein* and *Dipl.-Ing. Steffen Sänger* for their contributions and for fostering a positive and supportive working environment.

A very special thanks goes to my loving husband, *David*, whose unwavering support, patience, and encouragement have been a constant source of strength throughout this journey. Through every late night, every challenge, and every moment of doubt, he stood by me with kindness and reassurance. This achievement would not have been possible without his presence and sacrifices.

I am also deeply grateful to my parents, *Mehri* and *Alireza*, and to both of my sisters *Bahare* and *Sahar* for their unconditional love, guidance, and sacrifices over the years.

[1]Research project "Netz-Stabil" is financed by the European Social Fund (ESF/14-BM-A55-0015/16)
[2]OffWiPP is supported by the Federal Ministry for Economic Affairs and Energy (03El4037A) on the basis of a decision by the German Bundestag.

Abstract

The rapid increase in the penetration share of power electronics has led the AC grid to an unprecedented mutation. In this transition, additional inertia and short circuit power along with other capabilities of a synchronous machine will be necessary to maintain security of the AC grid. In order to stay in the track with this transition, these challenges can be addressed using grid forming converter control. The approach has shown positively influencing system stability in offshore and microgrid application.

This thesis addresses the approach to adopt the grid forming control to be compatible with extracting inertia from wind turbine rotor and to meet the requirements for transmission grid. A wind turbine with back-to-back converter configuration is considered and implementation of a full grid-forming control is addressed. The grid forming solution which is proposed in this work offers the following key features: working in optimum torque range during normal operation, provision of inertia emulation and participation in the voltage and frequency control during dynamic situations. Detailed analysis and studies is performed to assess the functionality of the developed control facing transients from the AC grid.

In recent years, many studies have shown the influence of grid forming in stabilizing the grid following certain disturbances. In this work, a comprehensive overview and study is given by detail EMT simulations on different aspects which are influencing the minimum required inertia. The influence of load on the required inertia or required percentage of grid forming units is vastly investigated in this work. Along with that, other factors like varying depth of disturbances and impact of operation point of wind turbines is studied and discussed.

The thesis provides a trendline for each participating factor individually and compares them together. The final results of this work emphasizes on the necessity of load dynamics studies and provides a more realistic view over performance of a grid forming wind turbine in different disturbances within a small-scale network, rather than an infinite bus.

Abstrakt

Die rasche Zunahme des Anteils der Leistungselektronik hat das Übertragungsnetz zu einer noch nie dagewesenen Veränderung geführt. Bei diesem Übergang werden zusätzliche Trägheits- und Kurzschlussleistungen zusammen mit anderen Fähigkeiten einer Synchronmaschine erforderlich sein, um die Stabilität des Übertragungsnetzes zu gewährleisten. Um eine sichere Transition zu bekommen, können diese Herausforderungen mit einer netzbildenden Umrichtersteuerung angegangen werden. Dieser Ansatz hat sich als positiv für die Systemstabilität in Offshore- und Microgrid-Anwendungen erwiesen.

Die vorliegende Arbeit befasst sich mit dem Ansatz, existierende netzbildende Regelungen zu adaptieren, um die Trägheit des Windturbinenrotors auszunutzen und die Anforderungen des Übertragungsnetzes zu erfüllen. Es wird eine Windturbine in Back-to-Back-Konfiguration der Umrichter betrachtet und die Implementierung einer allumfassenden netzbildenden Regelung untersucht. Die in dieser Arbeit vorgeschlagene Lösung zeichnet sich durch die folgenden Hauptmerkmale aus: Arbeiten im optimalen Drehmomentbereich während des Normalbetriebs, Bereitstellung einer Trägheitsemulation und Beteiligung an der Spannungs- und Frequenzregelung während dynamischer Situationen. Detaillierte Analysen und Studien werden durchgeführt, um die Funktionalität der entwickelten Steuerung bei Transienten aus dem Wechselstromnetz zu bewerten.

In den letzten Jahren haben viele wissenschaftliche Arbeiten den Einfluss der Netzbildung auf die Stabilisierung des Übertragungsnetzes nach bestimmten Störungen gezeigt. In der vorliegenden Arbeit wird ein umfassender Überblick durch detaillierte EMT-Simulationen zu verschiedenen Aspekten gegeben, die sich auf den minimal benötigten Trägheitsgrad auswirken. Der Einfluss der Last auf die erforderliche Trägheit oder den Prozentsatz der netzbildenden Einheiten wird in

der vorliegenden Arbeit eingehend untersucht. Daneben werden auch andere Faktoren wie die unterschiedlichen Auswirkungen von Störungen und der Einfluss des Betriebspunktes von Windkraftanlagen untersucht und diskutiert.

Die vorliegende Arbeit liefert eine Tendenz für jeden der beschriebenen Faktoren und vergleicht sie miteinander. Die finalen Erkenntnisse unterstreichen die Notwendigkeit von Studien zur Lastdynamik und bieten eine realistischere Sicht auf die Leistung einer netzbildenden Windkraftanlage bei verschiedenen Störungen in einem kleinräumigen Netz und nicht in einem unbegrenzten Stromnetz.

TABLE OF CONTENTS

LIST OF FIGURES IX

LIST OF TABLES XII

GLOSSARY XIV

1 INTRODUCTION 1

1.1 Background & Motivation 1
1.2 Thesis Objective 5
1.3 Thesis Contribution & Outline 8

2 PERFORMANCE OF STATE-OF-THE-ART GENERATION 11

2.1 Introduction 11
2.2 Converter Control Classification 12
2.3 Review on Control Topologies Offering System Services 15
2.4 State-of-the-art Generation Units in the Power System 22
2.4.1 Synchronous Generator 22
2.4.2 Modeling & Control of Converter-Based Generation . . 26
2.5 Summary 33

3 GRID FORMING CONTROL APPLIED TO WIND POWER GENERATION 35

3.1 Introduction 35
3.2 Control Principles of Converters with Voltage Source Features 35
3.2.1 Virtual Synchronous Machine 36
3.2.2 Modified Virtual Synchronous Machine 38
3.2.3 Initial Control Concept for Rotating Voltage Vector Control 39

3.2.4 Comparing the Grid Forming Control Schemes 42
3.2.5 Modified Rotating Voltage Vector Control 47
3.2.6 Implementation of the Modified-RVVC in Wind Turbines 71
3.3 Dynamic Response to Grid Events 83
3.4 Summary 88

4 IMPACT OF LOAD ON STABILITY IN ISLANDED NETWORKS 90
4.1 Introduction 90
4.2 Load Modeling 91
4.2.1 Modeling Aggregated Loads 91
4.2.2 Breakdown of Loads Across Various Consumer Sectors 92
4.2.3 Dynamic Model of Three-Phase Motor Loads 100
4.2.4 Modeling Power Electronic Loads 101
4.2.5 Load Response to Frequency and Voltage Steps 102
4.3 Island Network Study 105
4.3.1 Definition of Inertia at the Plant and System Levels . 105
4.3.2 Stability Criteria for Evaluation of Test Cases 106
4.3.3 Structure of the Test Network 109
4.4 Influence of Load Characteristic in Island Network 112
4.4.1 Situation I: 24% Import Loss 112
4.4.2 Situation II: 24% Export Loss 127
4.5 Summary 139

5 MINIMUM REQUIRED GRID FORMING UNITS 141
5.1 Normative Incident for System Split 141
5.2 Required Network Time Constant for Islanded Operation . . . 141
5.2.1 Islanding with ±24% Power Loss (Below Rated Power) 143
5.2.2 Islanding with ±40% Power Loss (Below Rated Power) 155
5.3 Impact of Operation at Rated Power with ±24% Power Loss . 165
5.4 Required System Strength for Induction Machine Startup . . 176
5.4.1 Need for Studying Induction Machine Inrush Current . 176
5.4.2 Initializing Simulation Scenarios 177
5.4.3 Scenario I: Evaluation of System Strength Sufficiency . 179

5.4.4 Scenario II: Reevaluating System Strength Needs . . . 186
5.5 Summary . . . 191

6 SUMMARY **195**

7 APPENDIX **201**
7.1 Synchronous Generator Parameters . . . 201
7.2 Dynamic Equations for Active and Reactive Powers . . . 202
7.3 Islanding Study Cases . . . 211

BIBLIOGRAPHY **222**

DECLARATION IN LIEU OF OATH **237**

LIST OF FIGURES

1.1 Market data on converter-based generation and consumption 2
1.2 Illustration of grid with grid forming and following converters 4

2.1 Definition of grid forming according to ENTSO-E 14
2.2 Block diagram of a SG with AVR and Governer 22
2.3 Control scheme of LFSM-O for a synchronous generator 24
2.4 Block diagram of GSC control for type 4 PMSG wind turbine 28
2.5 Block diagram of the closed-loop voltage oriented control 29
2.6 Extension for grid support on GFL-WT 32

3.1 Block diagram of VSM with inertia emulation and reactive power control 38
3.2 Block diagram of modified-VSM with inertia and reactive power control 39
3.3 Control structure of initial RVVC 40
3.4 Performance of RVVC in load variation and angle jumps 41
3.5 Operating principle of a GFM unit 42
3.6 Close-loop frequency response of three grid-forming control schemes 44
3.7 System dynamics response with three grid forming schemes 45
3.8 Comparison of linear vs. nonlinear models with 10-degree angle jump 49
3.9 Frequency response of $T_{p\delta}$ and $T_{q\delta}$ at operation point of $P_{ac} = 1$ pu . 49
3.10 Block diagram of the virtual resistor in the dq reference frame 51
3.11 Frequency response of $T_{p\delta}$ and $T_{q\delta}$ with and without static virtual resistor 52
3.12 Angle jump response: linearized vs. nonlinear with virtual resistor . 54
3.13 Frequency response of $T_{p\delta}$ and $T_{q\delta}$ with and without TVI, $(X/R = 0)$ 55
3.14 Frequency response of $T_{p\delta}$ and $T_{q\delta}$ with and without TVI,$(X/R = 10)$ 56

3.15 Overall GFM control scheme using modified-RVVC structure in the GSC . . . 57
3.16 Root locus of the closed-loop poles with variation of R_v . . . 60
3.17 Root locus of the closed-loop poles with variation of X/R for TVI . 61
3.18 Root locus of the closed-loop poles with variation of k_p . . . 63
3.19 Root locus of the closed-loop poles with variation of grid SCR . . . 64
3.20 Reference step responses of RVVC: linear vs. nonlinear model results 65
3.21 Implementation of the current limiting virtual impedance in dq frame 67
3.22 Steady state representation of the system after a fault at PCC . . . 68
3.23 System dynamics during three-phase fault and -30 degrees angle jump 70
3.24 Control structure of PMSG wind turbine as a GFM unit . . . 72
3.25 DC-link voltage controller implemented in the MSC . . . 75
3.26 MPPT and LFSM-O implementation in the GSC . . . 77
3.27 LFSM-O activation mechanism while operating at MPPT . . . 78
3.28 Response of the GFM-unit to an over frequency event . . . 79
3.29 Compensation scheme to enhance inertia emulation in MPPT . . . 81
3.30 Inertia emulation via rotor speed modification during frequency ramps 82
3.31 Equivalent circuit of test network for assessing grid forming behavior 83
3.32 Response of GFM, GFL Unit, and SG to 10 degrees angle jump . . . 84
3.33 Response of GFM, GFL Unit, and SG to -1 Hz/s frequency ramp . . 85
3.34 Response of GFM, GFL Unit, and SG to 15% voltage drop . . . 87

4.1 Diagram of component-based load modeling . . . 92
4.2 EU electricity consumption by sector (2020) . . . 93
4.3 Summary of 10 load classes with component percentages . . . 100
4.4 Block diagram of the PE load . . . 102
4.5 Comparing performance of three load components in different grid events . . . 104
4.6 FRT boundaries for type 1 & 2 of generation plants . . . 108
4.7 Single-line diagram of the two-node network for islanding studies . . 110
4.8 Performance of base scenario in 24% import loss . . . 114
4.9 Base scenario performance from 0-1 s under 24% import loss . . . 116
4.10 Base scenario vs. load classes LC_2-LC_5 under 24% import loss . . . 120

4.11 Comparing performance of load classes LC_7-LC_{10} under 24% import loss . . . 122
4.12 Performance of the base scenario (LC_1) under 24% export loss 128
4.13 Performance of base scenario between 0 to 0.1 s under 24% export loss 130
4.14 Performance of LC_2-LC_5 versus LC_1 under 24% export loss 134
4.15 Comparing performance of LC_6-LC_{10} under 24% export loss 136

5.1 Annual duration curve of acceleration time constant for Germany . . 142
5.2 Flowchart of testing two-node grid for acquiring minimum T_N 144
5.3 Minimum inertia and GFM units in 24% import loss 145
5.4 Varying network time constant for load class 1 (24% import loss) . . 147
5.5 Performance of LC_9 & LC_{10} with $T_N = 10$ s under 24% import loss . 149
5.6 LC_1 performance at $T_N = 6$ s under 24% import/export loss 150
5.7 Uncertainties in system split studies focused on resistive loads 154
5.8 Minimum inertia and GFM units in 40% import/export loss 155
5.9 Impact of higher time constant in LC_1 & LC_3 under 40% import loss 157
5.10 Required inertia/GFM under 40% & 24% export loss (partial load) . 159
5.11 GFM response to power surplus post-islanding 161
5.12 Risks of islanding study with only LC_1 at 24% & 40% export loss . . 164
5.13 GFM share in 24% import loss: rated vs. below-rated operation . . . 166
5.15 Required GFM in 24% export loss: below- vs. rated power 170
5.17 Load power factor in each load class 174
5.18 The two-node grid used to study motor startup 178
5.19 Network evaluation with minimum strength under three IM inrush . 180
5.20 Comparing performance of LC_1 facing inrush current of M_1, M_2 and M_3 181
5.21 Performance comparison: LC_1 vs. LC_3-LC_6 with IM inrush (M_2) . . 184
5.22 Minimum GFM share for stability with inrush from three IMs 186
5.23 Performance comparison: LC_1 vs. LC_3-LC_6 under IM inrush (M_3) . 189
5.24 Minimum required GFM units trendline by load characteristics . . . 194

7.1 VSC connected to an AC system through R-L circuit 202

LIST OF TABLES

2.1 Categorizing grid forming behavior 21
2.2 Parameters for active power response in FSM 23
2.3 LFSM-O parameters settings for a synchronous generator 26
2.4 Inverter and control parameters for grid following WT 31

3.1 Parameters of PMSG 76

4.1 Residential load profile, breaking down into individual components . 95
4.3 Industrial load profile, breaking down into individual components . . 96
4.5 Tertiary load profile, breaking down into individual components . . . 97
4.6 A mixed load profile, breaking down into individual components . . 98
4.7 Summary of system requirements for islanding studies 111
4.9 Summary of the results for 24% import loss 126
4.10 Summary of the results for 24% export loss 138

5.1 Utilized induction motor parameters 179
5.2 Comparison of LC_1 and LC_3-6 under IM inrush (M_3) 191

7.1 Synchronous generator parameters 201
7.2 Islanding test scenarios and descriptions 211
7.3 Test Configurations for S1 212
7.4 Overview of the test matrix for S1 213
7.5 Test Configurations for S2 214
7.6 Overview of the test matrix for S2 215
7.7 Test Configurations for S3 216
7.8 Overview of the test matrix for S3 216
7.9 Test Configurations for S4 217
7.10 Overview of the test matrix for S4 218

7.11 Test Configurations for S5 219
7.12 Overview of the test matrix for S5 219
7.13 Test Configurations for S6 220
7.14 Overview of the test matrix for S6 221

GLOSSARY

List of Abbreviations

ASDs	Adjustable Speed Drives
AVR	Automatic Voltage Regulator
CE	Continental Europe
CT	Constant Torque
DUT	Device Under Test
EMF	Electromotive Force
EMT	Electromagnetic Transient
ENTSO-E	European Network of Transmission System Operators for Electricity
FCR	Frequency Containment Reserve
FOC	Field-Oriented Control
FRT	Fault-Ride Through
FSM	Frequency Sensitive Mode
GFL	Grid Following
GFM	Grid Forming
GSC	Grid-Side Converter
HPF	High-Pass Filter
HVDC	High Voltage Direct Current
ICT	Information and Communication Technologies
IM	Induction Machine

LED ..... Light-Emitting Diodes

LFDD ..... Low-Frequency Demand Disconnection

LFSM-O ..... Limited Frequency Sensitive Mode-Overfrequency

LHP ..... Left Half-Plane

LPF ..... Low Pass Filter

MPPT ..... Maximum Power Point Tracking

MSC ..... Machine-Side Converter

NSG ..... Non-Synchronous Generation

OEL ..... Over-Excitation Limitation

OEMs ..... Original Equipment Manufacturers

PCC ..... Point of Common Coupling

PE ..... Power Electronics

PLL ..... Phase-Locked Loop

PMSG ..... Permanent Magnet Synchronous Generator

PT1 ..... First-Order Delay Element

PV ..... Photovoltaics

QT ..... Quadratic Torque

RENs ..... Renewables

RES ..... Renewable Energy Sources

RHP ..... Right Half-Plane

RoCoF ..... Rate of Change of Frequency

RVVC ..... Rotating Voltage Vector Control

SCP ..... Short-Circuit Power

SCR ..... Short-Circuit Ratio

SEBIR ..... Swing-Equation Based Inertial Response

SG ..... Synchronous Generator

SMPS ..... Switch-Mode Power Supply

SRF ..... Synchronous Resonant Frequency

TSO ..... Transmission System Operator

TVI ..... Transient Virtual Impedance

UEL ..... Under-Excitation Limitation

UFLS ..... Under-Frequency Load Shedding

VDE ..... Verband der Elektrotechnik

VSC ..... Voltage-Source Converter

VSM ..... Virtual Synchronous Machine

WT ..... Wind Turbine

Nomenclature

β ..... Blade pitch angle

λ ..... tip-speed ratio

ω_g ..... Grid angular frequency

ω_n ..... Rated mechanical angular velocity of the rotor

ω_r ..... Mechanical angular velocity of the rotor in turbine side

ω_0 ..... Angular frequency in rad/s

ω_m ..... Mechanical angular velocity of the generator rotor in rpm

ω_{pu} ..... Angular frequency in pu

ρ ..... Air density

τ_{dc} ..... Time constant of DC-link controller

τ_{PLL} ..... Time constant of PLL

τ_T ..... Time constant of turbine

A ..... Rotor harvesting radius

A ..... Torque coefficient of induction motor

C_p ..... Aerodynamic power efficiency

D ..... Damping Coefficient

f_g ..... Grid frequency

H ..... Inertia Constant

i_d ..... Grid current in d component

I_g ..... Grid current amplitude

i_q ..... Grid current in q component

i_{abc} ..... Three-phase grid currents

$I_{threshold}$ ..... Threshold current for over current activation

J ..... Rotor inertia

J_t ..... Lumped inertia of generator-rotor and gearbox

k ..... Proportional gain of the FRT curve

k_v ..... Proportional gain of the FRT curve for RVVC

k_d ..... Feedforward damping coefficient

$k_{p,vi}$ ..... Current limiting gain

k_{pf} ..... Feedback damping coefficient

k_v ..... Reactive power droop gain

L_c ..... Filter inductance

L_v ..... Virtual inductance

N_{gear} ..... Gearbox ratio

P_{EL} ..... Measured active power

P_{ref} ..... Reference active power from MPPT block

P_r ..... Rated power of the power electronic load

P_{Aero} ..... Wind turbine mechanical power

P_L ..... Total active power consumption of the load

P_m ..... Reference turbine mechanical power

R_c ..... Filter resistance

R_{vi} ..... Virtual resistor for over current circuit

R_v ..... Virtual resistor

S_n ..... Generator's rated apparent power

SPC ..... Synchronization power coefficients

T'_d ..... Transient reactance time constant

T_N ..... Acceleration time constant of the network

T_0 ..... Mechanical torque

T_0 ..... Motor mechanical torque at steady state

$T_{a,\mathrm{gt}}$ ..... Acceleration time constant of the drive train

T_{el} ..... Electromagnetic torque

$T_{initial-delay}$ .... Initial delay of the LFSM-O function

T_m ..... Mechanical torque

$T_{response}$ ..... Response time of the LFSM-O function

T_v ..... Voltage time constant

V_n ..... Nominal voltage of the network

V_n ..... Rated network voltage

v_{abc} ..... Three-phase grid voltages

V_{com} ..... Compensated voltage

V_c ..... Converter voltage amplitude

V_{DC} ..... DC-link voltage

v_{gd} ..... Grid voltage in d component

v_{gq} ..... Grid voltage in q component

V_g ..... Grid voltage amplitude

V_{PCC} ..... Voltage amplitude at point of common coupling

v_w ..... Wind speed

X_T ..... Network reactance

X_{vi}/R_{vi} ..... X/R ratio of the over current circuit

Z_c ..... Filter impedance

Z_{vi} ..... Virtual impedance for over current circuit

Z_v ..... Virtual impedance

S_G ..... Nominal Apparent Power of the Generation in an Island System

1 INTRODUCTION

1.1 Background & Motivation

The pledge to climate-neutral energy supply requires major deployment of Renewable Energy Sources (RES) and infrastructural changes for the actual power system to fit the future needs. In this transitioning phase, the probability of the stability issues has increased in the electrical grid by higher integration of Non-Synchronous Generation (NSG). This is attributed to the fact that until today, Synchronous Generators (SG) have exclusively undertaken the task of managing the entire system's operation and stability [1]. According to German government [2], the resolution until 2030, calls for 80% RES and until 2050, 100% of electricity demand has to be supplied by RES. This value may seem very high for the actual power system [3]. However, the actual data shows that even in locations supplied with an average of 50% RES annually, the combined percentage of onshore and offshore wind, along with photovoltaics (PV), exceeds 70% and occasionally reaches 100% of the total grid load several times a year [4]. A snapshot of such an exemplary period of time with high converter-based generation from *Deutsche Bundesnetzagentur*, is shown in Figure 1.1. As it is illustrated in the graph, the overall instantaneous generation from PV and wind accounts for almost 100% of the load consumption for multiple days in the period between 19th to 24th of December 2023 [5].

The problem of achieving high annual percentages of RES is that current state-of-the-art units are not designed to be the dominant generation source and rely heavily on a strong voltage source for grid synchronization. Therefore, looking at the actual trend and 2030 outlook reveal a bottleneck due to stability issues with these units, hindering further installation and integration of converter-based RES for power generation. These issues are well discussed in the literature [6–8]. The

main part of these stability issues are related to the voltage, frequency, rotor angle stability, reduction of inertia and short circuit power (SCP), etc. [8]. Other studies [9] have shown the borderline for further integration of Power Electronics (PE) based units due to control interaction and Phase-Locked Loop (PLL) instabilities, which is initially rooted from reduction of the system strength. The shift in system structure from SG dominance to converter dominance has increased the severity and likelihood of stability issues, threatening the security of the network, as reported by various Transmission System Operators (TSOs) in [10].

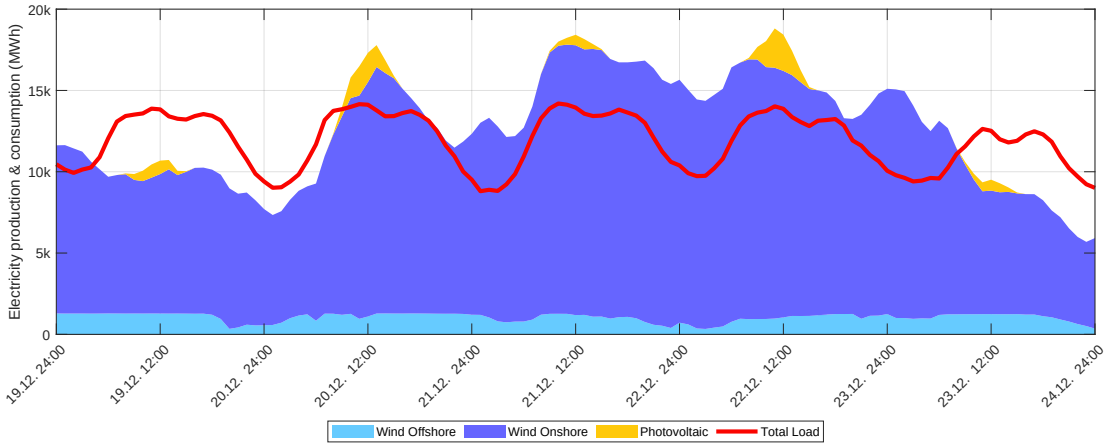

Figure 1.1: Market data on production and consumption for control area of *50Hertz* in the period from 19th December until 24th December 2023, only converter-based generation is selected for this period [5]

Another concern of TSOs is the increasing chance of severe system splits as it is also reported in [11]. In the actual power system with high local renewable energy generation, the likelihood of losing the last connecting line to the rest of the grid is high. This forms a partial network with shares of PE-based generation reaching up to 100% [11]. The actual control on the state-of-the-art renewable units enables them to operate at a fix operation point by following a stiff grid, which is equivalent to a Thévenin circuit with a low grid impedance. Loss of this connection causes serious stability issues in the separated area. This can become even more critical when the disconnected line is highly loaded, transferring power between two areas and causing a huge power unbalance after the separation. TSOs estimated for up

to 60% transit in the future, which might be the potential unbalance cases after system splits [8].

In order to bring back system stability, different solutions are taken into considerations. These solutions for provision of instantaneous reserve are namely gas-powered plants in phase shifting, pump storages in phase shifting, battery storages, STATCOMs with additional short-term storage, additional flywheel mass and offshore and onshore Wind Turbines (WT) [12]. However, due to limited number of such systems and sparse distribution of them in the power system, they can provide a limited contribution in system stabilizing throughout the power system. In this regard, wind and PV and storage units that are well distributed in the power system can be upgraded to provide instantaneous reserve and system services [8].

To this aim, the control of the converter in these units has to be substituted with Grid Forming (GFM) to be able to contribute in bringing back system strength similar to a SG unit. The grid forming concepts enables the units to behave like a voltage source behind an impedance and inherently counteracting variations in grid voltage magnitude and frequency. This requires instantaneous provision of active and reactive power to oppose voltage phasor changes [13]. The tasks and the requirements of a grid forming unit in comparison to Grid Following (GFL) are shown in Figure 1.2 [8].

The other side of these changes is related to the consumer side. In the conventional power system, a high portion of the loads can participate in the system inertia, depending on their type and dynamics [14]. Directly-connected induction motor loads for example which are common in the form of fans and pumps are grid friendly and add up for the power system inertia. In contrast, there are motor loads equipped with an inverter that do not show grid-friendly behavior due to the electrical decoupling of the motor with the grid [15]. Some studies indicate that 15-20% of motors are equipped with inverter [14]. This percentage is anticipated to grow as the deployment of motor drive systems and electric vehicle chargers increases. In [14], it is estimated that the share of converter loads rises to 70 percent or higher in future. That is mainly consumed by PE loads on the demand

side [16]. Given these changes, it is crucial to incorporate the transition toward power electronic dominant loads into the system studies.

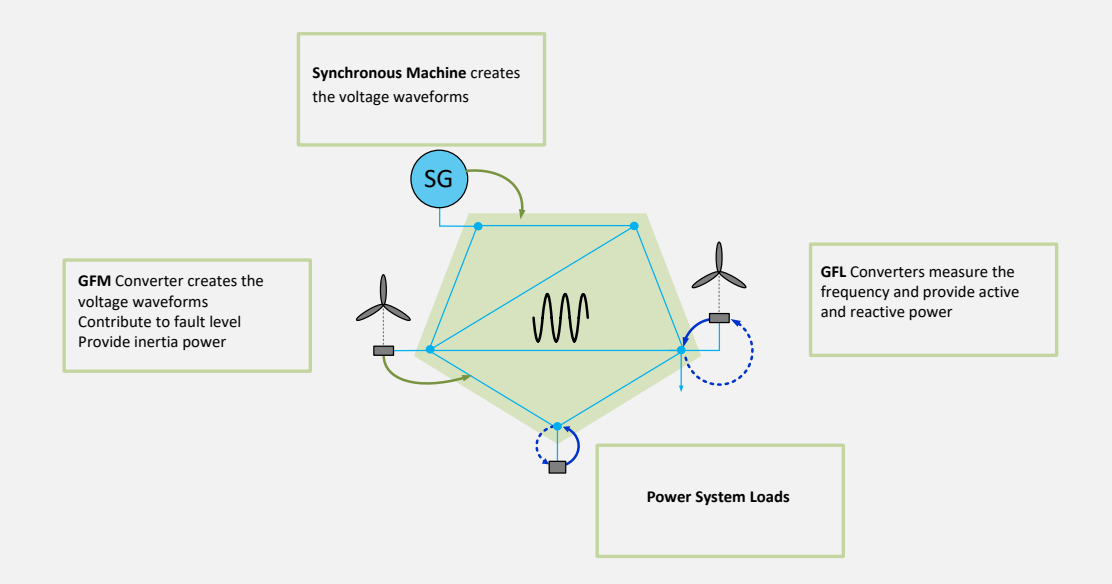

Figure 1.2: Illustration of the grid with grid-forming and grid-following converter generations [11]

Therefore, taking into the account the policy of 100% RES integration [2], the chance of higher transit losses and load migration toward PE-based consumption increases. There is a substantial need for studying the minimum-required inertia by upgrading converter based RES with GFM control [8]. It needs to be highlighted that these studies aim to define a withstand capability by not only assessing the current system, but also taking into account the future changes in the network. The goal is to draw attention to the possible loads which has to be equipped with grid friendly features [17], the infrastructural changes like Low Frequency Demand Disconnection (LFDD) and Limited Frequency Sensitive Mode-Overfrequency (LFSM-O), which ensure that control units function effectively during emergencies. Finally, it is important to identify the system's requirements for stabilizing the power system through converter-based solutions. The latter is the target of the current thesis. The focus in this work is drawn to achieve 90% converter-base generation, necessitating the upgrade of existing state-of-the-art grid-following with grid-forming control to effectively manage huge system splits. As 100% RES

scenario is not translated into 100% converter-based generation, the 90% target is selected.

1.2 Thesis Objective

Determining the minimum required inertia from converter-based generation, while considering system splits and stability-threatening disturbances, is a complex task requiring extensive simulations. Especially with the need of relying mainly on Electromagnetic Transient (EMT) studies, as the stability issues associated with power electronics significantly impact the dynamic behavior of the power system within a millisecond timeframe. Recent publications have focused on evaluating the stability enhancements provided by grid-forming units when replacing state-of-the-art converter generation in various system split scenarios. It is highlighted that grid-forming functionalities can improve system stability without constraining the share of power electronics-based sources in the generation side. However, these studies discard some limitations and modeling details for the consumer and generation side, that influences the stability border. Some of main simplifications are highlighted below:

- The current limitation of the converters hardware is often ignored under system split scenarios with loss of import/export.
- The initial operating point of the RES is not taken into consideration.
- In many cases, the source of the instantaneous reserve is unrealistic by employing an ideal voltage source with infinite amount of energy in the DC bus of the converters.
- Load characteristic and influence of the load in the consumer side is discarded very often in these studies.
- Modeling of the PE loads and increasing share of them is not taken into consideration.

Considering the aforementioned simplifications, the aim of this work is to continue the minimum-required inertia study by enhancing system stability through the use of grid forming control, taking into account the previously discussed aspects. This thesis addresses the challenge of conducting more detailed simulations on both the generation and consumer sides, considering the current limitations of converters. It implements a comprehensive GFM control strategy in a full-scale type 4 wind turbine, utilizing its rotary masses as a source of instantaneous reserve. Additionally, it focuses on modeling a more detailed load profile by accounting for the growing trend of power electronics-based consumers. The focus of this task is to ensure stable and reliable operation with a nearly 100% NSG share, even in the absence of grid-friendly loads, under various system splits scenarios according to TSOs estimation. Hence, the main questions of this thesis is mentioned below that must be addressed:

Can load dynamics be disregarded when determining the required inertia for future system split scenarios?

The following detailed research questions are implied by the above objective and will be answered in this thesis:

- Are simple voltage-dependent load models, such as R-L loads, sufficient to study dynamic behavior following a large disturbance?
- Which proportion of NSG units have to be upgraded with GFM to ensure stability against system split scenarios?
- What impact would it have on system stability if the GFM unit has a limited amount of inertia power?
- Can WTs operating near their nominal power enhance system stability?
- Can the 2030 generation horizon manage a historic system split scenario, such as 2006 Italy, without compromising stability in all load categories within the isolated grid?

- Do the actual control mechanisms, such as LFSM-O and LFDD, with their delays and constraints, affect voltage and frequency stability following an export or import loss?

Constraints on the Objectives As the power system is a complex unit, simplifying the network allows for a more focused analysis of the factors that significantly influence the thesis objective. The following assumptions have been made, as they are considered to have a less pronounced impact on the results compared to other factors under consideration, according to author's perspective.

- Tackling primarily instantaneous reserve, particularly during the critical first 10 seconds, to ensure system survival and provide additional time for other control units to engage.
- In order to analysis and understand the resulting phenomena after system splits or disturbances like turning on of an Induction Machine (IM), a two-node power system is formed. Avoiding multiple node grid enables us to reduce possible interactions between nodes and and conduct numerous simulation scenarios to determine the minimum required inertia boundaries.
- As wind speed varies slowly in time, all simulation scenarios assume a constant wind speed, without accounting for sudden gusts during the inertia emulation phase.
- Some state-of-the-art WT units have significant constraints when ramping down power during the activation of LFSM-O. However, grid codes now require a faster response. Therefore, this work does not consider slow emergency controls for LFSM-O in WT.

1.3 Thesis Contribution & Outline

The main contributions of the present thesis are seven fold:

1. Employing a grid forming control for a full-scale type 4 WT.
2. Designing the control of GFM to match the required damping and inertia and keep a reliable operation by variation of the connecting grid.
3. The analysis of the effects of load characteristics, in relation to import and export losses of similar magnitudes.
4. A component-based load modeling in three main sectors of residential, tertiary and industrial. Introducing high PE load classes to align with the trends observed by TSOs regarding the increasing integration of power electronics into the grid.
5. Determining the minimum required inertia for GFM-WT across various load classes and severe system split scenarios
6. An analysis of the impact of GFM-WT at their nominal power on system performance.
7. Analyzing system strength by evaluating the grid's time constant in relation to the increase of GFM-WT when facing disturbances, such as the sudden startup of an induction machine.

In the following a short summery is presented from the contribution of each chapter in this work:

- **Chapter 2** focuses on the generation source perspective, offering a comparison and categorization of various control techniques aimed at delivering system services within the range of 10 to 200 milliseconds. This is followed by a literate survey, presenting the functionality of these control concepts as a GFM control according to the ENTSO-E requirements. Following that, the conventional SG based generation is presented, with all the necessary emergency functions for the system studies of later chapters. A typical control

concept of state-of-the-art wind turbine is also presented in the following to be employed as existing NSG in the power system study.

- **Chapter 3** focuses on the control perspective of wind turbines and introduces the selected GFM concept that is suitable for implementation in the Grid-side Converter (GSC) of WTs. Based on the analytical studies, a step by step design procedure for the parameter of the GFM converter is identified and verified using small-signal model of the converter connecting to a stiff grid. Then the close-loop active and reactive power controllers are designed. Consequently, the designed parameters for GSC control is tested on a wide range of grid situations to satisfy grid-forming function requirements and borders for stable operation. An over-current strategy is designed to avoid exceeding the hardware current ratings. Based on the developed GSC control, the control of Machine-Side Converter (MSC) and WT is designed to be compatible with grid forming functionality of the unit. This chapter closes with validation of GFM functionality of the whole WT plant in different grid events recommended by *Verband der Elektrotechnik* (VDE).

- **Chapter 4** from the network consumer perspective, offers insights into the typical load components found across various load sectors. First, the component modeling in Matlab/Simulink is described. Then a component-based approach is taken to identify typical consumer type in each individual load sector. Subsequently, various load sectors are presented, ranging from the baseline scenario for system split cases featuring 100% resistive loads to scenarios with 100% PE loads. Consequently, the analytical value of the network time constant is used in this chapter to analyze symmetrical system splits under both export and import scenarios, enabling a comparison of load characteristics across different load classes.

- **Chapter 5** investigates various system split cases, involving power losses of up to ±40% to determine the threshold for stable operation by replacing a minimum percentage of NSG with GFM-WTs. The acquired border is then compared with similar system split scenarios in which RES are operating at their nominal power. As the final step, the stability border for each load

class is assessed by applying disturbances from the consumer side, ensuring that stability is maintained with the specified percentage of GFM-WT. To achieve this, the impact of a hard startup of an IM is tested during islanding, using various motor sizes rated up to 10% of Nominal Apparent Power of the Generation in an Islanded system (S_G). As a result, the stability border is reshaped and adjusted based on the findings from the motor startup analysis. The simulations are conducted throughout this work via Matlab/Simulink.

2 PERFORMANCE OF STATE-OF-THE-ART GENERATION

2.1 Introduction

In the last decade, by increase of installed capacity of RES, the stability issues corresponding to this transition has become more pronounced [11]. From system operator point of view, these stability concerns are categorized based on possibility and severity in [8],[10]. In order to address these challenges, restrictions on the penetration levels of converter-based generation have been suggested [8],[7], along with proposed solutions to mitigate issues related to PLL instability [9], [18].

Another approach for addressing grid instability challenges involves new control concepts developed in recent years, aimed at replicating the functionalities traditionally provided by SG in the network. In order to facilitate energy transition using converter-based generation as the main energy source, it is critical to identify which and what services these control concepts can offer [14], [19]. Distinguishing between different control strategies helps TSOs benchmark and specify performance requirements for newly installed assets.

One of the main terms that initially was used in the literature to distinguish a grid forming control from the state-of-the-art control was proposed in [20]. In [20], for the first time, the converter control was divided into grid forming, grid Following and grid supporting voltage and current source. The problem with this terminology was that conventional SG-based units could not be categorized as grid forming, which was misleading, as many studies used SG as a benchmark for comparing the performance of their control strategies. Similarly, state-of-the-art WT units cannot be classified as grid following since they are already equipped with certain supporting functionalities to comply with grid codes. Furthermore,

in the subsequent years, the term grid forming became predominantly associated with SG, while various converter control concepts were introduced and recognized as GFM systems. Although some of these concepts were not showing similar performance facing a similar grid event [21]. In the continuous of acquiring a proper way to distinguish and categorize different controls, TSOs within the workgroup of European Network of Transmission System Operators (ENTSO-E) defined the required functionalities/services of a grid forming unit from performance point of view [19].

In this chapter, first in chapter 2.3 a brief overview is given how different literature categorized their control based on the nature of the source, the system services offered, and also based on high/low level control. Subsequently, several recent control concepts will be briefly explained, focusing on their implementation, synchronization, and the system services they provide. Finally, based on the definition of GFM provided by the ENTSO-E, these concepts are categorized. Then in chapter 2.4, two state-of-the-art generation units which are used further in this work, are explained with their required control blocks.

2.2 Converter Control Classification

As there is not a consensus in academic and industrial world to define grid forming behavior, other vocabulary and categorizing is used in the last years in literature for naming and grouping control topologies, aiming to improve grid stability. The primary purpose of using different terminology is to specify the performance requirements for devices in a way that is understood by R&D groups, which is also acknowledged by system operators. Some of the main categories are outlined here; In [20], control of power converter is divided into categories of grid forming, grid following, and grid supporting.

- Grid Forming: The first one refers to an ideal voltage source behind an impedance with fix voltage amplitude and frequency.

- Grid Following: Grid following control models a Voltage-Source Converter (VSC) as a current source with a parallel impedance, with a fixed current set point.
- Grid Supporting: This refers to a group of topologies that provide support for the power system, by emulating a current source or voltage source behavior by adjusting its active and reactive power.

A grid supporting voltage source, emulates the behaviors of an AC voltage source, that dynamically counteract any variation in the power system voltage. Similarly, [21] identifies three categories:

- Grid Leading: Grid leading of [21], has a similar performance like grid forming control in [20], ensuring a constant voltage source with a constant voltage amplitude and frequency.
- Grid Forming: This behaves as a voltage source behind an impedance with a variable voltage amplitude and frequency.
- Grid Following: This is alike the grid-supporting current source in [20], incorporating grid support features in the outer loop to meet requirements outlined in grid codes, such as Fault Ride-Through (FRT) and LFSM-O, while adjusting active and reactive power accordingly.

A distinction between grid forming and other controls is made in [22] using a time frame for the response. After facing a disturbance with Device Under Test (DUT), the sub transient, transient and steady state time frame defines if a converter is grid forming or not [22].

- Grid Forming: In the subtransient range, it shows a constant voltage and frequency; In the transient range, the system regulates both voltage and frequency. It eventually stabilizes at a new equilibrium based on droop characteristics [22].
- Non-Grid Forming: In the subtransient range, the output current is kept constant; In the transient range, the active and reactive power is adjusted; It eventually stabilizes at a new equilibrium based on droop characteristics [22].

In this definition, the steady state performance can become very similar in both cases. These features became evident in different tests scenarios. If the state-of-the-art grid following unit is at the top of a hierarchy bar and grid forming units (having all system services like SG) is in the bottom, different inverter control are placed in between [22]. The aim of author in [22] was to avoid categorizing based on control structure.

Furthermore, in [7], [23], and [24], the control strategies are classified based on distinctions between upper-level and lower-level controls. The nature of the source is defined by the lower-level control, while the supporting features that require time for measurement delays are managed by the upper-level control. In [24], alphabetical labels are used to represent different types of control concepts and their functionalities, whereas [7] and [23] categorize the controls into two classes of current injecting and voltage injecting-based on the nature of the lower-level controller.

In ENTSO-E [25], however, the emphasis is placed on characteristics that are inherent to a voltage source. Figure 2.1 illustrates an example of the dynamic performance of a grid forming unit, reacting to disturbances in the grid [26]. In response to the challenges posed by the increasing penetration of RES, the ENTSO-E definition of grid forming capability is associated with meeting several key grid requirements: creating system voltage, contributing to fault level, contributing in inertia, sink for harmonics and unbalances, islanding operation possibility and preventing adverse control interaction.

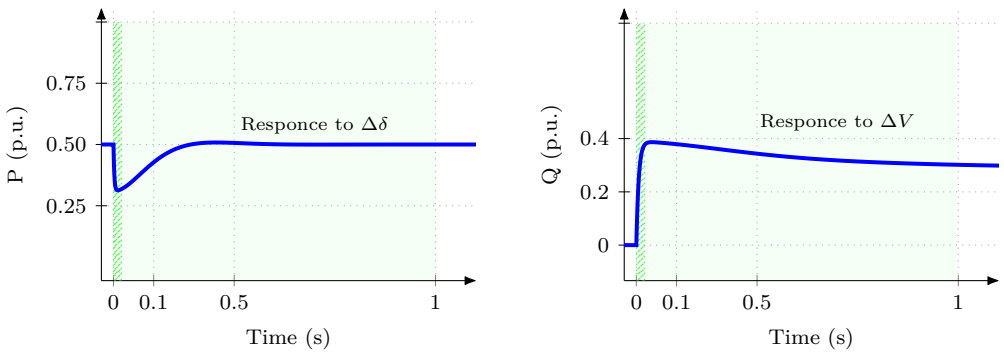

Figure 2.1: Definition of grid forming according to ENTSO-E

As mentioned earlier, all the aforementioned requirements are essential features of a synchronous generating unit. While converter-based generation cannot fully replicate the performance of a synchronous generator due to hardware limitations, employing grid forming control with the specified ENTSO-E features [25] can enhance overall stability in the power system and allows an smooth energy transition. A control with these features helps counteracting disturbances in the grid, enables islanding, and provides black start capabilities from a converter-based generation units, in contrast to a grid following control.

2.3 Review on Control Topologies Offering System Services

This chapter presents a brief overview of the implementation process, the nature of the sources, the methods of synchronization with the grid, and the various services that recent converter control concepts have introduced to enhance grid support in the recent years. The abbreviation *'CC'* refers to *'Control Concept.'* The names preceding the control concept numbers correspond to the original names used by the authors in the referenced literature.

CC1: Virtual Synchronous Machine (VSM) [27], [28], [29]
This control concept is originated to emulate the behavior of a SG with a VSC. The control scheme models the converter to behave like a voltage source. The VSM core is implemented in the outer loop, in which a 2nd-order model of drive train known as swing equation is implemented for active power. The reactive power droop control is also realized in the outer loop. The power controllers generate the angle and magnitude of the voltage vector for the converter. The resultant voltage vector then is either directly fed into PWM or via a cascaded voltage-current structure is controlled.

CC2: Grid-Supporting Current Source [20]
A grid-supporting current source allows a VSC to behave as a current source with a parallel impedance [20]. The primary control objectives consist of three components: first, droop control, which measures grid frequency using PLL and voltage magnitude to support the grid by adjusting active and reactive power.

Second, a power control loop which uses the measured grid voltages to convert the power set points into *dq* current components. Lastly, a current controller is implemented to regulate currents according to the desired reference values. The scheme employs PLL for measuring grid frequency and angle, facilitating synchronization and operation of the control loops.

CC3: Grid-Supporting Voltage Source [20]
In a grid-supporting voltage source, similar to a SG, the power transfer between the converter and the grid primarily depends on the converter voltage phasor and the impedance between two voltage sources [20]. This impedance typically comprises a physical component associated with passive elements and a virtual component that is emulated within the control scheme. A grid-supporting voltage source can regulate grid frequency and voltage magnitude by adjusting active and reactive power via the droop controllers, enabling connection to the AC network without a PLL, and it can form an islanded grid. The control structure consists of two droop controllers that creates frequency/angle, and voltage set points, along with a cascaded voltage-current control structure to control the converter voltage vector.

CC4: Strategy B [27]
In this strategy, converter is modeled as a current source. It uses PLL for synchronization to the grid. The outer active and reactive droop control allows for supporting frequency and voltage of the grid.

CC5: Strategy C [27]
In this strategy, converter is modeled as a voltage source. The outer active and reactive power loop allows for creating voltage reference and synchronizing the grid. Therefore, no dedicated synchronization unit is required. The generated reference voltage vector is then given to a cascaded voltage controller with under-laying current control in the inner loop. This concept is not universally applicable to all technologies; for instance, High Voltage Direct Current (HVDC) systems cannot utilize this cascade structure. Only those technologies that incorporate an LCL filter at the converter's output can implement such a configuration. This control can emulate inertia via Low-Pass Filter (LPF) which is implemented in the control loop and has damping of the load-angle oscillation. Current limitation is directly

applied on the reference current in the inner loop.

CC6: Strategy D [27]
This control models converter as a voltage source. The outer loop contains reactive power droop. A PLL combined with a droop control is employed in the outer loop for grid synchronization. Inertia emulation is achieved via tuning time constant of the LPF in the power/angle loop. The voltage reference is given to a cascaded voltage-current structure, enabling direct limitation of the current references.

CC7: Strategy F [27]
This control models a converter as a voltage source. The outer loop uses the core of VSM for creating voltage vector. It uses a PLL for synchronizing, although it can operate without PLL as well. A cascaded voltage-current structure exist to control the voltage in the filter terminal and the currents. Current limitation is applied via current reference saturation here.

CC8: Grid Forming VSC-PWM [26]
This control models the unit (VSC or HVDC station) to behave as a voltage source. In this approach, the outer loop incorporates a droop characteristic for active and reactive power, allowing the unit for creating the voltage angle and self-synchronizing with the grid. The First-Order Delay Element (PT1) in the power-angle loop allows for emulating inertia similar to VSM. The generated voltage vector is given to a Transient Virtual Impedance (TVI) to create current reference for the current controller. The current limitation can be applied either by current saturation or via the over-current virtual circuit.

CC9: Grid Forming Control [30]
This control models the unit as a voltage source. It uses droop control in the outer loop for active and reactive power. A PT1 is implemented in active and reactive power loops. In the active power loop, it is used for inertia emulation and in reactive power loop for filtering measuring signal. The voltage reference is supplied to the inner cascade structure. Current limiting is realized via threshold current control principle, rather than directly on the current references, to ensure a better post-fault recovery response while maintaining the voltage source nature during current limitation.

CC10: Direct Voltage Control (DVC) [31]

This concept models the converter as a current source. To comply with grid codes, the control scheme implements FRT functionality in the outer reactive power loop and LFSM-O in the outer active power loop. In addition, a synthetic inertia known as Swing-Equation-Based-Inertial-Response (SEBIR) is also introduced in the outer active power loop. The outer loops generate ΔP and ΔQ, which are then fed into the inner current controllers. For grid synchronization, DVC uses a PLL to estimate the frequency and angle. For current limitation, a virtual resistor scheme is implemented to reduce the voltage reference.

CC11: Grid Forming Control [6]

The control is modeling the unit as a voltage source. It uses active power-frequency loop for self-synchronizing. In the outer loop, there are active- and reactive power loops. The active power loop uses a PI controller for getting the rotational speed of the converter voltage vector. A PLL is used for measuring frequency in the grid which is used in the proportional frequency control for grid support. In addition, the PLL is used for synchronizing to the grid. To be able to control the currents, the control concept switches from voltage mode to current source mode. In this condition, the unit looses its voltage source behavior and acts as a current source. This makes operation in islanding partially feasible, and limited to operation below current rating of the unit. Upon activation of the current limitation, the source loses its capability to function as a voltage source and becomes decoupled from the outer control loops. The 100% inverter-based islanding scenario confirms the earlier discussion that stable island operation is constrained by maintaining a sufficient SCP [6]. Below a certain SCP, any transient might cause instability which is not necessarily counteracted by the control concept.

CC12: Extended Current Control [32]

This control models the power converter as a current source. It uses a PLL for grid synchronization. The state-of-the-art converter control is modified to have outer loops containing SEBIR inertia emulation and LFSM-O. Additionally, the current controller bandwidth is reduced compared to typical schemes (300-500 Hz) to enhance grid support capabilities and ensure stability and robustness when using an extended control structure. The voltage support to fulfill FRT requirements is

also provided in the outer loop. The current reference saturation in this scheme allows for protection against excessive currents.

CC13: Synchronous Power Controller [33], [34], [35]
Synchronous power controller models the power converter as a voltage source. The outer active and reactive power loops generate the converter reference voltage vector. Synchronization is achieved via power-frequency loop which uses a PI controller to control the rotational speed. A virtual admittance is used to create the reference currents from reference voltages. The current limiting is realized via saturation of current references.

CC14: Synchronverter and Enhanced Synchronverter [36]
Synchronverter uses similar principle like a VSM, it emulates the behavior of a synchronous machine to create voltage vector of the converter. Therefore, the control models the power converter basically as a voltage source. The electrical and mechanical (swing based) part of a SG is modeled in the outer loop, which gives the information of the load angle and voltage magnitude. Typically, this type of control uses a PLL for synchronization to the grid. However, the modified version known as Enhanced Synchonverter can eliminate the PLL and use it only as a optional solution. In this way, it has possibility for self-synchronizing to the grid.

CC15: Rotating Voltage Vector Control (RVVC) [37], [38]
RVVC models the power converter as a voltage source, aiming for compatibility with existing control schemes to enable grid-supporting functionality. This scheme employs a cascade control structure in which the outer loop controls the DC-link voltage, while the inner loop regulates the active power by adjusting the load angle. The reactive power loop is also realized via a PI controller, which generates the converter voltage magnitude. The control concept self-synchronizes to the network without a need to a PLL. Due to the cascade structure and dynamic of the DC-link controller, grid support is partially possible as long as an extra energy storage is not connected to the converter DC bus.

CC16: Modified Rotating Voltage Vector Control (RVVC) [39]
Modified RVVC is used in this thesis as the main control for GFM wind turbine which is explained in detail in chapter 3.2.5. The modified RVVC enhances the

original structure by enabling the grid-side converter of the wind turbine to function as GFM, similar to the inner control mechanism of CC15, while shifting the DC-voltage control to the machine-side control. This configuration facilitates maximum power injection into the grid during normal operations and allows the wind turbine to participate in inertia emulation during grid disturbances. Subsequent chapters will elaborate on this control method, including its capabilities for voltage generation in islanding situations, inertia emulation and its performance in low Short-Circuit Ratios (SCR).

Table 2.1 categorizes the mentioned literature above based on the expected functionality from a grid forming unit and the performance that a grid forming control concept should include according to ENTSO-E [25] and VDE [22]:

Table 2.1: Categorizing grid forming behavior according to [25] and [22]

CC	Create Voltage	Inertia Contribution	1st Cycle Response	Self-Synchronizing	Sink for Harmonics	Contribute in SCR	Islanded Operation	Operation in Low SCR	Parallel Operation
CC1	+	+	+	+	+	+	+	+	+
CC2	-	-	-	-	-	-	-	-	+
CC3	+	+	+	+	+	+	+	+	+
CC4	-	-	-	-	-	-	-	-	+
CC5	+	+	+	+	+	+	+	+	+
CC6	-	+	+	-	+	+	-	+	+
CC7	+	+	+	+	+	+	+	+	+
CC8	+	+	+	+	+	+	+	+	+
CC9	+	+	+	+	+	+	+	+	+
CC10	-	(+/-)[1]	-	-	-	-	-	-	+
CC11	+	+	+	-	+	+	(+/-)[2]	(+/-)[3]	+
CC12	(+/-)	(+/-)[4]	-	-	-	-	+	+	+
CC13	+	+	+	+	+	+	+	+	+
CC14	+	+	+	(+/-)[5]	+	+	+	+	+
CC15	+	(+/-)[6]	+	+	+	+	+	+	+
CC16	+	+	+	+	+	+	+	+	+

[1]SEBIR based inertia does not meet ENTSO's definition for response within 20 ms, primarily participating in the FFR range. [40]-[41].
[2]The control switches to current mode once the nominal current is reached, islanding is only possible when operating below nominal.
[3]Operation in low SCR can cause instability as the control switches to current mode once once the nominal current is reached.
[4]Due to the measurement delays in SEBIR's inertia emulation, the response falls within the range of fast frequency support.
[5]Synchronverter uses PLL for synchronization.
[6]Limited inertia due to high DC-voltage deviation; unstable operation may arise from slow voltage regulation during high dynamic.

2.4 State-of-the-art Generation Units in the Power System

2.4.1 Synchronous Generator

Directly connected synchronous generators in the conventional generation units are the core of the electrical power system. In this thesis, a three phase synchronous machine is realized using parameters in Table 7.1[42]. The SG model which is shown in Figure 2.2 employs an Automatic Voltage Regulator (AVR) consisting of an AC alternator and an uncontrolled rectifier to generate the necessary DC field current for the machine [26], [43]. The AVR uses also the signals of Over Excitation Limitation (OEL) and Under Excitation Limitation (UEL) to limit the machine's reactive power capability [44]. Reactive power limitation is influenced by various factors related to the machine's capability and design. However, in this work, it is solely limited by the armature current and represented as a circle in the P-Q plane, with a radius equal to the apparent power [45].

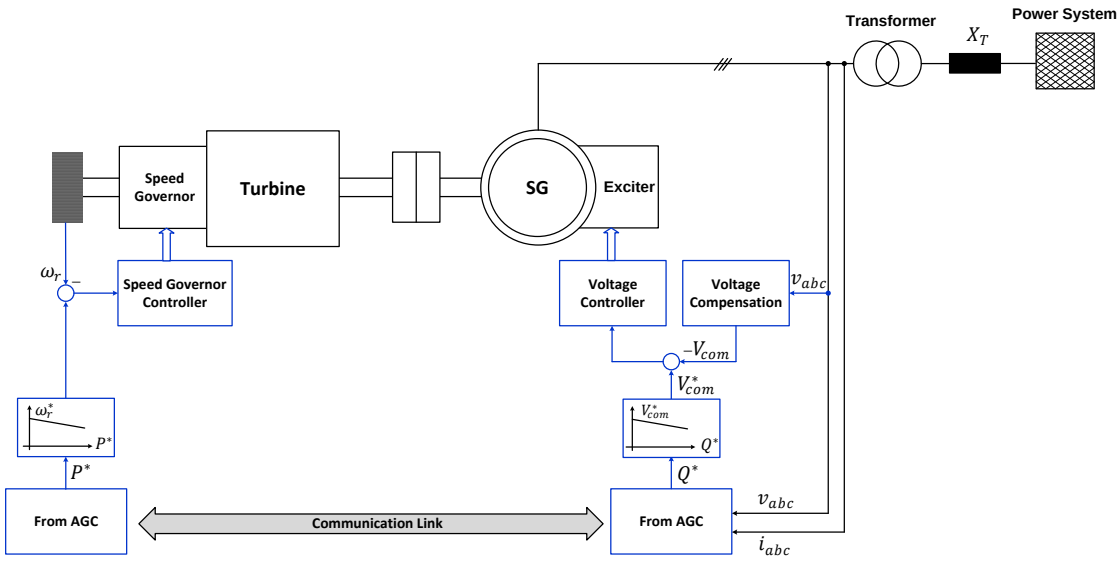

Figure 2.2: Block diagram of a synchronous generator with AVR and Governer [26][42][46]

In addition, a model of a prime mover is provided with a speed governor to regulate the speed based on the speed droop characteristic [44]. Active power limitation

is realized in the model by limiting the mechanical power set point of the prime mover [42]. During transients, the behavior of governor and AVR control can be ignored due to their slow reaction; The control functions are introduced for the secondary effect when the transition is happening towards stationary.

Frequency Sensitive mode

In the two-node power system, which will be discussed later in Chapter 4 for the transient study, the Frequency Containment Reserve (FCR) is achieved through the Frequency Sensitive Mode function in the solely integrated SG-based generation unit. A frequency containment reserve, aims to stabilize system frequency, at a stationary value, after a disturbance. FCR is a group of generation & demand units, which are available for TSOs to operate in FSM [47]. Within a synchronous area, FCR is dimensioned to cover the normative contingency (reference incident) for interconnected operation in Continental Europe (CE) [47]. This incident is the loss of two largest generating units connecting to the same busbar, defines the required primary reserves of 3000 MW [47]. This reserve is enough to cover such an incident, which has to completely deployed at a frequency deviation of ±200 mHz within 30 seconds [47].

Table 2.2: Parameters for active power response in FSM [47]

FSM Parameters	CE	Two-node Power System
Active power range of unit |ΔP1|/Pmax	1.5 – 10%	10% (to fulfill FSM requirement)
Droop	2 – 12%	20% (to fulfill FSM requirement)
Frequency response insensitivity	Between 10 – 30 mHz	20 mHz
Max initial delay	2 s	2 s
FSM full activation	30 s	30 s

With the growing integration of power electronics into the electrical grid, the risk of islanding is increasing [7]. A separated subsystem could become dominated by NSG. According to [47], a single power generation unit is not permitted to provide more than 5% of the FCR in a synchronous area. In this study, since the NSGs in operation do not contribute to the FSM, the sole unit responsible for system

services during islanding scenarios is the synchronous generator. Consequently, the available reserve is limited to the SG's share in the isolated power system. The parameters for FCR are specified according to NC RfG Article 15.2.d [47]. In Table 2.2, these parameters have been adjusted to meet the requirements for the reference incident when the share of SG is 100% [48].

Limited Frequency Sensitive Mode-Overfrequency

Limited frequency sensitive mode- overfrequency gets activated during an emergency state, when following a severe system split and power surplus, the frequency rises higher than +200 mHz [49]. In such a situation, FCR is too less and too slow to be able to manage such an imbalance and to stabilize frequency. Therefore, LFSM-O is activated to decrease the generated active power in accordance with operational limitations and grid codes. After triggering of FCR and LFSM-O, frequency should be brought back to below 51.5 Hz to gain time for other power system control actions to reduce frequency [49]. According to grid codes, every generation unit has to participate in LFSM-O, and in the emergency state, has to reduce its power as fast as it is technically and physically feasible with a certain droop [50].

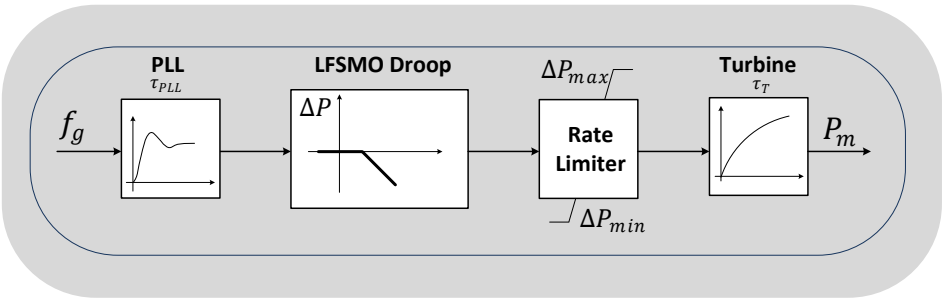

Figure 2.3: Control scheme of LFSM-O for a synchronous generator

Figure 2.3 illustrates simplified representation of the LFSM-O response in a conventional plant. According to the regulations in [51] and [1], the recommended response time for reducing active power in reaction to an increasing frequency for type 1 generating plants should be within 8 s, with a power reduction activation time of less than 2 s. This corresponds to a 45% change in active power relative to the

maximum power [49]. In Figure 2.3, the turbine model is represented as a first-order delay with a time constant of $\tau_T = 1.5$ seconds. Taking into account the combined delays from the turbine and generator time constants, it results in a response time of approximately 8 seconds to reach 90% of the power setpoint, as specified in the LFSM-O scheme [1]. Due to the slower response time of the turbine-generator model, the ramp rate limiter is set higher to ensure that the LFSM-O response aligns with the 8 s response time for conventional units. Additionally, a critically damped second-order delay with a time constant of 40 ms is used to model the PLL measurement delay [32]. It should be noted that certain exceptions, such as slow power rate limits, are acknowledged for various types of industrial plants as outlined in [1], but these exceptions are not considered in this work.

The LFSM-O droop characteristic is determined based on Equation 2.1 [49]:

$$\frac{\Delta P}{P_{ref}} = 20 \cdot \frac{(50.2\,\text{Hz} - f_g)}{50\,\text{Hz}} \tag{2.1}$$

In Equation 2.1, P_{ref} is the instantaneous power of the unit. It is recommended in NC RfG [1] that P_{ref} can be the max power of the unit, no matter of the actual operation point, in case of type 1 generating units[2] [1]. However, for type 2 power generating plants [3] (excluding storage units), P_{ref} can be the operation power at the instant when the value of 50.2 Hz is exceeded [1].

The response time primarily depends on various technical constraints, including unit specifications, operating conditions, and ambient factors. Following the power surplus event of 2006, studies indicate that to withstand a similar power surplus, the response time for LFSM-O performance should be less than 1 s [50].

[1] NC RfG stands for the Network Code, which describes the grid connection requirements for generators at all voltage levels.
[2] Type 1 power generating unit is generation unit which is solely comprises synchronous generators directly connected to the network (via transformers only).
[3] power generating unit not complying with the conditions specified for type 1.

Table 2.3: LFSM-O parameters settings for a synchronous generator, based on [49]

LFSM-O Parameters	Designed Value
Tolerance range of P_{ref}	±5%
LFSM-O threshold	50.2 Hz
$T_{response}$	$\leq$ 8 s according to [52]
$T_{initial-delay}$	$\leq$ 2 s according to [52]
τ_{PLL}	40 ms
τ_T	1.5 s
Droop gain (K)	-20 pu/pu

2.4.2 Modeling & Control of Converter-Based Generation

In the most renewable generation units that are connected to the grid via a VSC, the control mechanism emulates the behavior of a controlled current source than a voltage source [20]. As previously mentioned for CC2 in Chapter 2.3, in these types of controls, a set of power set points is provided, which are ultimately translated into the i_d and i_q references used in the current control loops [20]. The controller's objective is to track these reference DC current quantities in a fast reliable manner. In wind turbine applications, the bandwidth of the current controllers is typically selected in the range of 300-500 Hz. As a result, at harmonic frequencies above this range, the VSC behaves according to its true nature, functioning like a voltage source. However, for slower dynamics below 300-500 Hz, the controller operates as a controlled current source, capable of generating sinusoidal, distortion-free currents, even when the voltage at the PCC is distorted. These converters are unable to supply non-linear loads independently and they rely on another voltage source to establish the voltage and to absorb or supply the harmonic currents required by non-linear loads [53]. The operation mode is limited to the interconnected operation, and they will not contribute to voltage distortion mitigation and they don't naturally support the frequency gradient in case of unbalances after system splits [54].

Without major changes in these technologies, some extension can be implemented that current source converters emulate synthetic inertia similar to CC12 [54]. According to converter control classification in 2.3, such control concept are non

grid forming. In these control concepts, inertia emulation relies on the Rate of Change of Frequency (RoCoF) measurement and is not an inherent feature of the control concept. On the other hand, determining RoCoF is another challenge as it is susceptible with large errors and noises. Consequently, the overall performance in response to disturbances in the network is delayed due to measurement and filtering. If the measurement window is too large, it renders inertia emulation ineffective, as achieving a response within the first 20 ms becomes difficult due to the aforementioned delays. Additionally, measuring RoCoF over a small window and reducing the filtering lag may lead to overreactions due to high df/dt, potentially resulting in instability in the control actions in response to such high RoCoFs. Thus, SEBIR-based inertia provision performs similarly to fast frequency control with droop controllers in supporting frequency deviations [41]. However, neither can mitigate the initial df/dt nor enhance the overall network's resilience against imbalances and system splits.

Control of Power Converters in Wind Turbine Generation

Power electronic converters are applied in the renewable generation units for power conversion. For a general overview, Figure 2.4 illustrates a grid-side converter utilized in wind turbine applications along with its associated control system. The controller of the grid-side converter is responsible for controlling active and reactive powers, as well as power flow in the DC link, as illustrated in Figure 2.4. Additional features, such as FRT, can also be incorporated into the GSC control to ensure compliance with grid codes and provide voltage support at the point of connection [55]. The control unit of the machine side converter is responsible to capture maximum power from the wind, while the outer control loops implement pitch and speed control.

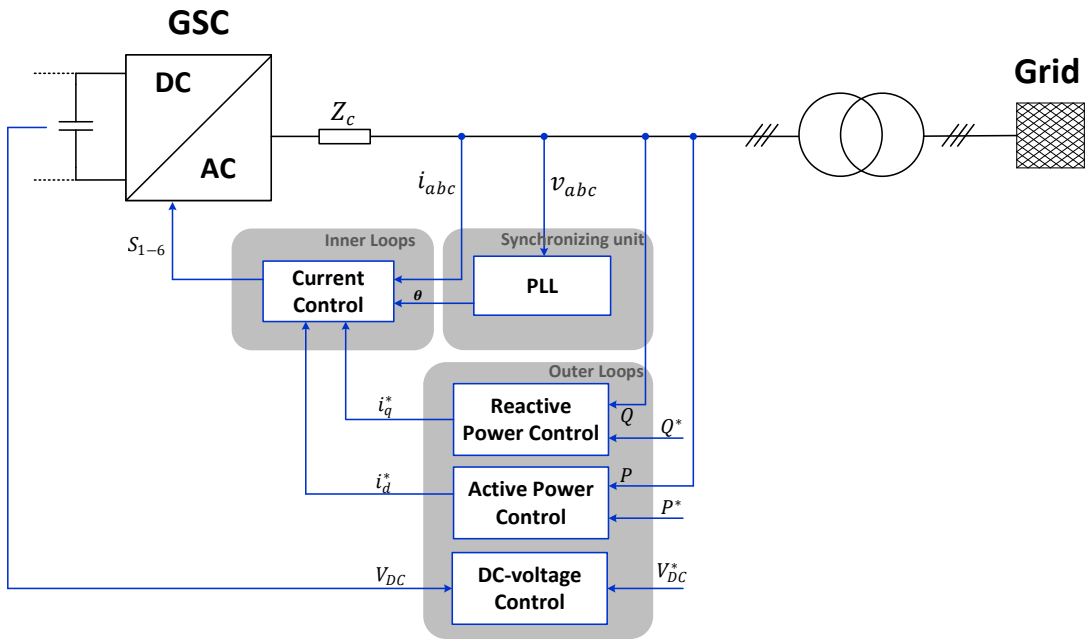

Figure 2.4: Block diagram of a grid side converter control for a type 4 wind turbine unit with permanent magnet synchronous generator

This thesis uses a simplified model of the GFL wind turbine. In this model, the Permanent Magnet Synchronous Generator(PMSG) and the active rectifier are replaced by a current source that feeds into the DC-link and acts as a constant power source. This is chosen due to two key factors. First, the studies in Chapters 4 and 5 focus on the impact of GFM wind turbines on islanding scenarios. Second, these GFL units, equipped with full-scale power converters and their control structure, completely decouple the generator from the grid. Therefore, a simplified GFL wind turbine is adequate for studying these scenarios, effectively representing the already installed GFL units that operate as current sources. In the following, the control of grid-side power converter used in wind generation plants is explained briefly.

In typical wind turbine applications, the grid-side converter is connected to the network through an LC filter [55]. However, since high-frequency harmonic attenuation around the switching frequency is not the focus of this work, the filter is simplified to an L-filter, as shown in Figure 2.4 [56], [57]. A common approach to control the inverter output voltages is via controlling the currents. In this way,

the three-phase current is transformed to stationary reference frame, resulting in the *dq* current components. The method, known as *Voltage-Oriented Control*, is illustrated in Figure 2.5 [55]. To simplify the control tasks, the two controllers operate on DC current quantities [55]. The DC-link voltage controller's output sets the d-component of the current reference for the inner controller, while the setpoint for the q-component is initially set to zero to maintain zero reactive power at the PCC. In the following, the control scheme is extended with upper-level controllers that adjust the current setpoints based on grid frequency and PCC voltage, which will be discusses in Section 2.4.2.

In this method, a synchronization unit is needed to yield precise detection of the phase angle and amplitude of the grid voltage. A synchronous reference frame PLL (SRF-PLL) provides the information of the grid voltage amplitude, frequency and phase angle for the control unit of the grid side converter to synchronize to the grid in the connection point, as shown in 2.4. The PLL converts the three-phase voltage vector from the abc reference frame to the rotating *dq* reference frame. A PI controller keeps the error of the *q* component of grid voltage zero and via that, it regulates the angle. Therefore, in the steady state, the voltage of the grid is aligned to the *d* component [18], [55].

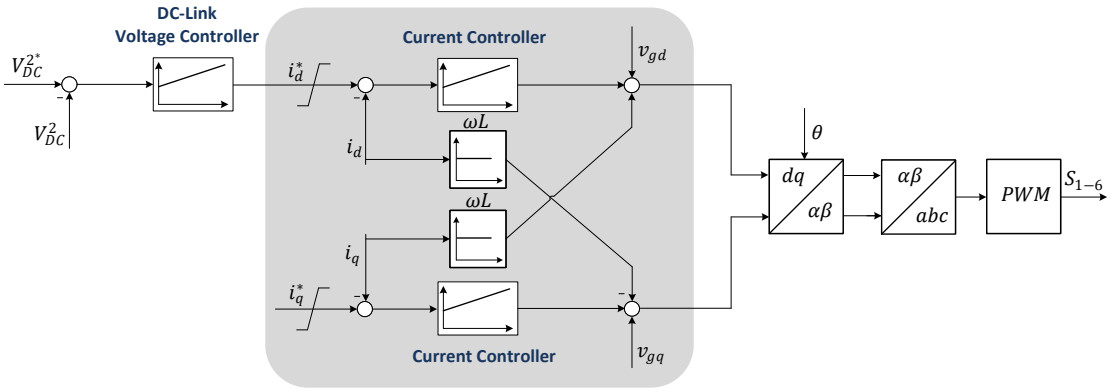

Figure 2.5: Block diagram of the closed-loop voltage oriented control based on the synchronous dq frame

Based on the grid voltage information, the desired power transfer can be achieved by controlling the converter voltages through a cascaded control loop [55]. The

outer controller regulates the DC voltage to control the power flow, with the primary objective of ensuring rigidity and stability in the DC-link [55]. The *Feedback Linearization* method is a well-established and proven control technique, widely used in various literature for regulating DC-link voltage in back-to-back configurations. Therefore, this method has been selected in this thesis for controlling the DC-link voltage in the GSC [58]. In this method, the square of the DC voltage, $E = V_{DC}^2$, is used to represent the dynamics of the DC voltage, rather than using V_{DC} directly. The bandwidth of the DC-link controller is selected to be 10 times smaller than that of the inner loops to effectively decouple the inner loop dynamics from the outer loop design [55][18]. The two internal current controllers are designed to generate the converter voltages, enabling rapid power delivery to the grid. This control approach is well-documented in the literature; see [59], [56], [60], and [55].

The currents are controlled in the inner loops to manage the active and reactive powers. The active power flow is determined by current d component and q component determines the power factor for operation in under excitation or over excitation region based on the grid codes [61]. Based on the instantaneous power theory, considering that $v_{gq} = 0$, the active power is proportional to i_d, while the reactive power is proportional to i_q [55].

$$P = \frac{3}{2}(v_{gd}i_d + v_{gq}i_q) \tag{2.2}$$

$$Q = \frac{3}{2}(v_{gq}i_d - v_{gd}i_q) \tag{2.3}$$

The design of the internal current controllers in this work is implemented using an *Internal Model Controller* [58]. Typically, the current control time constant is selected in the range of 1-2 ms to achieve a good tracking of the reference currents as well as dynamic stiffness.

Table 2.4: Inverter and control parameters for grid following WT

Parameters	Values
Rated current I_n (RMS)	2930 A
Rated grid voltage V_g (Ph-N RMS)	398 V
Rated apparent power S_n	3.5 MVA
τ_{PLL}	40 ms
Switching frequency (f_{sw})	5 kHz
Filter inductor L_c	4.45×10^{-5} H
Filter resistance R_c	0.0014 Ω
X/R	10
DC voltage (V_{DC})	1100 V
DC capacitor (C_{DC})	15 mF

Control of Power Converters with Grid-Supporting Capabilities

The control used in chapter 2.4.2 models the wind turbine as a controlled current source, where the current flow is dependent on the voltage at its terminals. Due to the current source nature, high controllability over current, and a synchronization unit with high dynamic performance, the GSC can adjust its output voltage almost instantaneously (within 2 ms) during transients to maintain constant current references [23], [20]. Although a voltage source converter can naturally respond to grid voltage variations within a few milliseconds outside its bandwidth, it lacks the capability for prolonged responses to counteract voltage fluctuations over periods ranging from several milliseconds to 20 milliseconds or longer. This is shown later in chapter 5 during islanding tests with a weak grid with a high proportion of GFL wind turbine units.

However, to enhance power system stability, grid codes mandate a fast frequency-sensitive mode when the frequency exceeds 50.2 Hz to rapidly reduce power generation as a necessary remedial action for rebalancing the load in a power system dominated by Renewables (RENs) [62]. Frequencies above 50.2 Hz are considered a critical network state, requiring all generating units to participate in reducing power imbalance. Wind turbine generators also adjust their power feed-in when the LFSM-O is activated [1]. During interconnected operation, the unit may disconnect

from the rest of power system, if the frequency reaches 51.5 Hz; however, this does not apply to all units [1]. The GFL wind turbine extension for LFSM-O utilizes a P(f) droop controller [31], as illustrated in Figure 2.6.

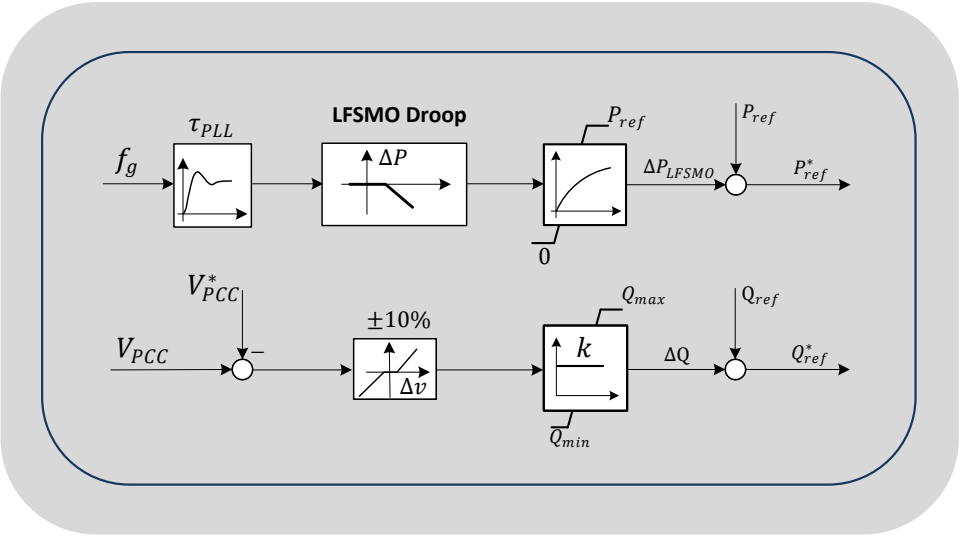

Figure 2.6: Extension for grid support on GFL-WT

The droop coefficient and response time for the LFSM-O is determined in accordance with the grid codes [1]. The LFSM-O response is characterized by a first-order delay with a time constant of $t = \tau_{LFSM-O}/3$, which results in a response time of 2 s to reach 90% of the power setpoint. The output of LFSM-O adjusts the active power set point, similar to CC2 and CC12 in [32],[20]. In this work, the simplified GFL-WT model allows to directly decrease the generator's power input by modifying the current source set-point. The SEBIR-based inertia extension, however, which is designed for inertia/fast frequency support, requires an external energy source in the GSC, which is beyond the scope of this thesis.

In addition, as the power system strength decreases due to reduced short-circuit power, wind turbines need to contribute to voltage support as well. Reactive power control for injecting fault current can be achieved by modifying the control system of a standard GFL wind turbine unit through the implementation of a proportional reactive power controller [62]. Figure 2.6 shows the extension for grid voltage support via Q(V) droop.

The dynamic voltage controller block shown in Figure 2.6, is responsible for the grid voltage support during grid faults. The amplification factor k is selected by the network operator to range between 2 and 6, aiming to achieve specific stability objectives during the planning phase [1]. According to [63], if a response similar to that of a synchronous generator is desired, a constant factor of 1.9 - 2.2 can be assumed for the wind turbine controller at the high voltage terminal.

Additionally, a dead band of $\pm 10\%$ is applied to the voltage to prevent the controller from overreacting under normal operating conditions [31]. Upon fault detection, active power in-feed should be reduced in favor of the reactive current, which can increase up to 100% of nominal current depending on the voltage dip. According to grid codes, the reactive current's step response must be within 30 ms, with a settling time below 60 ms [1], [21],[62].

2.5 Summary

This chapter primarily focuses on identifying the control requirements for RENs to replicate the performance of conventional synchronous generator units in the power system and subsequently investigates which control concepts can meet these requirements.

Various terms are used to describe newly developed control concepts. As a first step, three different methods were compared based on criteria for classifying control methods that aim to replace synchronous generators. The ENTSO-E requirements were ultimately selected as the standard for categorizing different control concepts under the term "Grid Forming." In chapter 2.3, a comprehensive literature review was conducted, focusing on recent publications concerning control concepts developed to stabilize AC network. The findings, summarized in Table 2.1, highlight the key requirements for control methods to achieve GFM functionalities as outlined by ENTSO-E.

In chapter 2.4, a conventional unit with synchronous generator along with its control blocks, as well as a GFL-WT is explained. System-level controls, such as LFSM-O and the extensions for GFL-WT units, have been introduced as well

to make them capable of supporting a weak AC network. The generation units developed in 2.4 are used in Chapter 3 to benchmark the performance of GFM-WT during grid events in comparison to these units. In addition, in chapters 4 and 5, these units are tested as conventional generation units alongside GFM-WTs in islanding scenarios.

3 GRID FORMING CONTROL APPLIED TO WIND POWER GENERATION

3.1 Introduction

When a voltage source converter is controlled to function as a voltage source, its control must incorporate the essential characteristics of a synchronous machine. This includes modeling the mechanical rotor, such as the inertia constant, damping factor, and other steady-state control functions similar to those of a traditional synchronous machine governor. In these schemes, the converter operates as a balanced positive-sequence voltage source behind an impedance. Since the magnitude and phase of the voltage source vary with a low bandwidth (typically below 5 Hz), it inherently mitigates and counters voltage vector changes by absorbing and injecting current [19]. According to ENTSO-E, such converters can generate voltage, respond intrinsically to frequency and angle deviations, and deliver fault current within their physical limits [19].

3.2 Control Principles of Converters with Voltage Source Features

With a GFL-WT, grid support can be achieved by modifying the control loops, as discussed in Chapter 2.4.2. However, providing instantaneous reserves, which is critical immediately following an event (within the first 20 ms), is hindered in GFL units due to the measurement time of the PLL and delays associated with RoCoF measurements [64]. As a result, the crucial response time needed to protect the grid during such events is missing, which could endanger the stability of the power system and lead to system splits. Additionally, in power systems dominated by GFL units, the reduction in short circuit power leads to increased voltage sensitivity.

This results in a so-called low-strength grid, which is vulnerable to various transients and disturbances. Consequently, it is required that the share of GFL units becomes limited, particularly in relation to the remaining synchronous generator units in order to maintain system stability [7], [64]. To facilitate higher integration of NSG while maintaining grid stability, GFM units have been introduced that can operate independently in both grid-connected and islanding modes. Their active and reactive power delivery depends on the AC voltage to which they are connected or the loads. They can mimic SG features, such as power sharing and inertia emulation, by considering their design criteria and physical limitations.

Several control concepts from the literature that aim to replicate the desired properties of synchronous machines was discussed in Chapter 2.3. Many of these methods use a 2nd-order rotor transfer function, linking the virtual rotor angle to active power, which enables synchronization to the grid through active power control and the resulting load angle. The 2nd-order swing equation is used in Virtual Synchronous Machine [27], Power Synchronization Control [33],[53], Synchronverter [65],[29], Droop Controller [66], among others [67],[68],[69],[70],[71].

In Chapter 3.2.1, the inertia emulation and power controllers for the VSM are discussed. Subsequently, the VSM is compared with the modified VSM and RVCC using the quasi-stationary transfer function of the closed-loop controller to highlight differences and similarities in their control strategies, particularly in terms of inertia provision, response to angle changes, and frequency ramps. The remainder of Chapter 3 presents a comprehensive GFM concept based on CC16 (Modified Rotating Voltage Vector Control) for wind turbine applications.

3.2.1 Virtual Synchronous Machine

The main goal of the VSM concept is to emulate the inertia and damping characteristics of a synchronous machine without relying on a full-order mathematical model. In a 2nd-order swing equation, the inertia constant (H) and damping coefficient, unlike in a real synchronous generator, are design parameters that can be selected to achieve the desired dynamic behavior [27]. The swing equation is

initially expressed in terms of torque, as shown in equation 3.1:

$$J\frac{d\omega}{dt} = T_0 - T_{el} - D(\omega - \omega_g) \tag{3.1}$$

In 3.1, J is the rotor inertia, ω is the rotating speed of the virtual machine, ω_g is the grid angular frequency, T_0 is the mechanical torque and T_{el} is electromagnetic torque [27]. By replacing the torques with power and scaling the entire equation to nominal power, equation 3.1 can be reformulated as follows [27]:

$$T_a \cdot s \cdot \omega_{pu} \approx P_0 - P_{el} - k_{pf}(\omega_{pu} - \omega^*_{pu}) \tag{3.2}$$

The mechanical time constant is expressed as $T_a = 2H$ in 3.2. The virtual rotor angular position in a VSM is obtained by integrating the frequency, ω_{pu}. This angular position determines the phase angle of the voltage generated by the VSM model [27], [28]. The amplitude of the VSM voltage can then be given by either a reduced order electrical model of the synchronous machine or directly by a separate reactive power control loop [27]. Figure 3.1 illustrates the power-angle controller of the virtual synchronous machine, along with an overview of the VSM reactive power control structure [27], [28].

The core of the GFM can be modified to meet different grid-forming requirements, such as inertia, damping properties, and steady-state droop characteristic. The outputs of these two controllers within the VSM core adjust the converter's voltage vector to transfer a specified amount of active and reactive powers.

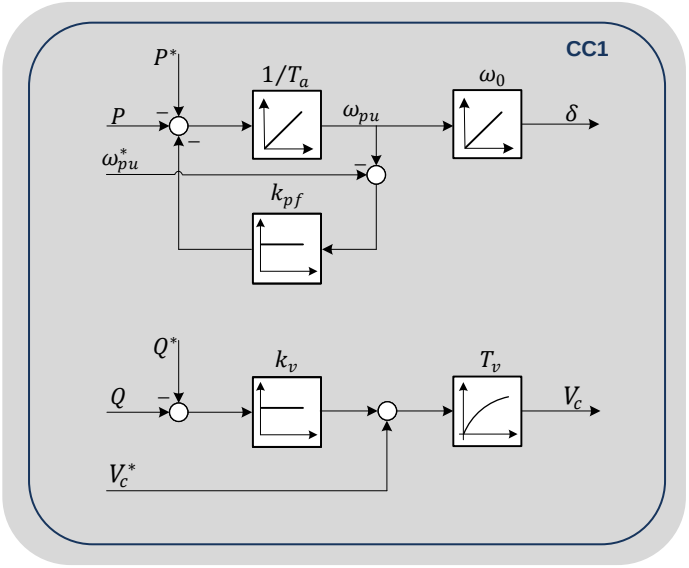

Figure 3.1: Block diagram of VSM with inertia emulation and reactive power control

In the control shown in Figure 3.1, P^* is the reference active power, P is the measured active power, and the k_{pf} is the damping and the droop coefficient for the primary frequency control. The damping parameter is necessary to keep the stability of the closed-loop system [32]; However, it imposes a contribution from the primary frequency response, which is undesirable in wind turbine applications. Sections 3.2.2 and 3.2.3 discuss alternative GFM methods that allow the unit to deliver instantaneous power without contributing to primary frequency control.

3.2.2 Modified Virtual Synchronous Machine

In order to eliminate the effect of the primary frequency control, or make it an optional choice without impacting dynamic stability, modified GFM methods have been introduced [32]. In Figure 3.2, the feedback damping coefficient k_{pf} enables proportional frequency control. Alternatively, when proportional frequency control is not desired, a feedforward signal is adding an offset to the controller angle to avoid oscillation caused by having two consecutive integrators [32], [72]. This method which is a modification of VSM is referred here in this work as *Modified-CC1*.

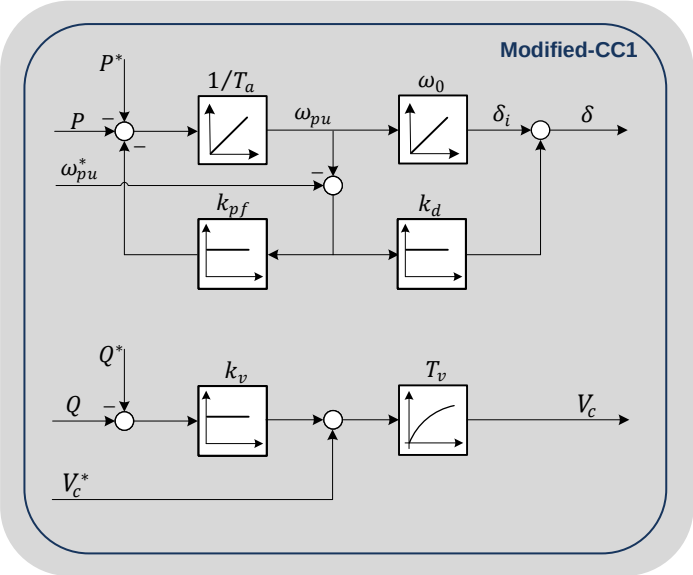

Figure 3.2: Block diagram of Modified-VSM with inertia emulation and reactive power control

In Figure 3.2, the inertia constant is selected based on the requirements, while the feedforward damping coefficient is a design choice that can be adjusted to achieve a specific damping ratio in the closed-loop system [72].

3.2.3 Initial Control Concept for Rotating Voltage Vector Control

The Rotating Voltage Vector Control (RVVC) was first introduced in 2017 [37], as an alternative approach for controlling a VSC to function as a voltage source and emulate inertia. The concept aims to modify the control of the GSC in existing wind generation units to provide instantaneous reserve, within their operational limits and with minimal changes in the control strategy. The block diagram of the RVVC concept is illustrated in Figure 3.3. The control concept replaces the state-of-the-art GFL control of the grid-side converter in wind turbines with a system that synchronizes to the external grid using its internal angle. This control emulates inertia, operates in island mode, offers optional primary frequency control, and provides support to the grid during transients such as angle jumps, frequency variations, and voltage amplitude changes [37].

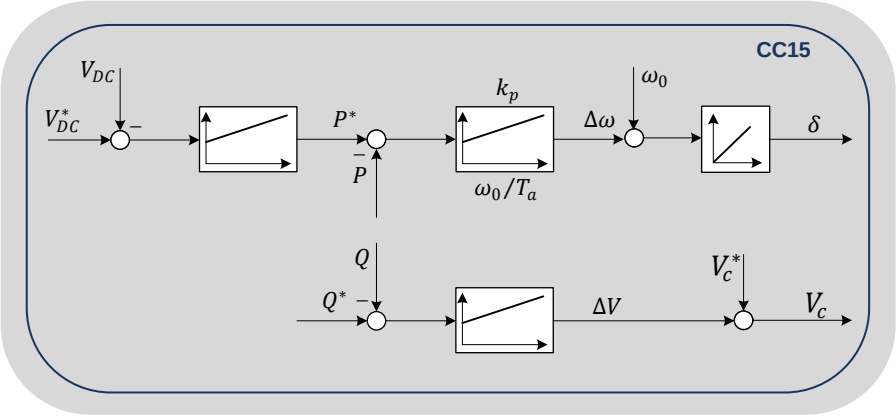

Figure 3.3: Control structure of initial RVVC [37]

As shown in Figure 3.3, the inner controller determines the angle of the converter's internal voltage vector (δ) by regulating the active power. The outer control, similar to a traditional GFL control configuration, controls the power flow to the grid by regulating the DC voltage [58]. The reactive power loop uses a PI controller to regulate the magnitude of the converter voltage vector. Therefore, this control approach eliminates the need for a PLL for synchronization and provides an initial inertia response using the energy stored in the DC-link capacitor. However, there are several concerns regarding this control structure, which are summarized below [37]:

- The concept is proposed for WT applications, in which DC-link voltage margin is very low. The choice of DC-link capacitor is realized to keep the voltage in the DC bus stable, and meet certain criteria for the manufactures. Therefore over dimensioning is additional cost and design burden, as the provision of system services has not been required for renewable energy sources so far. Hence, with the typical values used for the wind turbine capacitors, the energy content headroom is very limited before meeting the modulation index limit and further discharging of the DC link [37]. Taking into account that the voltage of the DC-link capacitor can drop by only about 10% before reaching the limit of the modulation index and losing controllability over the converter's voltage vector, the energy content of the DC-link capacitor is not comparable (several hundred times smaller) to that of a synchronous

generator with lumped inertia from the turbine and generator mass. This feature is illustrated in Figure 3.4, which displays the performance of the RVVC in response to a negative 10-degrees angle jump in the grid.

- Another issue concerns the control design. Due to the low bandwidth of the inner control loop, maintaining the stability of the cascade structure is not feasible unless the DC-voltage controller operates with a very low bandwidth (0.5 - 1Hz). This has a major drawback regarding disturbance response of the controller. When the wind turbine loading changes rapidly due to gusty wind conditions or after a sudden angle jump in the grid, the DC-link controller is unable to track these fast transients. For instance, in the case of a negative angle change, the DC-link discharges to a level where, due to modulation index limitations, maintaining the operating point becomes impossible. Consequently, in response to this angle change, the reactive power output becomes larger than the active power, as illustrated in Figure 3.4.

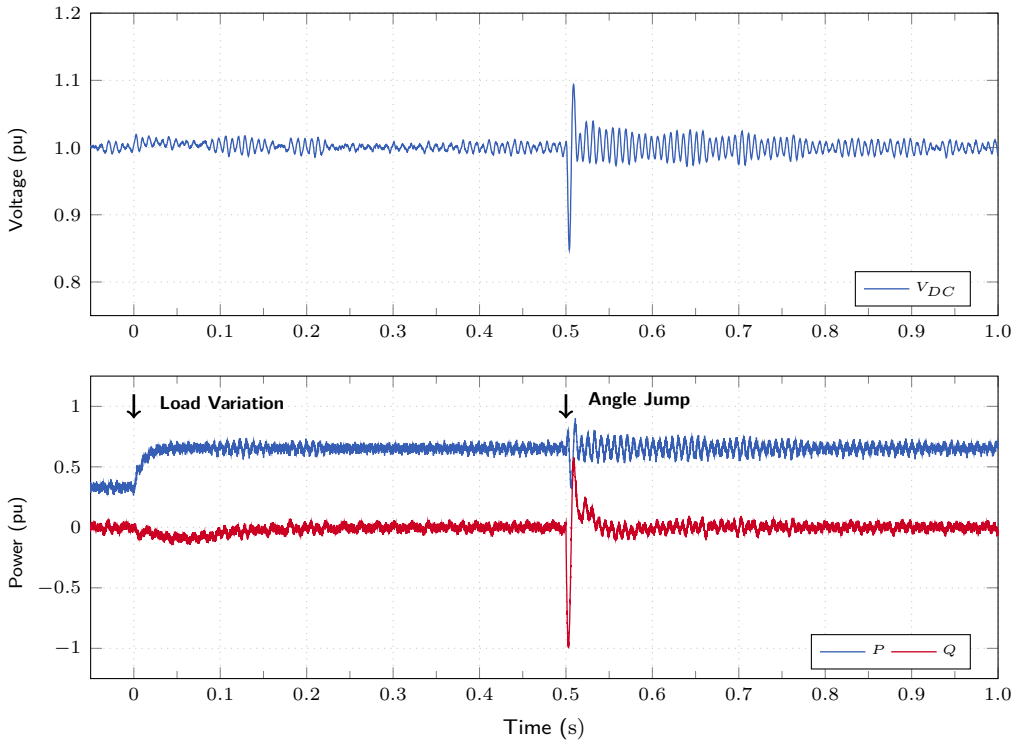

Figure 3.4: Performance of RVVC in load variation and angle jumps

With the structure shown in Figure 3.3, the DC-link controller in the GSC provides limited grid support, depending on the severity of the disturbance and the ability of the DC chopper to dissipate excess energy during a grid load rejection. To release the inertia stored in the generator and rotor in a wind turbine application, the RVVC structure needs to be modified. Chapter 3.2.5 discusses in detail how the modified RVVC is implemented, making it suitable for WT operation by linking grid disturbances to generator-side control and enabling the provision of inertia from the WT to the grid.

3.2.4 Comparing the Grid Forming Control Schemes

This chapter compares three aforementioned control concepts, on their core of GFM, their dynamic performance for inertia emulation and primary frequency support. In the following a basic principle of the GFM unit is introduced, which allows investigation of the unique features of each control techniques. A converter with GFM control is connected to an infinite bus, which is represented as Thévenin equivalent model with a short circuit ratio (SCR = inf), via an inductive impedance. The power exchange between converter and the grid is shown in Figure 3.5.

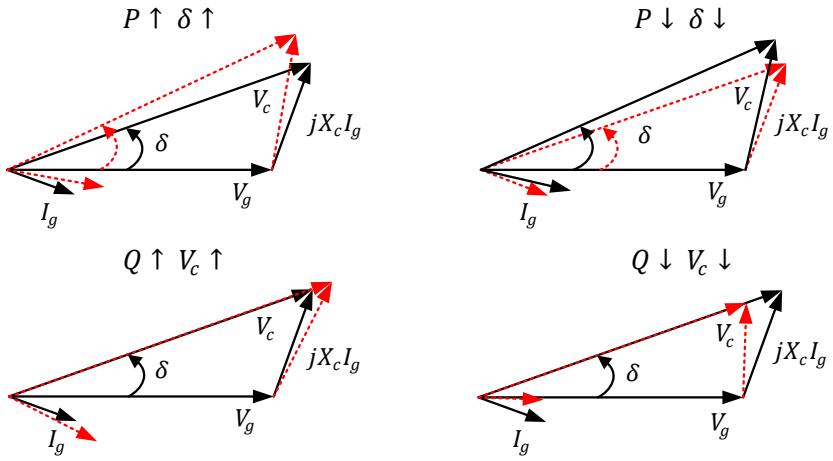

Figure 3.5: Operating principle of a GFM unit

According to Figure 3.5, V_g and V_c are the grid and converter voltage vectors, respectively. The active power can primarily be controlled via the angle between

two voltage sources, and the difference between the sources voltage magnitude determines the direction of reactive power flow. As the grid voltage is assumed to be stiff, then adjusting the angle controls active power, and adjusting voltage of converter, the reactive power, respectively. This angle is known as a load angle [44] and typically, the value of it aligns in the linear area of the sine function even with low $SRC \approx 2$. This assumption is used for linearization of 3.3 and 3.4 around load angle ($\sin(\delta) = \delta$ and $\cos(\delta) = 1$):

$$P = \frac{V_c V_g sin(\delta)}{X_c} \approx \frac{V_c V_g \delta}{X_c} \tag{3.3}$$

$$Q = \frac{V_c^2 - V_c V_g cos(\delta)}{X_c} \approx \frac{V_c(V_c - V_g)}{X_c} \tag{3.4}$$

The above assumption is true in the linear area of sine function (approximately up to 30 degrees). In case the power converter is connected to a very weak grid (SCR = 1.1 or lower) or facing very severe grid events (above 30 degrees angle jumps), the aforementioned assumption is not true anymore, and the control performance may differs from the desired behavior in these events.

Using Equation 3.3, and assuming the power converter behaves as an ideal voltage source, the linearized grid behavior can be described as [72]:

$$SPC = \frac{V_c V_g cos(\delta)}{X_c} \approx \frac{V_c V_g}{X_c} \tag{3.5}$$

In Equation 3.5, SPC denotes the Synchronizing Power Coefficient. Taking Equation 3.5 into account and considering the active power-angle control loops of all three control strategies, the closed-loop active power response of each scheme can be illustrated. In the following discussion, the virtual synchronous machine approach is referred to as *CC1*, the modified VSM as *Modified-CC1*, and the Rotating Voltage Vector Control as *CC15*.

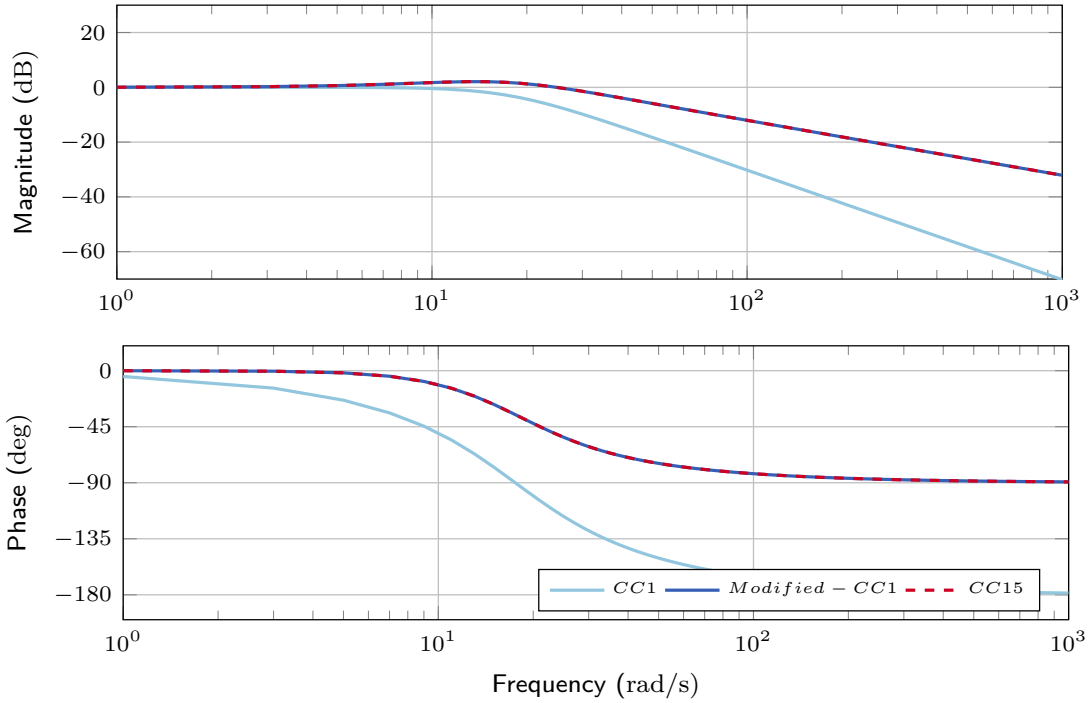

Figure 3.6: Close-loop frequency response of CC1, Modified-CC1 & CC15, using the static plant model

Figure 3.6 compares the close-loop frequency responses of the three control strategies. All three concepts use the same inertia constant. The design parameters, namely, k_{pf} of CC1 (see Figure 3.1), k_d in Modified-CC1 (see Figure 3.2) and k_p in CC15 (see Figure 3.3) are selected to achieve the desired damping in the closed-loop control system.

As shown in Figure 3.6, both CC15 and Modified-CC1 controllers have significantly higher bandwidth than the CC1 controller. This makes them more effective at responding to high-frequency changes and disturbances, which is particularly useful in dynamic systems and beneficial for a cascaded control structure. In contrast, CC1 has a bandwidth around 3 rad s^{-1} similar to a traditional synchronous machine and it introduces more phase lag compared to the CC15 and Modified-CC1 at frequencies above 10 rad s^{-1}.

Figure 3.7 compares the performance of the three controllers in terms of command tracking and their response to angle and frequency disturbances. The step responses

of both CC15 and Modified-CC1 methods are identical, as are their responses to the angle jump. In contrast, CC1, which has a lower bandwidth, exhibits a slower step response and a longer angle jump power due to the integration of the damping power in response to angle variations. This is evident in Figure 3.7 at 1 s, where the response of CC1 to an angle jump is prolonged compared to the other two concepts. This can be explained by looking at the swing equation in 3.2.

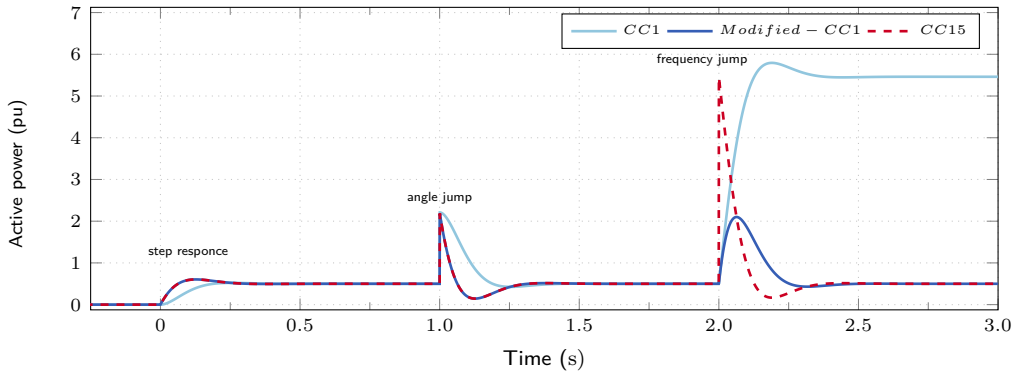

Figure 3.7: Step jump, angle jump and frequency jump response of close-loop power frequency controller with VSM (CC1), Modified-VSM (Modified-CC1) & RVVC (CC15) using the static plant model

For small deviations in angular frequency following the angle jump, the damping factor k_{pf} which mimics the behavior of a damper winding, generates a damping power given by $\Delta p = k_{pf}\Delta\omega$. This damping power is proportional to the frequency deviation. Depending on the sign of the speed deviation, this power is either added to or subtracted from the electrical power P_{el}, leading to damped rotor oscillations following a disturbance. This behavior is akin to that of a synchronous generator responding to an angle jump. A more detailed explanation can be found in [46].

In addition, a frequency jump is applied to the grid at 2 s. As mentioned earlier, both Modified-CC1 and CC15 are able to eliminate the power-frequency droop function of CC1. As it is illustrated in Figure 3.7, in a steady state range of the event, both CC15 and Modified-CC1 exhibit a power contribution of zero in response to disturbances in grid angular frequency. In contrast, CC1 adjusts its power output in proportion to this disturbance in angular frequency. Hence,

according to the above comparison and discussion of each concept's performance, the following conclusions can be drawn:

- The Modified-CC1 method [32], [72], developed to eliminate the inherent droop characteristics of the CC1 approach, demonstrates performance comparable to the CC15 method. The original CC1 method is economically impractical under the current policy of operating wind turbines in Maximum Power Point Tracking (MPPT) mode, as it requires WTs to curtail a portion of their available power, causing the wind farm to operate similarly to a conventional power unit.
- The use of the Modified-CC1 and CC15 methods ensures that, in the event of a frequency deviation, wind turbines contribute only during the dynamic phase without providing power during the steady-state phase. This approach eliminates the risk of WTs falling to the cut-in speed range while operating in MPPT mode.
- In the future, where WTs will be required to participate in ancillary services, they need to operate in curtailed mode. As a result, the economic viability and reliability of providing primary frequency support, given the variable nature of wind energy, remain uncertain.

Based on the above discussion, it is clear that the RVVC core of the GFM method (CC15), is a suitable option when only inertia from the rotating mass of the wind turbine is required. However, in Chapter 3.2.3, certain issues were highlighted, explaining why the RVVC structure shown in Figure 3.3 cannot meet the following control objectives: 1) operating in MPPT mode and injecting all available wind power into the AC grid under normal conditions, and 2) providing instantaneous reserve in both directions during grid disturbances. To address these challenges, the RVVC structure is modified in Chapter 3.2.5 for application in a WT system with a back-to-back configuration. The design procedure is detailed to ensure stability under varying grid conditions. Finally, the system is tested under different grid disturbances and its performance is compared to that of a conventional unit with SG and GFL unit.

3.2.5 Modified Rotating Voltage Vector Control

In order to make RVVC compatible with wind turbine application, certain modifications are required in the control structure [39]. The core control mechanism for active and reactive power remains almost unchanged compared to the structure shown in 3.3. In this section, the modeling and control aspects of the modified RVVC applied to the GSC of an onshore wind turbine will be discussed. Based on dynamic modeling, additional control features will be introduced, followed by the selection of parameters for the closed-loop control, considering grid-forming functionalities, stability factors, and the physical limits of the converter.

Dynamic Performance Analysis Using Small-Signal Model

To derive the dynamic model in the dq rotating frame, the following assumption is made: the d-axis is aligned with the grid voltage, where $V_{gd} = V_g$ and $V_{gq} = 0$. Based on this alignment, the converter's direct and quadrature voltage components can be expressed as $V_{cd} = V_c \cos(\delta)$ and $V_{cq} = V_c \sin(\delta)$. In addition, as the grid frequency ω_g varies only within a small range, its deviation can be neglected and assumed to be $\omega_g = 1$ pu. The dynamic currents in the dq frame are then given by [30]:

$$\frac{d}{dt} i_{gd} = \frac{\omega_0}{L_c} V_c cos(\delta) - \frac{\omega_0}{L_c} V_g - \frac{R_c \omega_0}{L_c} i_{gd} + \omega_g \omega_0 i_{gq} \tag{3.6}$$

$$\frac{d}{dt} i_{gq} = \frac{\omega_0}{L_c} V_c sin(\delta) - \frac{R_c \omega_0}{L_c} i_{gq} - \omega_g \omega_0 i_{gd} \tag{3.7}$$

The nonlinear terms $V_c \cos(\delta)$ and $V_c \sin(\delta)$ are then linearized around the operating point δ_0 and substituted into the current equations. Using the instantaneous power theory (details provided in Chapter 7.2), the following transfer functions in the

Laplace domain for active and reactive power are derived [30]:

$$\begin{bmatrix} \Delta P_{ac}(s) \\ \Delta Q_{ac}(s) \end{bmatrix} = \begin{bmatrix} T_{p\delta} & T_{pV} \\ T_{q\delta} & T_{qV} \end{bmatrix} \begin{bmatrix} \Delta\delta(s) \\ \Delta V_c(s) \end{bmatrix}$$

$$\begin{bmatrix} \Delta P_{ac}(s \sim 0) \\ \\ \Delta Q_{ac}(s \sim 0) \end{bmatrix} = \begin{bmatrix} \frac{V_{c0}V_g}{L_c\omega_g}\cos(\delta_0) & \frac{V_g}{L_c\omega_g}\sin(\delta_0) \\ \\ \frac{-V_{c0}V_g}{L_c\omega_g}\sin(\delta_0) & \frac{V_{c0}-V_g\cos(\delta_0)}{L_c\omega_g} \end{bmatrix} \begin{bmatrix} \Delta\delta \\ \\ \Delta V_c \end{bmatrix} \tag{3.8}$$

The complete transfer function is illustrated in Chapter 7.2 and can be simplified according to the equation 3.8. Focusing on the region with slow dynamics and assuming ($R \ll X$), the MIMO transfer function can be reduced to four static gains. In the power matrix, the diagonal elements play a significant role in determining both active and reactive power ($cos(\delta) \sim 1$), while the off-diagonal elements contribute minimally ($sin(\delta) \sim 0$) [30]. Subsequently, the frequency response of the linear model will be examined over various frequency ranges and compared with the non-linear model. The validation of the transfer functions is essential for their use in designing the closed-loop system.

Step Response Analysis: Linear vs. Nonlinear Models

To validate the linearized model, a step change in angle ($\Delta\delta$) is applied to both the linearized and non-linear models in MATLAB. Since the zeros of the transfer functions (see Chapter 7.2) depend on the initial operating point, the step responses of $T_{p\delta}$ and $T_{q\delta}$ are shown in Figure 3.8 for an operating point of 1.0 pu. The step response highlights the similarities between the two models. As shown, both models exhibit stationary cross-coupling between active and reactive power, along with undamped oscillations at the fundamental frequency of 50 Hz.

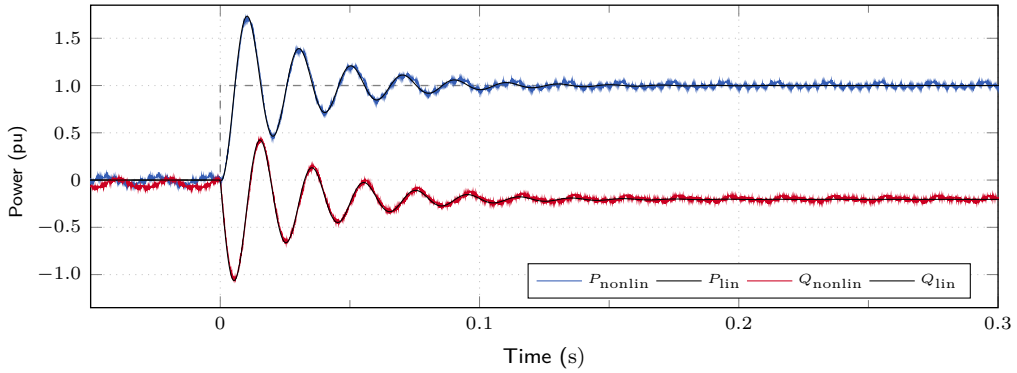

Figure 3.8: Comparing linear vs. nonlinear model with 10-degree angle jump, $V_c = 1$ pu, $V_g = 1$ pu

Figure 3.9 illustrates the Bode plot for $T_{p\delta}$ and $T_{q\delta}$. The plots reveal a pronounced peak in magnitude around the frequency of 314 rad s^{-1}, indicating resonance at this frequency for both transfer functions.

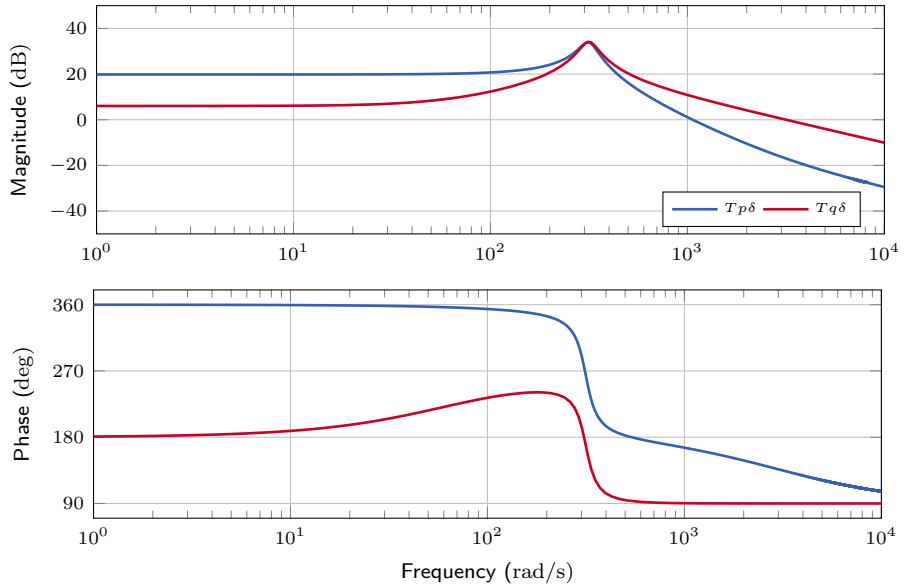

Figure 3.9: Frequency response of $T_{p\delta}$ and $T_{q\delta}$ at operation point of $P_{ac} = 1$ pu

It can be observed that in the operation point of 1.0 pu, $T_{p\delta}$ is dominant comparing to the $T_{q\delta}$ in frequencies below 314 rad s^{-1}, assuming the voltage of both voltage sources are constant. However, at frequencies close to the resonant frequency and afterwards, the gains of non-diagonal transfer function ($T_{q\delta}$) is amplified [30]. This increases the cross-coupling between active and reactive power during high dynamics, and make the control tasks more complicated.

$$z_{1-2} = \pm\omega_g\omega_0 = \sqrt{\frac{cos(\delta_0)}{\frac{V_g}{V_{c0}} - cos(\delta_0)}} \tag{3.9}$$

The full transfer function of the MIMO system is shown in 7.2. Looking at the zeros of transfer functions particularly $T_{p\delta}$ reveals their dependency on the operating point. The zeros are located in both the Left Half-Plane (LHP) and the Right Half-Plane (RHP). The RHP zeros induce a delay and difficulties for the bandwidth of the closed-loop control [73]. The zeros reach origin in $[\pm\pi/2]$. In weak grids, where the load angle or initial voltage amplitude is high, the zeros move closer to the origin, making stable feedback control unfeasible [73]. Furthermore, as shown in 7.2, a pair of conjugate poles is located at the grid frequency which was seen in Figure 3.9 as well. These poles can be formulated as [30]:

$$s_{1-2} = \underbrace{-\frac{R_c}{L_c}\omega_0}_{\Re} \pm \underbrace{j\omega_g\omega_0}_{\Im} \tag{3.10}$$

The damping of these pole pairs depends on the values of the converter filter and the grid impedance at the connection point [30]. Connection to medium-voltage transmission lines, the impedance is typically much larger than the resistance ($X \gg R$), resulting in poor damping of the pole pairs. Assuming connection to a very stiff grid with $SCR = inf$, the location of the pole pairs depends solely on the filter's ($X \gg R$) ratio. Given that the filter impedance corresponds to 10% short-circuit voltage and $X/R = 10$, the pole pairs approach the imaginary axis,

resulting in very low damping [30]:

$$\zeta_{s_{1-2}} = \frac{\Re}{\sqrt{\Re^2 + \Im^2}} = \frac{R_c}{\sqrt{R_c^2 + (L_c\omega_g)^2}} \approx 10\% \tag{3.11}$$

This resonant peak introduces challenges for control, primarily by reducing the system's phase margin and causing power oscillations. Additionally, the system's damping is minimal, making stability vulnerable across various operating points. This issue has been highlighted in other studies, addressing the Synchronous Resonant Frequency (SRF) damping challenges in all swing-based grid-forming approaches [2], [74], [75], [76].

Virtual Resistor

To enhance the damping of the SRF, adding virtual resistance (R_v) helps by shifting the pole pairs into the LHP [76]. The approach involves subtracting the virtual voltage drop from the converter voltages along the dq axis relative to the grid currents. Figure 3.14 illustrates virtual resistor block diagram in the dq reference frame.

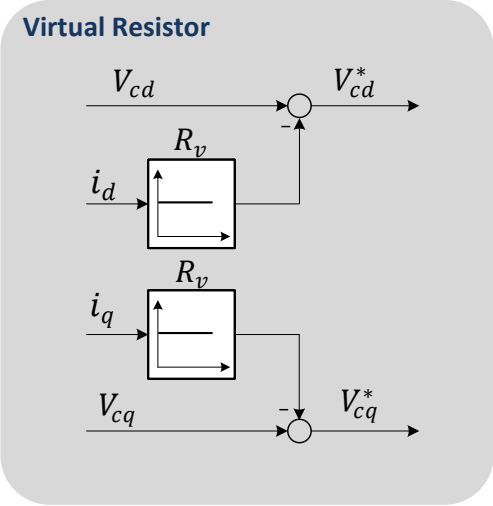

Figure 3.10: Block diagram of the virtual resistor in the dq reference frame

For a damping target of 70%, the required value of the virtual resistance is

approximately $R_v = 0.09$ pu. This R_v value is incorporated into both the nonlinear model and the dynamic linearized transfer functions. The bode diagram of Figure 3.11 shows the $T_{p\delta}$ and $T_{q\delta}$ at operation point of $P_{ac} = 1$ pu with and without virtual resistor.

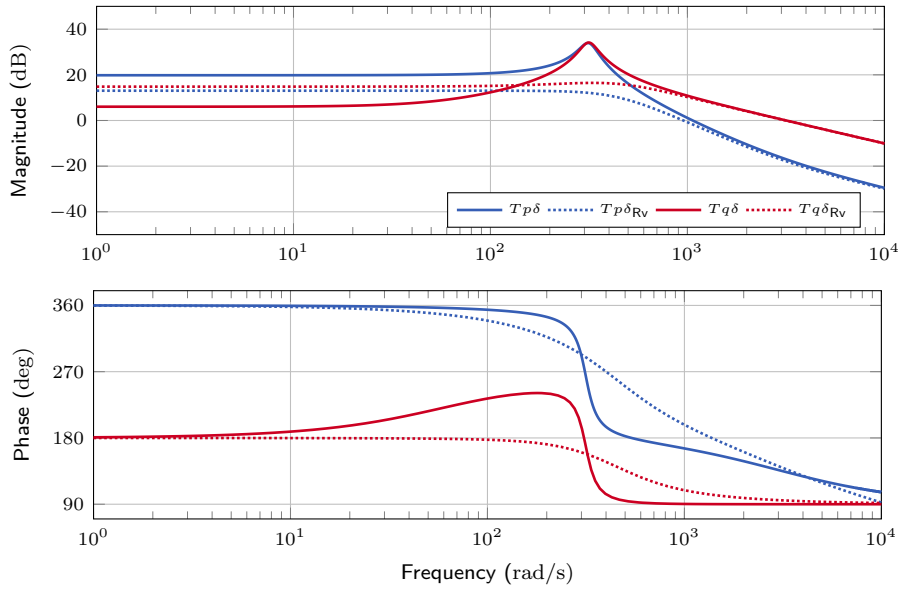

Figure 3.11: Frequency response of $T_{p\delta}$ and $T_{q\delta}$ with and without static virtual resistor at operation point of $P_{ac} = 1$ pu

The inclusion of R_v has improved damping of the SRF to the desired level. This is illustrated in Figure 3.11, where a reduction in peak gain of approximately 18 dB is observed at 314 rad s^{-1}. Consequently, in the lower frequency range ($s \sim 0$), the gain of $T_{q\delta R_v}$ surpasses that of $T_{p\delta R_v}$. In this scenario, reactive power is primarily influenced by the load angle instead of the voltage magnitude, which is not desirable [77]. The phase responses of $T_{p\delta R_v}$ and $T_{q\delta R_v}$ exhibit a greater phase margin, showing enhanced stability in the control system. However, at higher frequencies, all phase curves converge, indicating that the active and reactive power control responses start to behave similarly at very high frequencies (above 10^4 rad s^{-1}).

Transient Virtual Impedance

To diminish the effect of stationary resistor at low frequency range, a Transient Virtual Impedance (TVI) is introduced using a High-Pass Filter (HPF) in *dq* domain [78]. The transient virtual impedance consists of a virtual reactance component and a virtual resistor (see Figure 3.15). The new transfer functions of the MIMO system in Chapter 7.2 are derived by incorporating a HPF into the virtual impedance terms, as shown in 3.12 and 3.13 [78]:

$$v_{d,\mathrm{TVI}} = R_{\mathrm{v}} i_d \frac{s}{s + \omega_{c,\mathrm{hpf}}} - \omega_g L_{\mathrm{v}} i_q \frac{s}{s + \omega_{c,\mathrm{hpf}}} \tag{3.12}$$

$$v_{q,\mathrm{TVI}} = R_{\mathrm{v}} i_q \frac{s}{s + \omega_{c,\mathrm{hpf}}} + \omega_g L_{\mathrm{v}} i_d \frac{s}{s + \omega_{c,\mathrm{hpf}}} \tag{3.13}$$

A high-pass filter in the *dq* domain attenuates both high- and low-frequency components around the fundamental, effectively acting like a band-stop filter [32]. This ensures that the voltage drop at the positive-sequence fundamental frequency (appearing as DC in *dq*) decays to zero in steady state in *abc* frame [78] and enables the TVI to be active at almost all frequencies except the fundamental frequency. Therefore, the active power flow through fundamental frequency will not change in contrast to static virtual resistor (R_v). To realize transient virtual impedance concept in the model, the block diagram in Figure 3.15 is used, which will be discussed in section (3.2.5). Figure 3.12 shows the step response of the linear and non-linear models with inclusion of R_v with a high pass filter (as in Equations 3.12 & 3.13) facing the same angle jump as in Figure 3.8.

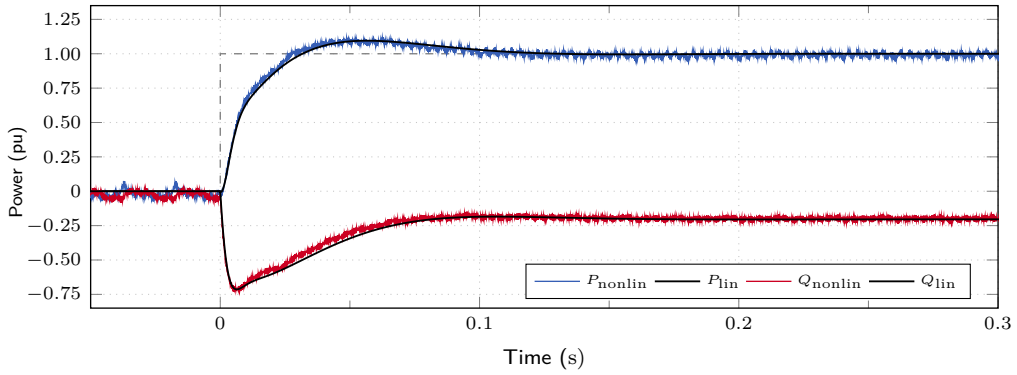

Figure 3.12: Step response of the linearized plant vs. non-linear model with transient virtual impedance (X/R=0) to a 10-degree angle jump

In Figure 3.12 only resistive component is considered in the transient virtual impedance circuit. The results indicate that in response to this angle jump, reactive power has a high contribution during transients, while the gain diminishes in steady state. It is clear that the transient virtual resistance is inactive at low frequencies, which is advantageous compared to a static virtual resistor (shown in Figure 3.8). It is also evident in Figure 3.12 that while the synchronous resonant frequency is dampened, the coupling between active and reactive power remains strong in dynamic region.

Based on the pole locus of $T_{p\delta}$ in Equation 3.10, to maintain high damping of the SRF while minimizing cross-coupling between P & Q during current transients, the transient virtual reactance components must also be included in the $T_{p\delta}$ [78]. Looking at the poles of $T_{p\delta}$ including TVI in 3.14, shows that varying X_v causes the plant poles to appear at higher frequencies than synchronous resonant frequency (50 Hz). Hence, if $L_v = L_c$ is applied in the TVI circuit, the poles frequency shift to twice the grid frequency (see 3.14) [74].

$$\begin{aligned} T_{p\delta}(\text{TVI}) &= \frac{as^2 + bs + c}{\left(\frac{L_c}{\omega_b}s + R_c\right)^2 + (\omega_g L_c)^2} \\ \xrightarrow{\text{(poles)}} s_{1\&2} &= -\frac{(R_c + R_v)}{L_c}\omega_0 \pm j\omega_g\omega_0\frac{(L_c + L_v)}{L_c} \end{aligned} \tag{3.14}$$

Figure 3.13 & 3.14 show the Bode diagram with the inclusion of TVI. In Figure 3.13, the Bode plots for $T_{p\delta}$ & $T_{q\delta}$ are compared with and without transient virtual resistor. While, Figure 3.13 compares $T_{p\delta}$ & $T_{q\delta}$ with and without transient virtual impedance with X/R=10. The synchronous resonant frequency in both plots is attenuated; however, in Figure 3.14, the peak frequency is shifted to 628 rad/s. Furthermore, Figure 3.14 clearly illustrates that the inclusion of the inductive component reduces the coupling between P & Q in the range of [10-628] rad/s. This reduction is beneficial for designing feedback control systems and enhancing the performance of active and reactive power during transients. This effect will be further discussed in Chapter 3.2.5.

Considering Equation 3.11 and the preceding discussion, it has been shown that the resistive component of the transient virtual impedance mainly contributes to damping at the synchronous resonant frequency and increase the reactive component. However, increasing the X/R ratio reduces the coupling between active and reactive powers.

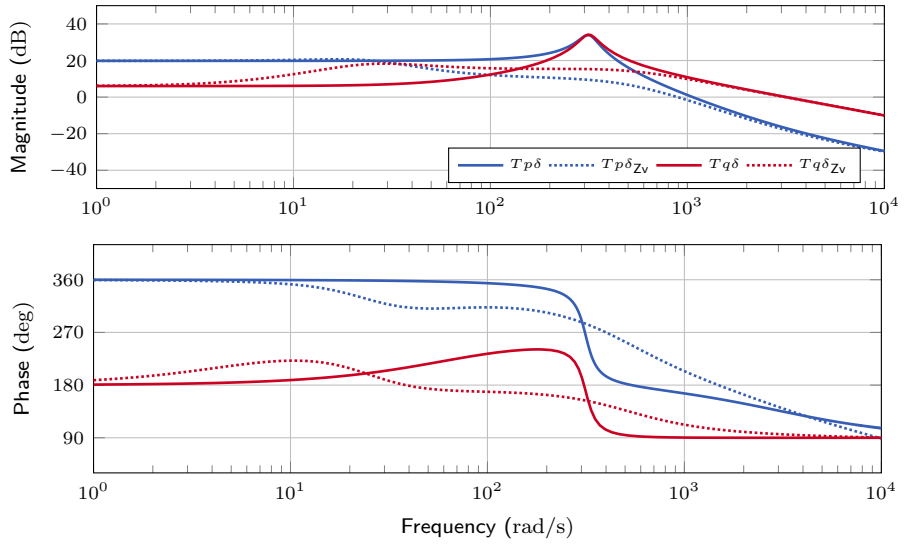

Figure 3.13: Frequency response of $T_{p\delta}$ and $T_{q\delta}$ with and without TVI: solid lines represent the case without TVI, and dotted lines represent the case with TVI. $(X/R = 0)$, at $P_{ac} = 1$ pu

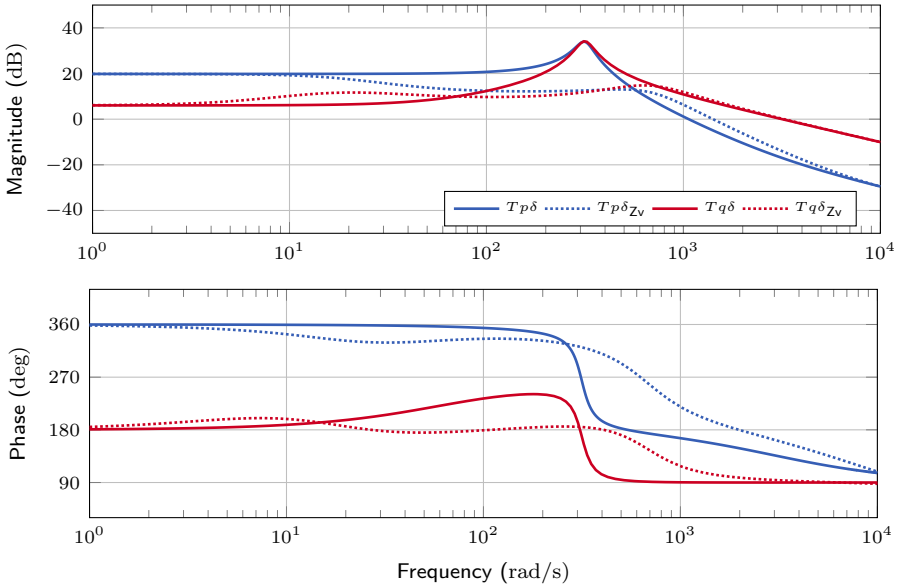

Figure 3.14: Frequency response of $T_{p\delta}$ and $T_{q\delta}$ with and without TVI: solid lines represent the case without TVI, and dotted lines represent the case with TVI. $(X/R = 10)$, at $P_{ac} = 1$ pu

The selection of Z_v is a critical design consideration as increasing the Z_v and R_v beyond a certain limit can lead to control challenges which may cause instability for the main GFM core controller (see Figure 3.16). Therefore, in control design, a trade-off is considered between damping the SRF and the dynamic performance of both active and reactive power, as well as the controller's damping. In the next chapter (3.2.5), first the feedback control design is explained, followed by selecting the parameters for the Z_v to meet the design requirements.

Active & Reactive Power Controller Design

This chapter begins by providing a detailed explanation of the feedback control for active and reactive power, including the transient virtual impedance circuit and the over-current limitation scheme. Next, the design procedure is discussed, and the performance of the close-loop control system is evaluated. Figure 3.15 shows the modified-RVVC concept which realizes a voltage source behavior on grid-side converter and is compatible with wind turbine application [39].

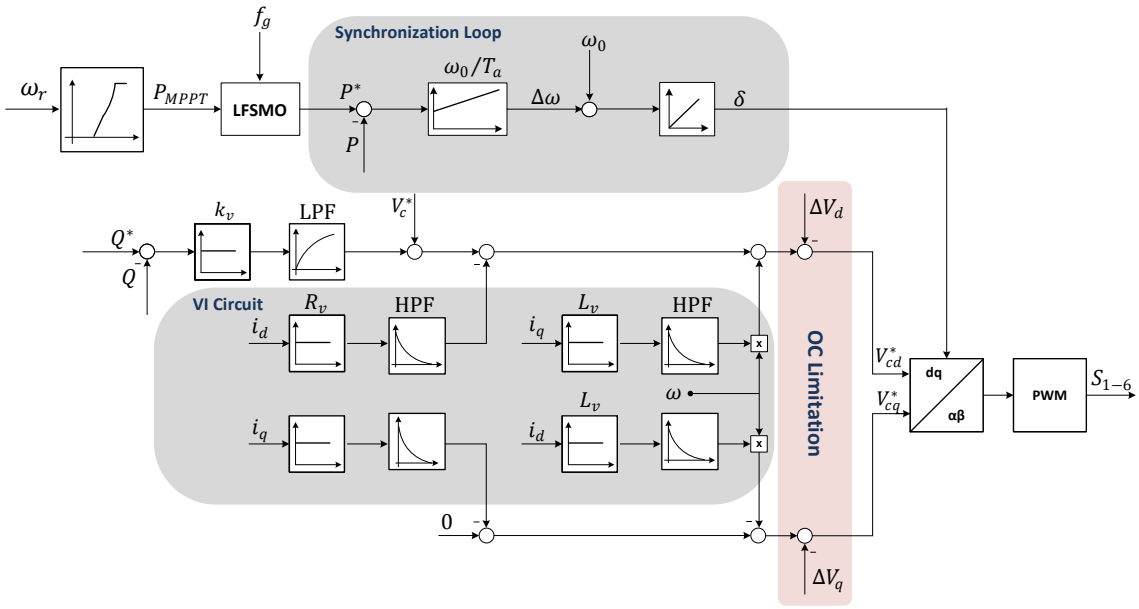

Figure 3.15: Overall GFM control scheme using modified-RVVC structure in the GSC

The active power controller output is the load angle information which is required for the Park transformation in the dq rotating reference frame. In addition, the reactive power loop aligns the converter voltage vector on the direct component of the dq frame. The q component of the converter voltage vector is set to zero. To increase the power flow between the converter and the grid, the angle is increasing to shift the d-component of the converter voltage relative to the grid voltage, until a new stable operating point is reached. To vary the reactive power transfer to the grid, the d component is modified to inject either over-excited or under-excited reactive power into the PCC, similar to a synchronous generator [79].

To achieve the desired dynamic response of the closed-loop system, specific levels of inertia and damping for the closed-loop pole pairs is considered. In the close-loop transfer function for active power, three sets of pole pairs are observed, each located at different frequencies. The design procedure involves examining the locus of these roots while varying the design parameters. The sequence of the design steps is as follows:

- Inertia time constant $T_a = 10\,\mathrm{s}$ is selected based on the specifications (see Chapter 5.2).
- For the TVI circuit, the values of R_v or, more generally, Z_v, are determined based on the following assumptions:

$$\begin{aligned} \Delta p = \frac{V_c V_g X \cos(\delta_0) - V_c V_g R \sin(\delta_0)}{X^2 + R^2} &\xrightarrow{\text{having } X \gg R \,\&\, \cos(\delta_0) \approx 1} \\ \Delta P = \Delta\delta \cdot \frac{V_c V_g}{X} &\xrightarrow{\text{for 10 deg angle jump}} 0.17\,(\mathrm{rad}) \cdot \frac{1(pu) \cdot 1(pu)}{0.1(pu)} = 1.7(pu) \\ &\xrightarrow{\text{for } \Delta P = 1(pu) \text{ in 10 deg angle jump}} (X_c + X_v) = 0.34(pu) \end{aligned} \tag{3.15}$$

In Equation 3.15, X and R represent the combined reactance and resistance of the converter filter, including the virtual components introduced by the TVI circuit.

This assumption in Equation 3.15 is used to determine Z_v in order to fulfill the required performance for FNN scenarios described in [80]. According to [80], with a 10-degree angle jump while operating at 50% of the nominal power, the system's response should remain in the linear region without triggering the overcurrent limit. Based on this assumption and having $Z_c = 0.1$ pu, in the transient virtual impedance circuit, the value of Z_v should be approximately 0.24 pu. This value is estimated as the minimum required to achieve the desired performance for the FNN scenario. As Z_v increases, the virtual electrical distance between the converter and the grid also increases, resulting in reduced participation of the DUT in angle jumps or grid events.

After selecting T_a and Z_v, the impact of the other parameters on the root trajectory of the closed-loop system will be investigated. In the first step, the effect of sweeping resistive component of TVI between (0.05-0.5) pu on the trajectory of the eigenvalues for the closed-loop system is shown in Figure 3.16 in the whole frequency range.

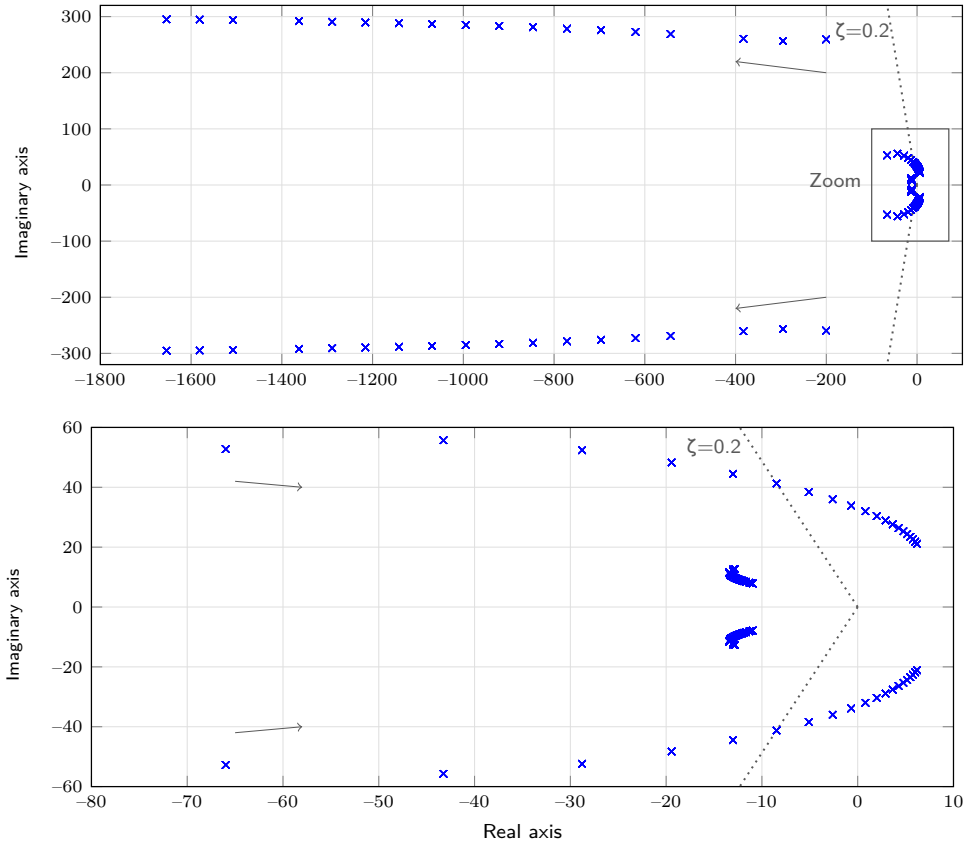

Figure 3.16: Root locus of the closed-loop poles with variation of R_v from (0.05-0.5) pu; Other design parameters: (k_p=0.008, f_{HPF}=14 Hz)

It is evident that increasing R_v dampens SRF. However, in the low-frequency region, it inversely affects the damping of the GFM controller, as illustrated in the zoomed-in view in Figure 3.16. Both pairs of poles in the low-frequency region, associated with the GFM core, shift toward the RHP as R_v increases. Beyond $R_v \geq 0.3$ pu, the GFM core becomes unstable.

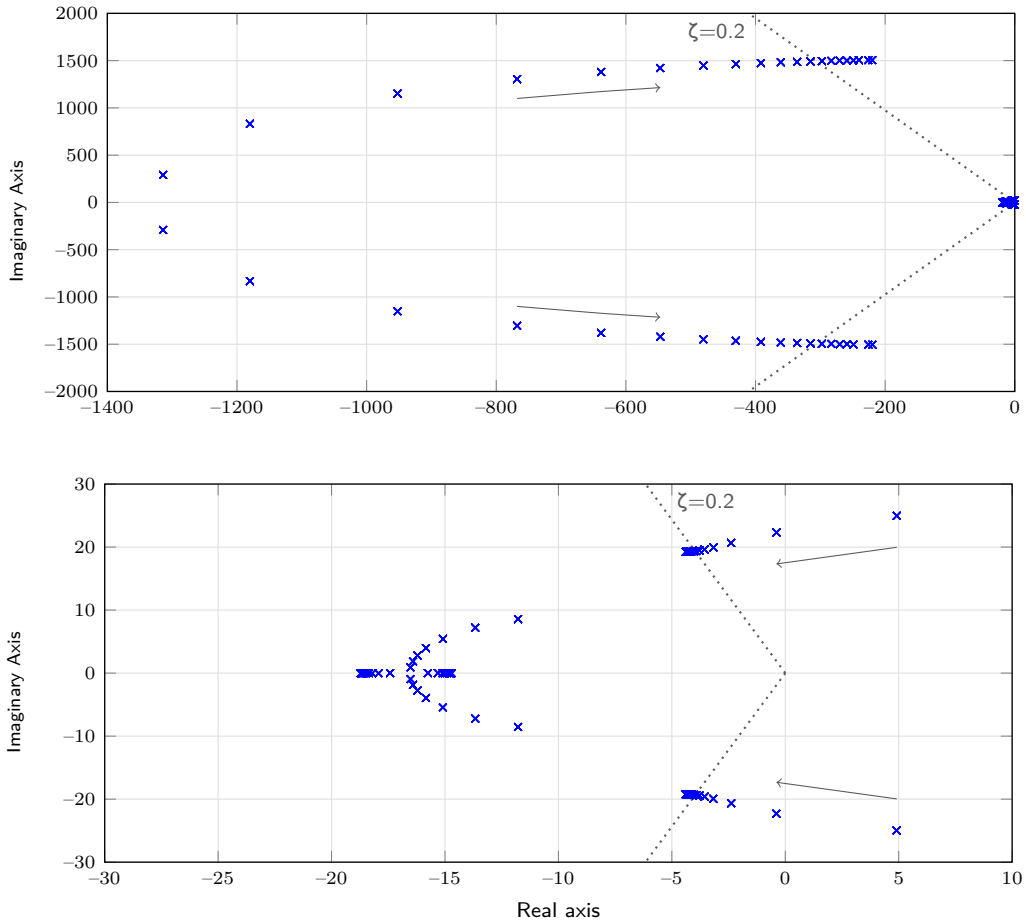

Figure 3.17: Root locus of the closed-loop poles with variation of X/R ratio for transient virtual impedance from (0-10); Other design parameters: (Z_v=0.24 pu, k_p=0.008, f_{HPF}=14 Hz)
Upper figure: poles trajectory in medium frequency related to SRF.
Lower figure: low frequency pole pairs for the GFM core and HPF

Figure 3.17 illustrates the closed-loop eigenvalues at $Z_v = 0.24$ pu, while varying the X/R ratio of the TVI circuit from (0-10). It can be observed that in the medium frequency range ($50 < f < 240$) Hz, as the X/R ratio transitions from resistive to inductive, the damping of the pole pairs decreases and the pole frequencies shift from 50 Hz to higher frequencies. The graph indicates that a damping ratio of approximately $\zeta \approx 50\%$ for the SRF is achieved with an $X/R \leq 3$. Furthermore, as previously mentioned, an inductive TVI with an $X/R \leq 3$ reduces cross-coupling between active and reactive power during transients, resulting in a smaller gain for

$T_{q\delta}$ compared to $T_{p\delta}$.

Focusing on the lower frequency range in Figure 3.17, two sets of pole pairs are observed within the frequency range of [0 - 5]Hz. These low-frequency modes are associated with the core of the GFM controller. As the X/R shifts to inductive, the damping of the pole pairs corresponding to the power-frequency loop improves. Additionally, this shift causes the conjugate poles to move toward the real axis while maintaining sufficient damping in both cases.

Another design parameter in the active power-frequency loop is the proportional gain of the PI controller (k_p). Figure 3.18 illustrates the impact of increasing k_p from 0.001 to 0.06 pu, as shown in the root locus graphs.

In Figure 3.18, the other design parameters, $Z_v = 0.24$ pu and a $X/R = 2$, are selected from the previous design steps. In the medium frequency range, variation in k_p do not significantly affect the pole pairs, and the damping remains relatively adequate at $\zeta \geq 60\%$. In the low frequency range, increasing k_p enhances the damping of the grid-forming core to $\zeta \geq 34\%$. The other two pole pairs remain on the real axis with a trajectory toward the right half-plane, yet they remain stable within this range of k_p.

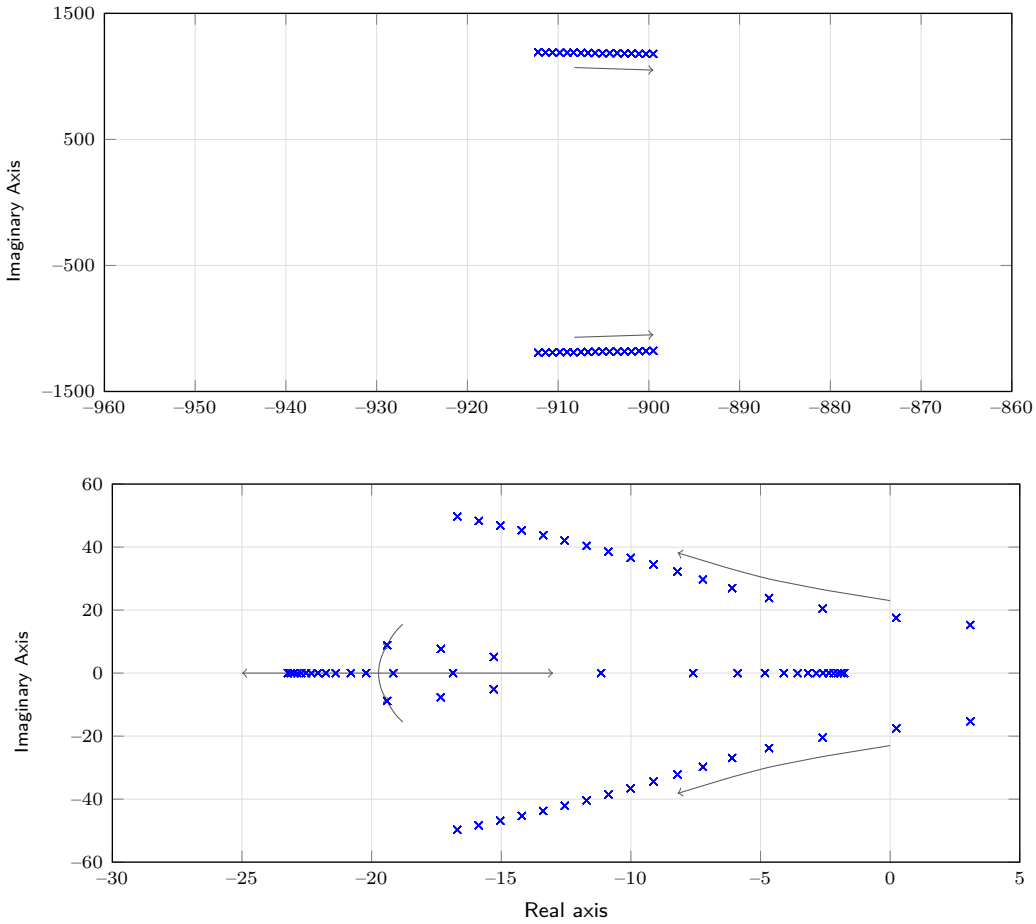

Figure 3.18: Root locus of the closed-loop poles with variation of k_p=(0.001-0.06); Other design parameters: ($Z_v = 0.24$ pu, X/R=2, f_{HPF}=14 Hz)
Upper figure: poles trajectory in medium frequency related to SRF.
Lower figure: low frequency pole pairs related to the core of grid forming and the HPF

In interconnected power systems, the network SCR is typically specified to assess the dynamic performance and stability of the plant at the point of connection. However, during system splits and islanding, the SCR may change depending on the contingency. It is crucial for converter control to maintain reliable performance under low SCR conditions and varying X/R ratios. Therefore, evaluating the stability of the control system with the designed parameters across different network SCR and X/R ratios is essential.

Figure 3.19 illustrates the root locus of the poles for the designed controller parameters across a range of SCR values: 10, 5, 2, with network X/R ratios varying from 10, 5, 1. The upper plot in Figure 3.19 provides an overall view across the entire frequency range, while the lower plot in Figure 3.19 focuses on the frequency range $f < 8$Hz. The results indicate that decreasing network SCR from 10 to 2 reduces the damping of the pole pairs in the medium frequency range from 38% to 30% at $X/R = 10$. However, in the low frequency region, the damping of the controller's pole pairs improves with the reduction of SCR. Notably, in the same low frequency range, another pole pairs remain unchanged along the real axis.

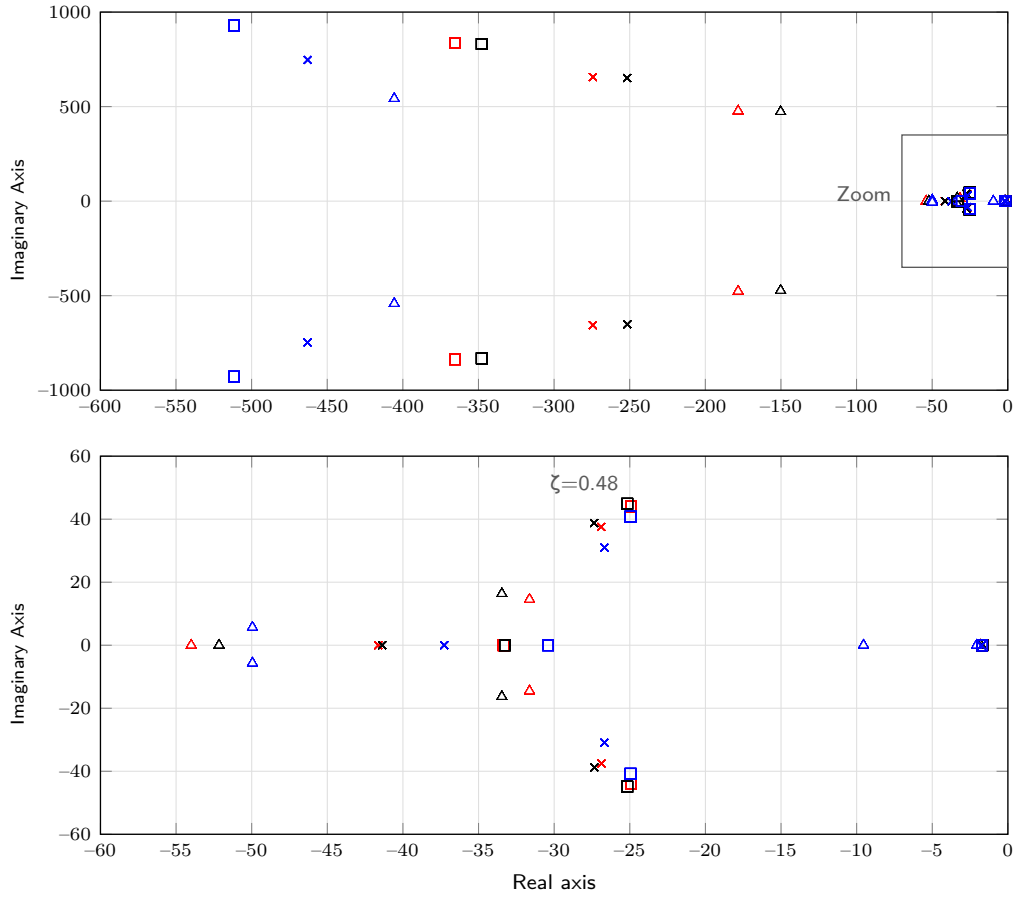

Figure 3.19: Root locus of the closed-loop poles for variation of the grid strength, SCR= (10,5,2), and for varying network X/R ratios =(10,5,1),
Upper figure: The whole eigenvalues. Lower figure: Zoom on slower modes

When the network X/R ratio decreases from 10 to 1, as expected, the damping of the SRF improves. Additionally, changing the X/R ratio from inductive to resistive increases the damping of the conjugate pole pairs associated with the GFM core, with no effect on the real pole pairs. As shown in Figure 3.19, using the selected control parameters, the minimum damping remains around $\zeta = 30\%$, even in the worst-case scenario at SCR= 2 and X/R ratio of 10 (black triangle in Figure 3.19 (the upper plot)). In addition, In the low-frequency range, a minimum damping of $\zeta = 48\%$ is achieved with SCR=10 and $X/R = 10$ (black square).

The designed parameters are implemented in the control scheme illustrated in Figure 3.15. To validate the dynamic response of the closed-loop system, a step jump is applied to the active power, adjusting the setpoint from 0 to 0.5 pu at t=0 s.

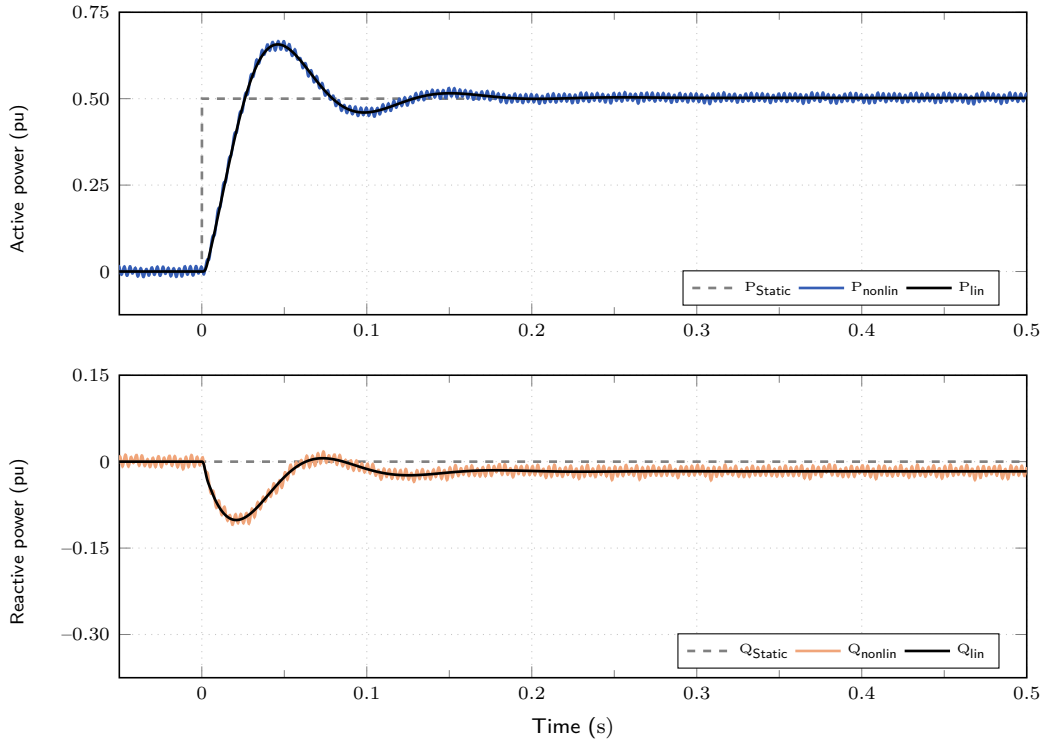

Figure 3.20: Reference step responses of the RVVC, results of the linear model, and non-linear model with k_i= 10π pu, k_p= 2.53 pu, f_{HPF}=14 Hz, Z_v = 0.24 pu, X/R=2

It is important to note that during this test, the reactive power droop path is disabled, and turbine and machine-side dynamics are not taken into account. As demonstrated in Figure 3.20, the active power controller effectively tracks the setpoint changes, exhibiting an initial overshoot followed by appropriate damping. In addition, it illustrates that the linear model accurately represents the system dynamics, confirming the effectiveness of the controller design.

Dynamic Voltage Support

To model the behavior of a synchronous machine during short circuits and voltage sags, a droop control is integrated into the voltage control of the GSC. During short circuits, a SG injects fault current depending on its transient reactance time constant $T_d^{'}$, typically around 1 s [63]. To enable wind turbines to emulate this behavior and contribute to short circuit current similar to an SG, a droop branch with a proportional controller is added. According to the grid codes [52], the droop gain k can range from 2 to 6, with a value of 6 providing maximum reactive current support. Therefore, in this work, a comparable droop gain ($k_v \sim \frac{1}{k}$) between the reactive power and the voltage magnitude of the converter is introduced, as shown in the reactive power branch in Figure 3.15.

In case of modified-RVVC, since the equivalent reactance $(X_c + X_v)$ is much smaller than $X_d^{''}$ in a SG, the initial response following a short circuit at the PCC has a significantly higher amplitude compared to that of an SG, as long as current limitations is not triggered. After this initial phase, the current in an SG decays with a time constant of $T_d^{'}$, while in GSC of WT, the droop control with the k_v factor regulates the reactive current response [63].

Using the SG model with the previously defined parameters in Chapter 2.4.1, a k_v factor is selected in this work to closely match the performance of modified-RVVC and an SG under nominal fault current conditions. This comparison is discussed in detail in the grid event in Chapter 3.3.

Threshold Virtual Impedance Current Limitation

The task of the current limitation on the GFM concept is to maintain grid-forming functionality while protecting power electronics from exceeding their rated current [81]. Among the various current-limiting methods available [82], threshold virtual impedance current limiting is considered effective in maintaining GFM performance during faults and grid disturbances [78]. In grid-forming schemes like modified-RVVC, where the modulated voltage resulted from the active and reactive power controllers is directly input to the PWM, current limitation must be achieved by constraining the quadrature and direct components of the converter voltages. Therefore, certain modification of the control structure is required to enable this current limiting capability. The placeholder of this over-current limiting scheme has already been incorporated into Figure 3.15. Figure 3.21 in the following illustrates the details of this scheme.

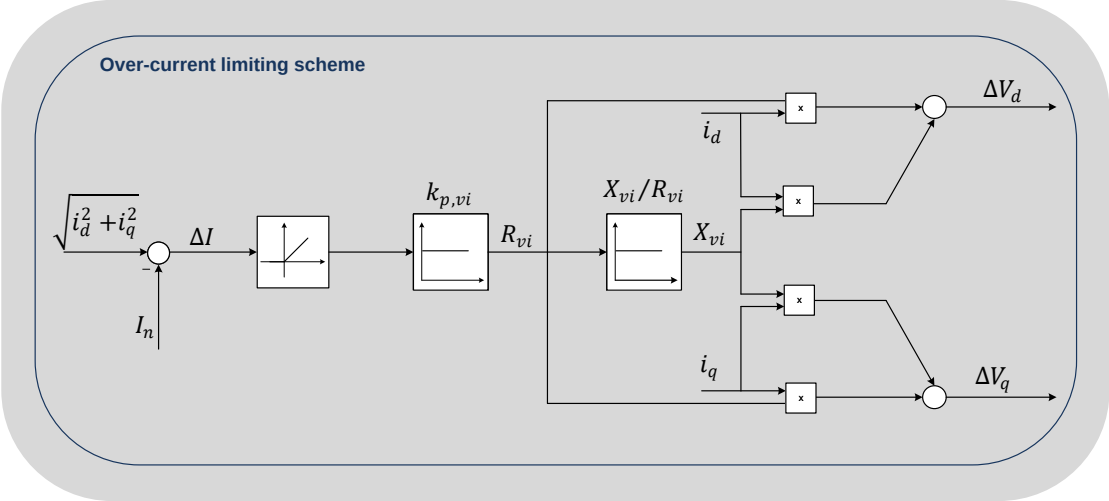

Figure 3.21: Implementation of the current limiting virtual impedance scheme in dq frame

The current limitation block shown in Figure 3.15 employs a nonlinear virtual impedance to control currents indirectly. This is achieved by introducing an additional proportional controller to emulate a virtual voltage drop across the d- and q-axes. Through this approach, high currents resulting from short circuit faults

or overloads are effectively limited. This additional controller is referred to as virtual impedance current limiting [30]. The proportional gain gets activated when the current exceeds a specified threshold. As shown in Figure 3.21, the first block detects the magnitude of the overcurrent.

When the current exceeds the threshold, the overcurrent detection in Figure 3.21 gets activated, generating a ΔI signal for the virtual impedance path. By enabling this calculation path, it determines the necessary gain $k_{p,vi}$ to reduce the measured overcurrent. Finally, virtual voltage drops are created and subtracted from the internal converter voltages, allowing the current to be limited to the threshold level in steady-state. A compromise is made between selecting appropriate Z_{vi} values and the X_{vi}/R_{vi} ratio to facilitate overcurrent limitation while ensuring an adequate dynamic response.

To determine the current limiting gain $k_{p,vi}$, it is necessary to establish the maximum current flowing through the converter. Since estimating I_{max} is not straightforward, the value of $k_{p,vi}$ is chosen based on a worst-case scenario. When the generation unit is connected to the PCC, a three-phase bolted fault can cause up to 10 times the nominal current to flow at the fault point ($\frac{1}{Z_c} = 1/0.1$). This assumption is used to select $k_{p,vi}$ parameter. Figure 3.22 illustrates the equivalent steady-state representation of the system following a three-phase bolted fault directly at the PCC [26].

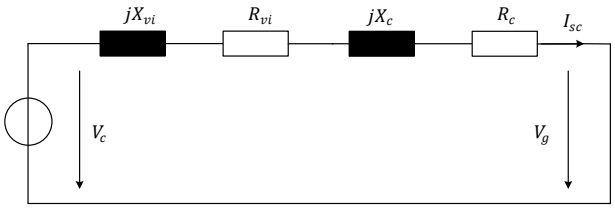

Figure 3.22: Steady state representation of the system after a fault at PCC

Assuming that the short-circuit current in this scenario is equivalent to the maximum current ($I_{sc} = I_{max}$) in steady state, the following relationship is established between

$k_{p,vi}$ and the virtual gains [26]:

$$\begin{cases} \left(\frac{V_{c0}}{I_{max}}\right)^2 = (R_c + R_{vi}(I_{max}))^2 + (X_c + X_{vi}(I_{max}))^2 \\ \Delta R_{vi} = max\left(k_{p,vi}\sqrt{i_d^2 + i_q^2} - I_{threshold}, 0\right) \\ \omega_g \Delta L_{vi} = \Delta R_{vi}(\frac{\Delta X_{vi}}{R_{vi}}) \end{cases} \tag{3.16}$$

In 3.16, $\Delta X_{vi}/R_{vi}$ ratio represents the X/R ratio of the current-limiting impedance, while $I_{threshold}$ denotes the threshold current at which the overcurrent scheme is activated. By selecting the values for I_{max}, $I_{threshold}$, and $\Delta X_{vi}/R_{vi}$, the current limiting gain ($k_{p,vi}$) can be calculated from Equation 3.16. Choosing a small I_{max} that is close to $I_{threshold}$ necessitates a higher virtual impedance to produce a greater voltage drop, while maintaining a more resistive $\Delta X_{vi}/R_{vi}$ ratio could lead to stability issues for the GFM controller (see Chapter 3.2.5). A trade-off is required in selecting these parameters to ensure stable operation across a wide range of operating points. To validate the current limiting performance, two test scenarios are analyzed. The first scenario involves applying a symmetrical three-phase bolted fault for duration of 100 ms at the PCC at $t = 0\,\text{s}$. The second scenario applies a -30-degree angle jump at $t = 0\,\text{s}$ as illustrated in Figure 3.23.

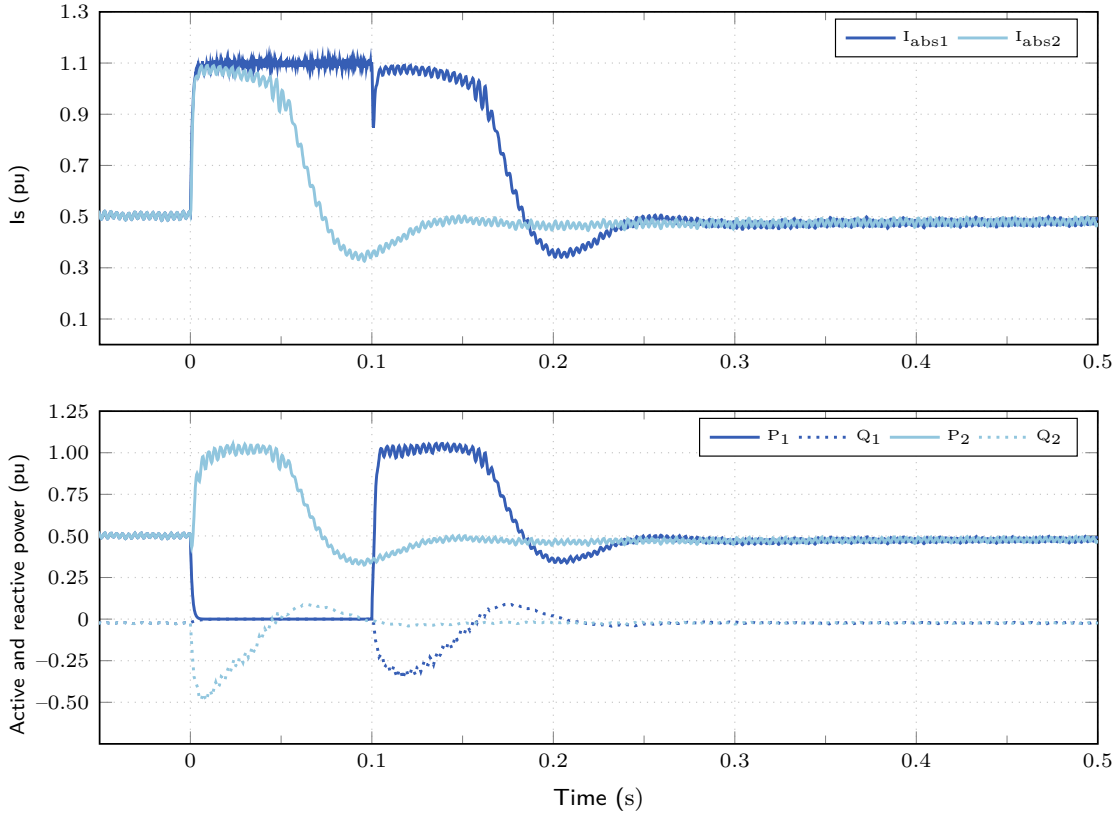

Figure 3.23: System dynamics during symmetrical three-phase fault (subscript 1) & -30 degrees angle jump (subscript 2)

In the first scenario, the results demonstrate that immediately after the fault, the current remains within the range of $I_{threshold} < I < I_{max}$ which indicates the desired performance. After fault clearance at $t = 0.1\,\mathrm{s}$, the current limitation persists for an additional $t = 50\,\mathrm{ms}$ due to the increased converter angle during the fault. Consequently, the overcurrent remains active until the converter adjusts its angle to the required level to restore pre-event power flow.

In the second scenario, a -30-degree angle jump is applied at $t = 0\,\mathrm{s}$, causing the active power to rise to its nominal value. During this event, inertia provision is constrained by the current limitation for the first $t = 20\,\mathrm{ms}$. After the power response decays, the current limitation is subsequently deactivated.

3.2.6 Implementation of the Modified-RVVC in Wind Turbines

Many of the GFM concepts introduced in chapter 2.3 primarily focus on the GFM properties and implementation of the concept on the grid-side converter of photovoltaic systems or wind turbines. The power required for these system services is typically supplied either by an ideal DC-voltage source [32], battery storage systems [32], [83], or supercapacitors [84]. However, the implementation of control systems focused on adapting system architecture specifically for wind power plants, based on time-domain simulation, is not widely addressed. Omitting the dynamics and available power of the energy source in system stability studies leads to results that differ significantly from scenarios where the energy is actually drawn from the rotating masses of a wind turbine [85].

In the following, provision of inertia from wind turbine is investigated with the control concept presented in Chapter 3.2.5 [86]. This chapter focuses on implementing modified-RVVC on a type-4 wind turbine unit with a full-scale converter and a PMSG. The Chapter 3.2.6 begins with an overview of the wind turbine model and the complete control scheme for both the grid-side and machine-side converters. Following this, the application of modified-RVVC and inertia emulation using the wind turbine are discussed in detail. To clarify how inertia emulation functions in a wind turbine context, the necessary functions and required modification for turbine control, as well as for grid-side and machine-side converters, are outlined.

At the end of this chapter, the implemented GFM wind turbine unit is tested against other state-of-the-art generation systems under various grid events.

Figure 3.24 provides an overview of the control structure for a wind turbine equipped with a full-scale back-to-back converter, functioning fully as a GFM unit. The grid-side converter employs modified-RVVC to enhance system inertia and includes a dynamic voltage support loop, as discussed in Chapter 3.2.5. Other system-level functionalities include LFSM-O and optionally, proportional primary frequency support. Additionally, MPPT is moved to grid-side converter control to set the active power reference for the power-frequency loop and deliver available wind

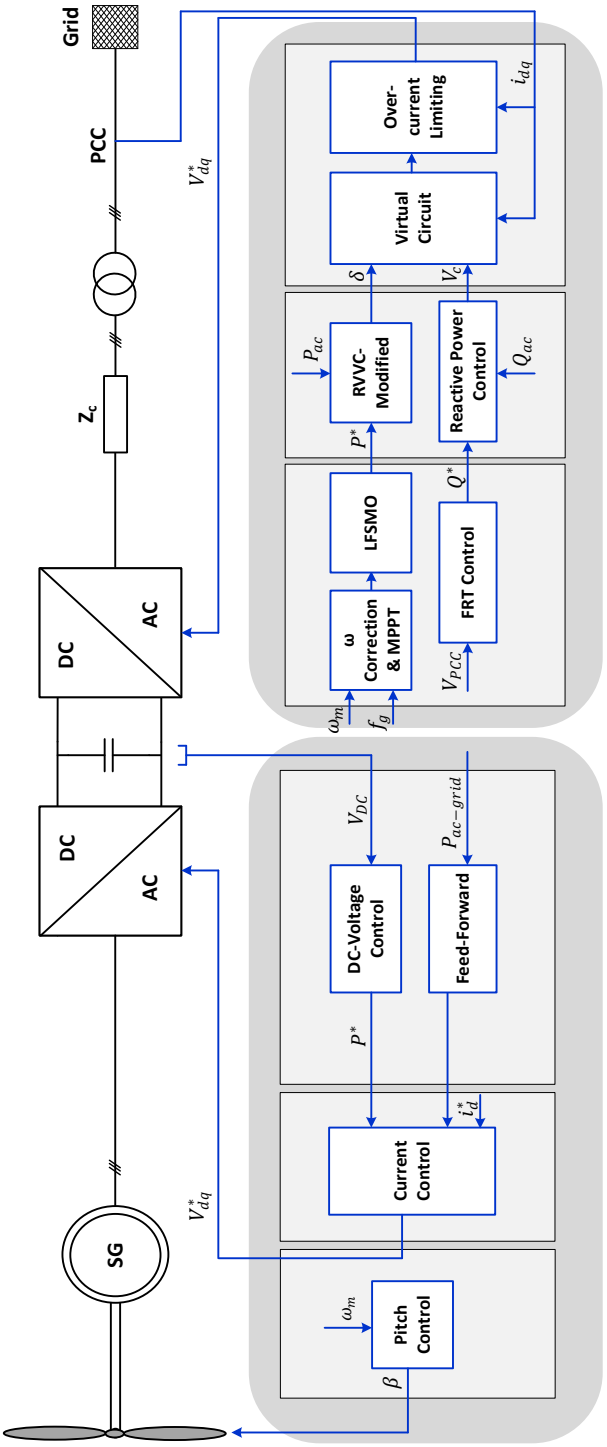

Figure 3.24: Total control structure of the PMSG wind turbine, behaving as a GFM unit

power to the grid. The following sections provide a detailed discussion of both grid-side and machine-side control functions.

In addition, a compensation scheme for rotor speed, shown in Figure 3.24, is introduced to mitigate the negative effects of rotor speed deviations during inertia emulation. The details of this scheme, will be discussed in the following section. Moreover, to achieve full GFM functionality, modifications to the generator and MSC control are necessary, as shown in Figure 3.24. This involves re-positioning power flow management via DC-link voltage control to the MSC controller [56], [60], which will be discussed in the following.

Modeling & Control of Wind Turbine

The rotor's aerodynamics is modeled by Equation 3.17. According to 3.17, the mechanical power that can be harvested by the rotor blades from the available wind primarily depends on aerodynamic power efficiency, drive train modeling, and pitch control [87]:

$$P_{Aero} = \frac{1}{2} C_p(\lambda, \beta) A \rho v_w^3 \tag{3.17}$$

In 3.17, A is the rotor harvesting radius, v_w is the wind speed, ρ is the air density, and C_p is the aerodynamic power efficiency [87], [88]. To extract maximum power from the available wind, C_p must be maximized. This occurs when the blade pitch angle is zero ($\beta = 0$), and the tip-speed ratio is at its optimal value ($\lambda \sim 8.1$).

$$\lambda = \frac{\omega_m r}{v_w} \tag{3.18}$$

In 3.18, the rotor radius is denoted r and the aerodynamic power characteristic, P_{Aero}, is represented by a series of curves that depend on the power coefficient C_p, tip speed ratio λ and wind speed v_w [87]. The maxima of these aerodynamic curves are connected together to form the generator operation curve under maximum power point tracking. The MPPT can be achieved at below rated wind speeds by operating at specific points on the generator curve where each rotational speed of the generator corresponds to a distinct C_p, allowing for maximum power extraction.

Above rated wind speed, pitch control gets activated to control the generator's speed. At this stage, power output is limited to the nominal power by adjusting the angle of the blades, as it is illustrated in Figure 3.24.

The drive train model of the generator is represented with a single-mass shaft model, coupling turbine and generator sides. The drive train model can be expressed as Equation 3.19, where T_m is the mechanical torque, T_e is the electrical generator torque, N_{gear} is the gear ratio and ω_r is the rotor speed in the turbine side [88].

$$J_t \dot{\omega}_r = T_m - N_{\text{gear}} \cdot T_e \tag{3.19}$$

$$H = \frac{J_t \cdot \omega_m^2}{2 \cdot S_n} \tag{3.20}$$

Given the lumped inertia J_t of the generator, rotor, and gearbox in $(\text{kg} \cdot \text{m}^2)$, the inertia time constant of the drive train can be normalized using Equation 3.20, which is $T_{a,\text{gt}} = 2H = 12\,\text{s}$ for the modeled wind turbine. In Equation 3.20, S_n represents the rated apparent power of the generator, and ω_m denotes the rotational speed of the generator in $\text{rad}\,\text{s}^{-1}$.

Control of Machine-Side Converter

As illustrated in Figure 3.24, Field-Oriented Control (FOC) is employed in the machine-side control to regulate the stator voltages of the PMSG in dq rotating frame. The control principle relies on two inner current control loops, with the reference for the d-axis stator current set to zero ($i_d^* = 0$) to achieve the maximum torque-to-current ratio and prevent the demagnetization of the PMSG [86]. The set point for the quadratic component of the stator current i_q^* is derived from the outer control loop, which regulates the DC-link voltage [56], [60]. Figure 3.25 illustrates how the DC-link controller is implemented in the MSC control.

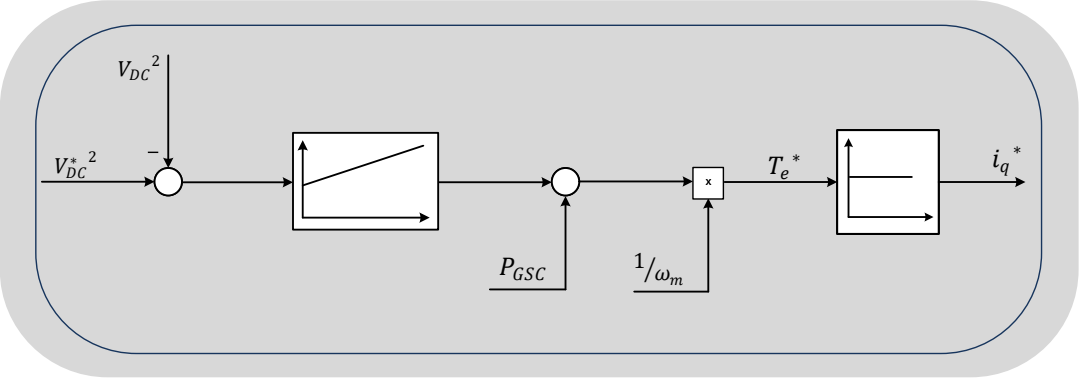

Figure 3.25: DC-link voltage controller implemented in the machine-side converter control

As depicted in Figure 3.25, the controller output is combined with a feedforward component that represents the grid-side AC power [89]. This enables the rapid dynamics of the grid, which occur during inertia support or in short-circuit scenarios, to be quickly reflected in the machine side control. Therefore, it enables the generator side to follow these fast dynamics by adjusting the machine's torque.

Control of Grid-Side Converter

The control concept of the modified-RVVC for the GSC control is discussed in detail in Chapter 3.2.5. This concept includes two inner controllers: the active power controller, which determines the angle of the converter voltage vector to achieve the desired operating point, and the reactive control loop, which provides the magnitude of the converter voltage vector (see Figure 3.24). Additionally, the inertia constant, mechanical swing damping as well as TVI parameters are selected within these two control loops to model a voltage source behind an impedance, as described in Chapter 3.2.5.

In addition to GFM capabilities, other system-level functionalities have been integrated to ensure compliance with grid codes, specifically LFSM-O [31] and dynamic voltage support [90]. A maximum power point tracking block is also incorporated into the GSC control scheme to enable operation at the maximum

available power during normal grid conditions. This configuration enables the available wind power to be fed into the grid under normal conditions and supports the grid through inertia provision from WT during grid events. However, operating in MPPT mode can limit inertia emulation at certain operating points which will be addressed in the following of this chapter. It should be noted that, operating the WT in MPPT mode for inertia response and other grid services may introduce additional costs and mechanical constraints [91], which are beyond the scope of this work. Table 3.1 summarizes the parameters used for the simulated wind turbine generator.

Table 3.1: Parameters of PMSG

PMSG Parameters	Values
ω_m	431 rpm
Pole pairs	12
f	86.2 Hz
T_{nom}	70.6 kNm
I_r	2760 A
P_n	3120 kW

LFSM-O Functionality in Wind Turbine

The performance of LFSM-O was discussed in detail in Chapter 2.4. According to German grid codes, onshore WTs must reduce power output based on the unit's operating point prior to activation [1]. Additionally, the maximum rate of power change is restricted by unit constraints, posing a further challenge in transitioning to an inverter-dominant power system, as highlighted in [32], [50]. Given the importance of LFSM-O in future grid stability [50], this constraint on the rate of power reduction is adjusted in this work to better align with the needs of a future power system.

In this study, the WT is designed to have a step response time below 2 s for a power change of $\Delta P = 50\% P_{pre}$ [1]. During LFSM-O operation, if the frequency changes from 51.5 Hz to 51.2 Hz, an increase in power is required. However, this increase

takes place at a considerably slower rate than the power reduction, extending the event's timescale beyond the scope of the tests conducted in this work [1], [92].

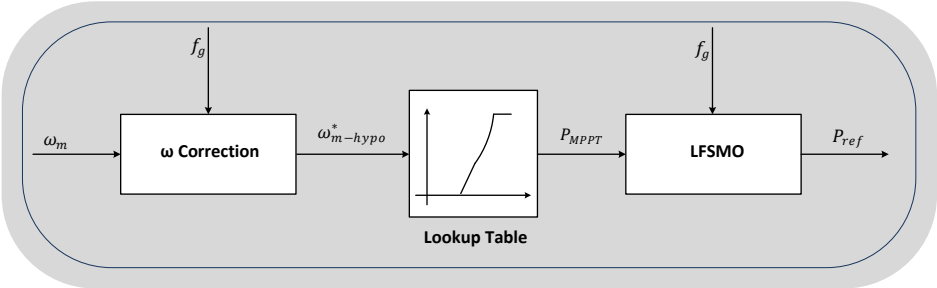

Figure 3.26: MPPT and LFSM-O implementation in the GSC [86]

Figure 3.26 illustrates the implementation of LFSM-O in the grid-side converter control. In GSC, when LFSM-O is activated, the P_{ref} command is generated by the LFSM-O block by reducing P_{MPPT} according to frequency increase. This drop in the power reference changes the generator electric torque, and due to difference between electrical and aerodynamic torque, the rotor speed ω_m increases. Figure 3.27 shows the performance of LFSM-O using $C_p - \lambda$ curves of the wind turbine [93]. It also highlights an example of the turbine controller's behavior when LFSM-O is activated and its impact on wind turbine operation.

As ω_m rises, the operation point shifts to the right (from point A to point B). If a new stable operating point is reached based on the external ΔP command from LFSM-O, the wind turbine settles at a new equilibrium as long as the LFSM-O power reduction is active. When the LFSM-O signal is deactivated, (P_{MPPT} is restored based on the generator-speed curve), allowing the turbine to decelerate and return to MPPT operation.

If the required power curtailment from the LFSM-O block further decreases, the rotor accelerates beyond the nominal speed. In this scenario, the pitch controller limits the speed to nominal by adjusting T_{Aero} without allowing further acceleration (from point B to C). When the LFSM-O signal is eventually disabled in this condition, the pitch controller first returns the operating point to an angle of zero

($\beta = 0$) (from point C to B), and then deceleration brings the system back to the MPPT point at A.

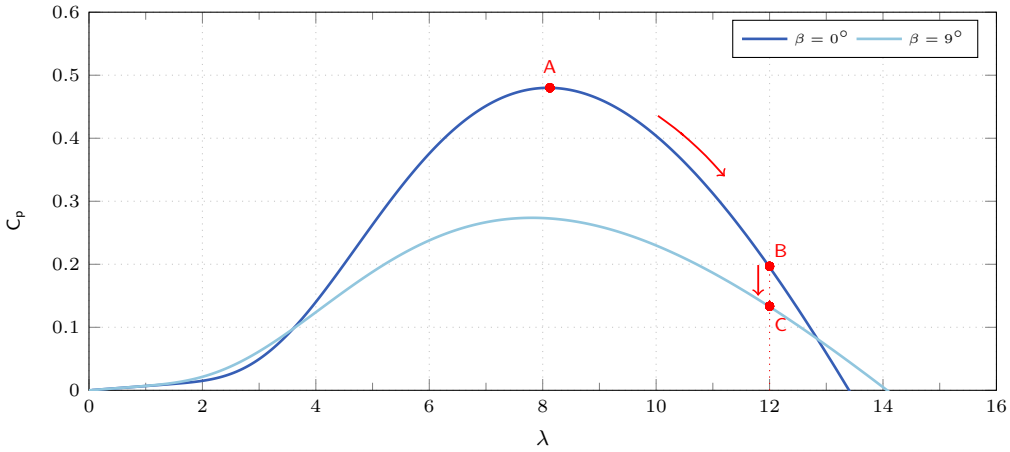

Figure 3.27: LFSM-O activation mechanism while operating at MPPT

To verify the performance of the LFSM-O in WT unit when grid frequency exceeds the LFSM-O threshold, a frequency jump is applied to the network, as it is shown in Figure 3.28. The dark blue curve represents the power command (P_{ref}) at the output of the LFSM-O logic. When the frequency reaches 50.2 Hz or higher, LFSM-O is activated. During LFSM-O activation, power curtailment shifts the operating point to the right on the turbine's power curve. As a result, rotor speed initially accelerates; once it reaches nominal speed, the pitch controller engages to maintain nominal speed by adjusting blade angle, further reducing turbine power. This is observed in Figure 3.28 around 1.5 s, when rotational speed exceeds 1 pu. Due to the slow dynamics of the pitch controller, it gradually adjusts the blade angle to a new steady-state value, in order to regulate the rotational speed back to its nominal value. The steady-state response is not depicted in the current plot.

As shown in Figure 3.28 for the AC power, there is an initial sudden reduction due to inertia provision in response to the frequency jump. Following this, the AC power adjusts with the changes of the power set-point, determined by the LFSM-O block output. It is observed that with the implemented LFSM-O logic, a response time of under 2 s is achieved [50].

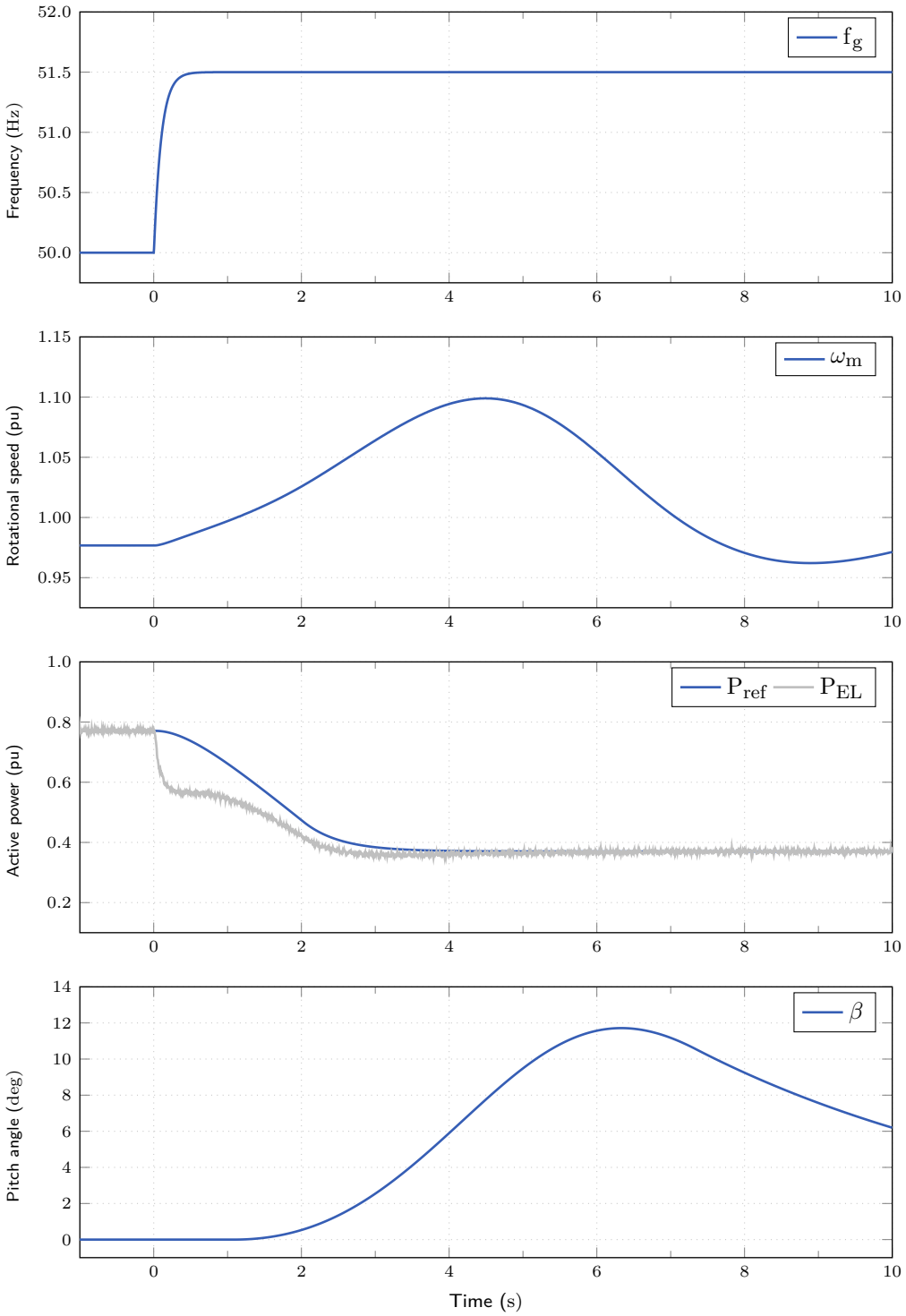

Figure 3.28: Response of the GFM-unit to an over frequency event

Compensation Scheme for Inertia Emulation in MPPT

In response to a negative RoCoF in the network, a power offset in the GSC causes rotor deceleration. At above-rated wind speeds, the pitch controller actively regulates the rotational speed. When a deviation from the nominal speed occurs during inertia emulation, the controller responds by decreasing the pitch angle, which in turn increases the aerodynamic power. As a result, the power set-point (P_{ref}) remains constant, preventing any undesired interactions during inertia emulation in above-rated wind speed [32]. However, at below-rated wind speeds, rotor deceleration shifts the operating point away from maximum aerodynamic power. This deviation interferes with MPPT operation, degrading inertia support during events comparing to the performance of the unit at above-rated wind speeds.

The literature suggests some solutions to enhance WT performance while operating at below-rated wind speed. One approach involves freezing the pre-event power set-point when inertia provision is required during a grid event [94]. However, this method disregards potential changes in wind speed during the event, which can lead to a reduction in aerodynamic efficiency. Although it can be optimistically assumed that wind speed remains constant during a brief period of grid support, this assumption can be flawed. In such cases, there is a significant risk of losing generation capacity, as power generation becomes completely decoupled from the available wind power [32].

In this work, a solution is adopted based on the method which is proposed in [32]. The method described in [32] takes into account the entire generator-rotor inertia to estimate rotor deviation during inertia emulation. By measuring frequency deviation, a new hypothetical rotor speed ω_{m-hypo} is introduced to compensate for the initial deviation during inertia emulation. However, some modifications are necessary since the model used in [32] overlooks converter and DC-link control dynamics that can influence rotor speed deviation.

When a step change in power is introduced in [32], the rotor speed exhibits a deviation in phase with the measured frequency of GSC. However, in the more

detailed model used in this work, both GSC and MSC control along with DC-link control is included. Therefore, when there is a frequency deviation in the grid, the AC power changes, which directly influences the electromagnetic torque (T_e) in the MSC control. Additionally, a portion of the torque is derived from the output of the DC-link control (see Figure 3.25). This setup prevents the behavior observed in [32] from occurring in the same manner with the more detailed wind turbine model used in this work. Therefore, it is necessary to account for these delays for the control and incorporate them into the compensation block.

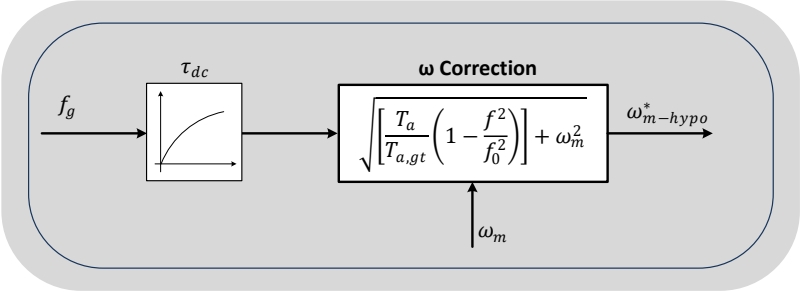

Figure 3.29: Compensation scheme to reduce adverse effect of inertia emulation while operating at MPPT [32]

Figure 3.29 shows the block diagram of the compensation scheme. The delay which is related to the bandwidth of the DC-link control is applied to the measured frequency to compensate for the DC-link controller dynamics. The measured frequency is then passed to the speed-modifying block [32], which uses an equation for ω_m, to keep rotor speed deviation nearly constant by incorporating frequency deviation. Additionally, because the initial rotor speed is included in the formula, variations in wind speed result in reduced inertia emulation, helping to prevent the rotor from falling below the cut-in speed [32].

To verify the performance of the suggested scheme for inertia emulation of the WT at below-rated wind speeds, a frequency profile featuring a rapid negative and a slower positive df/dt is given to the external grid, as shown in Figure 3.30. This figure also shows the rotor speed deviation with (ω_m) and without (ω_{m0}) compensation during inertia support. As shown, without compensation, the rotor speed decreases in response to the reduced grid frequency, leading to a 12% decrease

in the power reference. In contrast, with the compensated scheme, the variation in the rotor speed during inertia support is negligible. As a result, the power set point remains nearly constant, with a maximum deviation of less than 0.5%. This enables a higher inertia provision during frequency ramps as it is illustrated in Figure 3.30.

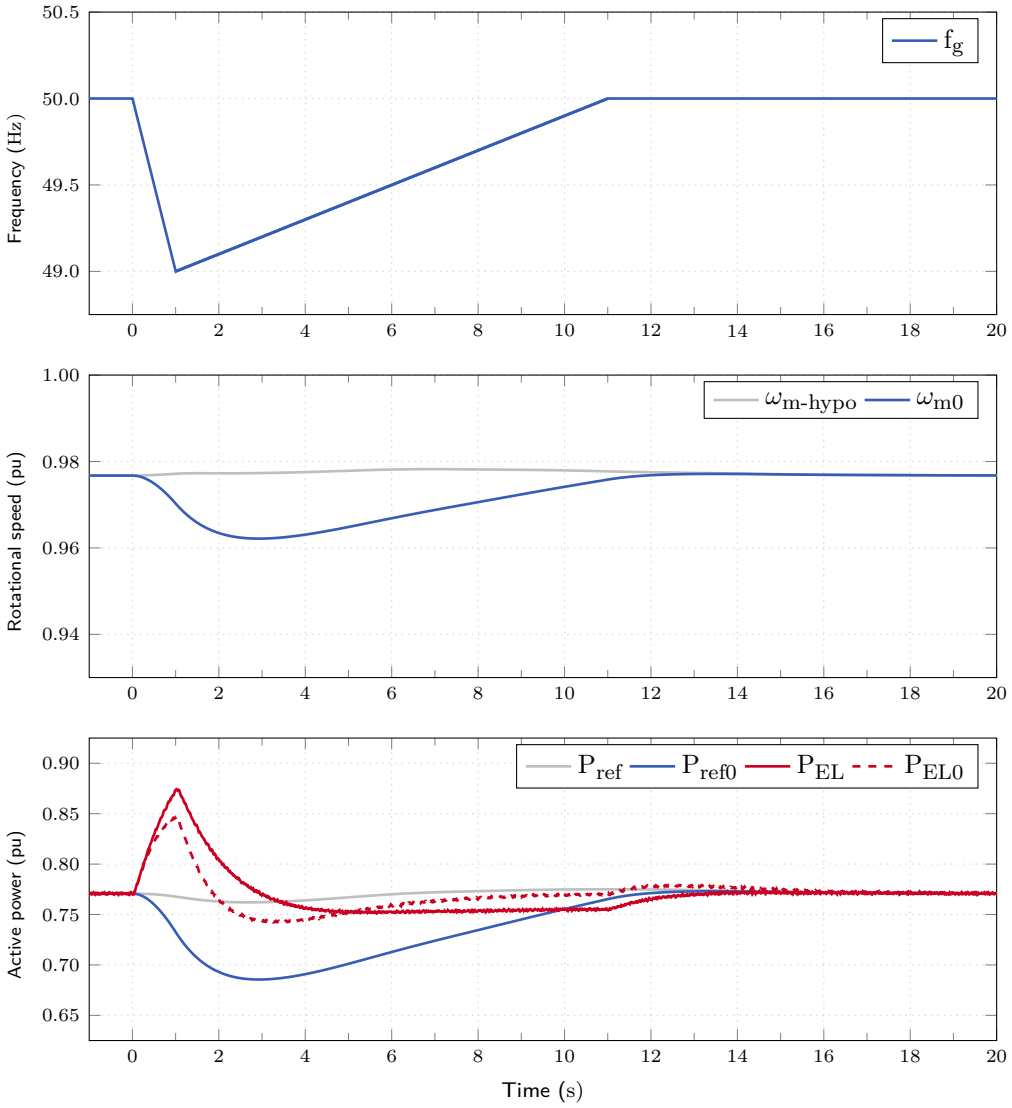

Figure 3.30: Inertia emulation following frequency ramps in both negative and positive directions in the grid using the modification scheme for rotor speed; P_{ref} and P_{ref0} are MPPT power references with and without compensation; P_{EL} and P_{EL0} are the corresponding injected active powers into the grid

As shown, during the negative frequency ramp, P_{EL} increased from 0.77 pu to a peak of 0.88 pu, corresponding to a 12% rise in active power. In contrast, without compensation, P_{EL0} plateaued at 0.84 pu, resulting in only a 7% increase, since the power set-point in this scenario does not remain constant. During the positive frequency ramp, a higher inertia contribution is also observed when the compensation scheme depicted in Figure 3.29 is applied.

3.3 Dynamic Response to Grid Events

In this chapter, the performance of the generation units will be compared together; These systems are namely, a GFL unit; a GFM-WT unit which was developed earlier in this chapter (see chapter 3.2.6); and lastly a traditional SG unit. The generation units are designed to be used for the islanding study in Chapters 4 and 5. To assess their compliance during grid events, their performance is validated against FNN scenarios as a benchmark [80]. The FNN test scenarios are proposed to confirm the GFM functionality of HVDC systems [80], however, these test cases also allow for verifying the GFM functionality of onshore wind turbines. The criteria for acceptable performance are based on remaining within the FNN envelope curves. The test scenarios are conducted on the test network depicted in Figure 3.31.

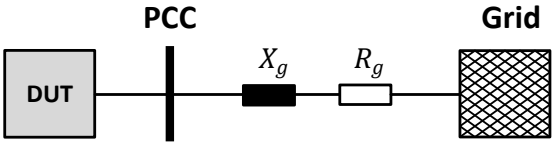

Figure 3.31: Equivalent circuit of test network for assessment of the grid forming behavior according to VDE FNN [80]

The device under test in Figure 3.31 refers to one of these three generation units used in the simulated power system. In all scenarios, the DUT operates at 50% of its nominal power, with a reactive power set point of zero. The three test scenarios include a 10-degree phase angle jump in the negative direction, a frequency ramp, and a step change in voltage magnitude. The goal of the developed GFM unit

is to mimic the behavior of a synchronous generator in counteracting these grid disturbances and achieving a stable operating point afterward.

Figure 3.32 illustrates the response to a 10-degree angle jump in negative direction in the grid. The instantaneous active and reactive power are shown for each generation unit. For the SG, after the initial inertia response, the oscillations decay with a swing mode characteristic. With the GFL unit, which operates as a current source, the PLL tracks and locks onto the new angle following the angle jump, showing no involvement in initial angle support, as expected. The GFM unit demonstrates initial inertia support within the first grid cycle [8]. As depicted in Figure 3.32, the active power reaches its peak at 20 ms and then gradually decays with its swing frequency. The swing eigenfrequency in the GFM-unit is higher compared to the SG, and damping is increased through tuning the control parameters, which is an advantage of the grid-forming control unit. Further increasing the damping coefficient would lead to an over-damped response, which would no longer resemble an inertia response.

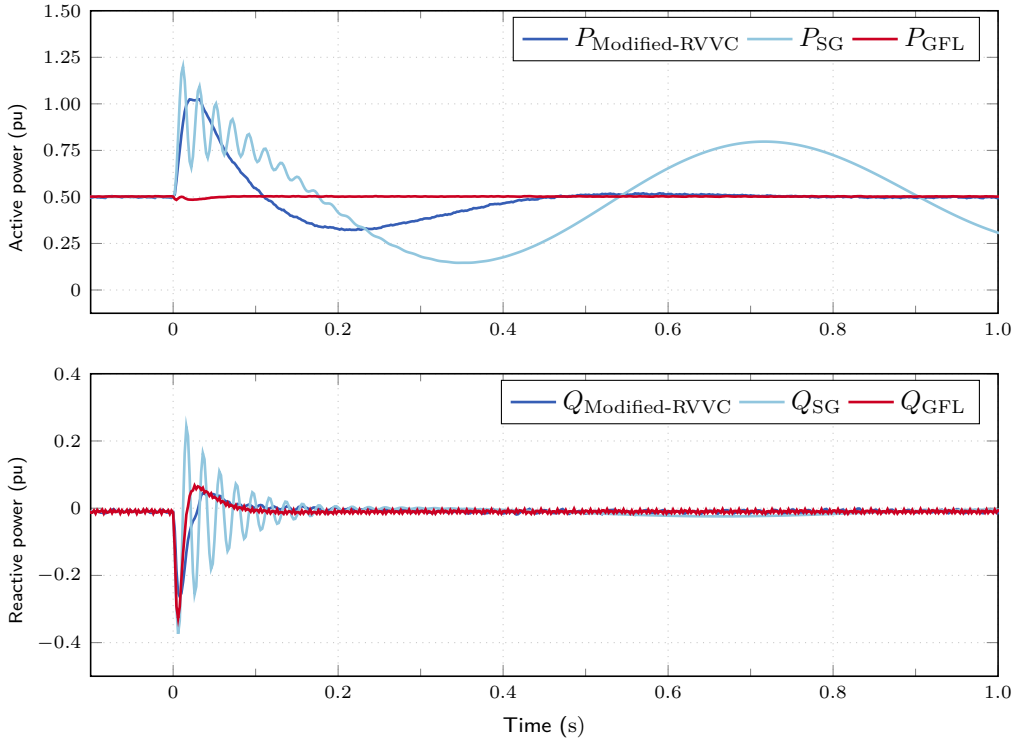

Figure 3.32: Response of GFM-unit, GFL-unit and SG to a 10 degrees angle jump

Additionally, it is shown that the response to this angle jump remains within the unit's linear operating range, without activating current limitations. Looking at the powers of the GFM unit, it is evident that the coupling between active and reactive power is small in response to the angle jump and the active power makes the main contribution in the response.

Figure 3.33 illustrates the active and reactive power response of all three units to a frequency ramp of -1 Hz/s. Given the fact that the inertia constant of SG and GFM-unit is $H = 5\,\mathrm{s}$, it is expected that after a transient period (or initial inertia response), the active power increases by 20% during the stationary phase of the frequency ramp.

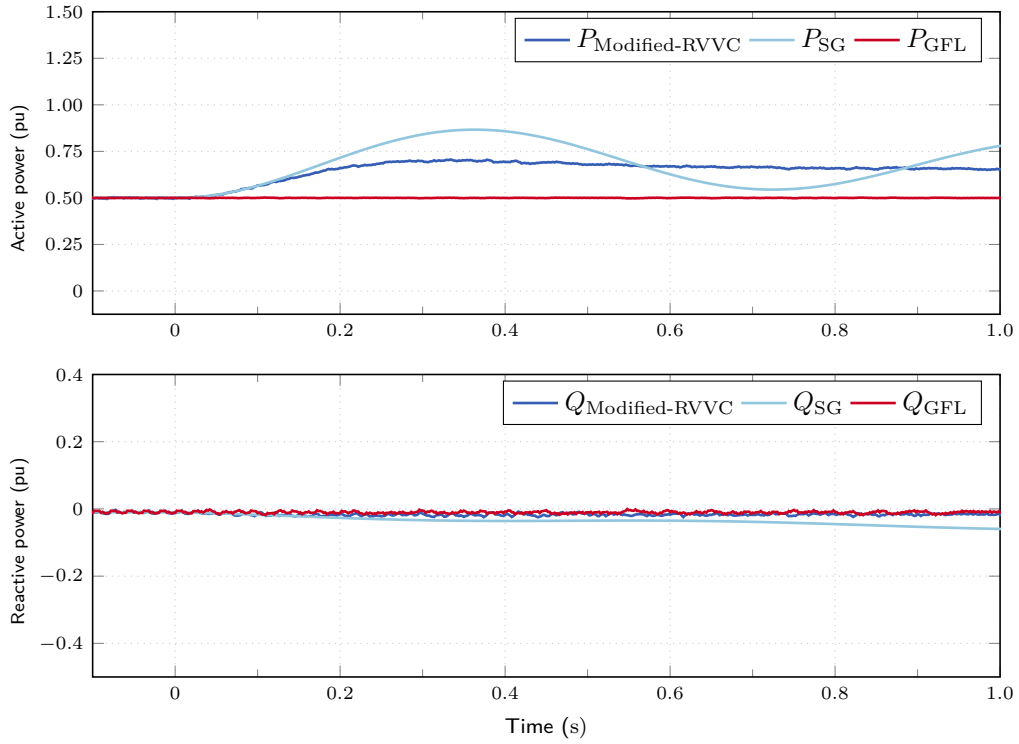

Figure 3.33: Response of GFM-unit, GFL-unit and SG to a frequency ramp of -1 Hz/s in the grid

As illustrated in Figure 3.33, the active power of the SG unit increases; however, it continues to oscillate with swing frequency within the timescale of the results. In the GFL unit, there is no active power participation during the frequency drop. As

the event begins, the PLL tracks the new angle and frequency. Consequently, the converter voltages are rapidly adjusted with the feed-forward components of the grid voltages. This results in a constant current trajectory and a stable operating point during the frequency variation.

The performance of the GFM unit shows that the active power increases in response to the frequency ramp, reaching a peak of 20% around 0.3 s. As shown in Figure 3.33, the dynamic response is influenced by the damping of the swing eigenfrequencies. With the designed parameters in this test grid, a damping of 80% is achieved for swing frequency for the GFM unit.

However, as the grid frequency continues to drop and along with that the rotor speed decreases, the active power begins to decrease slightly. This reduction in power is due to the maximum power tracking behavior at below-rated wind speeds, with inclusion of rotor speed compensation scheme (see Chapter 3.2.6). Using this scheme has improved the performance by minimizing the adverse effects of MPPT operation, limiting the power drop to around 4% at 1 s.

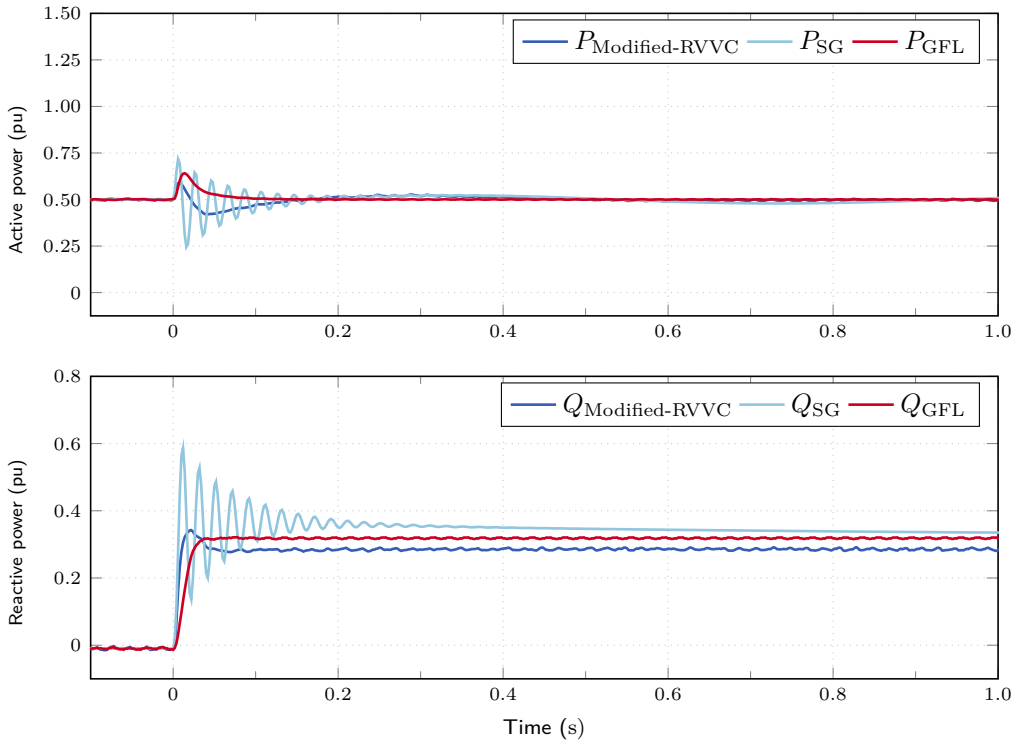

Figure 3.34: Response of GFM-unit, GFL-unit and SG to a 15% voltage drop in the AC network

The third FNN test verifies how the units participate in the fault current following a voltage magnitude jump and how it performs regarding fault ride-through capability. Figure 3.34 shows the active and reactive power for all generation units, following a -15% voltage jump in the network. According to the grid code for FRT, a reactive current injection is required, with a step response time of 30 ms and a settling time of 60 ms [52].

In an SG, the short-circuit current is primarily determined by the X''_d and X'_d parameters, especially for a fault at the PCC point. Typically, an SG supplies fault current for a duration of 1 to 1.5 seconds, depending on the short-circuit time constant T'_d [63]. The GFM unit also inherently contributes to mitigating voltage drops by injecting reactive current into the faulty area. Since the sum of $(X_c + X_v)$ in the GFM unit is much smaller than the transient and sub-transient impedance of the SG, without FRT, a much higher reactive current would be injected into the

low-voltage bus for a short period. However, to achieve comparable performance to a real SG within the converter's ratings, the FRT unit adapts the converter voltage magnitude, resulting in a prolonged short-circuit current for the converters. The dynamic performance is influenced by the FRT dead-bands, its response time, and the droop factor. In this work, the $k = 4$ is used for GFL unit and a $k_v \sim \frac{1}{k}$ for the GFM unit. As the transient virtual impedance parameters were selected according to the stability criteria (see Chapter 3.2.5), by adjusting the converter voltage vector through the FRT coefficient, a performance closer to that of a real SG is achieved.

It is observed in Figure 3.34 that the response of the GFM unit and SG to a voltage sag is inherent, with a very fast injection of reactive current before the full activation of the FRT in the GFM unit. In contrast, for the GFL system, as the entire dynamic performance depends on the FRT logic, the 30 ms step response is barely achieved. Active power oscillations are seen mainly in SG and GFM unit. The active power oscillation of GFM unit, decay according to their swing eigenfrequencies. In the GFL unit, active power deviates from pre-event operation point due the adjustment of the converter voltage vector to inject more reactive current following the event. By varying the q-current component, the load angle between the two voltage sources temporarily increases. Once the i_q settles at a new equilibrium point, the dq components of the converter voltage stabilize as well. As a result, the pre-event active power is restored after approximately 150 ms.

3.4 Summary

In Chapter 3, a GFM control scheme (Modified- RVVC) for application in a wind turbine unit has been introduced. The design process carefully considers multiple factors to achieve adequate dynamics, stability, and robustness, while also ensuring compliance with grid code requirements. As the design process can be conflicting regarding aforementioned criteria, a trade-off was made in selecting the control parameters.

In the GFM unit developed in this chapter, the design process begins by selecting

the inertia constant and the virtual impedance. Then, the system's dynamic model is used to determine the parameters for other controller variables. In this way, virtual circuit parameters are chosen to achieve acceptable decoupling between active and reactive power, ensure compatibility with FNN reference curves, and provide sufficient damping at the grid frequency resonance. To verify the controller's performance, it is tested under a variety of grid conditions, ranging from highly inductive to purely resistive networks with different grid short-circuit ratios. The designed controller maintained stability and adequate damping across these grid conditions.

From a hardware protection perspective, a voltage-based overcurrent protection scheme is implemented through a nonlinear virtual impedance. This setup enables operation as a voltage source while maintaining current within safe limits. The effectiveness of this scheme is evaluated in two grid scenarios: a negative 30-degree angle jump and a 3-phase bolted short circuit at the converter connection point. In both cases, the protection scheme successfully limits the current and provides an acceptable transient response.

Since the GFM control is intended for wind turbine applications, the entire control architecture is designed to leverage the WT's rotating mass for inertia and system support services, allowing it to provide instantaneous reserve in both directions. The control structure is adapted for the MSC and DC-link controllers, enabling grid support while respecting operational constraints. Given that the WT unit operates at maximum available power, a modification to the GSC power set-point is introduced to maximize inertia support availability at below-rated speeds. Finally, the fully designed GFM-WT unit is tested and compared with other generation units across three FNN test cases, verifying its grid-forming functionality.

In Chapter 4, the GFM-WT unit will be evaluated in various islanding scenarios to determine the stability limits for islanded operation in a network with a high proportion of inverter-based generation.

4 IMPACT OF LOAD ON STABILITY IN ISLANDED NETWORKS

4.1 Introduction

As mentioned earlier, the need for detailed power system modeling is evident when the system contains a high proportion of power electronic components, which introduce non-linearity due to their inherent limitations, on both the generation and consumption sides, and when the system experiences high dynamic events. Additionally, other types of loads, such as directly connected motor loads, must be accurately represented by their dynamic equations to show their impact on system stability following an event.

The focus of this dissertation is on these three types of load. Apart from constant impedance loads, induction motors are chosen due to their significant share in power consumption across various sectors, particularly in industrial applications [95]. Additionally, the growing trend toward the using power electronic loads, driven by their efficiency, performance, flexibility, and alignment with climate-neutral energy goals, is considered [10]. This shift emphasizes the increasing prevalence of power electronic loads in modern power systems, making them a crucial component to study in terms of their dynamic behavior during grid disturbances.

4.2 Load Modeling

4.2.1 Modeling Aggregated Loads

Many studies investigating the impact of reduced inertia in power systems have primarily focused on simplified load models, often representing loads as constant impedance only [96], or using a limited set of static load representations [4]. Despite the recognized importance of accurately modeling load characteristics, a survey conducted with TSOs across multiple countries highlighted a gap in the adequacy and application of existing load models, especially for capturing dynamic stability within the microsecond to second range [10]. This highlights the need for more detailed load representations in power system analysis.

In this work, the "A-to-D approach" is applied for load representation, as described in [95]. In this method, the load model, which includes multiple components, is first identified based on surveys or literature. Then, the model parameters are derived in a similar manner, drawing either from literature or knowledge bases. Typically, load models use static, dynamic, or a combination of both for load representation [97], [98]. Static load modeling represents the load with a voltage-dependent static polynomial or exponential load representations, which is widely used in steady-state power system analysis and long-term network planning, where system condition changes have minimal or slow effects on load characteristics [95]. However, for analyzing transient stability, which is the focus of this work, a static load representation is inadequate. In load classes dominated by electronic or rotating machine loads, a more detailed model, referred to as dynamic load modeling, is necessary.

This dissertation focuses on the transient stability of a system with various load classes that exhibit time-variant characteristics, such as dominant induction motors in industrial areas or high penetration of power electronics loads. In Chapter 4.2.2, the process of identifying the load model begins with categorizing the load components and determining the percentage of each component based on available data. This is followed by calculating the proportion of each load category accordingly. Three primary load categories are considered and modeled in this dissertation:

constant impedance loads, a three-phase induction motor model, and an active rectifier supplying a constant load. The modeling of directly-connected IM and power electronic loads are discussed in detail in Chapters 4.2.3 and 4.2.4.

4.2.2 Breakdown of Loads Across Various Consumer Sectors

The following section presents a load bus, which aggregates various load sectors and types of load components. Each load component represents different electrical devices typically found in specific end-user categories. The structure of this load modeling approach is illustrated in Figure 4.1 [95].

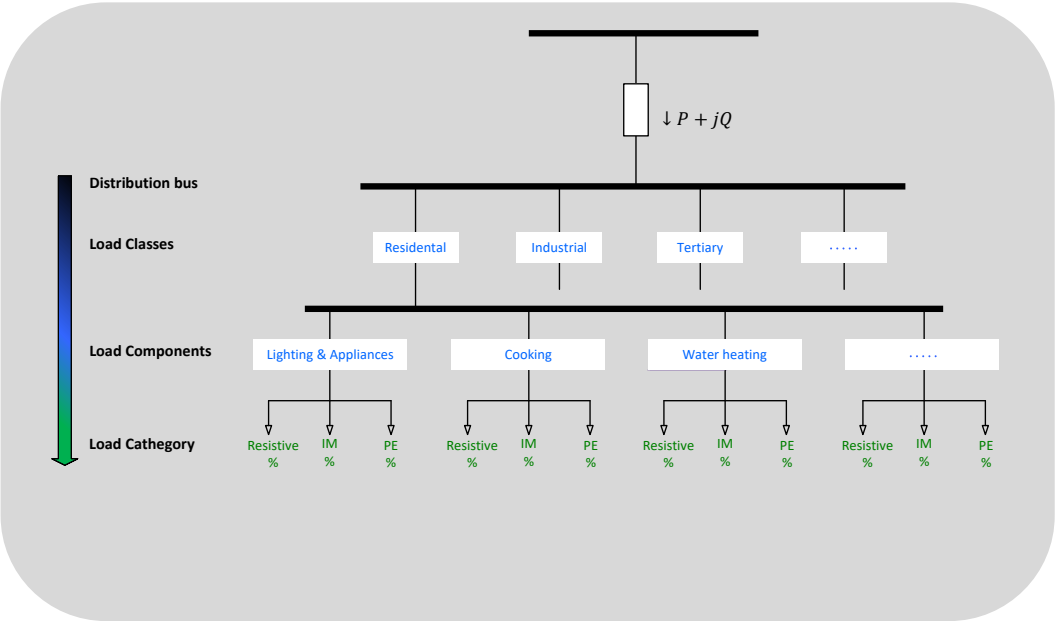

Figure 4.1: Diagram of component-based load modeling, in accordance to [95]

The three main sectors of electricity consumption are residential, industrial, and tertiary. According to [99], these sectors accounted for 95% of total electricity usage in Europe in 2020 (see Figure 4.2), with the industrial sector consuming 37.1%, the residential sector 29.9%, and the tertiary sector 28.4%. Since the components within each sector vary, it is important to identify which components consume the majority of power and their respective percentages.

To determine the percentage contribution of each component, customer surveys and literature are used, though the data may vary based on factors like geographical location, time of day, and season [95]. The approach in this work uses typical component data for each sector and classifies each component into three load categories based on its characteristics:

- Resistive loads
- Three-phase directly connected motors
- Three-phase power electronic loads

According to the literature [95], most loads in the residential, industrial, and tertiary sectors can be represented by one of these load types. The contribution of each load category in different sectors will be discussed in the following.

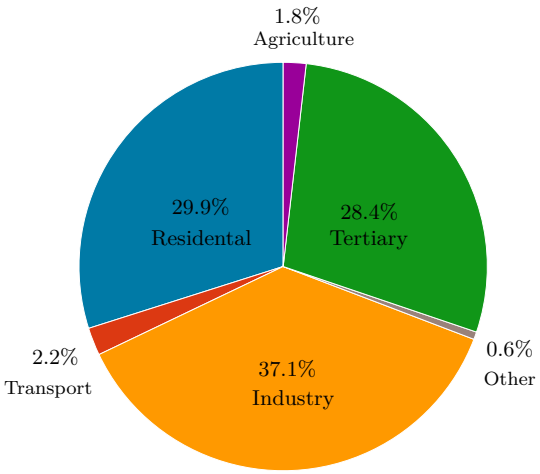

Figure 4.2: EU electricity consumption by sector (2020) [99]

Residential Load Class (LC_3)

This sector and its subsectors include power consumption in settings ranging from apartments, houses, and skyscrapers in high-density, urban areas, to smaller houses and 2-3 level apartments in remote locations with weak networks and low

power density [95]. The main components of this sector include cooking, heating, ventilation, air conditioning, Information and Communication Technologies (ICT), and lighting. According to power consumption data in the residential sector across various EU countries [99], the majority of EU member states consume the largest share of electricity for lighting and appliances, which includes load categories such as resistive, constant current, and motors.

Table 4.1 categorizes the loads in the residential sector into their respective components, with approximate percentages based on [100]. The data presented in Table 4.1 is sourced from [95] and [99] for the residential sector, with adaptation from the component breakdowns provided in [100] and [101]. As shown, approximately 47% of power consumption is attributed to lighting and appliances. Typical loads in this component include fluorescent lamps and LEDs, which are widely used. LED lighting typically operates using direct current (DC), supplied by an AC/DC converter [16]. This component is then further subdivided into the percentages of resistive, IM, and PE loads, as detailed in Table 4.1.

The second major component in Table 4.1 is cooking, which accounts for over 23% of electricity consumption in residential sector in Germany. This primarily consists of resistive loads for ovens and hobs, as well as power electronic loads for microwaves [100]. Another component with significant contribution is space and air heating, which has increased in recent years. This category includes resistive loads and IM for heat pumps.

Table 4.1: Residential load profile, breaking down the load demand into individual components

Load Components	Percentage	R	IM	PE	Notes
Lighting and appliances	47.3%	9.7%	31.2%	6.4%	Lighting = 16.1% (60% R + 40% PE); Appliances = 31.2% (100% IM QT & CT)
Cooking	29.0%	23.2%	–	5.8%	Resistive cooking = 80%; Microwave = 20%
Water heating	11.4%	5.7%	5.7%	–	Water heating = 50% resistive + 50% heat pump
Space heating	7.5%	3.8%	3.7%	–	Space heating = 51% resistive + 49% heat pump
Space cooling	1.3%	–	1.3%	–	100% IM QT
ICT, Electronics, and other users	3.5%	–	–	3.5%	Considered PE
Aggregate	**100%**	**42.4%**	**41.9%**	**15.7%**	

The last component is ICT, electronic and other users which mainly includes two load types: Switch-Mode Power Supply (SMPS) loads, which are DC power supplies, and three-phase Adjustable Speed Drives (ASDs) [95]. Typical SMPS loads in residential sectors include consumer electronics such as PCs, TVs, printers, and certain home appliances. These devices often incorporate AC/DC converters, with or without power factor correction, to supply a load. Load types like ASDs, on the other hand, include a rectifier and a three-phase inverter to feed a motor in the back to back configurations. Given the fact that all these loads either use a rectifier to supply a DC load directly or a back-to-back converter structure to feed a three-phase motor, they are categorized as PE loads with constant power consumption.

As shown in Table 4.1, the residential sector (LC_3) is approximately comprised of 42.4% resistive load, 41.9% IM load, and 15.7% PE load.

Industrial Load Class (LC_4)

Power consumption in the industrial sector is more diverse compared to residential and tertiary sectors. Industrial loads include electrical devices used across various businesses, including materials processing, construction, iron and steel production, and manufacturing [99]. Developing a general load model for the industrial sector is challenging, as each type of industrial activity varies significantly from others. Cross-cutting electricity consumption across different industries, as shown in [102], includes lighting, electric motors, pumps, ventilation, cooling, and process technology.

A common feature of these technologies is the large share of directly-connected machines. Therefore, when analyzing the impact of network disturbances and the dynamic interactions between loads and the power system, it is essential to model large industrial loads. Due to their dynamic nature, disturbances can have a significant influence on voltage and frequency stability in the load bus.

Table 4.3: Industrial load profile, breaking down the load demand into individual components, adopted from [102]

Load Components	Percentage	R	IM	PE	Notes
Motors	70.3%	–	70.3%	–	Mostly IM with QT or CT
Process technology	23.0%	1.2%	–	21.8%	5% R - 95% PE
Lighting	6.7%	–	–	6.7%	100% LED lighting = PE
Aggregate	**100%**	**1.2%**	**70.3%**	**28.5%**	

According to the energy consumption breakdown across various industrial sectors presented in [102], the combined contributions of process technology, lighting, and motors were measured for each industry and then averaged across 14 industries. This results in a 70.3% motors loads, 23.0% process technology and 6.7% lighting in average, shown in Table 4.3. According to [95], the industrial sector is estimated to have a total motor load share of 70%.

Tertiary Load Class (LC_6)

The tertiary sector contains a more diverse set of components than the residential sector due to its variety of subsectors. This sector includes power consumption in areas such as communications and transport, retail, hotel & catering, education, healthcare, and commercial offices [95]. As a result, the load composition differs across each subsector. For instance, commercial offices rely heavily on three-phase motor loads for heating, lifts, and ventilation systems. There is also significant consumption of electronic loads, such as laptops and PCs, which use power electronics. A similar trend is observed in the education subsector.

Table 4.5: Tertiary load profile, breaking down the load demand into individual components, adopted from [103]

Load Components	Percentage	R	IM	PE	Notes
Space & Water Heating	19.2%	16.3%	2.9%	–	Heating: 85% R, 15% IM
Office Lighting	20.8%	–	–	20.8%	100% PE
Street Lighting	4.7%	–	–	4.7%	100% PE
Motors (Refrigerator, Ventilation, Pumps, etc.)	36.6%	–	36.6%	–	Includes IM with QT
Electronics	6.0%	–	–	6.0%	100% PE
Cooking	5.0%	4.0%	–	1.0%	Cooking: 80% Resistive, 20% PE
Others	7.7%	–	–	7.7%	100% PE
Aggregate	**100%**	**20.3%**	**39.5%**	**40.2%**	

The healthcare subsector, however, features a more varied mix of loads, including PE loads, motors, lighting, and other components. Table 4.5 presents the major electricity-consuming components in the tertiary sector, along with their percentages and corresponding load categories [103]. This breakdown represents a cross-section of typical components in the tertiary sector and its subsectors.

Mix Load Class (LC_5)

An aggregate load bus can supply various load sectors simultaneously. As shown in Table 4.6, each sector's contribution is represented according to its share. This setup in LC_5 represents an islanding scenario, where the network connection is lost,

and all three sectors are present within the remaining island. Therefore, a fraction of each sector is incorporated here based on the percentages shown in Figure 4.2, identifying the main components within this mixed-load class and the proportions of each load category [99].

Table 4.6 provides a summary of the load category percentages within a bus containing all load sectors. This distribution results in 18.9% resistive load, 49.8% IM load, and 31.3% PE load. It should be noted that the islanding scenarios in this work is designed to represent the dynamic interactions between synchronous and non-synchronous generation and the load. Including these various load sectors allows for the observation of load dynamics across a spectrum from purely resistive to purely PE loads.

Table 4.6: A cross-section of a mixed load profile, breaking down the load demand into individual components, adopted from [99]

Load Components	Percentage	R	IM	PE	Notes
Industrial	37.1%	0.4%	26.1%	10.6%	–
Residential	29.9%	12.7%	12.5%	4.7%	–
Tertiary	28.4%	5.8%	11.2%	11.4%	–
Others	4.6%	–	–	4.6%	–
Aggregate	**100%**	**18.9%**	**49.8%**	**31.3%**	

Additional Load Classes: Case Studies

Case Study 1 (LC_1) This case study with pure resistive load which is introduced as (LC_1) serves as the base for all simulation scenarios in this thesis, aimed at assessing the necessary inertia following a significant power imbalance in the system. Since this load class is frequently used in the literature for islanding scenarios, it has been selected as the baseline scenario in this work [32], [65]. Due to the voltage-dependent nature of this load type, following an active power imbalance and any resulting voltage deviation, the load's active power consumption decreases proportionally with voltage, which generally supports stability in islanding in this case study.

Case Study 2 (LC_2) This load class offers a more realistic profile compared to a purely resistive load, while still exhibiting grid-friendly behavior, as R+IM loads account for 90% of the total power consumption. However, including 45% IM and 10% PE loads, causes that the power consumption profile diverges from that of purely resistive loads. Additionally, as previously noted, this setup also enables investigation across a spectrum, from purely resistive to high IM percentages, and eventually to predominantly PE loads.

Case Study 7-10 (LC_7-LC_{10}) Since load class 6 (LC_6), representing the tertiary sector, has the highest percentage of PE loads and provides a rough estimate of the actual PE load percentage in the grid, four additional load classes are introduced to cover higher PE load percentages. According to data collected from TSOs in a survey [10], it is expected that a significant portion of motor loads is being replaced by converter-fed drives. Additionally, some TSOs in this study estimated that approximately 70% of the total system load comes from PE loads [10].

Given the rising trend of electronic loads, there is a need to closely investigate the transient stability of the power system as these loads become the dominant category. Therefore, in case studies 7 to 10, the percentage of PE loads increases at almost a constant rate (17%), while the proportion of more grid-friendly loads (R+IM) decreases accordingly.

Considering the aforementioned trend and the proportion of typical load sectors in Section 4.2.2, this work defines ten load classes for investigating islanding stability with load impact. Figure 4.3 summarizes these ten load classes along with their corresponding load categories.

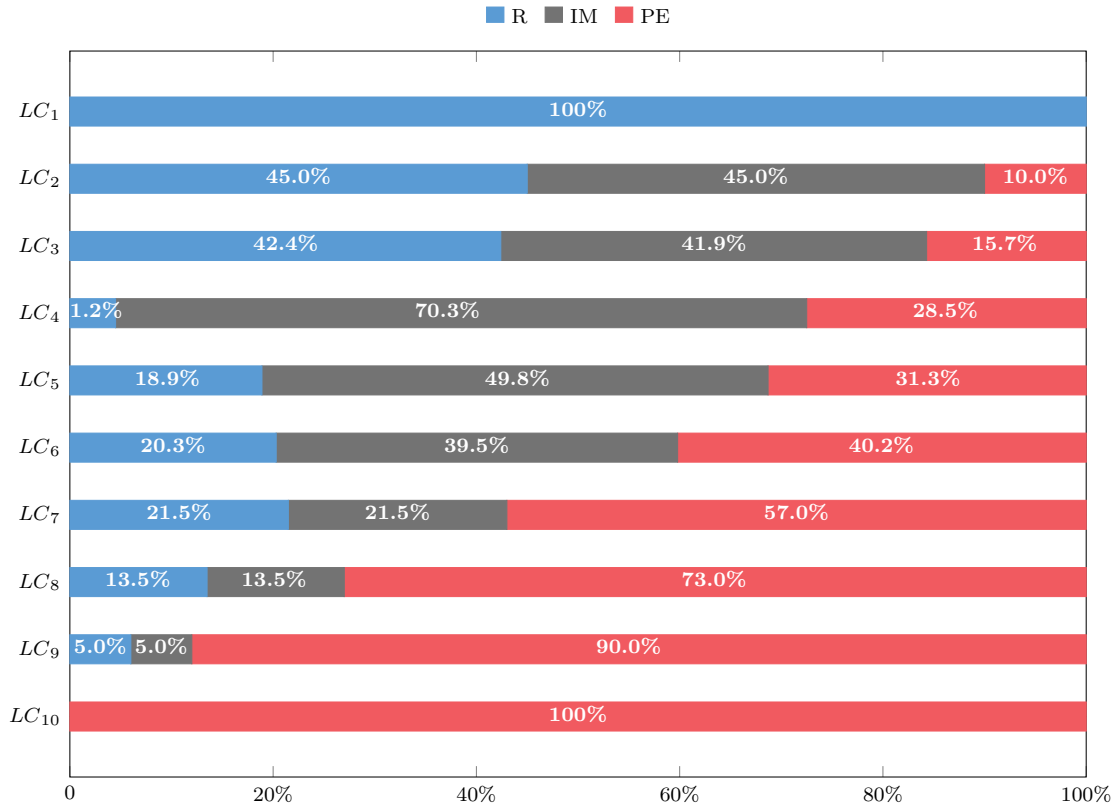

Figure 4.3: Summary of the ten load classes, including the percentage of each individual load component, used in the islanding scenarios in this study

4.2.3 Dynamic Model of Three-Phase Motor Loads

In this work, a model of a three-phase induction motor with a quadratic torque load is used in Matlab, which is directly connected to the AC grid. The motor's mechanical torque characteristic is determined using a polynomial model as shown in Equation 4.1 [95]:

$$T = T_0(A \cdot \omega^2) \tag{4.1}$$

Where the T_0 is the steady-state torque at synchronous speed and A is the torque coefficient, which varies depending on the motor's load type [95]. The Quadratic Torque (QT) load for the induction motor can be used to represent the following end-users:

- As a large industrial motor or power plant auxiliary with a quadratic torque model and an inertia constant of $H = 1.5$ s [95].
- As a small industrial motor, pump, or fan with a quadratic torque model and an inertia constant of $H = 0.7$ s [95].
- As a typical motor with quadratic torque loading in residential and tertiary areas, such as dishwashers, washing machines, dryers, and agricultural water pumps, with an inertia constant in the range of $H = (0.28 - 1.5)$ s [104] .

4.2.4 Modeling Power Electronic Loads

Power electronic loads represent a significant portion of various load classes, as shown in Chapter 4.2.2. These loads act as a constant power loads even during supply voltage variations as long as current and modulation index limitation of the converter allow [95]. As mentioned earlier, load types like adjustable speed drives are drive-controlled three phase motors with a back to back converter configuration. A common control approach for these drives involves current control on the active rectifier side and field-oriented control on the inverter side [58].

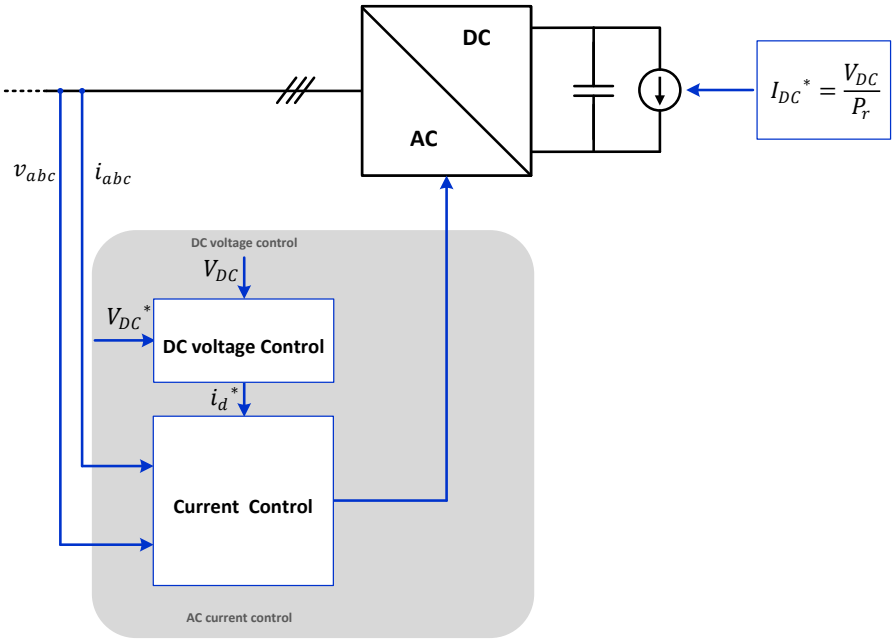

Figure 4.4: Block diagram of the PE load

In this work, the model of the PE load is illustrated in Figure 4.4 [101]. As shown, the rectifier supplies a constant DC load, which replaces the inverter and motor or the variable resistor which is typically found in SMPS configurations [101]. The current source maintains constant power consumption as long as it does not exceed its specified limit.

4.2.5 Load Response to Frequency and Voltage Steps

This chapter investigates the performance of the modeled loads during various grid events. A comparison is conducted to highlight the dynamic behavior of each load type, providing a foundation for analyzing more complex islanding scenarios in Chapter 4.3.

Figure 4.5 illustrates the response of each load type to a ±2% change in network voltage and frequency. For a resistive load, whose power consumption depends purely on voltage, an increase in network voltage results in a quadratic rise in power consumption. In the case of the induction machine, a 2% voltage increase leads to

an increase in electrical torque, as torque is directly linked to the stator voltage. Simultaneously, slip decreases, causing a slight rise in rotor speed. However, this variation in rotor speed causes a mechanical loading increase of less than 1%.

As shown in Figure 4.5, following a voltage jump during the dynamic phase, active and reactive power rise by 25% and 45%, respectively. However, in steady state, the active power shows only a slight increase (approximately 0.2%), while reactive power consumption rises more significantly, by about 7.6%. For the power electronic load, the increase in network voltage does not change active or reactive power consumption. This is primarily due to the DC-link controller, which maintains a constant power flow by adjusting the current setpoint (i_d^*) accordingly.

The load response to a 2% increase in network frequency is also illustrated in Figure 4.5. An increase in network frequency directly impacts the synchronous speed of the machine, causing a corresponding increase in rotor speed. This rise in rotor speed affects the mechanical torque quadratically and mechanical power by a cubic relationship (around 6%). Additionally, the machine's reactive power decreases by approximately 5% due to the substantial reduction in slip caused by the higher frequency. For the power electronic load, however, active and reactive power consumption remain unaffected by the frequency change, as these loads are independent of frequency deviations.

For a 2% decrease in network voltage or frequency (see Figure 4.5), the previously described effects apply in reverse, reflecting the load response in these scenarios.

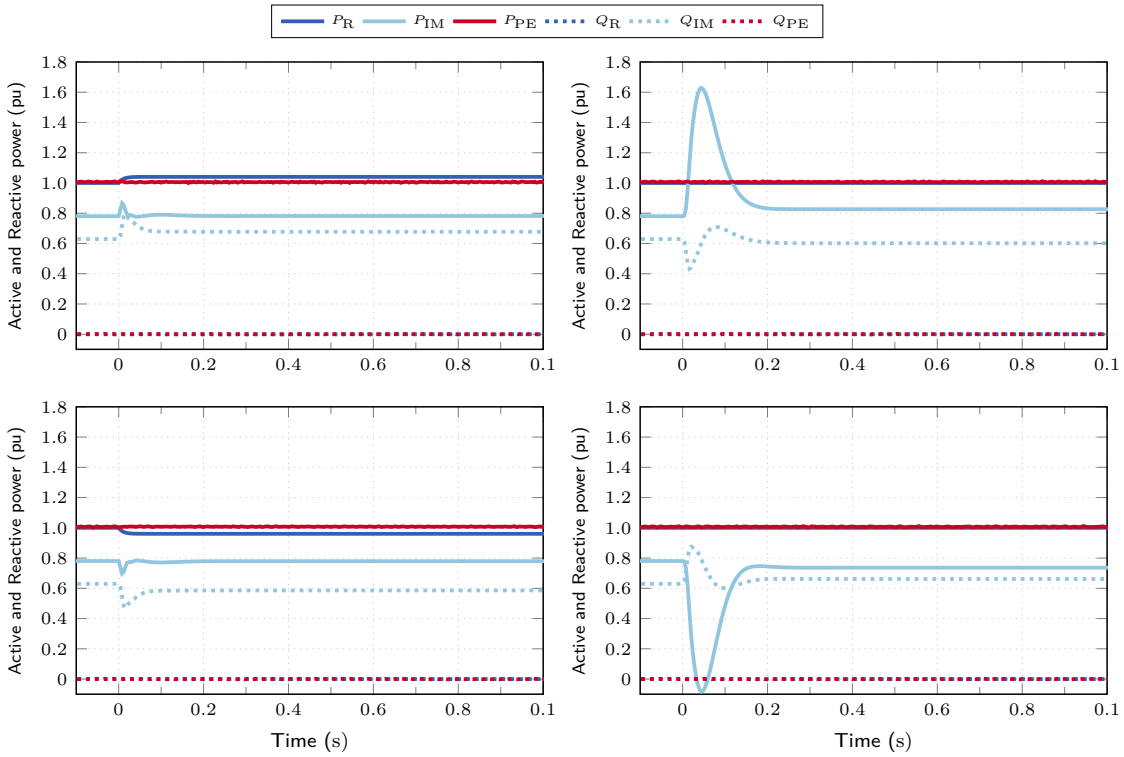

Figure 4.5: Comparing performance of three load components in different grid events, left: 2% increase in network voltage, right: 2% increase in network frequency

4.3 Island Network Study

In this chapter, the minimum system inertia is first determined for the subsequent islanding studies. Then, the structure of the test network is discussed in detail in Chapter 4.3.3, along with an explanation of the criteria for evaluation of the test cases. Finally, the network is tested under islanding scenarios across various load cases to evaluate the effect of load dynamics on the minimum required system inertia.

4.3.1 Definition of Inertia at the Plant and System Levels

The inertia constant in a plant level is described using [105]:

$$H = \frac{1}{2}\frac{J\omega_n^2}{S_n} \tag{4.2}$$

In Equation 4.2, J represents the moment of inertia for the entire turbine-generator of the unit, ω_n denotes is the rated mechanical angular velocity of the rotor, and S_n is the generator's rated apparent power. The inertia constant H indicates the duration in seconds for which the generator can supply load using the energy stored in its rotating masses. For a synchronous machine, the relation between acceleration time constant (T_A) known as 'Time Constant' and the inertia constant of turbine-generator (H) is defined as [19]

$$T_A = 2 \cdot H \tag{4.3}$$

The acceleration time constant of the network (T_N), can be defined as the ratio of the sum of the time constants of all units participating in inertia provision to the total network load [105].

$$T_N = \frac{\sum_{i=1}^{N} T_{Ai} S_{ni}}{S_{n,Load}} \tag{4.4}$$

In Equation 4.4, T_{Ai} and S_{ni} are the time constant and the rated apparent power of generator i, respectively. Since the generation units in this work include both

synchronous-based and non synchronous-based units, the acceleration time constant indicates the proportion of units contributing in inertia relative to the overall load. Thus, T_N represents the strength of the isolated power system and plays a key role in maintaining frequency stability after a power imbalance [106]. Equation 4.5 shows the minimum required time constant as a function of power imbalance and the maximum rate of change of frequency [106], [19]:

$$T_N = \frac{\Delta P}{P_{Load}} \cdot \frac{f_0}{RoCoF}$$

$$\xrightarrow{\text{for } \Delta P=24\% \text{ \& } T_N \text{ is in } pu_L} T_{N1} = 0.24(pu_L) \cdot \frac{50\,(\text{Hz})}{2\,(\text{Hz/s})} = 6\,\text{s} \tag{4.5}$$

In 4.5, the load imbalance is initially stated as pu_L, and T_N is defined as the ratio of all units contributing to inertia to the nominal power of the total load, as shown in Equation 4.4. Based on this, for a 24% imbalance and a maximum RoCoF of 2 Hz/s, a system time constant of 6 s is required.

The minimum required inertia derived from Equation 4.5 does not consider load and generation dynamics, voltage disturbance effects, or emergency network measures during major imbalances, factors that significantly affect frequency stability. These factors will be addressed in detail in the islanding simulations in Chapter 5.

4.3.2 Stability Criteria for Evaluation of Test Cases

Frequency

Frequency stability refers to the ability of an interconnected electrical system to restore a stable grid frequency and maintain an active power balance after a major disturbance [12]. Disturbances, such as load or generation failures, can cause deviations in frequency. To prevent issues like protection tripping and

disconnection of generation systems and loads, the frequency must be stabilized within the acceptable limits [8].

To assess test results according to the frequency stability, the maximum and minimum frequencies (frequency nadir) are compared against the permissible values. The upper limit is set at a maximum frequency of 51.5 Hz, which allows generation units to remain connected. The frequency nadir, defined as 47.5 Hz, represents the point at which a blackout becomes inevitable [1].

Rate of Change of Frequency

In an islanding event, the rate of change of frequency is crucial to the stability of the electrical grid. This value, which represents the time derivative of the power system frequency (df/dt), is derived from Equation 4.5 [19],based on the power imbalance ΔP and the system time constant T_N.

Following a significant increase in the transient frequency gradient after a major power imbalance, the system may be at risk of stability loss due to malfunctioning frequency-dependent mechanisms, such as Under Frequency Load Shedding (UFLS) and generator protection relays [106]. According to ENTSO-E, a RoCoF of 2 Hz/s must be considered for future scenarios, especially when determining the minimum required inertia in system split cases [8]. A RoCoF of 2 Hz/s ensures that DC-connected parks using HVDC (with a RoCoF withstand limit of 2.5 Hz/s) and type 1 generation units with synchronous generators remain connected during islanding events.

The recommendation for system split scenarios in future system development suggests a maximum imbalance of up to 40% [8]. Simulation results in Chapter 5 for system split cases with this level of power imbalance determine the amount of GFM units that must be integrated into the generation fleet in order to achieve a maximum frequency gradient below 2 Hz/s (measurment window of 500 ms, see Table 4.7).

Dynamic Voltage Stability

To assess voltage stability in different test scenarios, continuous operation within a range of ±10% of the nominal voltage (V_n) is permitted. Any voltage outside this range is evaluated according to the guidelines in [1], with consideration given to the duration for which the generation unit can remain connected at that voltage level.

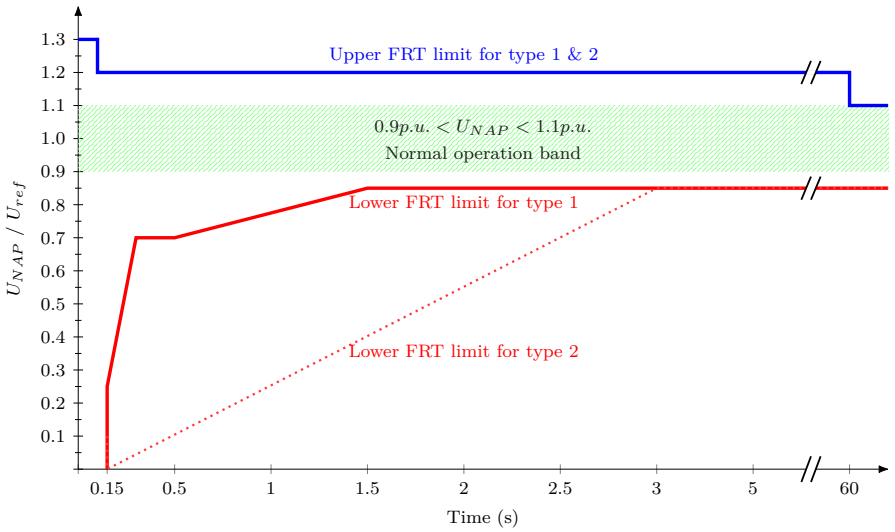

Figure 4.6: FRT boundaries for type 1 & 2 of generation plants [99]

Figure 4.6 illustrates the FRT curve for the voltage at the grid connection point for type 1 generation plants, which use synchronous generator. Within the operating range of the power generating unit, residual voltages after faults and voltage dips must stay within this boundary to prevent unit disconnection. The lines represent residual voltages for three-phase symmetrical faults. For type 2 generation plants, the time-voltage curves are more demanding compared to those for type 1 [1].

Since both type 1 and type 2 generation units are present in the islanding scenarios considered in this work, the criterion is to prevent disconnection of any unit in the network after islanding. Thus, the curve for type 1 generation units in Figure 4.6 is used for evaluating results [1]. If the voltage remains within the FRT band during

a test, allowing continuous operation of all remaining units in the network without disconnection, the test is considered successful regarding the voltage profile [10].

4.3.3 Structure of the Test Network

A two-node system is used in this study to test the performance of generation units, specifically REN's connecting to various loads. The connection to the grid, represented by a Thévenin equivalent source, was discussed in Chapter 3.3, where FNN test scenarios were conducted to differentiate between the performance of a GFM and a GFL unit. As the grid in these scenarios is very strong, the generation units have to follow the transient, which is imposed by the grid. In this chapter, the two-node system is used to investigate islanding scenarios with different load classes, presented in Chapter 4.2.2. In islanding scenarios, the proportion of GFL to GFM generation units, the loads in the island, and the magnitude of the power imbalance vary, leading to a range of network conditions from weak to very weak.

The main objective of this dissertation is to determine the extent to which GFM units must replace GFL units for stable operation after a major grid disturbance, and to assess how different load characteristics impact these boundaries. The reduced two-node network allows the execution of multiple test cases and scenarios [107]. Figure 4.7 illustrates the single line diagram of the test setup for the system split scenarios.

In the power generation sector in Figure 4.7, the SG and GFL unit use the model presented in Chapter 2.4. The frequency containment reserve is also implemented to maintain a balance between generation and consumption in the islanded network. The only unit capable of participating in primary frequency support is the SG, with a limited contribution of 10% of the total generation of the islanded network. Details of the frequency containment reserve implementation are provided in Table 4.7 [48]. The GFM-WT in Figure 4.7 is implemented based on the model developed in Chapter 3.2.6.

Figure 4.7 also depicts a load bus consisting of eleven load branches, each containing three types of loads. Additionally, the load shedding mechanism is implemented,

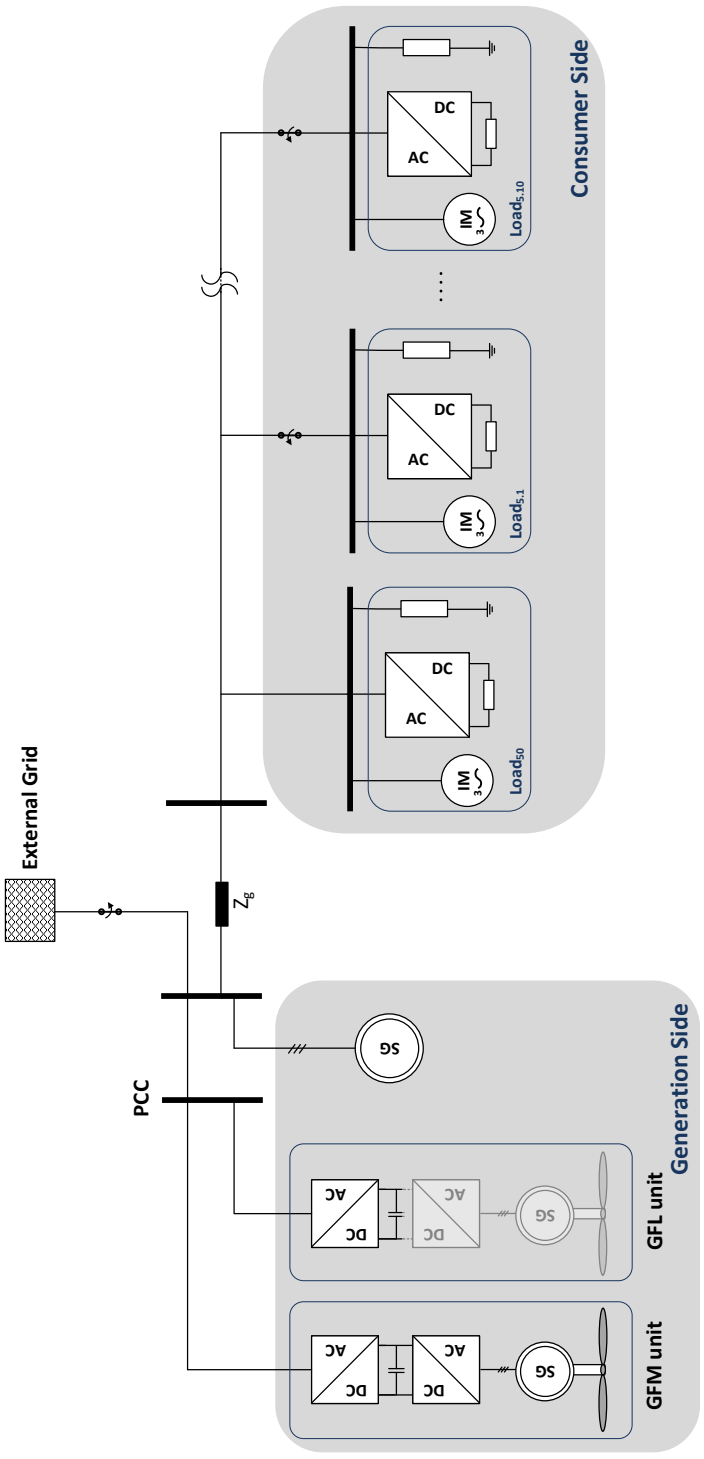

Figure 4.7: Single-line diagram of the two-node network used for islanding studies, including generation and load bus configurations

with 5% of the total load power being dropped at each shedding stage automatically [12], [108]. The load shedding mechanism is implemented across ten branches, capable of shedding up to 50% of the total load over ten stages. The measurement and triggering delays for the load shedding function are detailed in Table 4.7.

In the measurements section, a frequency measurement block is implemented using a PLL with a time constant of ($\tau_{PLL} = 40$ ms). The RoCoF measurement block takes the measured frequency as input and calculates the rate of change of frequency over a sliding window of 500 ms to mitigate the effects of noise in frequency measurements, providing more reliable and robust results [109], [110], [111].

Table 4.7: Summary of system requirements and control mechanisms for frequency regulation during normal and emergency operation in the islanding study

Generation Level	**Frequency Containment Reserve (FCR) [48]** • Droop gain: 5pu/pu=10%/Hz • Frequency range: [49.8 Hz - 50.2 Hz] • Power range: ± 0.1 pu	**Limited Frequency Sensitive Mode-Overfrequency (LFSM-O)** • Droop gain: -20 pu/pu = -40%/Hz • Frequency range: [50.2 Hz - 51.5 Hz] • Power range: $[-0.52 \text{ pu} - 0 \text{ pu}]$ • Activation delay: Tof = 2 s, according to grid codes [112]
Consumer Level	**Self-Regulating Effect** • 0-7%/Hz, depending on the load class	**Under Frequency Load Shedding (UFLS)** • Frequency range: [49 Hz - 48.1 Hz] • 10 stages of load shedding • Total power drop: 50% • Load disconnection in each stage: 5% • Frequency deadband: $[50 \text{ Hz} \pm 0.2 \text{ Hz}]$ • Measurement time constant: 40 ms • Max disconnection delay of breakers: $[80 \text{ ms} - 150 \text{ ms}]$
Power System Level	**Frequency Measurement** • Measurement time constant: 40 ms	**RoCoF Measurements** • Measurement window size: 500 ms according to [110] - [111]

4.4 Influence of Load Characteristic in Island Network

In this chapter, two islanding scenarios with symmetrical import and export imbalances are tested. The focus is on the first milliseconds to seconds after separation, where factors such as the non-linearity of PE loads, controller saturation, the inertia of induction motors, and other dynamics influence system stability. In the islanding studies presented in this chapter, the only variable is the network load, which varies from load class 1 to 10. This approach provides deeper insights into the impact of load dynamics on the stability of the island after separation, while keeping the generation configuration constant.

4.4.1 Situation I: 24% Import Loss

The first simulated scenario is a 24% import loss ($\Delta P = -0.24\%$), similar to the blackout in Italy in 2006 [113]. Among the ten load classes, the base scenario (LC_1) assumes a 100% resistive load to ensure comparability with many of the current literature on the minimum inertia requirements in power systems, see [4], [6],[32], [65], [96], [114].

To avoid operating near the stability margin and to analyze the influence of load dynamics in the scenarios of Chapter 4, an additional 2 s is added to the minimum required time constant from Equation 4.5. As a result, the time constant for the power system under ±24% power imbalances is set to $T_N = 8$ s

In this scenario, the SG's contribution is fixed at 10% of the total generation MVA of the system. To achieve a system time constant of $T_N = 8s$, the share of GFL unit is 20% and the GFM-WT unit accounts for 70% of the total generation. It should be noted that all units in this scenario are operating in curtailed mode. The test results for load classes 1-10 are presented in Chapter 4.4.1. At $t = 0$ s, the connection to the external grid is lost. This line was supplying 24% of the total load, resulting in a 24% power deficit in all test scenarios after islanding.

Analysis of the Import Test Cases

Base Scenario (LC_1)

Figure 4.8 presents the simulation results following grid disconnection with a 24% import deficit. For the base scenario, which assumes a 100% resistive load (LC_1), the frequency decreases after islanding due to the generation loss. As depicted in Figure 4.8, following to islanding, the voltage drops to 0.96 pu. In the case of a purely resistive load, this voltage reduction aids in frequency restoration. As a result, the RoCoF in this scenario reaches -1.5 Hz/s, which has a smaller magnitude than the calculated value of -2 Hz/s for this network time constant. The reduction in power imbalance due to the deviation of voltage from its nominal value, makes the inertia constant ($T_N = 8$ s) very conservative for this load class.

Figure 4.8 also illustrates the timing and magnitude of load shedding when the frequency reaches the load-shedding thresholds. A total of six load-shedding steps are activated, ultimately stabilizing the frequency at 50.5 Hz. This value remains within the range of the limited frequency-sensitive mode. Observing the overall trends in frequency, voltage profile, and RoCoF with LC_1, it is evident that stable operation is maintained within the first 10 s after the islanding event, without the risk of disconnection for the network generation.

Figure 4.9 illustrates the frequency, voltage at the load bus, and power generation of all three units over two time spans: $0 - 0.1$ and $0 - 1$ s. The main idea here is to have a closer look at the sequence of events following grid disconnection and the transition to islanding. During the first 100 ms, the two grid-forming units (SG and GFM-WT) cannot immediately adjust the voltage vector due to their voltage source nature. As 80% of the generation is supplied by the GFM units, contributing an inertia constant of $T_N = 8$ s in the network, and the SG's share is limited to 10% of the total generation, the performance of the dominant source (GFM-WT unit), is analyzed first in the following.

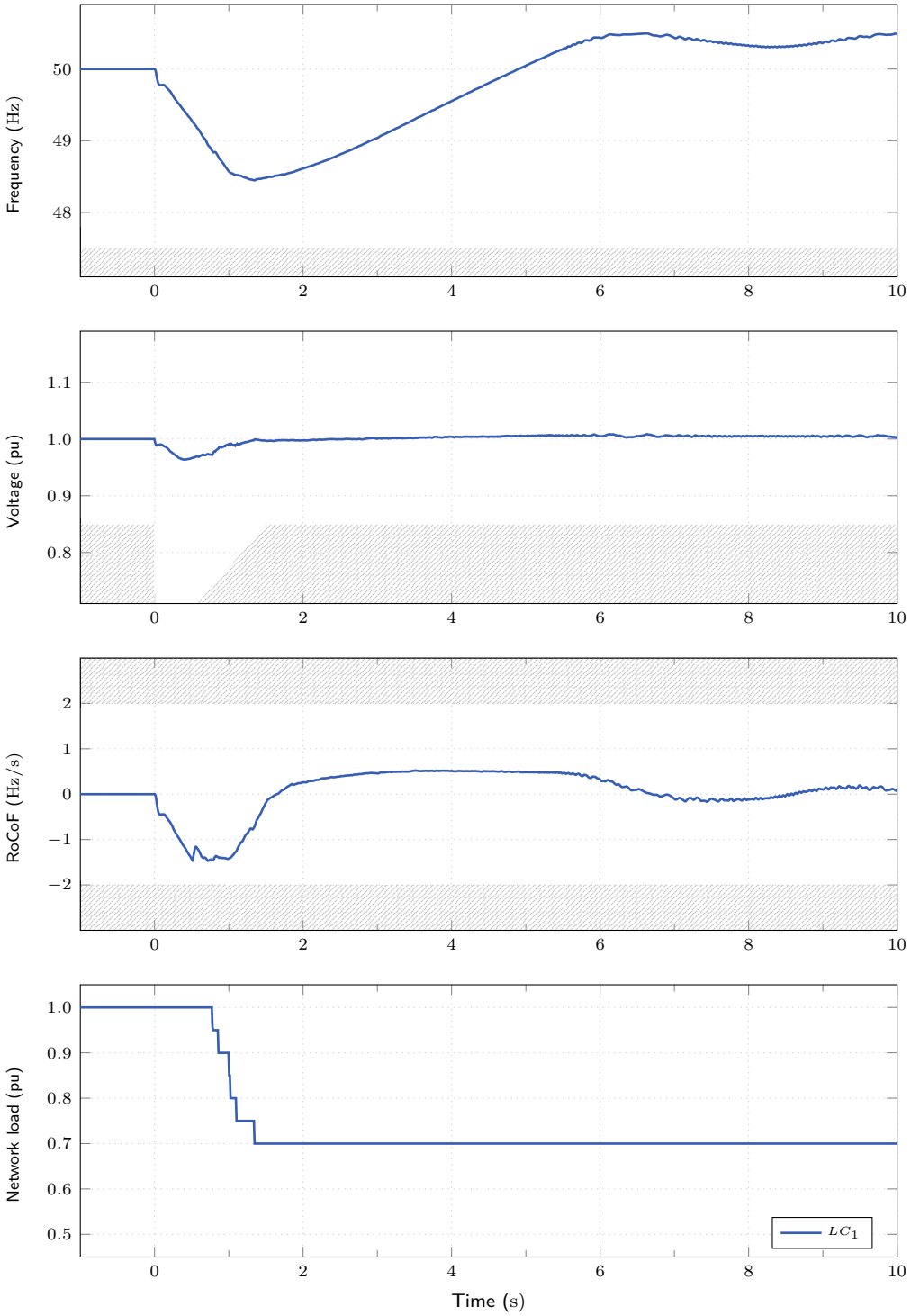

Figure 4.8: Performance of base scenario (100% resistive load) in 24% import loss

With the loss of in-feed from the grid, the voltage vector of the GFM units begins to decelerate, leading to a drop in grid frequency to 49.78 Hz, as depicted in Figure 4.9 between $0 - 0.1$ s. As a result, the GFM-WT unit releases inertia power from the rotating masses of the wind turbine. Figure 4.9 illustrates the active power output of the GFM-WT unit, which rises to 1.02 pu (scaled to the nominal power of each unit). Initially within the first 20 ms as inertia power is provided, the DC-link voltage drops until the MSC controller adjusts the power set point of the machine. This drop in DC-link voltage prevents the converter from fully maintaining its voltage vector, causing the network voltage to decline to below 0.99 pu due to the limitation of the modulation index. Additionally, as inertia power is delivered and the unit's current increases, the voltage drop across passive network elements also rises. This necessitates the converter further increasing its voltage vector to sustain the same voltage at the PCC.

A similar effect is observed for SG, where the increased voltage drop across the machine's impedance during inertia provision leads to a decrease in terminal voltage. The GFL-unit reacts by tracking the PCC voltage and frequency variations and delivers a similar active power, as shown in Figure 4.9 between $0 - 100$ ms.

After the initial phase, during the time span of $20 - 100$ ms, the DC voltage is regulated back to its reference value. However, since load consumption remains higher than generation, the voltage vector and consequently, the grid frequency continues to decelerate. As long as a mismatch exists between generated power and demand, the frequency continues to drop, and both GFM units continue participating in inertia provision. At $t = 30$ ms, the power output of the GFM unit reaches its peak, and current limitations prevent any further increase in inertia power, as shown in Figure 4.9.

During this period, the active and reactive power controllers begin adjusting the voltage vector of the GFM unit to achieve the desired active and reactive power outputs. The active power set point from the MPPT scheme decreases slightly, even though rotor speed deceleration is partially compensated, as discussed in Chapter 3.2.6. Additionally, with the recovery of DC voltage in the GFM-unit, it can inject capacitive reactive power to counteract the voltage drop.

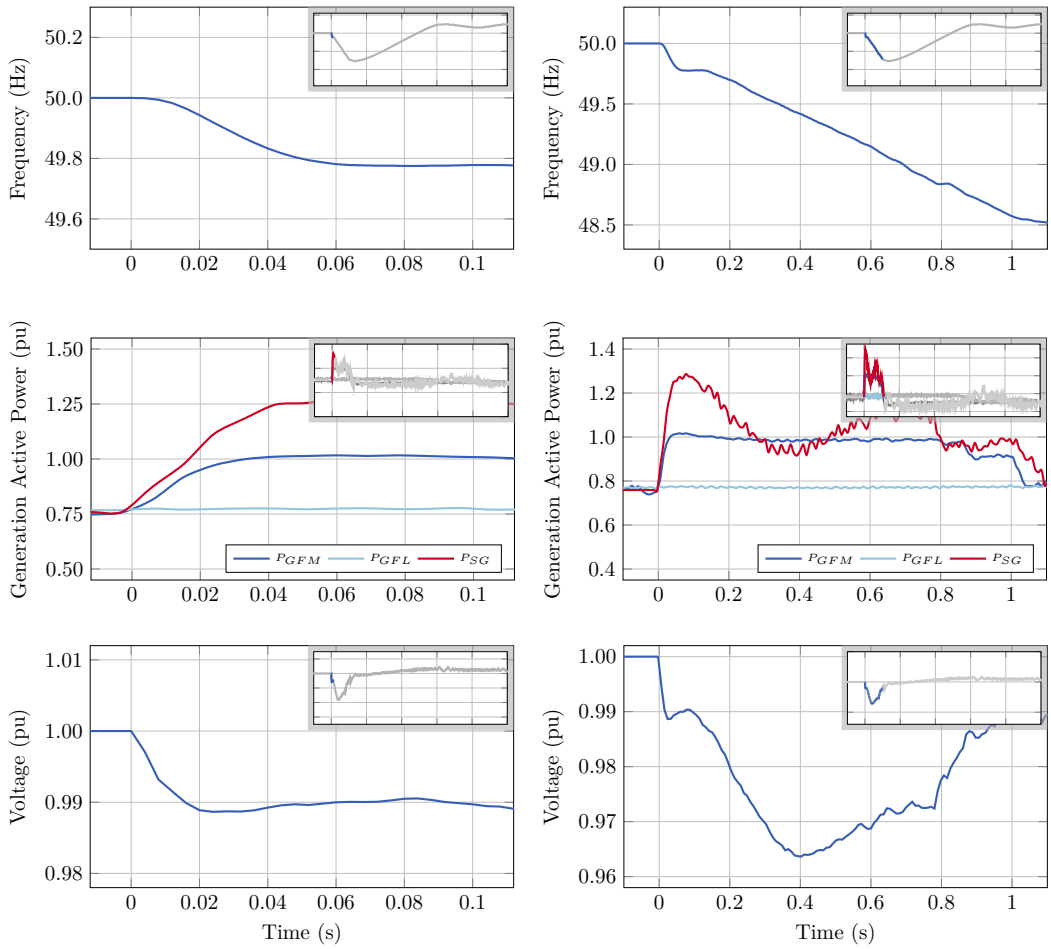

Figure 4.9: Performance of base scenario (100% resistive load) in 24% import loss in the [0, 0.1] and [0, 1] time frames

For the SG, a peak of 1.25 pu is reached for the active power at $t = 40$ ms. This results in an under-excitation operating point for the reactive power due to the greater voltage drop across its synchronous impedance.

Figure 4.9 depicts the signals over the time span of $0-1$ s as well. With a continuous negative RoCoF and sustained provision of inertia, there is insufficient headroom to maintain voltage support at the load bus. Consequently, the voltage drops to a minimum of 0.96 pu at $t = 0.4$ s, as shown in Figure 4.9. At $t = 0.7$ s, the frequency falls below 49 Hz. The load-shedding mechanism opens the breaker of the first

load branch and drops the total load by 5% at $t = 0.84$ s, when the frequency has reached already to 48.78 Hz.

During the $0 - 1$ s interval, two load-shedding stages are activated. Each step results in a noticeable change in the slope of the frequency change. As the power imbalance decreases, the deceleration of the SG and GFM voltage vectors slows, leading to reduced inertia provision. This behavior is observed in the active power output of both the GFM unit and the SG, in Figure 4.9. The reactive power of the GFM unit increases steadily between $0 - 1$ s. Around $t = 0.4$ s, as the initial RoCoF magnitude slightly decreases, the GFM unit's reactive power is able to increases further, causing the positive voltage deviation. As depicted in Figure 4.9, during this period, the active and reactive power of the GFL unit remain constant, as its controllers adjust the modulation index to maintain a steady power flow.

Comparing the Result of Import Scenario for Load Classes LC_2-LC_5

Load Class 2 (LC_2)

Figure 4.10 illustrates the results for a transition to islanding with a 24% power deficit where the consumer bus comprises 45% resistive load, 45% induction motor load, and 10% power electronic load. In this scenario, resistive load contributes to the voltage-dependent power reduction and induction motors contribute to the network's total inertia and exhibit a self-regulating effect, reducing the total power imbalance as frequency drops. Compared to LC_1, LC_2 demonstrates a smoother RoCoF at -1.43 Hz/s. The self-regulating behavior reduces inertia provision comparing to LC_1, enabling GFM units to have more headroom for voltage support.

As shown in Figure 4.10, six steps of load shedding are triggered with LC_2, shedding 30% of the total load by 1.62 s after islanding. Network voltage at the load bus and frequency profiles indicate that islanding with LC_2 does not compromise stability, allowing units to remain connected for the first 10 seconds post-event before other emergency measures activate.

Residential Sector (LC_3)

Figure 4.10 illustrates the system response during a transition to islanding under a 24% power deficit, with the consumer bus representing a residential load profile. In load class LC_3, the proportion of resistive load decreases to 42.5% compared to LC_1, although it remains the dominant component. Given that the combined share of resistive and induction machine loads is reduced by only 5% compared to LC_2, the overall system performance remains largely comparable to that scenario.

The main distinction lies in the rate of change of frequency, which exhibits a higher magnitude in RoCoF (-1.46 Hz/s) in LC_3 due to the 5% increase in power electronic load share. Additionally, load shedding is initiated slightly earlier in each step for LC_3 compared to LC_2. However, the frequency profile, load voltage, and RoCoF trajectories closely overlap across the two cases, reflecting the similarity in their load characteristic.

Industrial Sector (LC_4)

Figure 4.10 shows the results for islanding in an industrial area (LC_4). In this sector, IMs constitute a significant portion of the load, accounting for 70.3% of the total load. Due to the high dynamic nature of IMs and their dependency on both frequency and voltage, their behavior significantly differs from other load sectors. The performance of LC_4 can generally be divided into two main regions: a low-frequency region spanning $0 - 1.2$ s, and a over-voltage region from $1.2 - 3$ s (see Figure 4.10).

The low-frequency region begins with the disconnection of the grid, similar to LC_1. Following the drop in the angular frequency of the SG and GFM voltage phasors due to ΔP, the IMs in this sector decelerate. As the IMs' rotational speed decreases, the mechanical torque adjusts as a quadratic function of rotor velocity, reducing their total power consumption. This, in turn, lowers the power imbalance, achieving a 4% self-regulating effect, higher than the typical values of 1-2% which is assumed in network analyses [106]. As a result, the RoCoF in this test is smoother comparing to all other load classes, reaching to approximately

-1.23 Hz/s, as shown in Figure 4.10. Additionally, all the load shedding steps are activated later in LC_4 compared to LC_1 and other load classes. A total of eight load-shedding steps are required to stabilize the frequency deviation in this test, primarily due to insufficient generation and, subsequently, voltage deviations.

In this scenario with LC_4, following the first three steps of load shedding, a positive dV/dt is observed, as shown in Figure 4.10. The reduction in the imbalance power due to load inertia in LC_4, results in lower inertia provision and enhanced support for terminal voltage from the GFM units. As previously discussed, reduced inertia power leads to less voltage drop across the transient impedance of the SG and the filter of the GFM unit, contributing to an improved voltage profile across the network. After 1.2 s, the voltage improves further due to three initial load-shedding steps. However, this is followed by a dynamic over-voltage phase that impacts load power consumption in the industrial area. As voltage increases, the electrical torque of induction machines rises, decreasing slip and slightly accelerating the IMs. Consequently, load torque increases quadratically with rotor speed, leading to higher apparent power consumption and operation in a lower power factor for the IMs. As shown in Figure 4.10, during the overvoltage phase, the network's active power imbalance worsens, necessitating further consecutive load-shedding steps to stabilize frequency within the permissible emergency band.

Mix Sector (LC_5)

Figure 4.10 illustrates the results for islanding in a scenario where generation supplies a mixed sector comprising residential, industrial, and tertiary loads, referred to here as Mixed Sector LC_5 (see Chapter 4.2.2). From the consumer-side perspective, this scenario is comparable to the Flensburg event [115], where various feeders supplying different load sectors, from residential to heavily industrial areas, impacted island stability. The results for islanding with LC_5, as shown in Figure 4.10, is close to those of the residential area (LC_3) in terms of RoCoF, frequency nadir, voltage, and load-shedding timing.

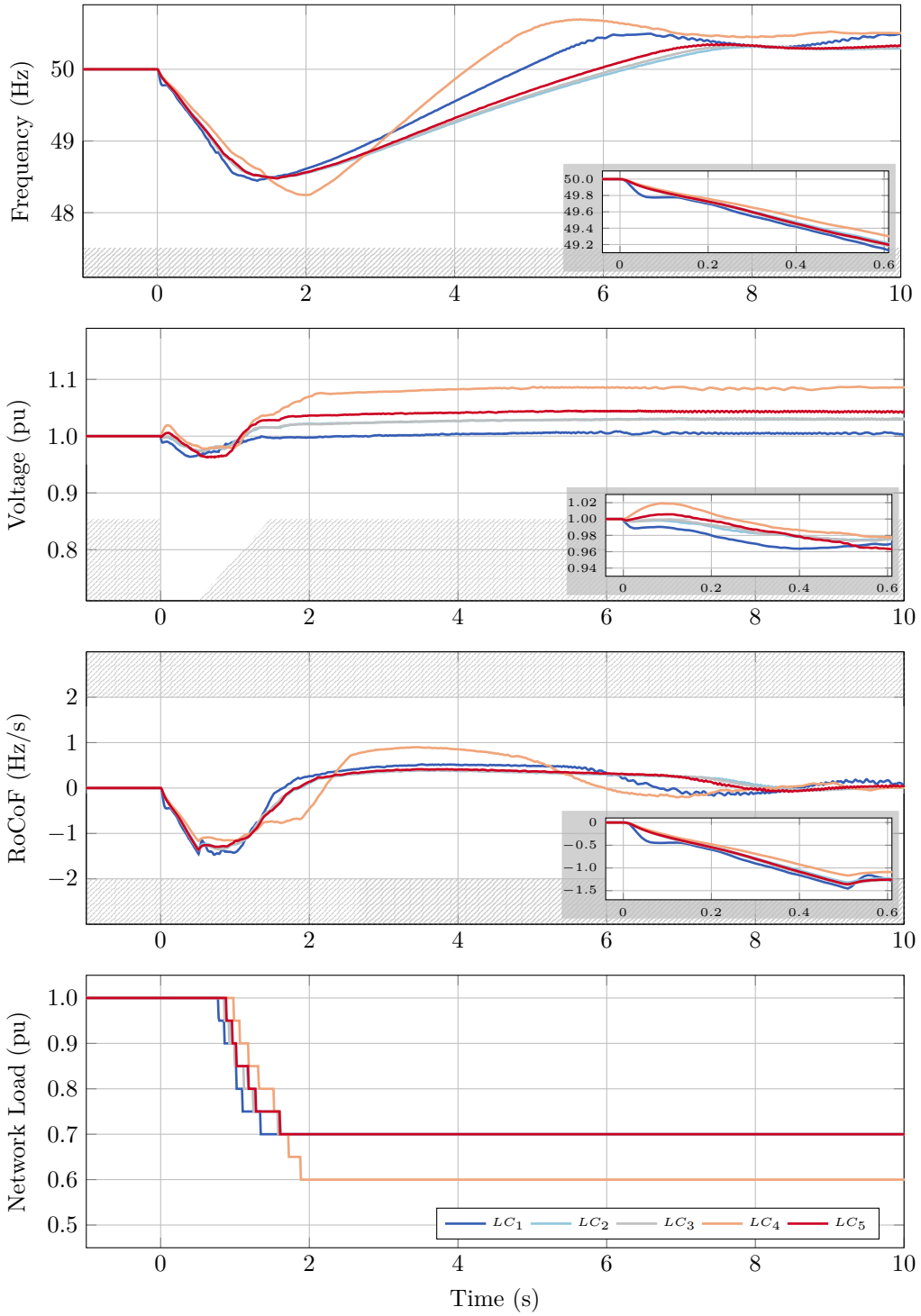

Figure 4.10: Comparing the performance of the base scenario (LC_1) against load classes LC_2- LC_5 under 24% import loss

Looking at the frequency profile in Figure 4.10, it is evident that although the share of IMs in LC_5 is 8% higher than in LC_3, the RoCoF reaches slightly higher magnitude (-1.48 Hz/s) compared to LC_3 (-1.46 Hz/s). The difference arises from the voltage-dependent power reduction of resistive loads, which are the second most dominant load component in LC_3. In contrast, LC_5 has PE loads as the second dominant component, characterized by constant power consumption. Consequently, despite the improved self-regulating effect, the higher imbalance in LC_5 leads to a more negative rate of change of frequency and a lower voltage minimum compared to LC_3.

As illustrated in Figure 4.10, after the second load-shedding step, the rate of change of voltage becomes positive, indicating sufficient reactive power from the generation units to support the network voltage. In this phase, three additional load-shedding steps are needed until the frequency stabilizes at 50.35 Hz in both LC_5 and LC_3.

Comparing the Result of Import Scenario for Load Classes LC_6-LC_{10}

Figure 4.11 presents the islanding results for LC_6 to LC_{10}. In LC_6, the dominant load component is PE loads, closely followed by IMs. After islanding, the voltage drops to a minimum of 0.94 pu, which is the highest among all load classes shown in Figure 4.11. In the initial milliseconds following islanding, the network frequency drops due to a mismatch between generation and the actual load, leading to reduced reactive power consumption by induction motors. This results in a comparatively improved voltage profile relative to other load classes with a lower share of IMs. In this period, reactive power support is primarily provided by the inherent response of GFM units, to oppose voltage deviations. During the first 0.4 seconds, the GFM units mainly provide inertia, temporarily limiting voltage regulation capability due to current limitations. This prioritization has a stronger impact on the network, as the synchronous generator contribution is restricted to only 10% of the total network generation. After this period, as the RoCoF magnitude decreases and 10% of the total network load is shed, the GFM units regain sufficient headroom to support voltage restoration. This is observed in 4.11, where the voltage gradually recovers and stabilizes at a new equilibrium above the nominal level.

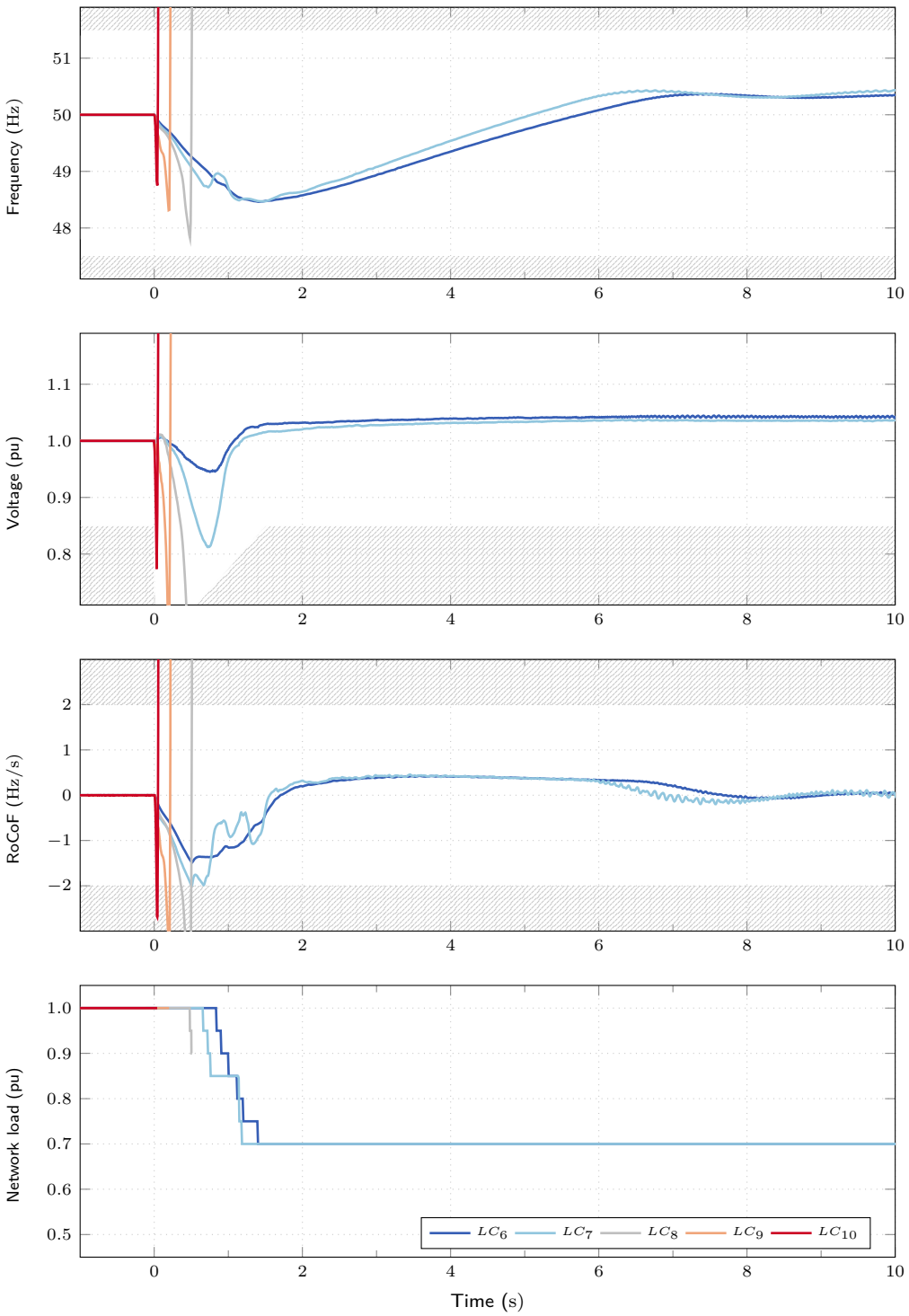

Figure 4.11: Comparing performance of load classes LC_7-LC_{10} under 24% import loss

In LC_7, which consists of approximately 21.5% IM and 60% PE loads, the RoCoF magnitude reaches slightly higher than -2 Hz/s. After islanding, the GFM-WT unit is unable to support its terminal voltage as it operates in under-excitation mode. Following the third load-shedding step at 0.76 s, the GFM unit is able to provide capacitive reactive power. The same occurs with the SG, where voltage support becomes possible only after 15% of the total load is shed. In LC_7, five load-shedding steps are triggered at 0.66, 0.72, 0.76, 1.14 and 1.18 s. During this period, the RoCoF magnitude temporarily decreases below -1 Hz/s, however, it subsequently increases, requiring positive inertia support from the GFM units to mitigate the continued frequency drop. In this interval, the voltage drops to 0.8 pu (see Figure 4.11). Despite this initial voltage drop, the voltage remains within the permissible LVRT threshold and recovers shortly after some load shedding steps.

In the islanding scenario with LC_7, the DC voltage of the GFM-WT unit drops to 90% of its nominal value due to the higher RoCoF compared to LC_1. In the case of the GFL unit, as the voltage falls below the normal operation band, it begins to support the grid voltage. However, its impact on voltage support is limited due to its lower rating relative to other generation units and its delayed response.

In islanding with LC_8, the frequency falls below 47.5 Hz within the first 460 ms after the onset of islanding, as shown in Figure 4.11. The results indicate that the system quickly enters an emergency state following grid disconnection, which leads to a blackout. The contingency in this scenario is so severe that system defense mechanisms such as FCR and UFLS [116] do not have sufficient time to mitigate the imbalance and restore stable operation. In LC_8, the RoCoF magnitude is nearly double that of LC_7, reaching approximately -4 Hz/s. Consequently, the inertia power of the GFM unit reaches the peak within the first 20 ms. The inertia provision is restricted to the interval from 0 - 0.46 s, as the GFM unit is unable to hold its voltage vector stable. During this period, both units (SG & GFM-WT) operate in under-excitation mode and voltage support is not feasible. Simultaneously, the GFL-unit operates in over-excited reactive power to mitigate the voltage drop in the network, but its contribution is insufficient to ensure dynamic voltage stability. Eventually, as the voltage continues to decline and drops further at 0.5 s, the system becomes unstable, resulting in test failure.

In LC_8, the combined share of IM and R decreases 16% compared to LC_7. This reduction is sufficient to push the system into instability within 500 ms after islanding. In contrast, while LC_7 experiences significant voltage deviations and a high negative RoCoF, it ultimately achieves stable operation after multiple load-shedding steps.

A similar trend to LC_8 is observed in LC_9 and LC_{10}, where 90% and 100% of the loads, respectively, consist of PE components. The simulation results for LC_9 indicate that the system fails within just 200 ms (see Figure 4.11). During this period, the voltage drops to 0.17 pu, and the frequency falls to 48.3 Hz, which is significantly below the FRT limit for generation units to remain connected, leading to the test failure. In LC_{10}, the failure occurs even faster, within 100 ms, as both voltage and frequency collapse.

Discussion & Outline of Import Loss Scenarios

Table 4.9 summarizes the simulated scenarios across ten load classes. In all import cases, load shedding contributes to frequency stability, except in LC_8-LC_{10}. Among the islanding scenarios, LC_3 and LC_2 exhibit the least frequency deviation, achieving higher frequency nadir and lower steady-state frequencies after load shedding. Conversely, the poorest frequency profile among the stable cases is observed in LC_4, which has the lowest nadir and the highest steady-state frequency.

In terms of the rate of change of frequency, LC_4 demonstrates the smoothest RoCoF, due to the strong self-regulating effect in the industrial area. Following LC_4, LC_2 and LC_3 exhibit lower RoCoF magnitudes compared to other stable scenarios. The highest RoCoF magnitude is observed in load class LC_7, which is 27% higher than the base scenario (LC_1)

Regarding dynamic voltage stability, the islanding test with LC_4 demonstrated the smallest initial voltage drop, while LC_7 exhibited the worst voltage profile among tests where voltage stability was not violated. All tests from LC_1 - LC_6 showed voltage deviations within $\pm 10\% V_n$. It should be noted that, LC_1 achieved the best

steady-state voltage, while LC_4 had the highest voltage (1.09 pu) in steady state. Overall, the industrial area (LC_4), characterized by a high share of motor loads, exhibited the highest voltage dynamics.

The results of the islanding scenario with import loss with a time constant of $T_N = 8$ s indicate that the best frequency profile, RoCoF, and voltage profiles are not achieved with LC_1. However, this load sector exhibits a different characteristics during islanding compared to load classes with higher proportions of IM or PE loads. It has to be noted that in islanding scenario with 24% import loss (-24%), pure resistive loads (LC_1) does not violate any stability criteria or push the system to its operational limits. In contrast, under similar islanding conditions with higher shares of motor loads or PE in other load classes, the system operates near the stability limit or fails to maintain stable operation. Therefore, in a similar islanding configuration as presented in Chapter 4.4.1, the test results confirm that pure resistive loads are not the optimal choice for evaluating dynamic stability following a major islanding event.

In addition, it was observed that load classes LC_8-LC_{10}, with a power electronic load share of 70% and above, did not meet the stability requirements for this islanding scenario. Given the fact that TSOs are observing a growing share of such loads in certain sectors, with some already reaching 70% [10], greater emphasis is needed on their impact on overall islanding stability, as this load composition can become more prevalent in the future.

Table 4.9: Summary of the results for 24% import loss

Import Cases	Load Type			Frequency Stability		RoCof	Voltage Stability		Time & Nb. Load Shedding (10 Stages, each 5%)										Overall
	R	IM	PE	F_{min} (Hz)	F_{max} (Hz)	Max (Hz/s)	V_{min} (pu)	V_{max} (pu)	T_{LSH1}	T_{LSH2}	T_{LSH3}	T_{LSH4}	T_{LSH5}	T_{LSH6}	T_{LSH7}	T_{LSH8}	T_{LSH9}	T_{LSH10}	
LC_1	100%	0	0	48.43	50.52	-1.6	0.96	1.01	0.78	0.86	1	1.02	1.1	1.34	—	—	—	—	Stable
LC_2	45%	45%	10%	48.47	50.4	-1.43	0.97	1.03	0.88	0.96	1.02	1.16	1.28	1.62	—	—	—	—	Stable
LC_3	42.4%	41.9%	15.7%	48.47	50.33	-1.46	0.97	1.03	0.86	0.92	1	1.12	1.24	1.58	—	—	—	—	Stable
LC_4	1.2%	70.3%	28.5%	48.24	50.7	-1.23	0.98	1.09	0.98	1.06	1.18	1.32	1.52	1.6	1.72	1.88	—	—	Stable
LC_5	18.9%	49.8%	31.3%	48.47	50.35	-1.48	0.97	1.04	0.88	0.96	1.02	1.18	1.28	1.6	—	—	—	—	Stable
LC_6	20.3%	39.5%	40.2%	48.45	50.36	-1.59	0.94	1.04	0.84	0.9	1	1.12	1.2	1.4	—	—	—	—	Stable
LC_7	21.5%	21.5%	57%	48.47	50.43	-2.03	0.8	1.04	0.66	0.72	0.76	1.14	1.18	—	—	—	—	—	Failed
LC_8	13.5%	13.5%	73%	N.M.	N.M.	N.M.	N.M.	N.M.	—	—	—	—	—	—	—	—	—	—	Failed
LC_9	5%	5%	90%	N.M.	N.M.	N.M.	N.M.	N.M.	—	—	—	—	—	—	—	—	—	—	Failed
LC_{10}	0	0	100%	N.M.	N.M.	N.M.	N.M.	N.M.	—	—	—	—	—	—	—	—	—	—	Failed

4.4.2 Situation II: 24% Export Loss

The second simulated scenario involves a 24% export loss ($\Delta P = +0.24\%$). The network time constant is determined, similar to Situation I as ($T_N = 8\,\mathrm{s}$). The network time constant is calculated as the ratio of the generation participating in inertia to the total network load in both import and export scenarios (see Chapter 4.3.1). In the export scenario, since generation is greater than the local network load, this results in a higher time constant for the same generation units as in the import scenario. Therefore, to achieve a similar time constant in the export scenario, the generation fleet should consist of 39% GFM-WT unit, 10% SG and 51% GFL unit. The test results for load classes 1-10 are presented in Chapter 4.4.2. At $t = 0\,\mathrm{s}$, the connection to the external grid is lost. This line was exporting an amount equivalent to 24% of the island's total load, leading to a 24% power surplus in all test scenarios following islanding.

Analysis of the Export Test Cases

Base Scenario (LC_1)

Figure 4.12 illustrates the islanding test results for a 24% export loss scenario with the base case (LC_1). As shown, following the islanding, the frequency increases to 51.03 Hz with an initial RoCoF of +1.5 Hz/s. The primary countermeasure to control the frequency rise after the inertia phase is the activation of LFSM-O, particularly by the converter-based generation units (GFL-WT and GFL). These units can curtail generation at a faster rate compared to SGs.

The voltage profile is also depicted in Figure 4.12. Following a small peak immediately after islanding, the voltage stabilizes at a steady-state level (1.06 pu) slightly above nominal value. Considering the export loss results reveals that the voltage is less disrupted compared to the similar import loss scenario, as the generation units remain within their operational limits.

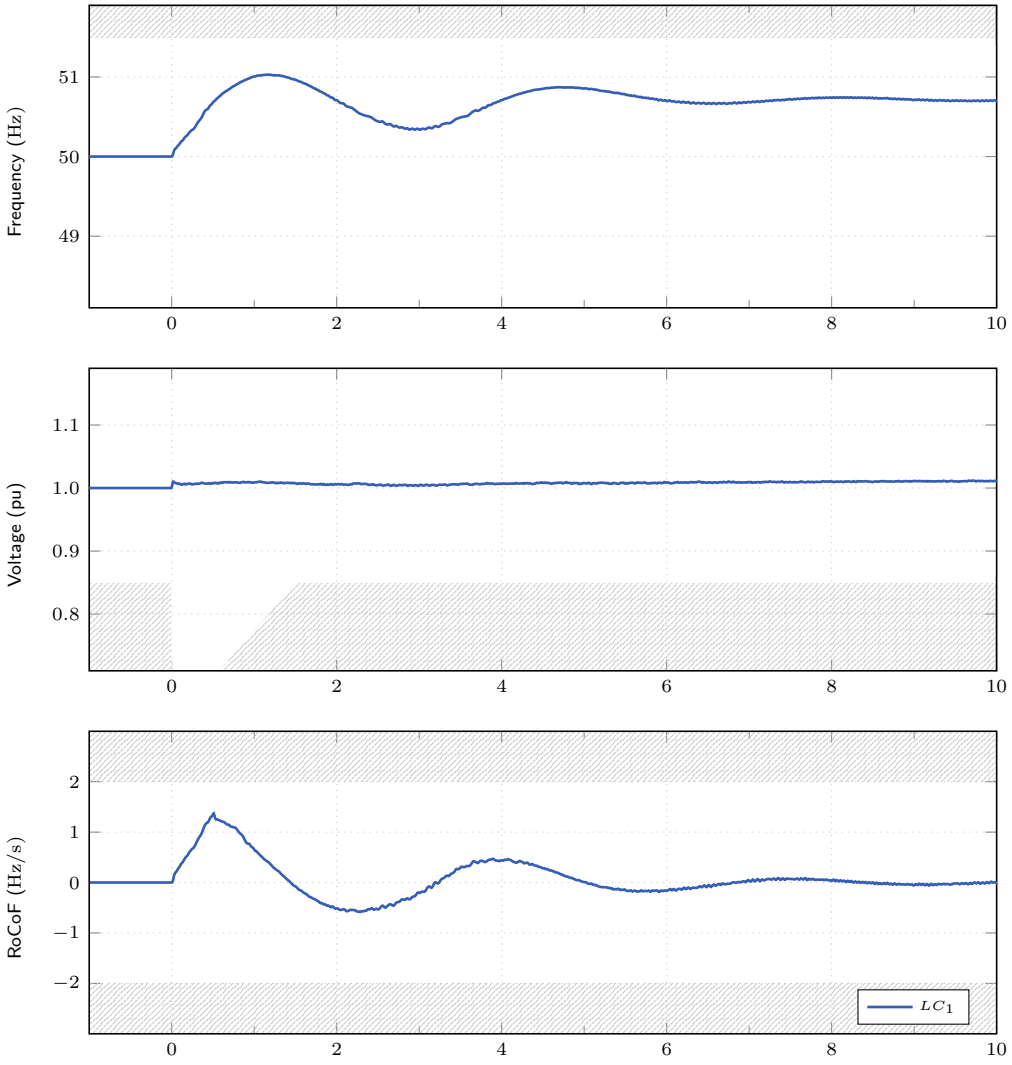

Figure 4.12: Performance of the base scenario (LC_1) under 24% export loss

In the following, the chain of events occurring within the first 100 ms for this test scenario is discussed.

1. Figure 4.13 illustrates the grid current and frequency during the first 100 ms following islanding. As observed, the current trajectory drops instantly upon islanding, decreasing steadily and reaching its minimum at 0.02 s.

2. Due to the decreased loading of the island following the export loss and the corresponding reduction in current through the loads, the voltage magnitude

at the PCC rises.

3. In addition, as a result of the power imbalance, the frequency and phase angle of the voltage vector of both GFM-WT and SG units experience a positive jump. This increase in frequency is shown in Figure 4.13.

4. During the same interval of 0-20 ms, both the GFM-WT unit and SG reduce their generated power by approximately 31%, providing support to the event through negative inertia provision (see Figure 4.13).

5. As the voltage amplitude at the PCC varies, the GFL unit adjusts its set-points to follow these changes in order to maintain the same active and reactive power. Due to the dynamics of the PLL while locking onto the new angle and frequency, and considering the bandwidth of the inner controller of the GFL unit (2 ms), a brief dynamic phase occurs. During this phase, the active power is slightly fluctuating.

6. Following the export loss, the voltage formation with the loads shifts the operating points of both voltage source units into under-excitation mode. The SG unit provides the highest per-unit reactive power compared to the other units, transferring approximately 0.2 pu of inductive reactive power (with respect to its rated power). The GFM-WT unit also provides an inductive reactive power of approximately 0.05 pu (scaled to its rated power). The reactive power is transferred between sources. As shown in Figure 4.13, GFL unit in the dynamic phase between 0-20 ms period, operates in over-excited mode, delivering capacitive reactive power.

7. After the dynamic phase (20 ms), the GFL unit stabilizes its active and reactive power to their pre-event values.

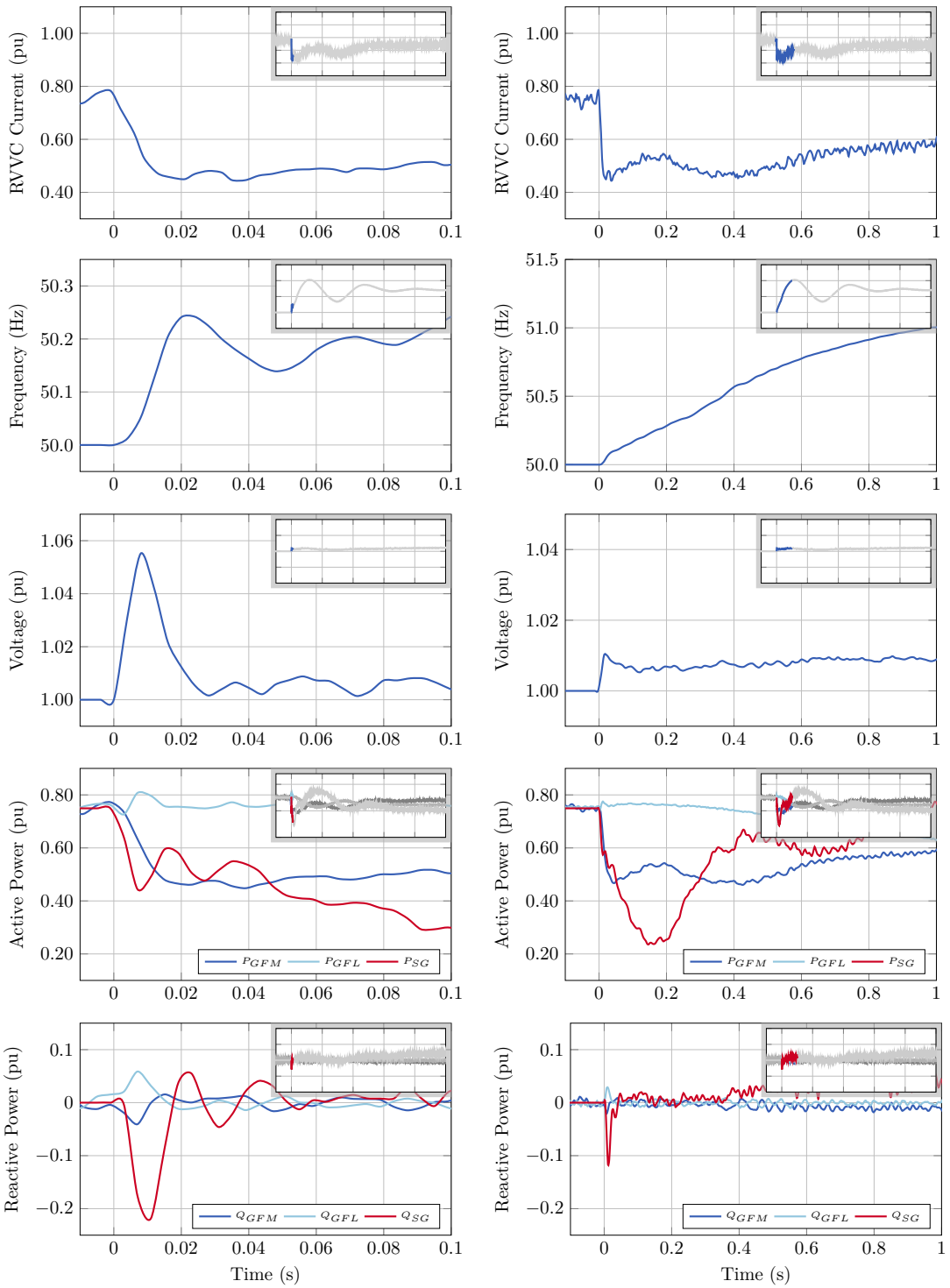

Figure 4.13: Performance of base scenario (LC_1) under 24% export loss in the [0, 0.1] and [0, 1] time frames

Looking at the trend of islanding with export loss with LC_1, shown in Figures 4.12 and 4.13, it is observed that while the frequency stabilizes within the emergency region (50.7 Hz), no stability criteria are violated. The detailed test results are listed in Table 4.10.

Comparing the Result of Export Scenario for LC_1 - LC_5

Figure 4.14 compares the performance of LC_1-LC_5 following islanding with a 24% power surplus. In the previous section, the chain of actions was discussed using LC_1 as the base scenario. Following the islanding and facing export loss, the voltage rises to a higher value, and a frequency increase is observed across all scenarios, as illustrated in Figure 4.14. The results indicate that, despite the same power imbalance in the network, the frequency jump and the resulting voltage vector at the load bus vary significantly depending on the load dynamics. The key characteristics of these load sectors are highlighted as follows:

- Compared to LC_1, the acceleration of the voltage vector is much smoother across all other load sectors, as illustrated in Figure 4.14. For LC_1, the RoCoF is the highest among these six load sectors, reaching 1.5 Hz/s. In contrast, the industrial area (LC_4) demonstrates the best RoCoF performance at 1.18 Hz/s. Excluding LC_1, a correlation can be observed between the RoCoF and the percentage of IMs in each load class.
- Looking at the frequency profile in Figure 4.14, it is observed that LC_1 reaches the highest plateau at 51.03 Hz. Frequency stabilization is achieved through the activation of LFSM-O around 2 s. As shown in Figure 4.14, after some oscillations, the frequency converges to a steady-state value. Unlike LC_1, the other load sectors exhibit more damped oscillations because of reduced interaction between inertia provision and the LFSM-O function in the GFM-WT unit. Except for LC_1, which stabilizes at 50.72 Hz, the steady-state frequencies of the other load sectors are nearly identical, settling at 50.56 Hz.

- The grid-forming units are SG, whose contribution is negligible compared to the two converter-based sources and GFM-WT unit, with a 39% share, forming the voltage vector in the island. The GFL unit behaves as a current source, maintaining constant active and reactive power as long as its modulation index remains within limits. Figure 4.14 illustrates the modulation index of the GFL unit in five load classes. The reactive power demand varies with each load class. For instance, in LC_4, the highest IM share requires higher reactive power provision from all units. This results in an increase in the voltage vector magnitude for the GFL unit, reducing its modulation index margin post-islanding. As seen in Figure 4.14, the modulation index for LC_4 is approximately 1.05 before the event, reaching its limit 50 ms after islanding. In contrast, the other four load classes did not trigger this limit.
- The voltage profiles for various load classes are shown in Figure 4.14, highlighting an inverse relationship between voltage rise and frequency increase. Considering the base load class (LC_1), it is observed that immediately following grid disconnection, the consequent current reduction leads to a frequency and angle jump in the voltage vector at the load bus. This reduced current also reduces the voltage drop across the converter filter in converter-based generation or the synchronous impedance in SG, causing an increased voltage at the load bus (see Figure 4.14). In addition, looking at the voltage profiles of various load classes shows that each stabilizes at a different steady-state value, mainly influenced by the load characteristics. As shown in Figure 4.14, the industrial area (LC_4) exhibits the highest voltage amplitude. Due to the higher reactive power demand in LC_4, the voltage vector amplitude must initially be greater than in LC_1 to supply this reactive power. As a result, following islanding, the voltage at the load bus in LC_4 rises and settles at a higher level (1.04 pu) compared to LC_1 (1.01 pu).

Looking at the export loss results shown in Figure 4.14, all test cases demonstrate stable operation in terms of frequency, RoCoF, and voltage stability. In all scenarios, the voltage stays within the normal operation band. The test results are listed in Table 4.10. Among the five load sectors, LC_1 shows the worst RoCoF, highest frequency peak, and least steady-state voltage deviation. The oscillations observed

in certain load classes, particularly LC_4 and LC_5, are below 1 Hz and are mainly due to load composition, over-modulation limits, and reduced damping at lower operating points.

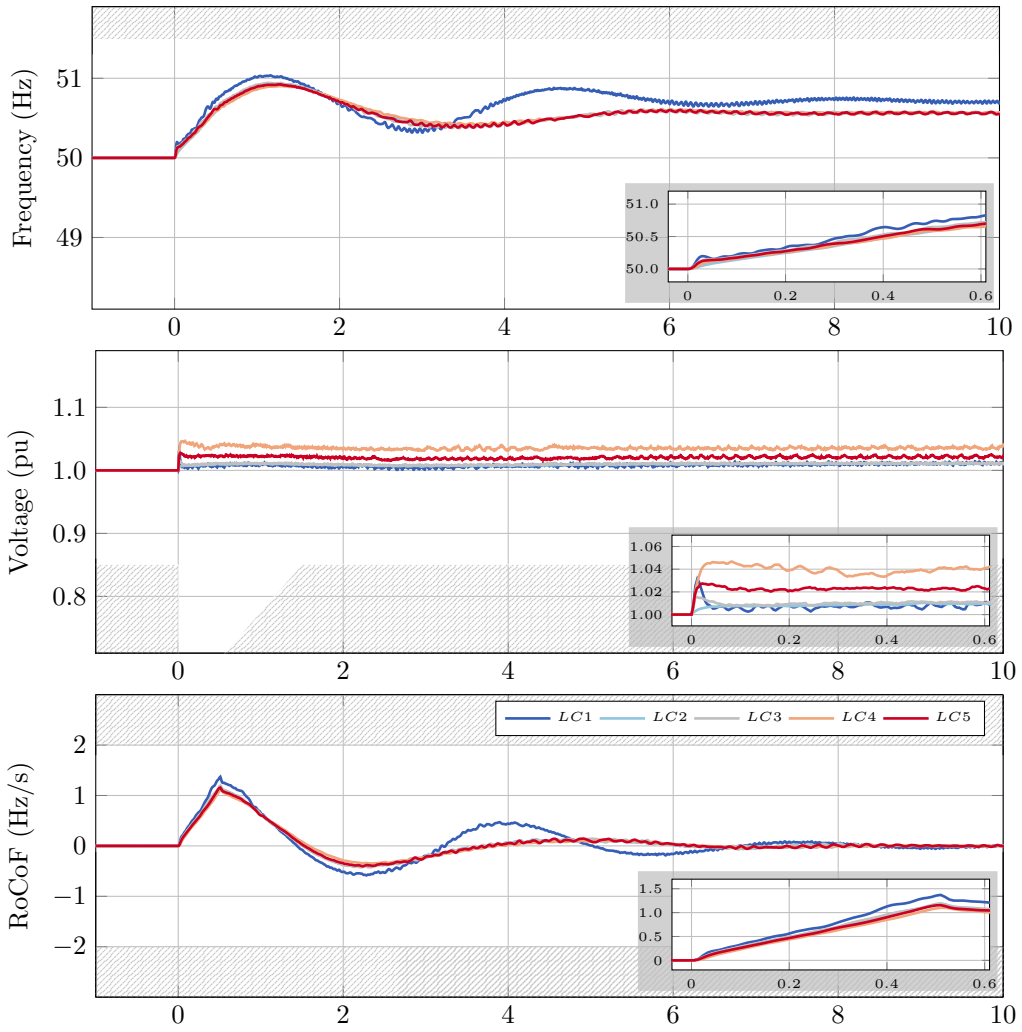

Figure 4.14: Performance of LC_2-LC_5 versus LC_1 under 24% export loss

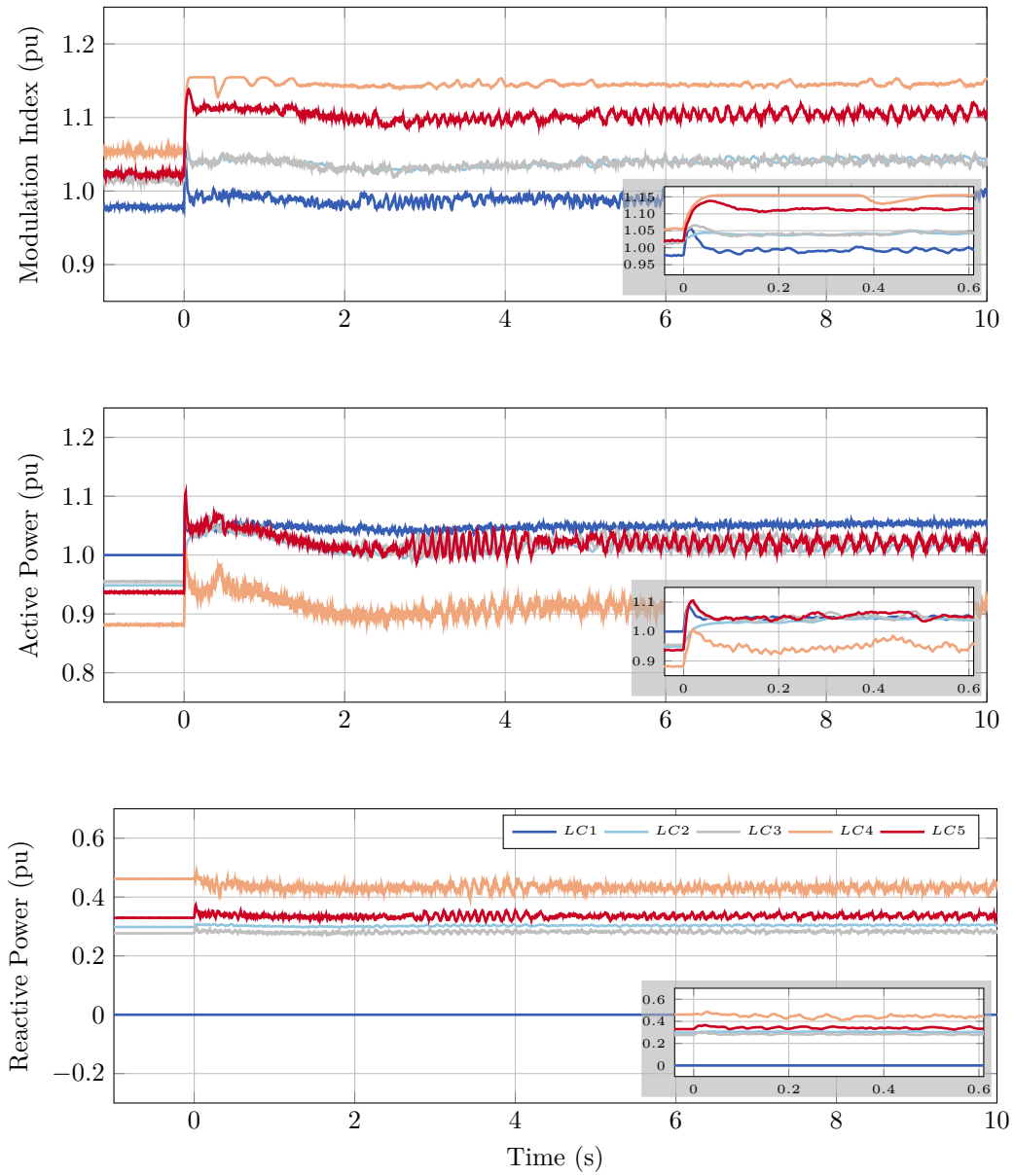

Figure 4.14: Performance of LC_2-LC_5 versus LC_1 under 24% export loss (continued)

Comparing the Result of Export scenario for LC_6-LC_{10}

Figure 4.15 shows the frequency and voltage profiles after islanding with export loss for load classes LC_6-LC_{10}. Among these test results, only LC_6 demonstrates

stability in both import and export scenarios, while LC_7-LC_9 maintain stable operation only under export loss conditions. The results with LC_7- LC_9 show that the frequency rises and stabilizes at approximately 50.8 Hz. The frequency plateau increases by variation of load classes from LC_7- LC_9, with LC_9 exhibiting a frequency peak of 51.1 Hz. Additionally, it is observed that with a growing share of PE loads, the RoCoF also increases, from 1.32 Hz/s for LC_6 to 1.57 Hz/s for LC_9, the latter being the highest RoCoF among all stable load classes. Looking at the voltage profiles in Figure 4.15 reveals an immediate rise in voltage following grid separation in LC_6-LC_9. For all four cases, the voltages settle in steady state in the normal operational range.

The voltage profile in Figure 4.15 shows that the network voltage in LC_9 is higher than in LC_6, despite LC_6 having higher reactive power consumption. As previously discussed (see Chapter 4.4.2), a higher reactive power flow prior to an event results in a higher resultant voltage vector after islanding. Another key factor influencing the voltage rise after islanding is the load characteristic, particularly the reduction of the self-regulating effect, which impacts the overall active and reactive power consumption of the loads. In LC_6, the IM share is 34.5% higher compared to LC_9, and IM loads depend on both frequency and voltage. Conversely, as more directly-connected machines are replaced by inverter-fed loads, the remaining load becomes less dependent on voltage and frequency, increasing both voltage and frequency vulnerabilities in the network. As illustrated in Figure 4.15, LC_9 with 90% PE consumers, exhibits the highest frequency jump, the highest steady-state voltage, and the highest RoCoF among all stable export loss scenarios.

In Figure 4.15, the frequency profile for LC_{10} shows that during the first 10 ms, the frequency remains unchanged. This time period is beyond the controller bandwidth of converter-fed loads, preventing them from reacting to dynamic grid changes. After 10 ms, the frequency moves in the opposite direction of the network's power imbalance, indicating that converter-fed loads are not able to sustain their pre-event power flow. This mismatch disrupts the stability between generation and loads. The voltage profile in Figure 4.15 further highlights this instability. Following an initial voltage rise, the voltage begins to decline after 40 ms, dropping to 0.7 pu, oscillating, and failing to stabilize. In contrast, reducing the share of PE loads by

10%, as in LC_9, allows the frequency to rise into the over-frequency region while maintaining the island's overall stability.

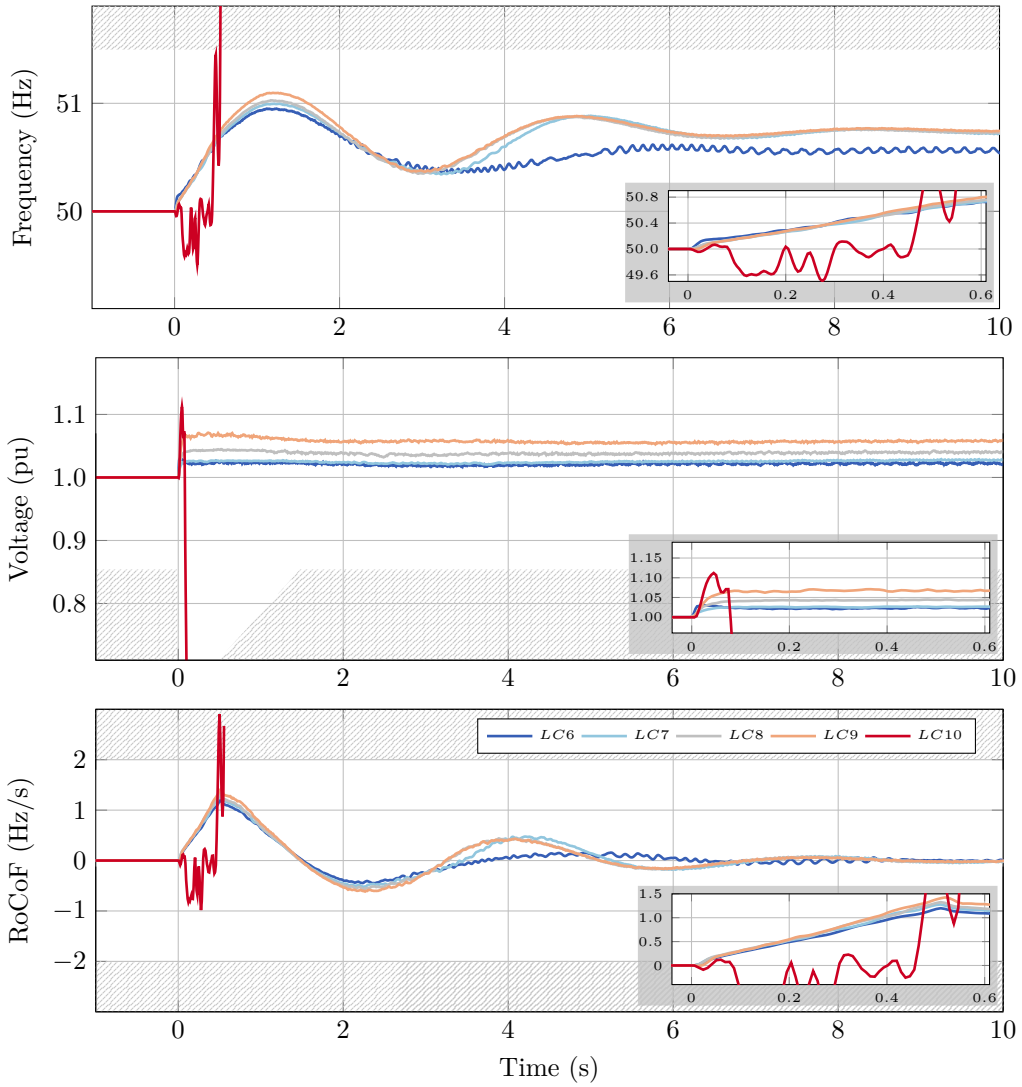

Figure 4.15: Comparing performance of LC_6-LC_{10} under 24% export loss

Discussion & Outline of Export Loss Scenarios

The following key observations are noted for the scenario with a 24% export loss:

- Table 4.10 summarizes information for all ten export scenarios. Regarding

frequency boundaries, load classes with the highest share of IM loads, particularly LC_4 (industrial sector) exhibit the most stable frequency profiles during both transient and steady-state phases. The worst frequency profile belonged to LC_9 with highest peak (51.1 Hz) and steady state value of (50.8 Hz).

- Looking at the test result in Table 4.10 reveals that the RoCoF values are maintained below 1.3 Hz/s as long as the dominant load in the sector is neither purely resistive nor predominantly PE load. The lowest RoCoF values are observed in the industrial sector (LC_4) at 1.18 Hz/s and the mixed-load class (LC_5) at 1.23 Hz/s.
- The voltage profile exhibits an inverse relationship to RoCoF values. The best voltage profile is observed in the base scenario (LC_1), attributed to the resistive components in the load sector.

Table 4.10 shows that all export test scenarios were successful, except for LC_{10}, which failed to maintain stable operation. Based on all three stability criteria, LC_2 and the residential area (LC_3) perform best overall performance. In terms of frequency and RoCoF, LC_2-LC_7 show better performance comparing to LC_1 under export loss. However, results for LC_8-LC_{10} indicate that LC_1 is very simplified and fails to capture system dynamics when loads include more PE components.

Table 4.10: Summary of the results for 24% export loss

Export Cases	Load Type			Frequency Stability		RoCof	Voltage Stability		Overall
	R	IM	PE	F_{min} (Hz)	F_{max} (Hz)	Max (Hz/s)	V_{min} (pu)	V_{max} (pu)	
LC_1	100%	0	0	51.03	50.71	1.5	1.01	1.06	Stable
LC_2	45%	45%	10%	50.93	50.57	1.3	1.01	1.03	Stable
LC_3	42.4%	41.9%	15.7%	50.94	50.56	1.3	1.01	1.04	Stable
LC_4	1.2%	70.3%	28.5%	50.9	50.56	1.18	1.03	1.05	Stable
LC_5	18.9%	49.8%	31.3%	50.92	50.56	1.23	1.02	1.04	Stable
LC_6	20.3%	39.5%	40.2%	50.95	50.56	1.32	1.02	1.05	Stable
LC_7	21.5%	21.5%	57%	51	50.73	1.38	1.03	1.07	Stable
LC_8	13.5%	13.5%	73%	51.03	50.73	1.44	1.04	1.09	Stable
LC_9	5%	5%	90%	51.1	51.76	1.57	1.06	1.13	Stable
LC_{10}	0	0	100%	N.M.	N.M.	N.M.	N.M.	N.M.	Failed

4.5 Summary

The first section of Chapter 4 introduces the aggregated load model, dividing it into different load sectors. Chapter 4.2.2 further details each sector, presenting its load components and predominant load category based on literature. The three main load categories of resistive loads, induction machines with quadratic torque, and power electronic loads are modeled to represent the primary consumers within each sector. Figure 4.3 summarizes all load classes and their respective load categories.

The second part of Chapter 4 discusses the required power system inertia as the baseline for test cases in this chapter. This baseline is obtained to maintain RoCoF within permissible limits following islanding with a 24% power imbalance. The chapter then discusses three key stability criteria of RoCoF, frequency, and network voltage in alignment with grid codes and generation-connection requirements.

The islanded network configuration is also presented in detail, comprising three generation units with system-level controls (including LFSM-O and FSM) and the consumer side with eleven load buses, ten of which are equipped with load-shedding relays. Subsequently, ten load classes are tested in two case studies, each subjected to a ±24% power imbalance following a system split. Two main conclusions were drawn from these 20 test cases:

- Comparing the load classes with the base scenario (LC_1) highlights the influence of other load categories, such as a high share of IM on frequency stability and PE on both frequency and voltage stability. In some load classes, unlike the base scenario, the power system was not able to maintain stable operation, even if the emergency measures were not fully activated in the base scenario (LC_1). Furthermore, the comparison of nine load classes with LC_1 indicates that in scenarios where stability was preserved, the steady-state values differed significantly from those observed for LC_1. This highlighted the influence of load characteristics on both dynamic and steady-state stability in islanding studies.
- Considering the transition towards high PE loads, the test results reveal that all cases with over 57% PE lost stability within milliseconds after the event

onset in import loss. In these cases, the entire system collapsed, while other load classes managed to maintain stable operation within the permissible range. This issue was less severe in export loss scenarios, as there was more capacity for generation units to support the grid. Therefore, unstable operation was only observed with 100% PE load (LC_{10}).

Overall, the islanding results in Chapter 4 has emphasized the vulnerability and restriction of converter-based generation and loads when facing high power unbalances, particularly in terms of modulation index and current limitations. The results confirm that, considering the hardware and control limitations of GFM units, it is crucial to consider load dynamics when assessing the required network strength for the loss of highly loaded feeders.

5 MINIMUM REQUIRED GRID FORMING UNITS

5.1 Normative Incident for System Split

According to ENTSO-E, the magnitude of power imbalances varies between interconnected operation and system split scenarios [106]. In case of system splits, which are the focus of this work, a line may be disconnected due to disturbances such as short circuits or overloading. The power that the line was exporting/importing prior to the event contributes to the imbalance magnitude following the split.

A normative incident needs be defined according to ENTSO-E, for system splits to determine the minimum required system inertia [106]. This involves considering the magnitude of the imbalance to achieve a specific RoCoF that remains within acceptable limits, based on the power system's constraints on frequency gradients. While predicting future system split scenarios is not feasible, a general approach suggests using the historical data from past events in the european network or following ENTSO-E's recommendations for future system splits regarding the minimum required inertia[106].

5.2 Required Network Time Constant for Islanded Operation

As a part of the sustainable energy transition and according to ENTSO-E, there is a downward trend in the annual estimated inertia time constant in the whole CE including Germany in the year 2030 [54].

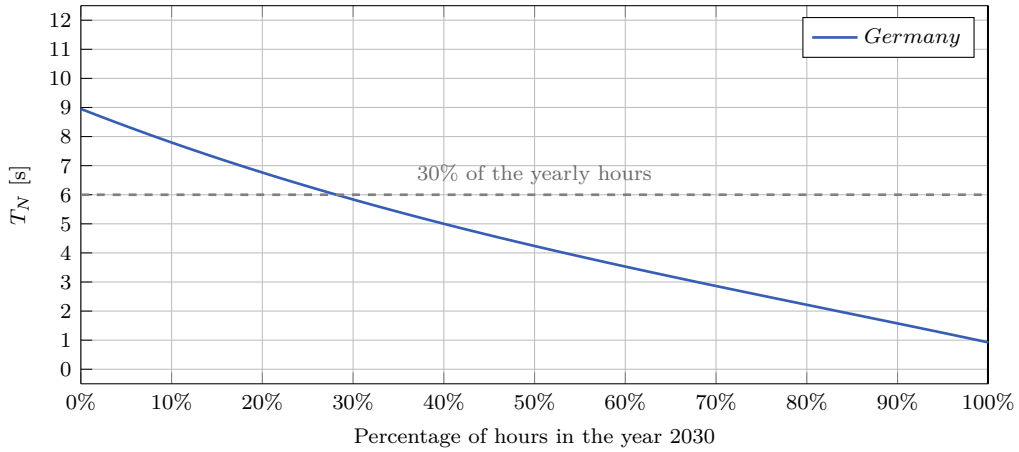

Figure 5.1: Annual duration curve of the acceleration time constant for Germany in the year 2030 [54]

A disturbance in the magnitude of ±24% requires a time constant of 6 s, which is available only 30% of the time in Germany in the year 2030 (see Figure 5.1). In addition, future system planning anticipates higher power exchanges, with maximum power imbalances reaching up to ±40% [106]-[117]. A ±40% power imbalance requires a time constant of 10 s, which, according to Figure 5.1, is unavailable at any time in Germany in 2030. Additionally, as shown in Figure 5.1, a time constant of 1 s is reliably available year-round, indicating the minimum contribution of units providing inertia throughout 2030.

This time constant is clearly inadequate for managing power imbalances of 24% or higher without exceeding the RoCoF limit of 2 Hz/s. This highlights the need to increase inertia from converter-based generation units. Chapter 5 investigates the required network time constant to manage various imbalance scenarios, taking into account the following aspects:

- What is the minimum required time constant for the network to manage a ±40% power imbalance?
- How does the required minimum time constant depend on load characteristics, and by what percentage does this value vary across different load classes?

- Given the estimated network time constant in Germany by 2030, with conventional units providing a minimum of 1 s, what percentage of GFL units must be replaced by GFM units to prevent system collapse?

5.2.1 Islanding with ±24% Power Loss (Below Rated Power)

To analyze the required minimum time constant for a ±24% power imbalance, LC_2-LC_{10} is considered alongside the base scenario (LC_1). In case of 24% import loss, all generation units in the island operate at partial load before islanding ($P_G\,(t=0) = 0.76\,pu_G$), with their nominal power equivalent to the total island load ($P_L = 1\,pu_G$). At t=0 s, the connection to the external grid which is feeding $P_{Imp} = 0.24\,pu_L$ is disconnected to initiate a system split. The simulated scenarios are based on the following criteria and test design:

- 10% percent of the load power is consistently supplied by the SG, ensuring a minimum time constant of 1 s in the power system (see Figure 5.1).
- Due to the numerous test cases, and to reduce the size of the test matrix for determining the minimum required time constant across all ten load classes, the network time constant is initially set to the value used in the two test cases from Chapter 4.4 as a starting point ($T_N = 8$ s). This value is then adjusted in steps of 1 s by varying the proportion of GFM to GFL units.
- The stability criteria for evaluating the test takes into account RoCoF, frequency range, and dynamic voltage stability (see Chapter 4.3.2).

To vary the network time constant in each simulation scenario, the load power consumption is scaled according to the generation. The simulation starts with $T_N = 8$ s as shown in the flow chart depicted in Figure 5.2. The results from this scenario are then analyzed to determine if the stability criteria are met with this network time constant. If the test is stable and the criteria are fulfilled, the time constant is reduced by 1 s in the next simulation, and the test is repeated. If the test is not stable or the criteria are violated, the time constant is increased by 1 s. This process creates a test matrix for each islanding scenario, as shown in detail

in Chapter 7.3. The process continues until the boundary of stable operation is achieved within the generation capability for each load class in the island.

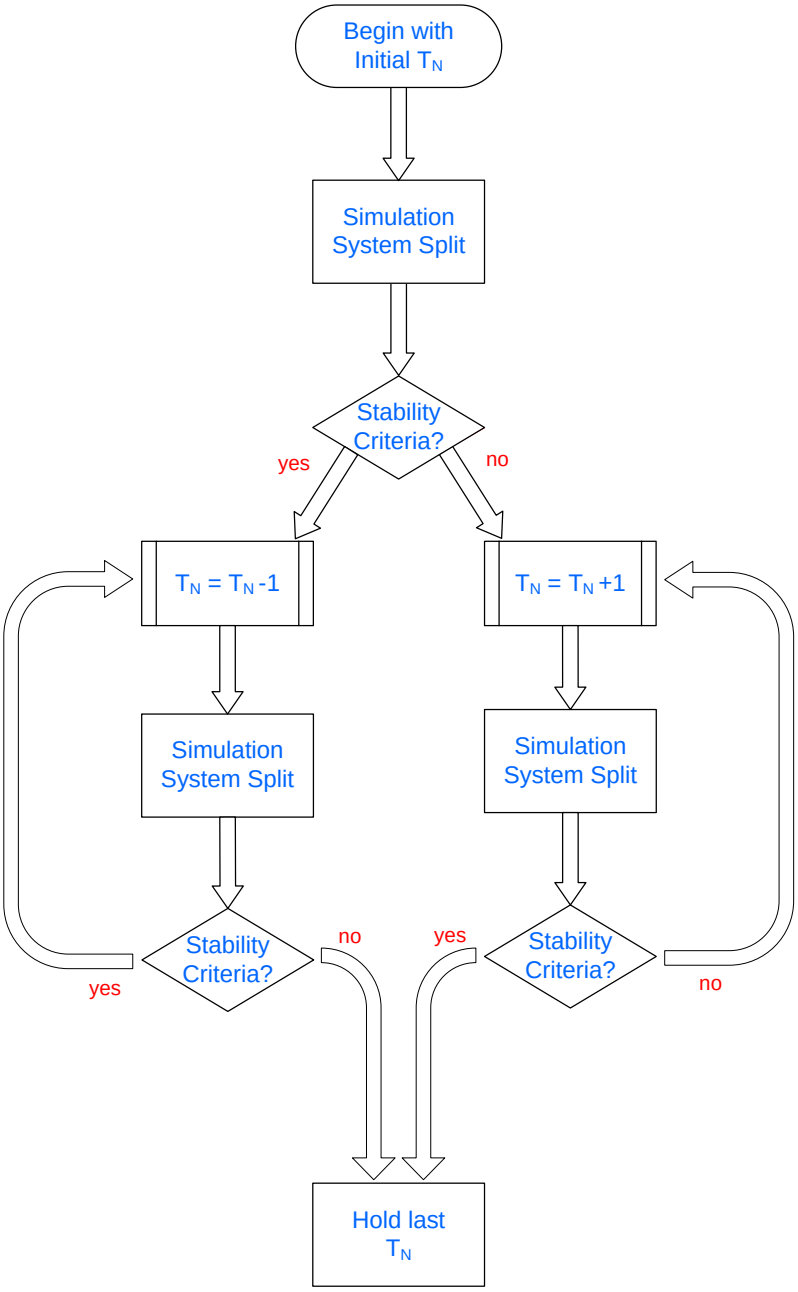

Figure 5.2: Flowchart of testing two-node grid for acquiring minimum T_N

For a 24% power imbalance in both positive and negative directions, Figure 5.3 summarizes the minimum required time constant to maintain stable operation and keep all grid parameters within range. The gray dotted line represents the estimated network time constant from Figure 5.1, indicating the average yearly inertia for 50% of the hours in 2030.

The minimum required time constant is shown in Figure 5.3 with orange color for a 24% import loss and in green for a 24% export loss, where the units are operating at partial load. With a 24% import loss, the inertia constant reaches a maximum of 10 s, accounting for 100% of GFM units including SG to the total generation share for LC_8. The percentage of GFM units to the total generation is shown on the second y-axis (right) in Figure 5.3.

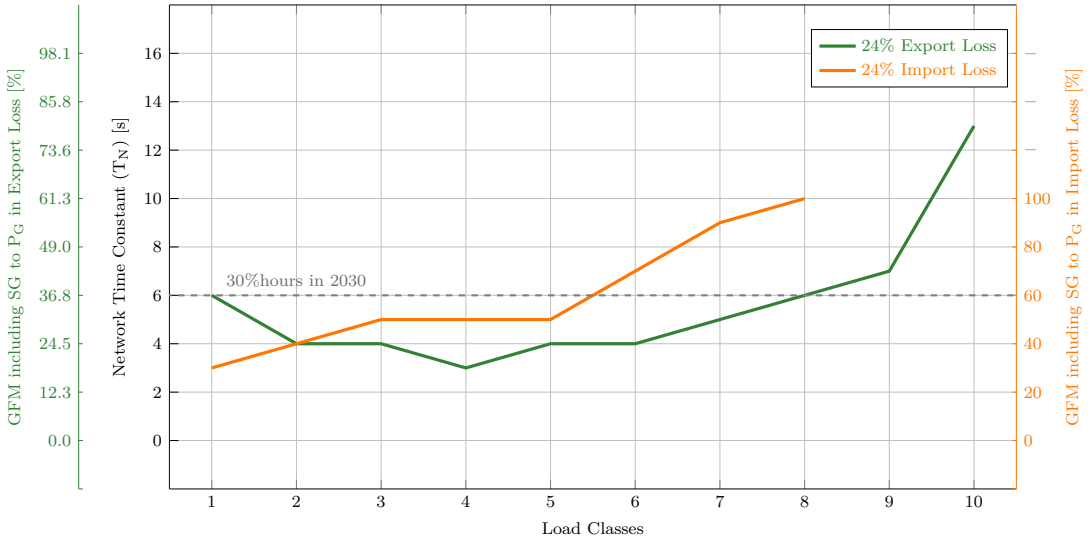

Figure 5.3: Minimum required inertia and GFM units in 24% import and export loss (below-rated power)

For the export loss scenario, the obtained time constant varies between 6 and 12 s across load classes 1-10. In the export loss scenario, where the load is smaller than the island's generation, and given the fact that the network time constant is relative to the total load, higher time constants can be achieved without reaching 100% GFM generation (see Chapter 4.3.1 & 4.4.2). The third y-axis, shown in Figure 5.3 in green, represents the percentage of GFM units including SG to the total

generation for the export scenario. In the following, the results of the islanding with ±24% power imbalance is discussed in detail.

I Why is it crucial to consider the load characteristic when dimensioning power system inertia?

Looking at Figure 5.3, it is evident that to obtain the minimum required network time constant, the influence of load must be considered. For import cases, the time constant varies between $3 \rightarrow 10$ s and for export cases, it ranges from $6 \rightarrow 13$ s. This shows that considering only resistive loads does not provide an accurate assessment of whether the required time constant is sufficient when the consumer side includes loads components other than only resistive. In the import scenario, an inertia constant of 10 s is three times higher than the required time constant in the base scenario (LC_1), and even this value is not sufficient when the proportion of PE loads on the consumer side exceeds 80%. In the case of a 24% export loss, the lowest required time constant is not achieved with LC_1, but the difference between LC_1 and LC_{10} in the island results in more than a fourfold increase in the required time constant.

II How is LC_1 affected by variations in the network time constant?

Figure 5.4 illustrates the result for a 24% import loss in the network with LC_1, where the network time constant varies from $T_N = 8 \rightarrow 4$ s. At the instance of islanding, the load remains unchanged. From the generation perspective, as GFL units do not participate in voltage support (as long as the voltage remains within the deadband) or frequency support, a higher share of GFL units (e.g., $T_N = 4$ s), reduces the generation's capability to support the network's voltage vector. Therefore, as shown in Figure 5.4, increasing the network time constant by increasing the share of GFM units improves voltage regulation in the grid. The minimum voltage varies in $T_N = 8 - 4$ s scenarios from 0.97-0.89 pu, receptively.

Despite better voltage support with higher GFM unit shares, the effect on frequency is negligible. As illustrated in Figure 5.4, between 0 - 1 s, there is a

slight increase in the magnitude of RoCoF when moving from $T_N = 8 \rightarrow 4$ s, but the difference is minimal. This is because the power consumption in LC_1 is quadratically influenced by network voltage. As shown in Figure 5.4, for $T_N = 4$ s, the final step of load shedding is not triggered due to very low voltage at approximately 1.5 s, in contrast to the $T_N = 8 - 5$ s scenarios. This omission results in a different frequency profile for $T_N = 4$ s where the frequency recovers gradually. In contrast, the additional load-shedding step in the $T_N = 8 - 5$ s scenarios causes the system to enter an overproduction phase, leading to a sudden positive RoCoF that pushes the frequency into the over-frequency region.

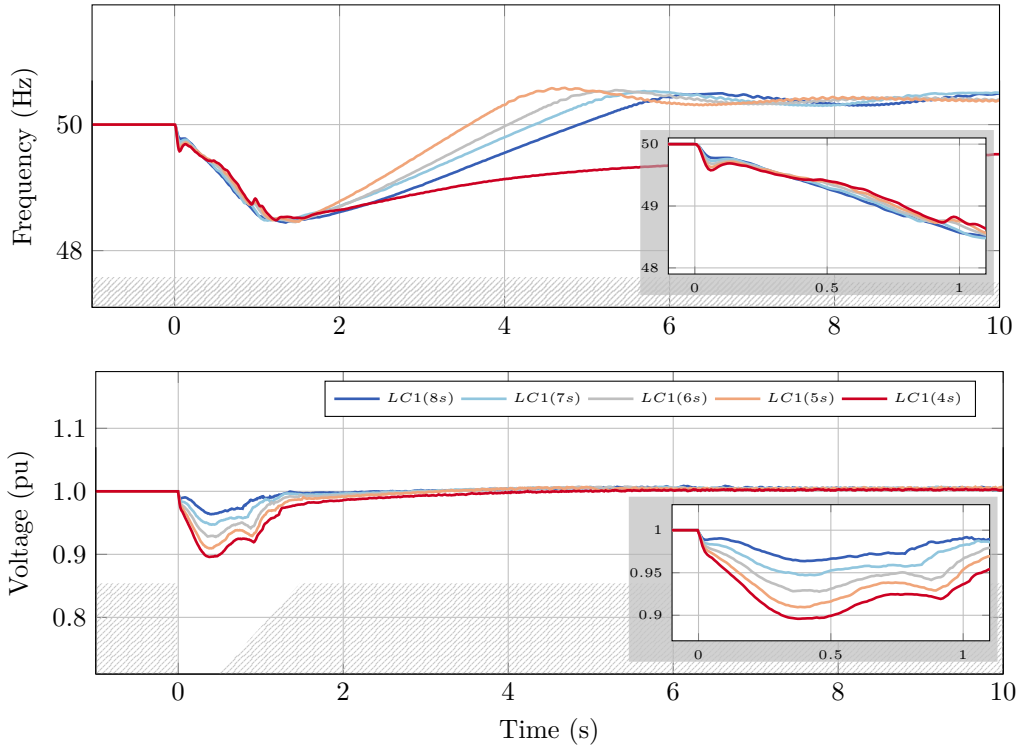

Figure 5.4: Varying network time constant in load class 1, in 24% import loss

Given the load characteristics in LC_1, decreasing the network time constant to $T_N = 4$ s does not significantly affect the frequency profile. Beyond this point, however, reduced damping torque in the system increases angular oscillations,

resulting in less stable operation and violations of RoCoF and frequency limits. Therefore, the minimum network time constant for a 24% import loss with LC_1 is determined $T_N = 3$ s from the simulation results.

III Why is a 24% import loss more challenging to manage than a 24% export loss?

The reason is mainly due to the current limitations of converters, which provide a smaller current margin in import scenarios. For instance, based on the selected inertia parameter for GFM unit, a RoCoF of -1 Hz/s requires a 20% current increase. Consequently, a RoCoF of -1.2 Hz/s would trigger the over-current limitation in the converter. Furthermore, due to voltage violations, GFM units actively regulate voltage by adjusting reactive power, which further reduces the available current margin. This limits the GFM contribution to overall system strength due to converter constraints. In contrast, during export loss, such limitations do not arise. A current reduction of 20 - 30% is feasible even under partial load, where the converters are operating in 0.76 pu.

IV Why do tests with LC_9 and LC_{10} fail in import loss scenarios?

Figure 5.5 illustrates the results of islanding with a 24% import loss for LC_9 and LC_{10}. These results are based on a scenario where the network time constant is $T_N = 10$ s for both load classes. It is evident that both load classes fail under these conditions. As discussed in Chapter 4.4.1, the further reduction of IM in LC_9 and LC_{10} weakens the grid even more compared to other load classes. A similar performance was previously observed and analyzed in Chapter 4.4.1, where the network time constant was $T_N = 8$ s.

According to the results shown in Figure 5.5, immediately after islanding, the voltage vector of the loads and GFM unit begins to decelerate, similar to other load classes. The GFM unit, as the main source in the island (90% of the total generation), counteracts the negative RoCoF through inertia injection. However, within the first 20 ms, the GFM unit reaches its current limitation threshold and starts restricting current output. During this period, the PE

loads in LC_{10} and LC_9 must synchronize with the network voltage to maintain constant power consumption. However, after the transition to islanding, the voltage drops, requiring PE loads to increase their current setpoints to sustain the same power consumption. This triggers current limitations in the PE loads themselves. The combined effects of these nonlinearities, current limitations, very fast dynamics of loads, and insufficient inertia power from generation prevent the system from establishing a stable voltage vector. As a result, the network cannot sustain stable operation, leading to voltage collapse after 300 ms for LC_9 and after just 20 ms for LC_{10}, resulting in test failure.

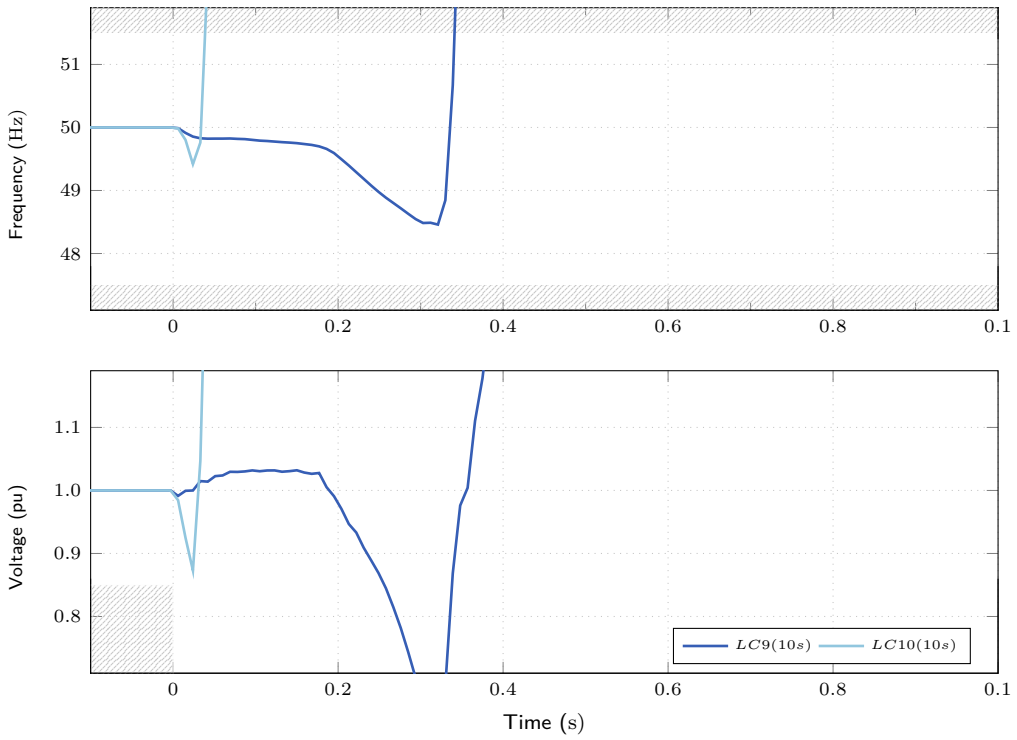

Figure 5.5: Performance of LC_9 & LC_{10} with network time constant of $T_N = 10$ s in the network, in 24% import loss

As in both scenarios, the test failed with 100% GFM units, a hypothetical solution could involve operating the GFM-WT in curtailed mode (below 76% of rated power), or to increase the inverter current limitation. These measures contribute to an increase in inertia power, enhance network strength, and could help maintain stable operation under the same imbalance conditions

with LC_9 and LC_{10}. However, this comes at the cost of reducing the profit margin for the wind farm owners.

V Why does a pure resistive load require 2 times higher network time constant to handle a 24% export loss compared to an import loss?

The pre-event operating point for a 24% export loss is identical to that of the import loss scenario. However, during export loss, the SG and GFM unit can maintain almost a constant voltage. Figure 5.6 compares the frequency and voltage responses after grid separation for both export and import loss scenarios with a network time constant of 6 s.

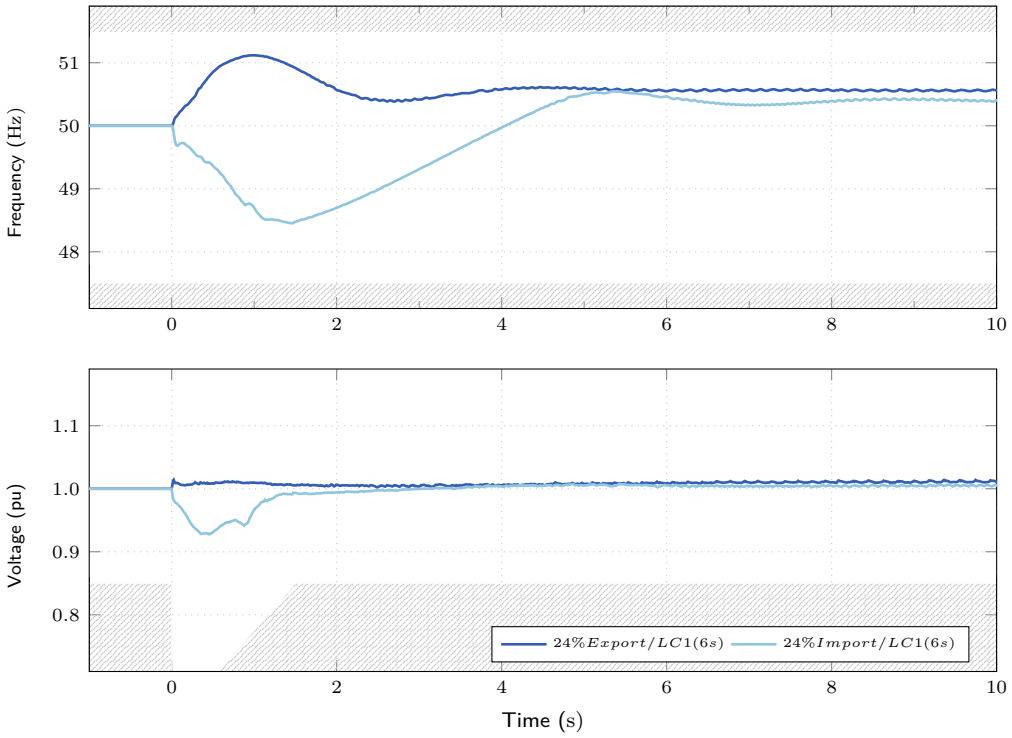

Figure 5.6: Comparison of LC_1 performance with a network time constant of $T_N = 6$ s under 24% import and export loss scenarios

In the export loss scenario, a peak of voltage in the positive direction occurs immediately after islanding, lasting for a few milliseconds. The voltage then stabilizes at a value slightly higher than the pre-event level. Since no

limitations are triggered during export loss, voltage support is sustained by the GFM unit and SG in the network. In contrast, during import loss, overcurrent limitations is activated while inertia provision, forcing the converter to reduce voltage to limit the currents. In this scenario, the remaining capacity of the GFM unit is primarily utilized to smooth the frequency gradient.

As shown in Figure 5.6, maintaining the voltage close to its nominal value prevents voltage-dependent power increases. Consequently, generation units must manage a higher power imbalance in the network compared to the equivalent import scenario. This difference impacts the RoCoF behavior following islanding in export scenarios compared to import scenarios. In Figure 5.6, the RoCoF for export loss is slightly below 2 Hz/s, whereas in import loss, the RoCoF is smoother and less sensitive to reductions in the network time constant, as already shown in Figure 5.4. However, in export scenarios, reducing the network time constant below 6 s causes the RoCoF to exceed the 2 Hz/s threshold.

VI Is the inertia dimensioning based on ENTSO-E estimations sufficient to ensure stable operation with potential islanding incidents in the future?

Considering the import graph in Figure 5.3 reveals that the required minimum network time constant for higher shares of PE loads exceeds the maximum inertia constant predicted for 2030 (see Figure 5.1). According to these estimations, the highest anticipated network time constant for 2030 is 9 s, which is expected to be available for almost zero hours in the year 2030. Even if new technologies, such as GFM-based converter generation, compensate for the deficit to increase availability of this time constant throughout the year, it would still be insufficient to handle higher-magnitude islanding incidents, particularly during import loss events with a high proportion of PE loads on the consumer side. Figure 5.3 demonstrates that any load composing more than 57% PE requires a network time constant exceeding 9 s in scenarios involving a 24% import loss. This highlights the critical role of load characteristics in inertia estimation and in the planning for integration of advanced technologies like GFM units to ensure system stability.

VII How feasible is it to increase the inertia time constant of wind turbines to enhance inertia provision while maintaining the same share of GFM units?

Extensive EMT studies on GFM units, especially wind turbine units, will allow TSOs, in collaboration with Original Equipment Manufacturers (OEMs), to more clearly define the grid codes and requirements for the integration of GFM units, with one of the key factors being the amount of inertia contribution. The extent to which WTs can contribute to inertia depends on several factors beyond the availability of wind. First, increasing the inertia contribution from WTs results in slower controller dynamics, which can hinder the unit's ability to respond quickly to grid demands as required by current grid codes. For example, during power recovery after a fault, a higher inertia setting slows the recovery process, potentially leading to operational challenges from the system operator's perspective [26]. Second, operating below nominal wind speed presents another challenge. Extracting a higher amount of energy from the rotating parts of WTs during inertia provision risks reducing the turbine speed below the cut-in speed, potentially resulting in the loss of the generation unit [32]. Even if the unit remains connected, drawing higher power from the WT for an extended period can prolong the recovery phase after inertia provision, especially if the WT was already delivering maximum wind power to the grid before the event. This extended recovery phase may have system-wide and economic implications that are unfavorable for both system operators and plant owners. Operating in a curtailed mode could address this issue, but that is beyond the scope of this work. Lastly, the economic impact of higher inertia provision must also be considered. For the same grid event, higher inertia requires a steeper torque gradient, leading to increased wear and tear on mechanical components [118]. This could result in higher maintenance costs for plant owners, potentially reducing revenue.

VIII To what extent does using only resistive loads influence the results of the minimum required grid time constant study?

To address this question and to observe the possible aspect of such simplicity, a study was conducted with a 24% import and export loss across 10 load

classes, including LC_1, which represents a purely resistive load. The simulation results for both scenarios reveal that this simplification in load representation significantly impacts the assessment of the minimum required grid time constant. This has a twofold effect on power system planning, as discussed below:

Economic and Stability Considerations

If detailed information about load characteristics is unavailable to power system planners or if simulation efforts are constrained, relying solely on simulations with resistive loads may misrepresent the grid's minimum time constant requirements (see Figure 5.7).

As shown earlier in Figure 5.3, a time constant of 3 s, which is sufficient for LC_1 under a 24% import loss scenario, is inadequate for other load classes. For these nine classes, the required time constant ranges from 33% to 333% higher than that for LC_1. Particularly, load classes with high penetration of PE loads (>88%) demand even higher time constants to ensure a stable transition to islanding. Simulations results indicate that time constants below 3 s fail to prevent system instability, risking generator tripping due to exceeding maximum RoCoF withstand capabilities, violating stability criteria, or losing consumers. Such failures can compromise system reliability and lead to increased costs for system operators.

In the case of a 24% export loss, the required network time constant for LC_1, is obtained 6 s (see Figure 5.3), which is an overestimation for seven load classes (LC_2-LC_7). This implies that more inertia is provided than necessary for 70% of the load classes. Conversely, for 20% of the load classes, this value represents an underestimation, indicating insufficient inertia to maintain stability. For the remaining 10% of load classes, $T_N = 6$ s matches the actual requirement, aligning with the stability needs after islanding with a 24% export loss.

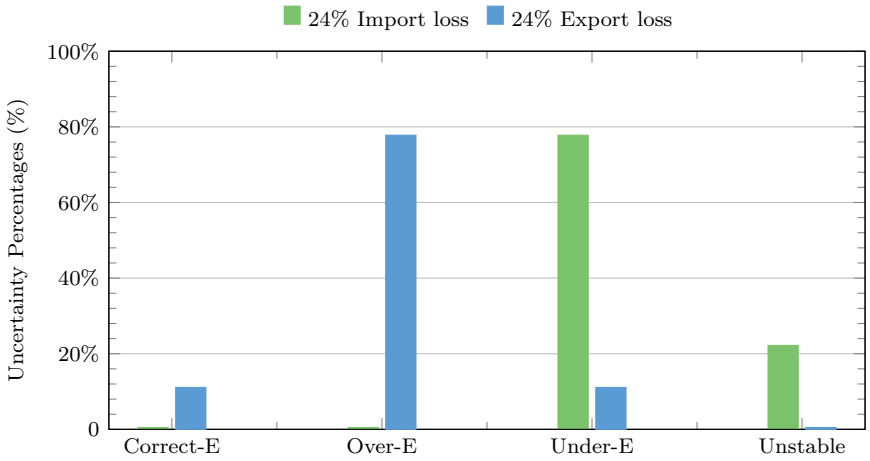

Figure 5.7: Level of uncertainties associated with system split studies focusing solely on resistive loads as the main consumer with 24% import and export loss

The under- or over-estimation of inertia requirements leads to significant economic consequences for system operators, such as increased operational costs, additional penalties, compensation for market imbalances, or for loss of loads, and inefficient resource allocation [119]. These issues highlight the critical need for improved transparency regarding load characteristics and their integration into grid studies. Addressing this gap ensures more accurate evaluations of inertia requirements, balancing system reliability and economic efficiency for operators.

5.2.2 Islanding with ±40% Power Loss (Below Rated Power)

Figure 5.8 illustrates the islanding results for scenarios with 40% import and export loss. In this case, the generation units are not operating at their nominal ratings, similar to the previous scenario discussed in Chapter 5.2.1. For the 40% import loss, the majority of load classes demonstrate a stable transition to islanding; however, they fail to meet stability criteria, particularly concerning RoCoF compliance. The only load classes exhibiting instability after islanding with the grid time constant (T_N = 10 s) are LC_9 and LC_{10}. This results is expected, as these load classes also displayed instability in the 24% import loss scenario under similar time constant, as previously discussed in Chapter 5.2.1.

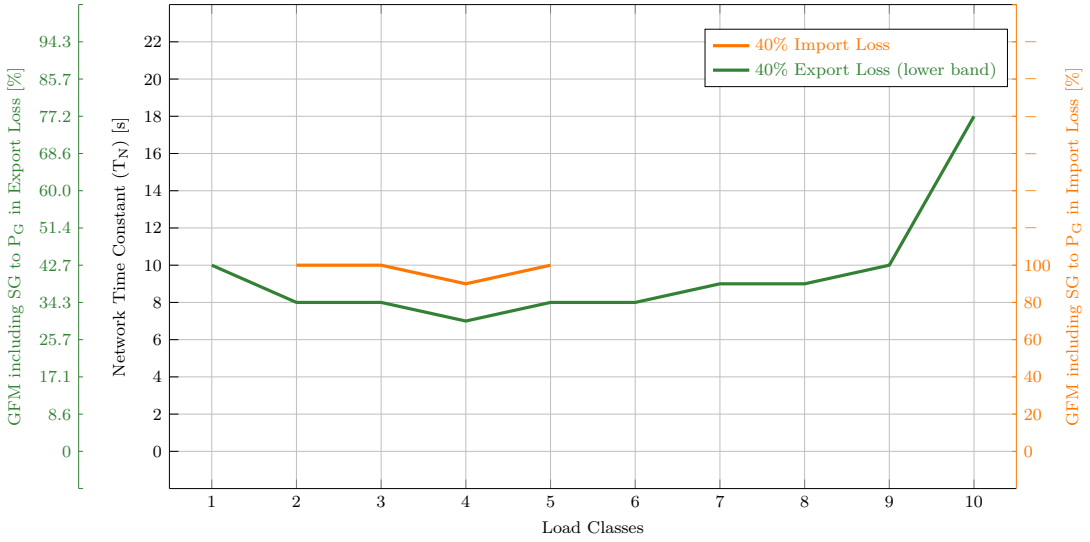

Figure 5.8: Minimum required time constant and percentage of GFM units for 40% import and export loss scenarios (below-rated power)

Based on the data in Figure 5.8, a minimum time constant of $T_N = 10$ s ensures stable islanding without generation trips only for LC_2-LC_5 in import loss scenario. Beyond this level, achieving stability demands impractically high inertia which is unfeasible from the generation perspective, as the system already comprises 100% GFM units relative to the total generation (see Figure 5.8). Except LC_9 and LC_{10}, all cases fail even with $T_N = 10$ s, as the RoCoF exceeds the threshold of -2 Hz/s.

Figure 5.9 illustrates the comparison between LC_1 and LC_3 as the network time constant increases from 7 to 10 seconds. In this comparison, LC_3 is highlighted as one of the scenarios where increasing the time constant to $T_N = 10$ s demonstrates acceptable performance with a 40% import loss.

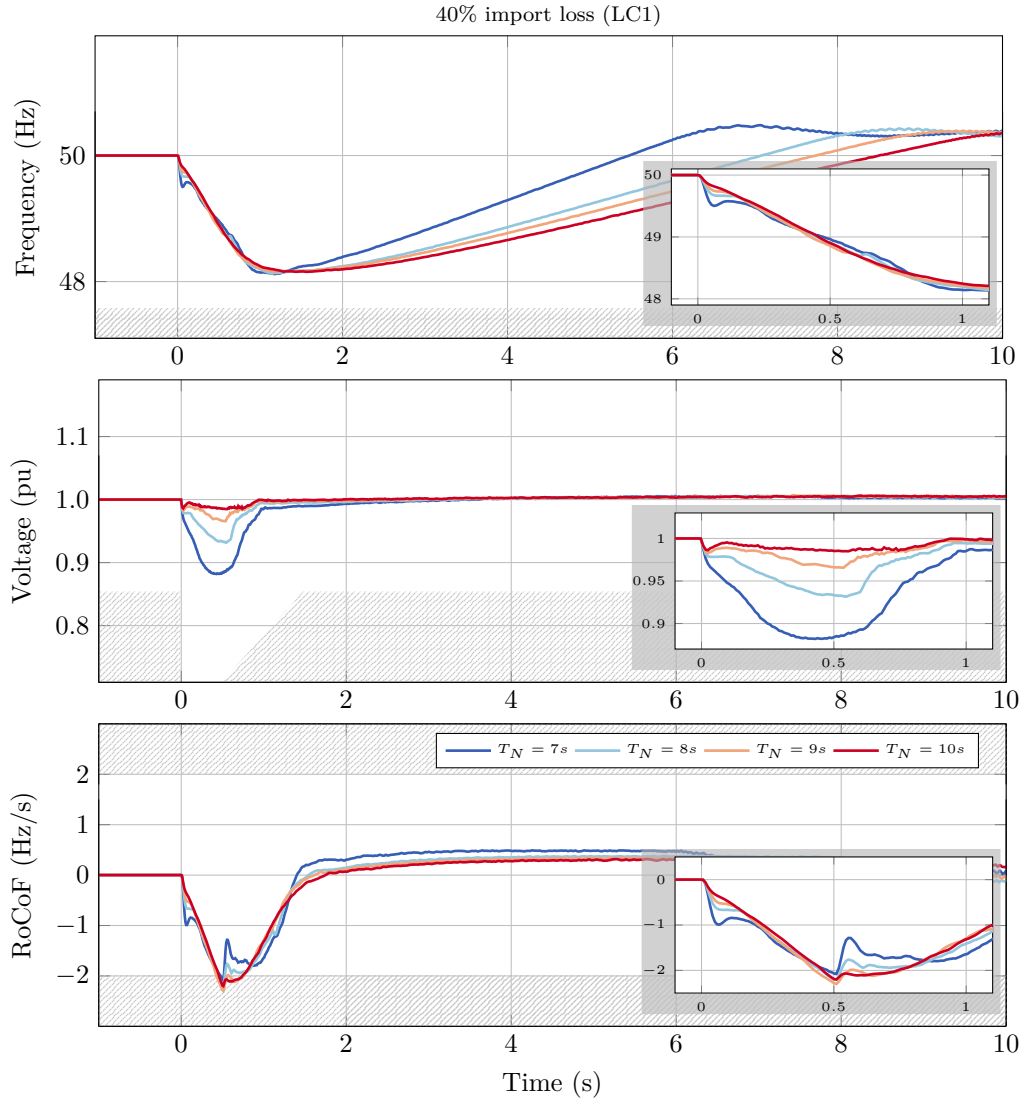

Figure 5.9: Impact of increasing network time constant under 40% import loss, in LC_1, (1/2)

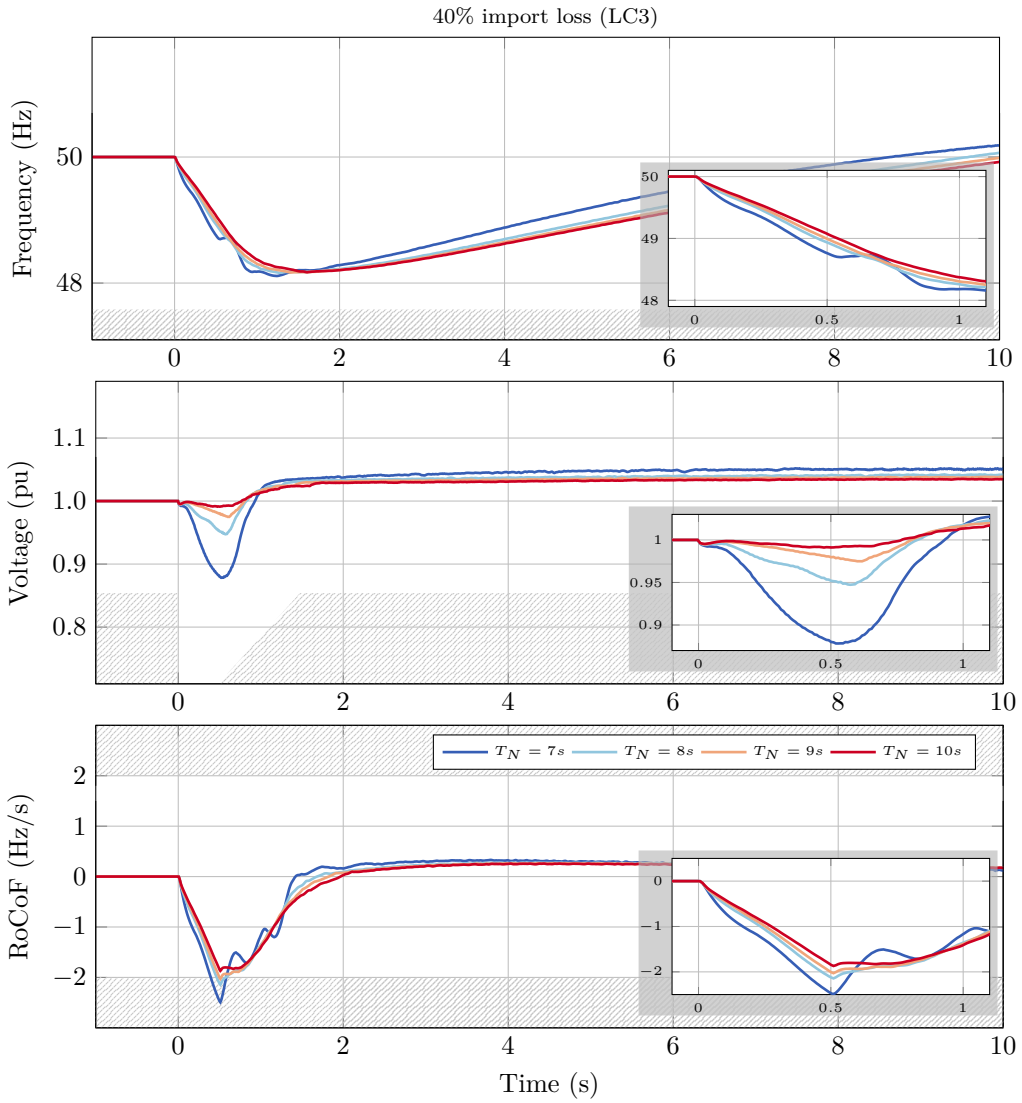

Figure 5.9: Impact of increasing network time constant under 40% import loss, in LC_3, (2/2)

As noted in Chapter 5.2.1, increasing the network time constant from 7 to 10 seconds, doesn't influence noticeably RoCoF in LC_1 (see Figure 5.4). As a result, there is no stable operating point for LC_1 that does not violate the RoCoF criteria. Figure 5.9 (2/2) shows the frequency and voltage profiles of LC_3, where the consumer includes all three load categories. As shown, increasing inertia has improved the RoCoF and voltage profile by increasing the strength in the islanded network. The results

indicate that $T_N = 10$ s can maintain system stability in case of 40% import loss with LC_3. By increasing time constants from 7 to 10 seconds through an increase in the share of GFM to GFL units, the capability of the generation fleet to support the load improves [120], [121].

The inertia increase in LC_1 is countered by a higher imbalance within the island due to voltage-dependent power variation. However, in LC_3, since the load exhibits dependency on both voltage and frequency, both active and reactive power consumption in the network varies in response to islanding and 40% power deficit. Thus, increasing the network time constant allows for greater support for the load in LC_3, resulting in a better voltage and RoCoF profile compared to LC_1, as depicted in Figure 5.9 (2/2).

In contrast to a 40% import loss, in 40% export loss scenario the whole imbalance can be theoretically managed by generation units through inertia power absorption and power reduction in LFSM-O mode. However, according to the test results shown in Figure 5.8, in some scenarios, the available inertia power is insufficient to maintain acceptable or stable performance. Since the LFSM-O performance depends on measurement and activation delays, it becomes necessary to increase the network time constant by increasing the share of GFM units to achieve stable operation. As the GFM units emulate voltage source behavior with inertia provision, a higher percentage of GFM units allows more energy to be absorbed by the rotating masses relative to the load's nominal ratings.

The results in Figure 5.10 indicate that, with a 40% export loss, the minimum network time constant varies between 7 and 18 seconds. Values below this level either result in performance exceeding the RoCoF limit or lead to instability, particularly in load classes 9 and 10. Similarly, for a 40% import loss, the inertia constant exhibits a parallel trend to that observed in the 40% export loss scenario, with a time constant difference of 2 seconds. Since the percentage of GFM to total generation reaches 100% at $T_N = 10$ s, further testing with higher time constants in the import loss scenario was not feasible.

Figure 5.10 compares the required time constants for 24% and 40% export losses, highlighting a markedly different behavior between the two cases. As expected,

increasing the magnitude of the export loss necessitates a higher time constant to address higher power imbalances, a trend clearly observed in Figure 5.10. For the 40% export loss, the lower threshold of the required time constant is generally about 4 seconds higher than that for the 24% export loss.

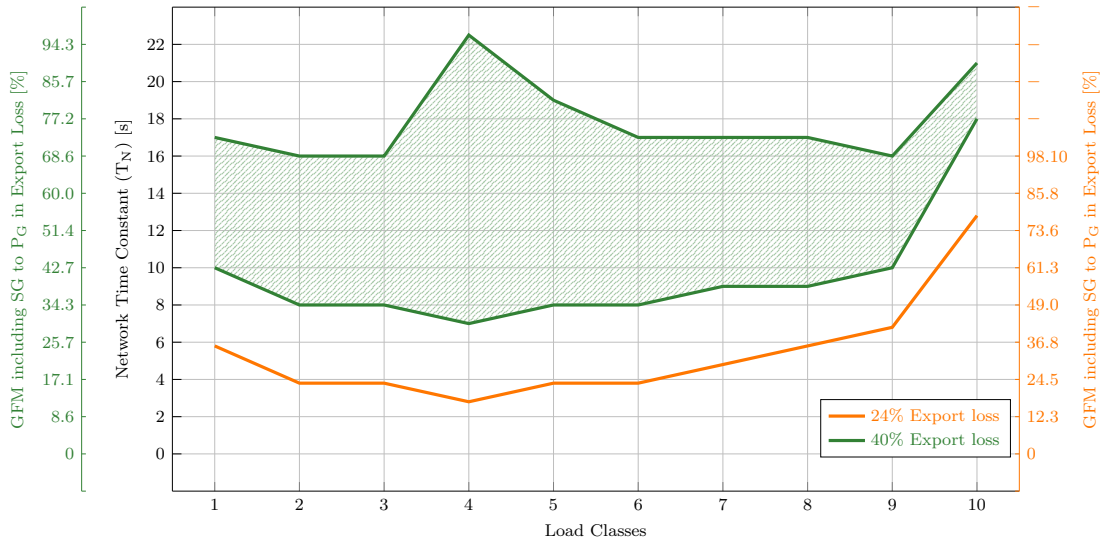

Figure 5.10: The acquired band of required inertia and GFM units in 40% export loss and 24% export loss (below-rated power)

However, beyond a certain threshold in each load class, further increasing inertia for the 40% export loss leads to distinct behavior. Figure 5.10 defines a permissible band where the system remains stable, maintaining voltage, frequency, and RoCoF within acceptable limits. Exceeding the upper boundary of this band breaches the stability criteria related to frequency limit. Conversely, falling below the lower boundary results in either a loss of stability or degraded performance due to excessively high RoCoF.

Under the 40% export loss scenario, there is no single GFM unit percentage that guarantees stable islanding across all load classes. This is primarily due to upper boundary conditions, which introduce a secondary limitation on the required GFM share. Specifically, taking the minimum GFM share of LC_{10} (approximately 77%) results in unstable operation for all other load classes except LC_4 & LC_5, as they fail to meet the stability requirements imposed by the upper boundary.

As shown in Figure 5.10, the allowable time constant band is widest around LC_4 and narrowest in LC_{10}. In this study, increasing the time constant corresponds to greater participation of GFM-based units. The formation of such boundaries is directly related to this increase, which is analyzed in detail below.

Figure 5.11 presents the test results for the islanding scenario with a 40% export loss under three different time constants for LC_5. As shown, for $T_N = 10$ s, the initial RoCoF is higher compared to the other cases. However, after the first swing, the frequency gradually settles at a new steady-state value. With $T_N = 20$ s, the initial RoCoF is smoother compared to $T_N = 10$ s; however, the second oscillation causes an overshoot in the frequency and the GFM unit's load angle, leading the frequency to breach the upper limit of 51.5 Hz. Reducing the network time constant by 1 s mitigates this second swing and prevents the frequency from hitting the upper boundary.

This result is attributed to the use of a GFM-based wind turbine unit. For WT applications operating in MPPT mode, interactions can occur between inertia provision, the wind turbine controller, and LFSMO activation due to grid over frequencies. These interactions can influence the system's frequency response. This effect is not observed when a GFM unit is modeled with an infinite amount of inertia, as seen in studies such as [32], [4]. The following section discusses a sequence of actions following grid disconnection across these three time constants.

Point 1, After the grid disconnection, a change in ΔP occurs in the GSC of the GFM-WT unit, leading to an acceleration of the voltage vector of the load. Due to the change in angle, the GFM unit must absorb this power surplus. The reduced active power is measured by the feed-forward element in the DC-link controller, which adjusts the machine's torque to absorb the excess power. This shifts the operating point of the WT to the right side of the power-speed (C_p, λ) curves. The higher the grid time constant, the greater the share of GFM units, and thus, the less the power imbalance shifts the operating point further to the right side of the curve. This is illustrated in Figure 5.11, where it shows P_{EL} at point 1, has a power offset in the negative direction, while P_{MPPT} remains close to its pre-event value.

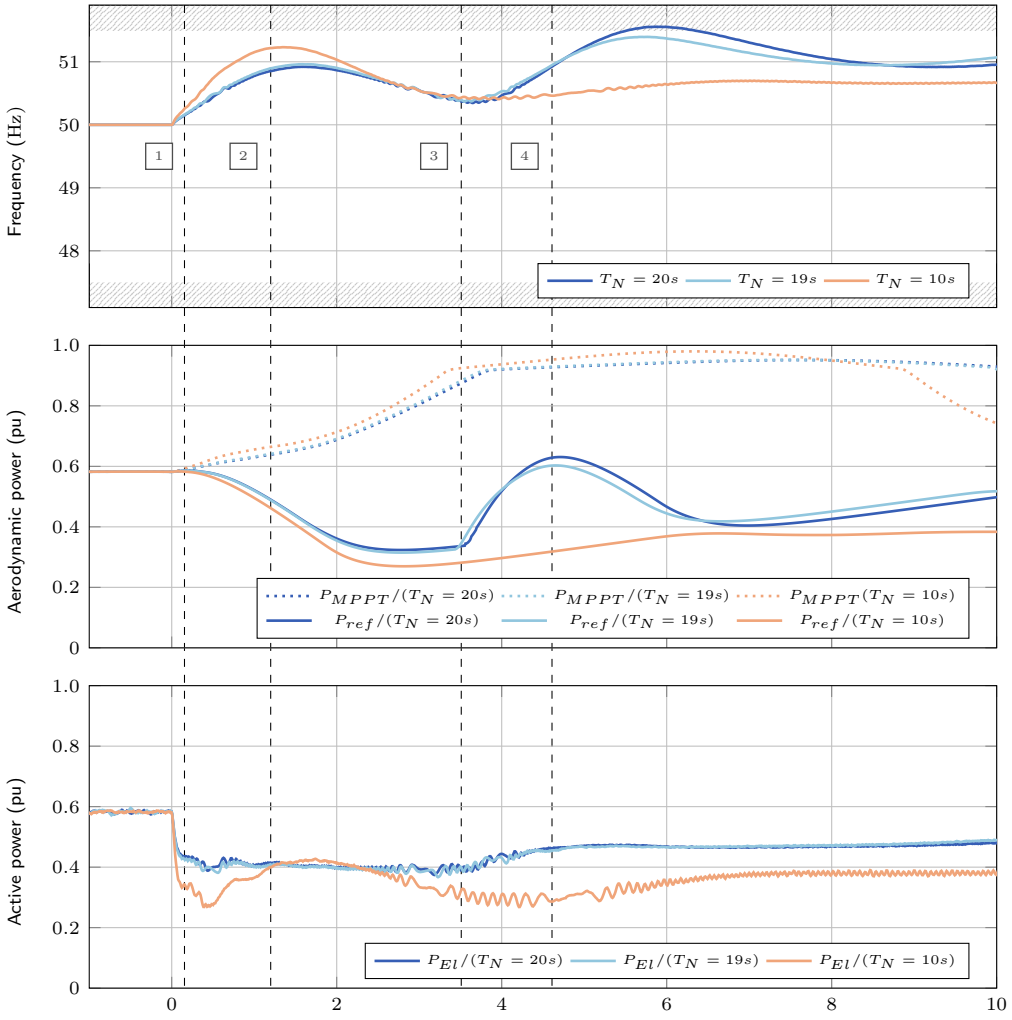

Figure 5.11: Reaction of GFM-unit to the active power surplus after islanding in different inertia in the network

Point 2, After the initial phase, the frequency reaches the LFSM-O threshold (50.2 Hz). At this point, the LFSM-O mechanism for adjusting P_{ref} is activated with a delayed reaction (see Chapter 3.2.6). As the frequency rises more sharply in $T_N = 10$ s compared to $T_N = 20$ s, the power offset for LFSM-O is larger, which further accelerates the GFM-WT. As shown in Figure 5.11, between points 1 and 2, P_{MPPT} starts increasing as the rotational speed of the turbine increases. At the border of point 2 to 3, P_{ref} has fallen below the actual measured active power, initiating the deceleration phase. As indicated in Figure 5.11, at point 2, the

frequency begins to drop.

According to the control concept, when the LFSM-O threshold is reached, P_{MPPT} is frozen, and a new power setpoint is sent to the GSC (see Chapter 3.2.6). During this period, as shown in Figure 5.11, acceleration causes P_{MPPT} to increase further. However, the setpoint is determined by the LFSM-O block, and the difference between the setpoint and the measured power directly affects the grid frequency. The interaction between the grid frequency and the wind turbine becomes more evident at this point. This is shown at point 2 that the frequency starts to decelerate, yet P_{ref}, which is driven by the grid's frequency, continues to drop due to the delay in the LFSM-O function.

Point 3, After point 3, the pitch controller activates to limit any speed exceeding the nominal value. In the $T_N = 10$ s scenario, pitch activation occurs before point 3 due to higher rotor speed. As shown in Figure 5.11, at the boundary of points 3 to 4, there is a sudden increase in P_{ref} in both $T_N = 20$ s and $T_N = 19$ s which is not present in $T_N = 10$ s. This sudden increase in the reference power is due to the frequency dropping to the threshold of LFSM-O and normal operation. As a result, in the $T_N = 20$ s and $T_N = 19$ s scenarios, the power setpoint doesn't reduce further and it begins to return to its pre-event value. This oscillation of power appears more damped in the $T_N = 10$ s case, where the participation of the GFM-WT unit in LFSM-O power reduction is reduced compared to other generation units. In contrast, in the $T_N = 20$ s and $T_N = 19$ s scenarios, the majority of inertia power and power reduction via LFSM-O comes from the GFM-WT unit, as the dominant generation unit in the island.

Point 4, At point 4, it is observed that P_{ref} reaches its peak with $T_N = 20$ s and $T_N = 19$ s. This is the delayed reaction to the frequency minima at point 3. This peak paralyses the emulation of inertia and LFSM-O power reduction by increasing the active power set-point. As a result, the frequency starts to rise again, reaching a second peak higher than the first at $t = 5.8$ s. After a certain inertia constant (from $T_N = 20$ s onward with LC_5), this second peak violates the stability boundary concerning the maximum frequency, a scenario that does not occur within the time constant range of $T_N = 8 - 19$ s.

To conclude, the lower network time constant boundary is associated with the required percentage of GFM units in the network to provide sufficient inertia power to counteract the initial RoCoF after islanding. In Figure 5.11, all time constants below $T_N = 8$ s were insufficient to keep the RoCoF below 2 Hz s^{-1}. Meanwhile, the upper time constant border is linked to the oscillations in frequency, resulting from the interaction between inertia provision and LFSM-O power reduction of WT-based GFM units. The oscillation starts at the grid side converter control, spreads to the WT controller and LFSMO function, and then returns to the grid. The higher the share of GFM units in the isolated grid, the more pronounced this oscillatory behavior becomes as the GFL unit contributes less to frequency regulation via LFSM-O. It should be noted that the upper boundary was not observed in the scenario with a 24% export loss. This is primarily attributed to the lower level of unbalance and the reduced stress on the GFM unit to absorb the power through inertia support and LFSMO-based power reduction. The upper boundary in Figure 5.11, resulting from this phenomenon, highlights the need for the level of GFM-WT units to stay within a certain limit to avoid violating the frequency boundary. This outcome is tied to the implementation of the LFSM-O function with GFM-WT unit.

Economic and Stability Considerations

Figures 5.8 and 5.10 illustrate the variation in the obtained time constant across all ten load classes. It is observed that the results for LC_1 deviate from the dynamic performance of the other load classes, indicating that it is too simplistic for accurately deriving the required time constant to manage large power imbalances after islanding. The uncertainties associated with estimating the network's required time constant based on LC_1 results are discussed below:

For a 40% export loss, it is shown that a time constant of $T_N = 10$ s, derived from the simulation using LC_1, represents an overestimation for LC_2-LC_8. Simulation results indicate that while this value is very conservative for a 40% export loss, it allows stable operation in the majority of load classes. However, the same cannot be stated for the import loss scenario. With $T_N = 10$ s, the majority of test cases

fail to achieve acceptable performance while maintaining RoCoF limits, including LC_1 (see Figure 5.8).

Additionally, Figure 5.12 compares the unreliability associated with using LC_1 for minimum network time constant studies under 40% and 24% export losses. Overall, as shown in Figure 5.12, $T_N = 6$ s for a 24% export loss is an overestimation for 66.7% of the load classes, matches the required value for 11%, and is an underestimation for 22.2% of the load classes. Since the lower boundary of the 40% export loss is parallel to that of the 24% export loss across most load cases, the overestimation percentages show similar uncertainties with only slight differences over LC_9 (see Figure 5.10).

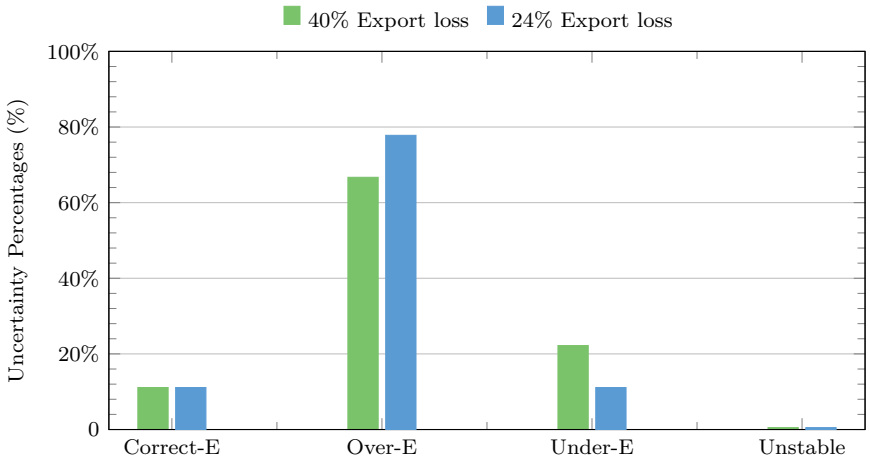

Figure 5.12: Level of uncertainties associated to the system split studies focusing solely on resistive loads as the main consumer in export loss of 24% & 40%

5.3 Impact of Operation at Rated Power with ±24% Power Loss

This chapter investigates the impact of wind turbines pre-event operation point on grid stabilization. In Chapter 5.2.1, wind turbines are not operating at their rated power due to wind speeds being below nominal levels. The effects of islanding with a 24% import and export loss under this condition were tested and discussed in detail in Chapter 5.2.1. In the following, a similar islanding scenario is investigated with generation operating at rated power, enabling a direct comparison with the results of Chapter 5.2.1 to assess the impact of operating point on the network performance after islanding.

Islanding with 24% Import Loss at Rated Power

In the first scenario, a 24% import loss is investigated, where generating units, including GFM-WT, operate at their maximum active power output. As in Chapter 5.2.1, test cases are defined across ten different load classes. Operating at nominal wind speed is advantageous for inertia emulation when wind turbine output is not curtailed. In this condition, there is minimal or no interaction with aerodynamic power, which could otherwise reduce the wind turbine's efficiency during inertia provision. However, at this operating point, the unit has very limited current headroom (15%, as discussed in Chapter 3.2.5) to support the grid.

To determine the minimum system strength required for each load class in the given scenario, the results from Chapter 5.2.1 were used as a baseline. The time constant was incrementally adjusted in 1 s steps to identify the threshold for stable operation. Figure 5.13 illustrates the findings for each load class under a 24% import loss scenario and compares them to the results for WTs operating at below-rated power.

The GFM values shown in Figure 5.13 for rated power operation correspond to test cases that achieved both stable operation and compliance with stability criteria. It is observed that the required GFM units for rated-power operation in LC_1-LC_5 needed to be increased by 50% ($\Delta T_N = 3$ s) to manage a comparable power imbalance. The test results indicate that for LC_5-LC_7, a transition to islanding without system

collapse is achievable with 100% GFM units, including SGs. However, the RoCoF exceeds the maximum allowable threshold of -2 Hz s^{-1}, and therefore, these points are excluded in Figure 5.13. From LC_8 onward, stable islanding could not be achieved at rated power, even with 100% GFM deployment.

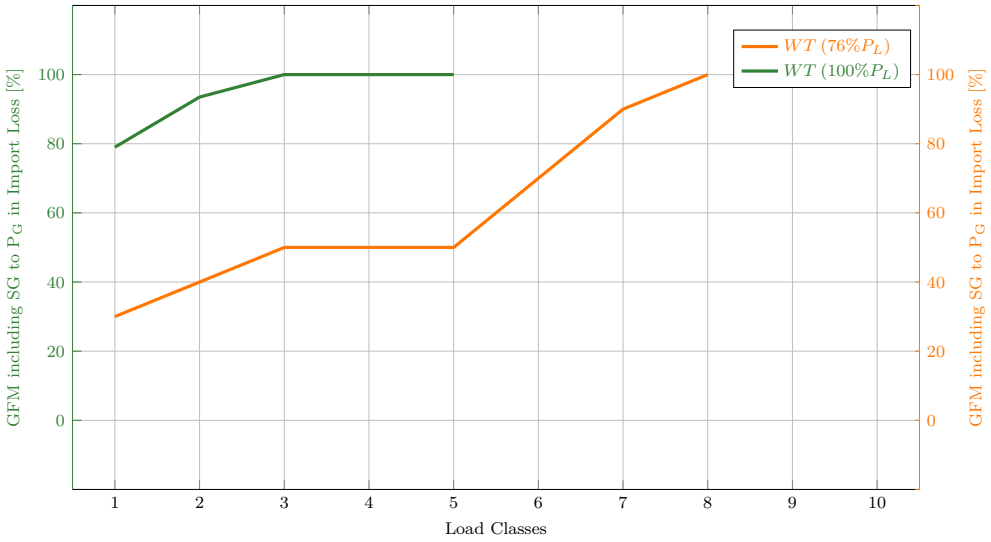

Figure 5.13: Comparing the minimum share of GFM units in 24% import loss in below-rated and rated-power operation

Under a 24% import loss, failure reason differ between rated and below-rated power. At below-rated power, most tests failed due to RoCoF exceeding the -2 Hz/s limit, despite acceptable voltage and frequency levels. In contrast, rated-power tests failed due to combined voltage instability and RoCoF violations, driven by reduced capability of generation units, particularly GFM units, to support frequency and voltage under full load.

Figure 5.14 illustrates the performance of LC_5-LC_9 across two scenarios. For LC_5, both scenarios demonstrated acceptable performance; however, when generation units operate at rated power, the required share of GFM units must increase from 50% to 100%. It is worth noting that the LC_5 results in Figure 5.14 (2/2) indicate that even with 100% GFM units, the RoCoF is only marginally below the limit of -2 Hz/s.

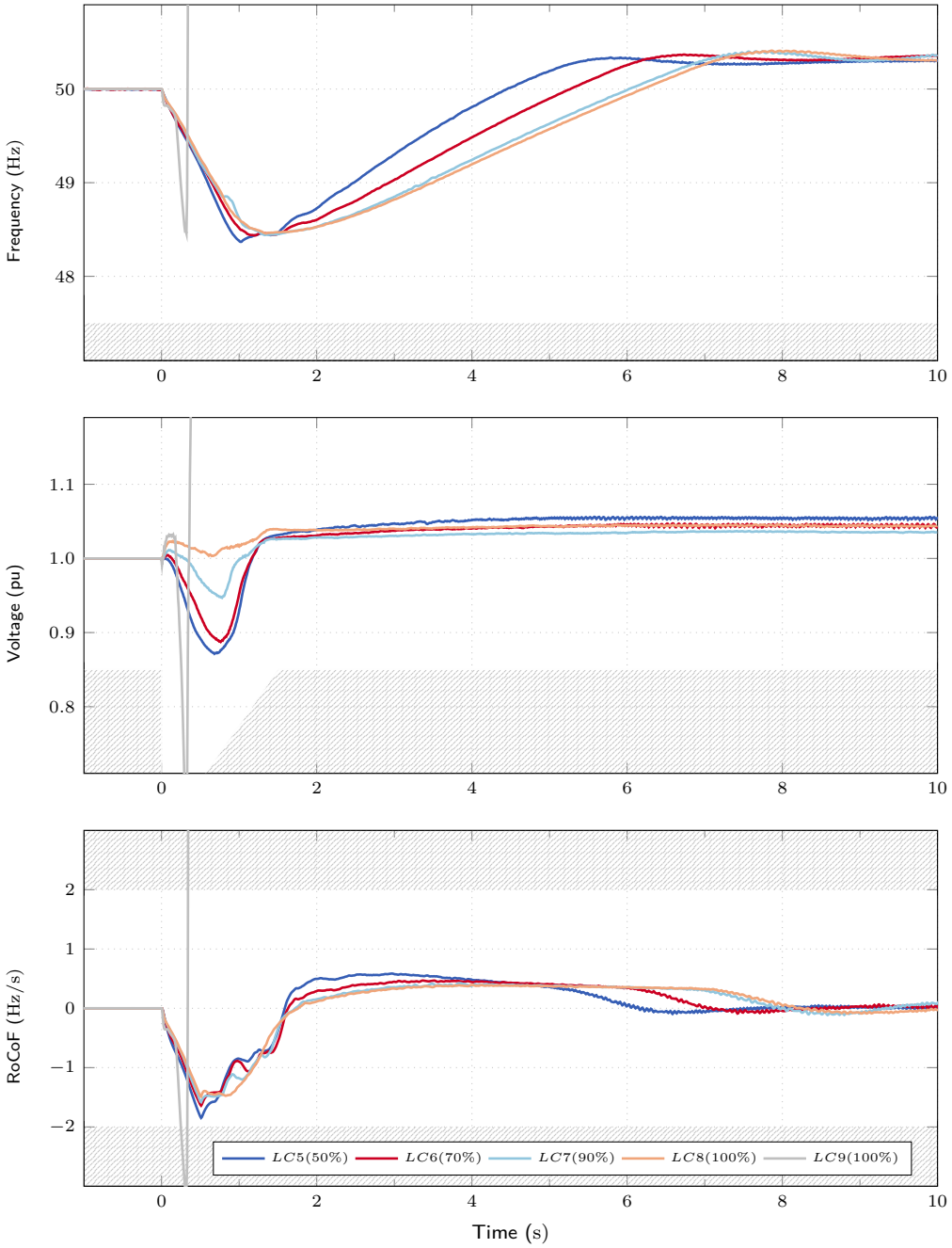

Figure 5.14: Comparing the performance of generation unit with the required GFM units for LC_5-LC_9 under 24% import loss, below-rated power, (1/2)

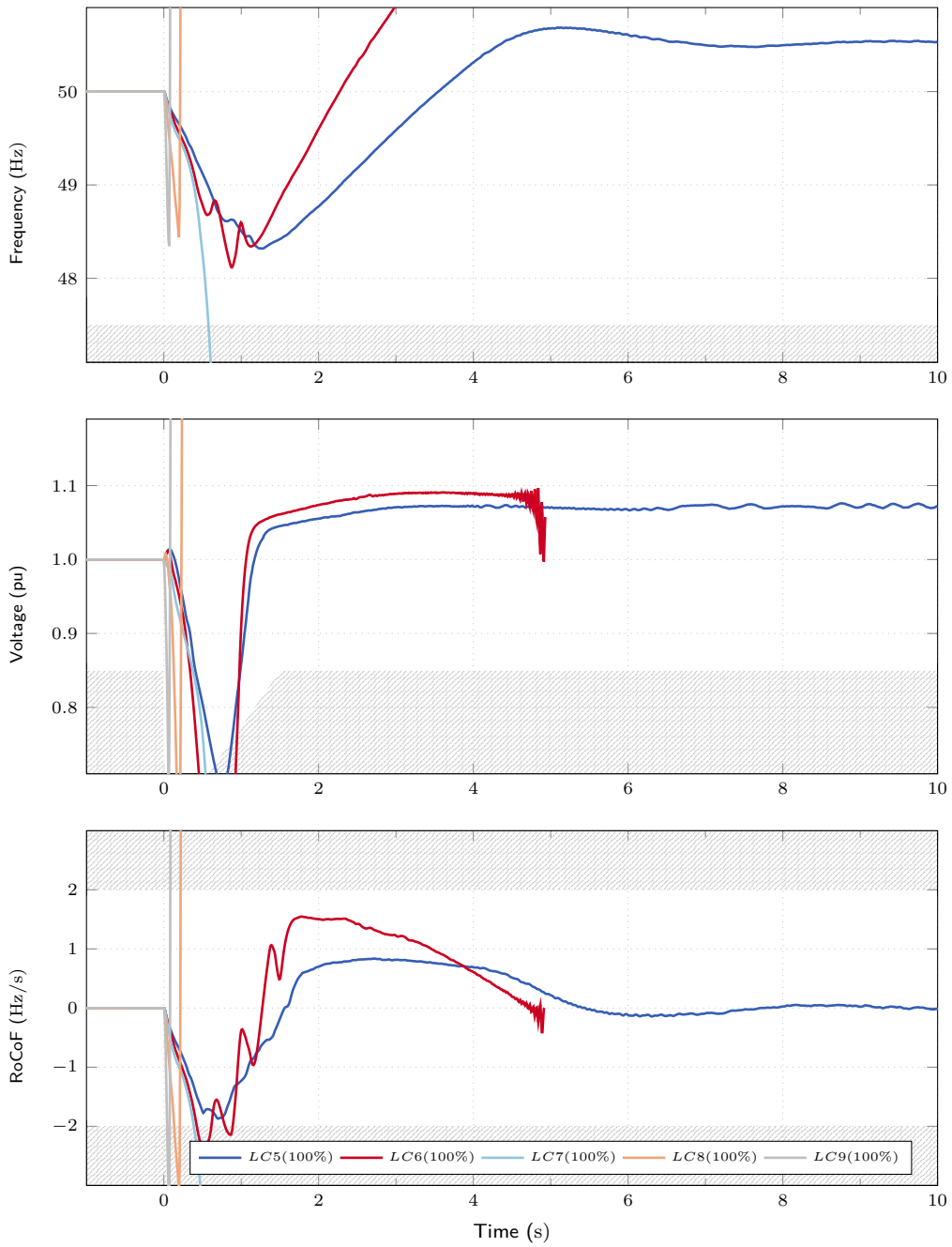

Figure 5.14: Comparing the performance of generation unit with the required GFM units for LC_5-LC_9 under 24% import loss, rated power, (2/2)

For LC_6, the required percentage of GFM units increases by 20% compared to LC_5 at below-rated power to ensure post-islanding stability. However, when operating

at rated power, since LC_5 already requires 100% GFM units, no further increase is possible for LC_6. The results for LC_6 with 100% GFM units are also shown in Figure 5.14 (2/2). Observing the test results indicates that the RoCoF exceeds the -2 Hz/s limit, voltage is severely violated, and frequency rises to 52 Hz within seconds after islanding, leading to a test failure. Additionally, instability is observed approximately 4.6 s after islanding, resulting in growing oscillations throughout the island and making the entire test scenario unstable. Due to these issues, the results are not further displayed in Figure 5.14 (2/2).

Assessing the performance of LC_7 and LC_8 reveals that both maintain stable operation in the below-rated power scenario with GFM shares of 90% and 100%, respectively. The increase in PE-load share from LC_7 to LC_8 necessitates a 20% increase in GFM units to achieve stability by adjusting the time constant. Similarly, the maximum GFM share (100%) was tested in both scenarios under rated-power conditions. However, stable operation could not be achieved in either case. As the PE-load share increases within the load class, the level of instability in the test scenario also rises. This instability is attributed to the high dynamics introduced by both the generation and consumer sides in the islanded system, stemming from the lack of sufficient balancing torque within the network.

In LC_9, similar to LC_{10}, stable operation could not be achieved after islanding. Regardless of the operating point of the GFM units, the presence of 90% PE-loads on the consumer side prevented a smooth transition to islanding in either scenario, even with 100% GFM units. As shown in Figure 5.14 (2/2), instability occurs more quickly during rated-power operation compared to below-rated power.

Figure 5.13 shows an almost parallel trend between the two graphs, indicating a 50% increase in the required share of GFM units when operating at rated-power. This highlights the sensitivity of system strength studies to the operational state of the generation fleet prior to islanding. The significant variability underscores the importance of considering this factor in studies, as the required GFM share for system stabilization under similar events is highly dependent on the generation fleet's operating point.

Islanding with 24% Export Loss at Rated Power

This chapter investigates the performance of generation units, including wind turbines operating at their nominal power, under islanding and a 24% export loss. Additionally, it compares the required proportion of GFM units in the network with the results presented in Chapter 5.2.1. It is expected in scenario involving a downstream power offset, the discrepancy in performance between below-rated and rated power should not be as significant as observed during import conditions. Furthermore, it is anticipated that due to enhanced inertia emulation at full load, the required proportion of GFM unit at rated power would be equivalent to or lower than that at below-rated power. However, the simulation results shown in Figure 5.15 do not fully validate this expectation.

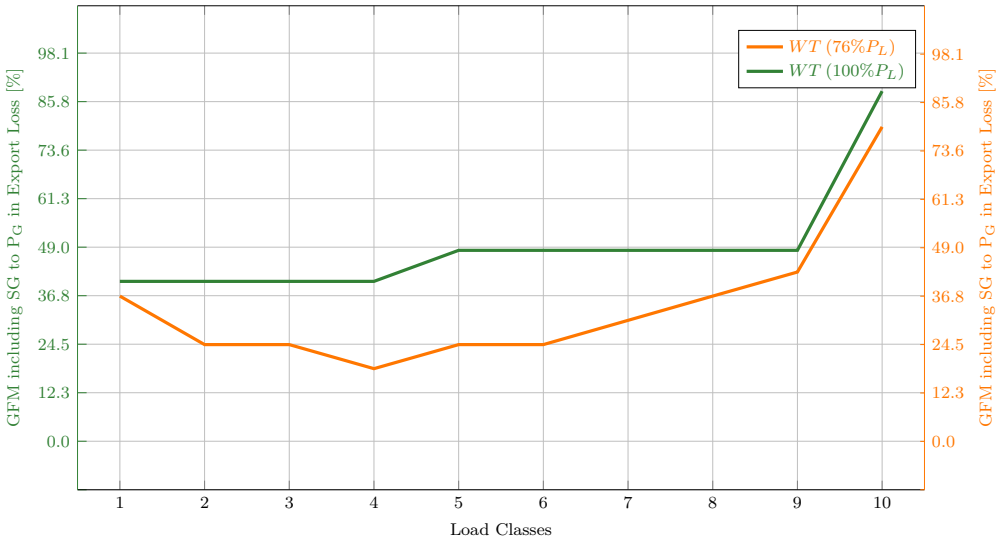

Figure 5.15: Comparing the required GFM units in 24% export loss in all ten load classes in below-rated power versus rated power

As observed in the results presented in Figure 5.15, a higher percentage of GFM is required across all load classes when generation units operate at rated power. In addition, it is observed that, for load classes LC_1- LC_9, a 49% share of GFM units including SG ensures stable operation regardless of whether the units are operating at rated power or below-rated power. In the following, the key highlights and observations from the test results are listed:

- In nearly all load classes, voltage disturbances are more pronounced when operating at rated power compared to below-rated power.
- In some cases, the failure is attributed to voltage collapse and reactive power limitations, particularly for SG operating at rated power. In contrast, at below-rated power, the primary reasons for test failures with specific time constants were violations of RoCoF boundaries or overall test instability.
- Operation at rated power enhances inertia and LFSM-O performance by decoupling power reduction from speed of the generator-turbine unit.
- At rated power, the pitch controller of the GFM-WT unit responds immediately after the onset of an event to regulate speed, whereas in below-rated power operation, its response is delayed by several seconds.

Based on the observations in Figure 5.15, specific test cases, including LC_1, LC_4, LC_8, LC_9, and LC_{10}, are selected for comparison. Figure 5.16 compares the performance of these load classes under two scenarios. In the scenario where generation operates below-rated power, the lower percentage of GFM units (lower time constant in the network) resulted in a high initial RoCoF following islanding and the subsequent power surplus in the network. It was observed from the simulation results that for LC_1-LC_9, GFM percentages lower than those depicted in the Figure 5.15 led to initial RoCoF values exceeding the 2 $\mathrm{Hz\,s^{-1}}$ threshold.

As previously noted, at rated power, the initial RoCoF is the primary cause of test failures. However, a secondary effect is also observed in the voltage profile at rated power. Reducing the share of GFM units below the levels in Figure 5.15 during rated power operation increases the impact of the SG on the voltage stability of the island. Operating at rated power, SG contributes to inertia provision immediately after the onset of the islanding event. As frequency rises, all three generation units begin curtailing power to counteract the frequency increase. However, the LFSM-O functionality in SGs restricts rapid changes in active power, causing the power output to adjust very slowly from its initial level. This slow adjustment imposes constraints on the SG's ability to support network voltage, as the apparent power limitation prevents the SG from providing additional inductive reactive power [122].

This limitation is reflected in the voltage profile (see LC_4 in Figure 5.16 (2/2)), and subsequently impacts the frequency and RoCoF measurements.

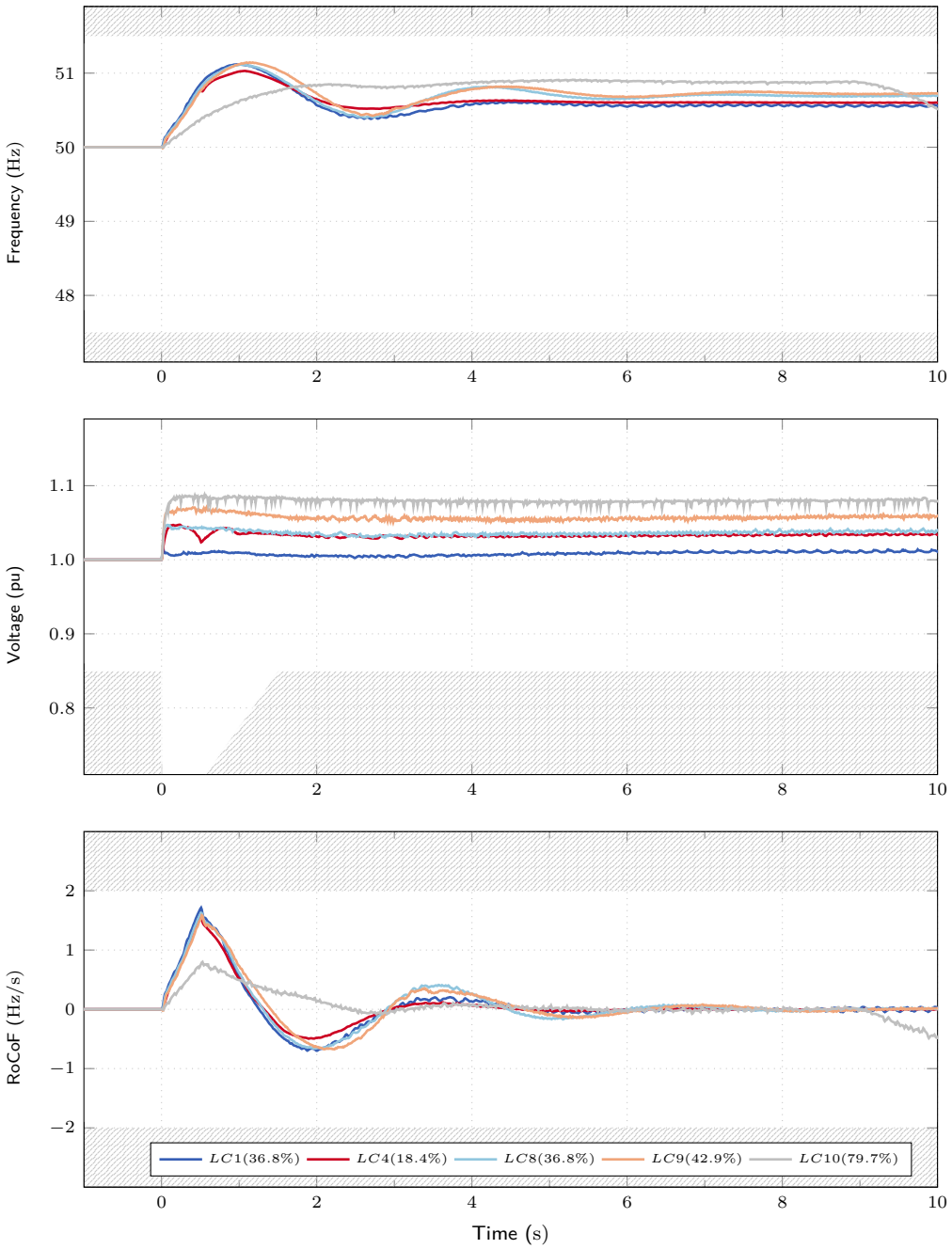

Figure 5.16: Comparing performance of generation unit with the required GFM units in selected load classes under 24% export loss, below-rated power, (1/2)

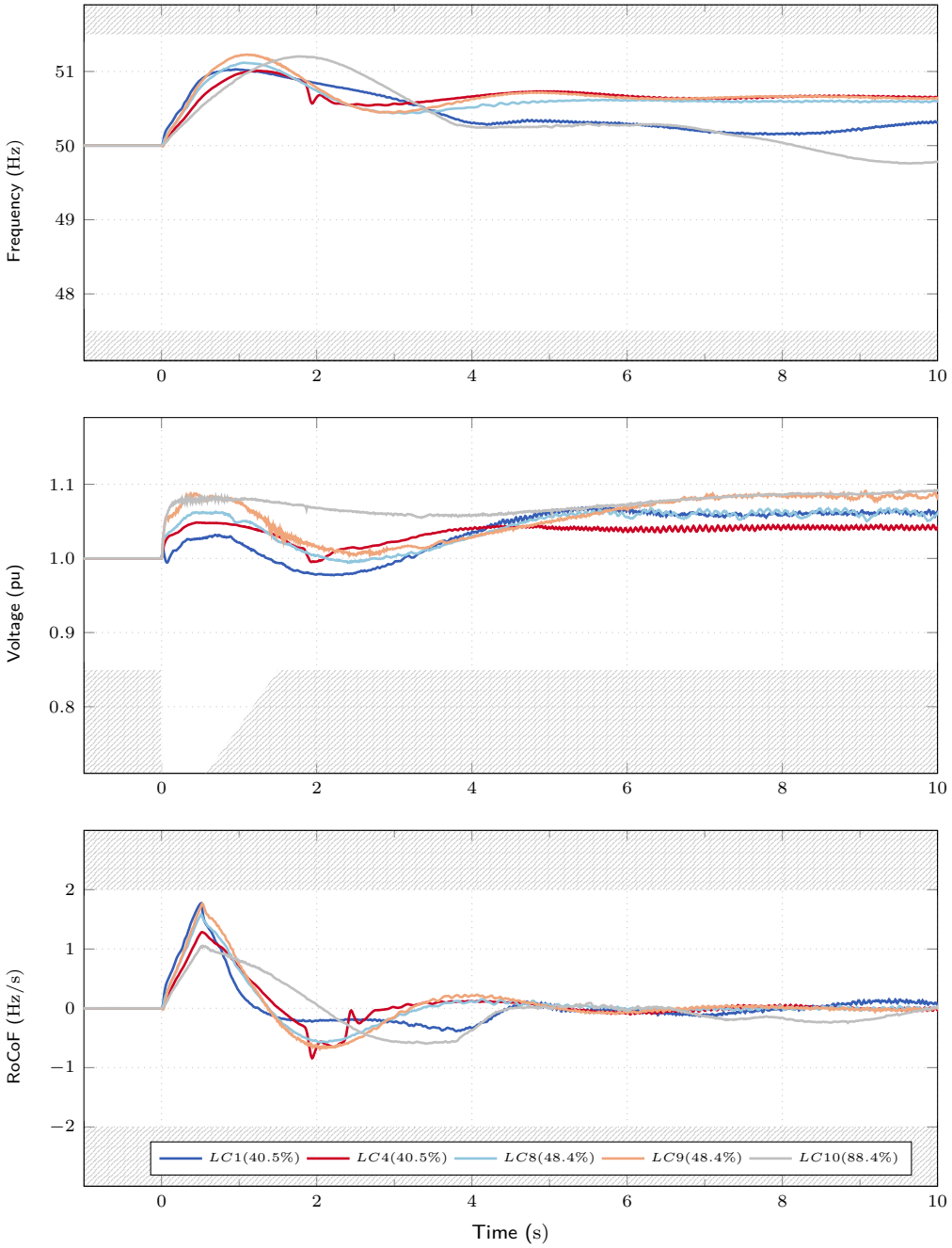

Figure 5.16: Comparing performance of generation unit with the required GFM units in selected load classes under 24% export loss, rated power, (2/2)

The voltage dip observed between 1-4 s across most load classes results in simultaneous changes in network frequency, resulting in a high RoCoF that, in some cases,

exceeds permissible limits when using the same GFM share as in the below-rated power scenario. This issue does not arise in GFM-WT units due to their much faster over-frequency active power reduction, which allows for higher voltage support. Additionally, such performance is not observed during below-rated operation, where sufficient headroom to the rated power enables generation units to maintain voltage stability within the island.

Figure 5.15 shows that the widest gap between the graphs occurs around LC_4-LC_6. Figure 5.17 illustrates the power factor of the load in each load class, showing a clear correlation between load classes with lowest power factors (LC_4-LC_6) and an increased need for a higher share of GFM units at rated power. The higher reactive power demand in LC_4-LC_6 compared to LC_1,LC_9 and LC_{10} makes the voltage more susceptible to instability, particularly when the generation units are operating at rated power and are limited in their ability to support voltage.

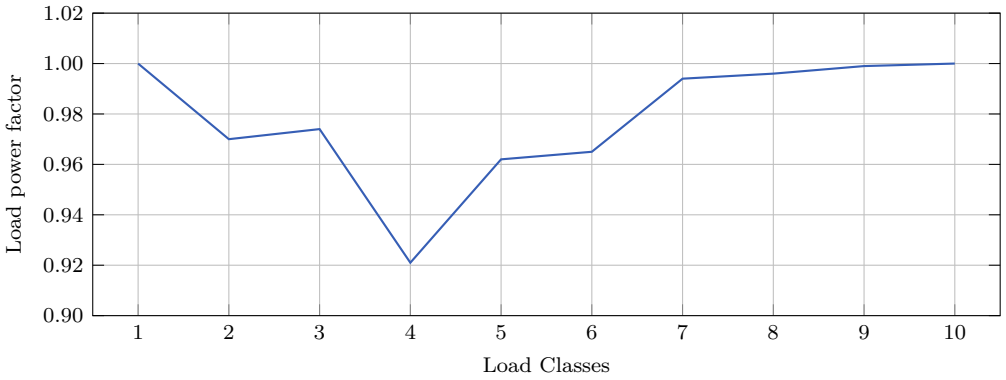

Figure 5.17: Load power factor in each load class

In addition, in LC_{10}, it is observed that the required share of GFM units including SG, is 88.4% at rated power, which is approximately 10% higher the value needed to manage a 24% power surplus under below-rated power operation. For LC_{10}, using GFM percentages below 79.7% at below-rated power and 88.4% at rated power led to instability following islanding. This instability arises from the rapid dynamics of converters on both the generation and consumer sides after islanding, resulting from the lack of balancing torque within the system, and primarily results in voltage collapse. These fast dynamics are mitigated, enabling a stable transition

to islanding, when 79.7% and 88.4% of the generation fleet consist of GFM units at below-rated and rated power, respectively. The smoother RoCoF and frequency rise observed in both scenarios (see Figure 5.16), are attributed to theses high shares of GFM units.

The trend line highlights several critical factors in assessing the required system strength for the power system. These include the need to account for generation-side limitations, the operational state of the units prior to the event, their physical constraints in supporting the grid, and, importantly, the use of more detailed load data for accurate analysis.

5.4 Required System Strength for Induction Machine Startup

5.4.1 Need for Studying Induction Machine Inrush Current

When a portion of the power system becomes isolated from the rest of the network, the system strength-including inertia and short-circuit level significantly decreases, relying primarily on the remaining on-site generation within the island. Under these conditions, the equivalent AC network as seen by the GFM unit may be very weak (SCR < 1) with low inertia. Consequently, any disturbance during islanding can endanger system stability and pose a high risk of disconnecting power system components due to protective measures [123]. Following such disturbances, the GFM unit plays a crucial role in regulating voltage and frequency within its operational capability limits [13].

In Chapter 5.2, the required time constant for the system to achieve a smooth transition to islanding is discussed. In the following analysis, it is assumed that a smooth transition to islanding occurs without any power imbalances prior to the event. Then the test scenario involves studying the impact of disturbances, such as inrush currents from induction machines, on the stability of the island. The objective is to determine the required system strength or equivalently, the necessary level of GFM units to manage such disturbances in the network.

Among common disturbances, the startup of a large induction motor relative to the total load in the island is frequently highlighted in the literature [124] [125]. According to [124], the startup of a large motor or a group of medium-sized motors starting simultaneously should be carefully studied, particularly in weak grids. The inrush current from these motors can cause significant disruptions in both voltage and frequency, affecting the primary motor bus as well as adjacent buses.

The primary factors contributing to voltage violations during motor startup are the motor's inrush current, the impedance between the grid and the motor bus, the short-circuit capacity of the isolated power system, and the presence of other loads near the motor bus [39]. Hence, this chapter performs various simulations to assess whether the power system strength achieved in Chapter 5.2, is sufficient to

handle such disturbances without exceeding protection relay thresholds or risking potential blackouts.

5.4.2 Initializing Simulation Scenarios

The two-node grid which is shown in Figure 5.18 is used here to study motor startup across different load classes. The information about the minimum system time constant is derived from the maximum value observed in each load class with ±24% import and export loss (see Chapter 5.2). Since LC_9 & LC_{10} showed instability even with $T_N = 10$ s, particularly under import loss, the maximum value of 10 s is selected for these specific load classes. All generation units in these test scenarios are operating under partial load conditions, at 76% of their rated power, similar to test scenarios in Chapter 5.2.

The startup of a large induction motor draws a significant amount of reactive current instantaneously. This directly relates to the strength of the isolated power system, which is affected by variations in the share of GFM units across different scenarios. To evaluate the sufficiency of the values obtained in Chapter 5.2, they can be used as initial parameters in these test scenarios. The goal is to determine the GFM share that provides sufficient system strength to withstand significant voltage violations.

The extent to which an IM startup affects the power system mainly depends on the size of the IM and the strength of the power system. Other factors contributing to voltage violations during startup include how quickly the excitation systems in the on-site generation respond, the loading of the machine, and the load characteristics of the neighboring buses. According to [124], if the isolated power system has a generation unit, the startup study should include motors in the range of 10-15% of the generation rating. It also mentions that under weak grid conditions, smaller motors should be studied as well. Hence, in Table 5.1, three motors are selected for IM startup study.

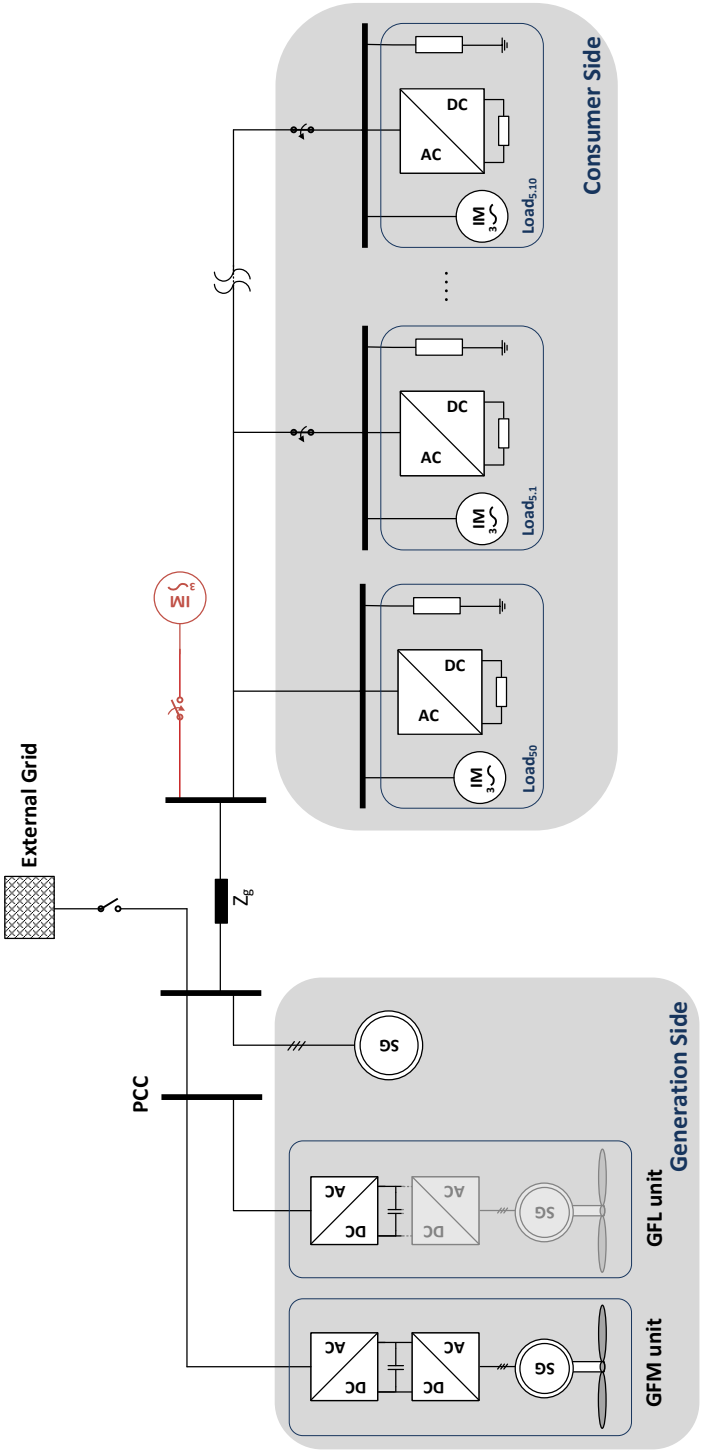

Figure 5.18: The two-node grid used to study motor startup

Table 5.1: Utilized induction motor parameters

Motor Name	$\mathbf{R_s}$(pu)	$\mathbf{X_s}$(pu)	$\mathbf{R_r}$(pu)	$\mathbf{X_r}$(pu)	H(s)	Rated Power
$\mathbf{M_1}$	0.0258	0.0413	0.0145	0.0424	1.5	5.0% S_G
$\mathbf{M_2}$	0.0258	0.0413	0.0145	0.0424	1.5	7.5% S_G
$\mathbf{M_3}$	0.0258	0.0413	0.0145	0.0424	1.5	10.0% S_G

5.4.3 Scenario I: Evaluation of System Strength Sufficiency

In the first scenario, a strong grid is connected to the network as shown in Figure 5.18 but does not transfer active power with the loads. An additional controller ensures $I_g = 0$ A before islanding occurs. The IM startup tests occurs after the connection to the external grid is lost and a stable island where voltage and frequency remain at nominal values is formed. Three IMs with different power ratings, as listed in Table 5.1, are tested. At $t = 0$ s, the induction machine begins accelerating without compensation for the startup procedure. Scenario I evaluates whether the GFM-WT unit can manage such disturbances in the island while operating with the maximum time constant obtained for the network (see Chapter 5.4.2). Simulation results for each load class are shown in Figure 5.19.

The gray area in Figure 5.19 represents the test cases and load classes where even with 100% GFM units in the network, stable operation cannot be achieved without violating one or more stability criteria. These cases are labeled as "FAIL" in Figure 5.19. The red area corresponds to scenarios with time constant levels exceeding 10 s. For test cases with $T_N = 10$ s, the proportion of GFM units relative to the total generation is higher than 76% (right axis in Figure 5.19). In contrast, this time constant in the scenario involving 24% import loss (see Chapter 5.2.1), is achieved only when 100% of the RENs are GFM.

Figure 5.19 illustrates that with the maximum time constant for each load class, as determined in Chapter 5.2.1, only the startup of M_1 (rated at 5% of the total generation) is manageable. For LC_1-LC_8, the M_1 startup does not violate frequency, voltage, or RoCoF boundaries. However, for LC_9 and LC_{10}, with $T_N = 10$ s, stable operation could not be maintained after the inrush current from M_1. For the other

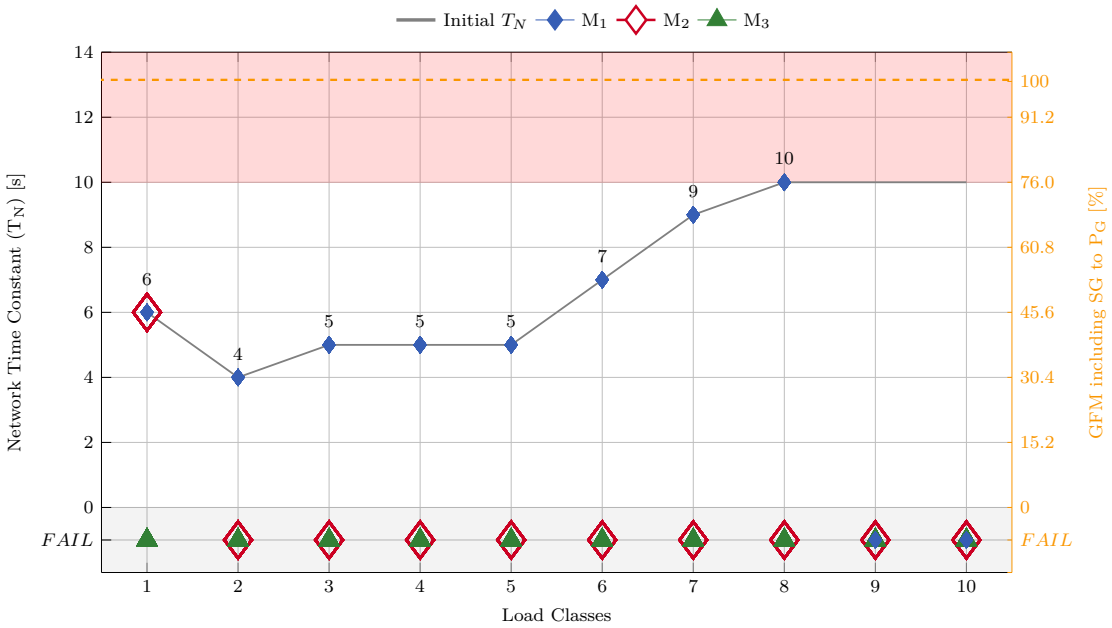

Figure 5.19: Evaluation of the network with the minimum strength from chapter 5.2 facing inrush current from three IMs

two IMs, M_2 and M_3, stable operation was not achieved, except for M_2 in LC_1. The key highlights of the simulation results are discussed below:

- **Are the considered time constants sufficient to handle the startup of all three sizes of IMs during islanding?**

  The results in Figure 5.19 indicate that only LC_1-LC_8 can successfully handle startup of M_1. In load classes with a higher share of PE on the consumer side (LC_5-LC_8), the simulation results show higher voltage violations following IM startup. However, these voltage deviations are compensated by the increased share of GFM units in those load classes to maintain stable operation after M_1 startup. Figure 5.20 illustrates the performance of LC_1 under different IM startups. The selected time constant of $T_N = 6$ requires approximately 40% generation from GFM units. Following the startup, a voltage deviation occurs, leading to a frequency rise into the over-frequency region due to the adjacent resistive loads near the motor bus. This over-frequency condition is effectively managed by the FSM and LFSM-O functionalities of the generation units.

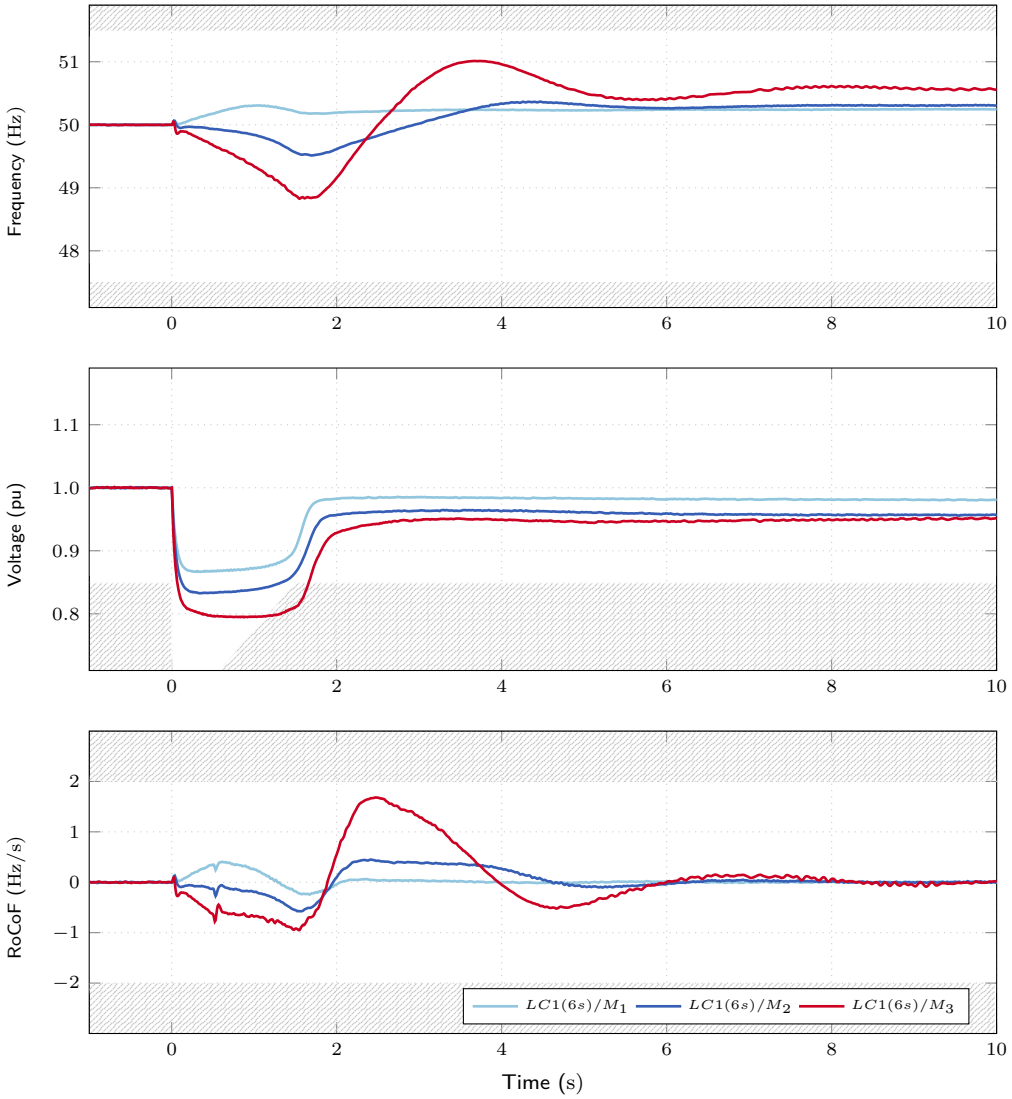

Figure 5.20: Comparing performance of LC_1 in a grid time constant of $T_N = 6s$ facing inrush current of M_1, M_2 and M_3

With M_2 ($S_{M2} = 7.5\% S_G$), all load classes except for the LC_1 violate the stable operation boundary with the initial inertia constant. Similar to the test with M_1, LC_1 demonstrates the best performance under grid voltage violations. As shown in Figure 5.20, the voltage drops below 0.85 pu but recovers before the generation units require disconnection from the network. During this time, the frequency deviation remains small between 0 and 0.5

s. Subsequently, as M_2 accelerates and the machine's slip and power factor changes, the frequency drops at a higher rate but recovers within the LFSM-O range without necessitating load shedding, as shown in Figure 5.20.

With the startup of a relatively large IM (M_3), the higher inertia of the motor results in a longer period to establish steady-state operation. During this time, the sources must sustain the motor's reactive power demand for an extended duration. Consequently, none of the tested load classes, including LC_1, achieve stable operation after M_3 startup. The results for M_3 startup with LC_1 are shown and compared with other motors in Figure 5.20.

Due to the higher rated power of M_3, the voltage experiences a significant transient drop and fails to recover above 0.85 pu within the FRT timeframe. Additionally, the RoCoF is higher in the M_3 startup scenario compared to M_2 and M_1. The results indicate a notable frequency peak in the over-frequency region for M_3 (51 Hz), significantly higher than in the M_2 scenario (50.35 Hz). For LC_2-LC_8, the voltage and frequency drop significantly almost immediately after the startup of M_3. Within 500 ms of startup, the voltage falls below 60% of the nominal value, and the frequency drops to 47.5 Hz. These results indicate that the generation units, in this configuration, are unable to sustain a stable operating point and meet the reactive power demand of M_3 during startup.

- **How do LC_9 and LC_{10} perform during the startup of the three IMs?**

  Load Classes 9 and 10 exhibit instability during operation for distinct reasons. In LC_9, the system transitions smoothly to islanding. However, after IMs startup, all three stability criteria including voltage, RoCoF, and frequency deviate from their permissible ranges. As a result, LC_9 is represented for all three IMs in the non-fulfilled region at the bottom of Figure 5.19.

  For LC_{10}, after disconnecting from the external grid and transitioning to islanding, the system collapses after a few seconds, failing to achieve a stable operating point. A similar issue was observed in Chapter 5.2.1, where a stable transition to islanding and voltage stability could not be maintained with an

time constant of $T_N = 10$ s under a 24% import loss. In this scenario, despite the absence of power imbalance following grid loss, LC_{10} still fails to achieve a stable transition to islanding with a $T_N = 10$ s. This instability might be attributed to the reduced short-circuit level, as 100% of the consumers are PE-based, which can lead to control instability for GFM units (see Chapter 3.2.5).

- **Why is LC_1 the only load class capable of safely managing the disturbance related to the M_2 startup?**

  Figure 5.21 compares the results for LC_1 with LC_3-LC_6 in the M_2 startup scenario. For LC_1 and LC_3, which are dominated by resistive load components, it is observed that both maintain voltage stability during the motor startup interval. Regarding frequency stability, although the frequency in LC_3 reaches the edge of the allowed band, both LC_1 and LC_3 stay within the boundaries. As explained in previous chapters, a key difference is that LC_3 (residential area) contains a mix of load components and characteristics, whereas LC_1 has primarily voltage-dependent power consumption. Therefore, after a significant voltage disruption after onset of the event, the power imbalance is higher in LC_3 compared to LC_1. This significantly affects the initial RoCoF. As shown in Figure 5.21, in LC_3, the RoCoF reaches -2 Hz s^{-1}, leading to the failure of the test case with M_2 startup.

  Figure 5.21 illustrates the performance of the industrial (LC_4) and LC_5, showing a system collapse within 500 ms after motor startup. It is observed that in both LC_4 and LC_5, the voltage drops significantly, and the frequency falls to 47.5 Hz within 1 s. In both load sectors, the majority of the load is composed of IMs. After M_2 startup, the motor draws high reactive current, initially causing a voltage deviation. Subsequently, the IMs in adjacent buses, influenced by changes in network voltage and frequency, begin to adjust their operating points and consume more reactive power. This leads to a voltage collapse, causing the entire test scenario to fail and highlighting the sensitivity of voltage dynamics, especially in feeders dominated by induction motors, such as industrial feeders, to such disturbances.

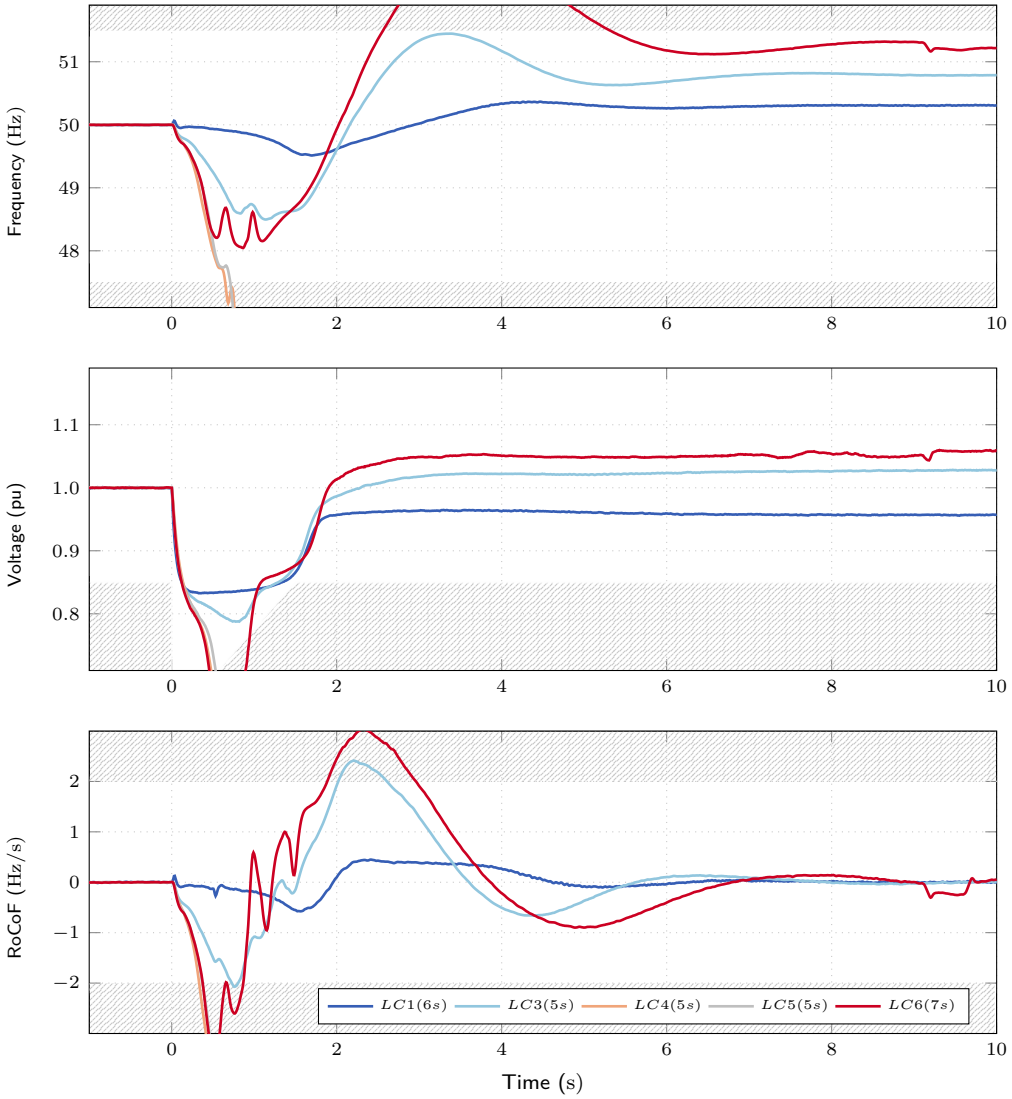

Figure 5.21: Comparing performance of LC_1 versus LC_3-LC_6 facing inrush current of M_2 (7.5% S_G)

The test scenario for the startup of M_2 with LC_6 is set up with a network time constant of $T_N = 7$ s. After M_2 startup, the voltage in LC_6 drops below 0.7 pu but is restored within 1.5 s, adhering to FRT specifications (see Chapter 4.3.2). As it is shown in Figure 5.21, the frequency with LC_6 initially drops, and after some load shedding steps (dropping 50% of the total load), it rises into the over-frequency region, reaching above 51.5 Hz at around 2.5 s. Beyond this

value, generation units can get disconnected from the network according to grid codes (see Chapter 4.3.2). Disconnection of the units becomes more likely when the RoCoF exceeds -2.5 Hz/s. Although the LC_6 test scenario does not meet the stability criteria, it does not exhibit the same collapse observed in the LC_4. There are two main reasons for this: first, the percentage of IMs in LC_6 is lower than in LC_4, which positively influences voltage stability; second, the initial time constant in LC_6 is $T_N = 7$ s which is higher compared to LC_4 with $T_N = 5$ s.

Therefore, based on the test results with M_2, it is observed that the startup of an IM with a rated power of ($S_{M2} = 7.5\% S_G$) is too significant to be handled by the system strength level acquired in Chapter 5.2.1. The only successful test case is the pure resistive load (LC_1), which demonstrates a completely voltage-dependent behavior, unlike the other load sectors in a real power system.

5.4.4 Scenario II: Reevaluating System Strength Needs

As in the previous case, Scenario II involves the disconnection from the strong grid prior to the induction motor startups. However, in this scenario, the required time constants for each load class, as tested in Chapter 5.4.3, are varied to handle the inrush disturbances from the three motors. The results of Scenario II are presented in Figure 5.22. For each IM and load class, the inertia is incrementally increased in steps of 1 s to determine the percentage of GFL units that must be replaced with GFM to manage the motor startup disturbances for each specific induction machine.

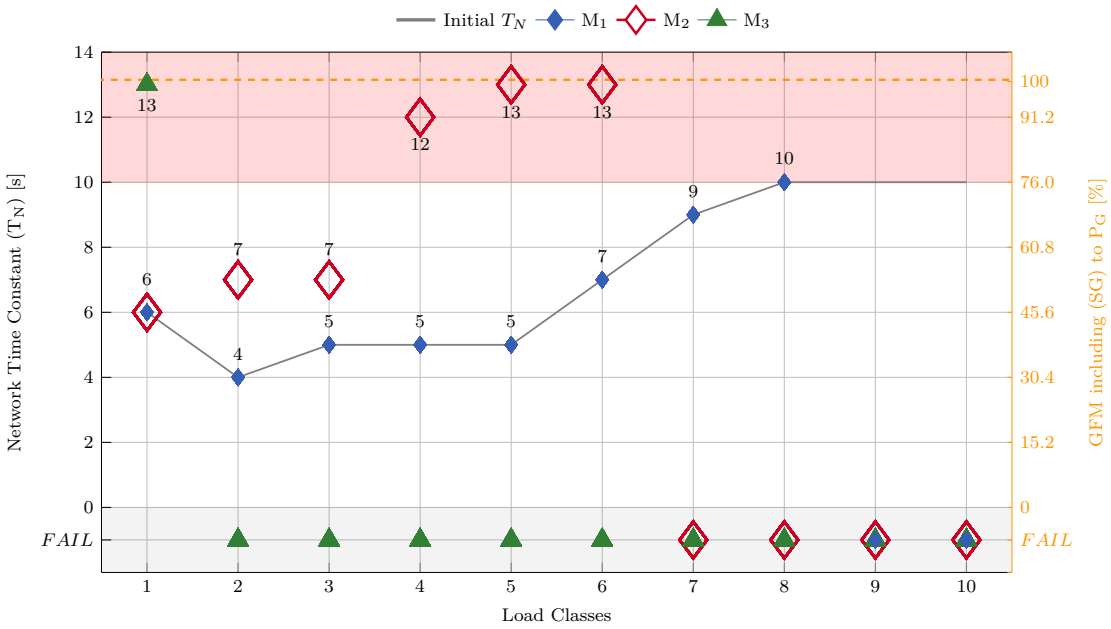

Figure 5.22: Comparing minimum required network inertia (percentage of GFM units) for an stable operation after facing inrush current from three IMs

The test results shown in Figure 5.22 reveal that only LC_1 can handle the startup of all three IMs. Additionally, it is shown that LC_1 can manage the inrush currents from both M_1 and M_2 while maintaining the same network time constant. However, for M_3, a significant increase of 7 s in the time constant (equivalent to 55% increase in GFM units) is required. Conversely, LC_9 and LC_{10} are unable to manage the

disturbances from any of the three IMs. The key findings from the test cases are discussed below:

- **What percentage increase in GFM units is required to manage the inrush currents of the three different IM?**

  The simulation results are presented in Figure 5.22. For the smallest motor (M_1), all load classes, except LC_9 and LC_{10}, manage the disturbance without violating stability criteria. However, the initial time constant levels appear to be optimistic for some load classes in this scenario. The results show that the voltage in all load classes remains above the FRT threshold, frequency stays within the permissible band, and RoCoF remains below the disconnection threshold. For LC_9 and LC_{10}, even with a 10 s time constant (equivalent to 76% GFM units in the actual scenario), the test fails. Further increasing the GFM share to 100% in these load classes, as illustrated in Figure 5.22, does not restore stable operation in these predominantly PE-based consumer classes. This is due to the characteristics of PE loads, as discussed in Chapter 5.4.3.

  The results for M_2 startup in Figure 5.22 reveals that, except for LC_1, all other load classes fail to maintain stability with the initial time constant level. By increasing the share of GFM units, LC_2 and LC_3 achieve stable operation when 53% of the total generation is replaced with GFM units ($\Delta T_N = 3$ s). For load classes LC_4, LC_5, and LC_6, a significant gap exists between their required time constant levels and the initial values. Simulation results indicate that the high share of IMs in LC_4 and the increased proportion of PE loads in LC_5 and LC_6 contribute to the substantial GFM requirement (see summary of ten load classes in Figure 4.3).

  In LC_4, a time constant of 12 s is necessary (equivalent to 91% GFM unit of the total generation) to manage M_2 startup. For LC_5 and LC_6, this value increases to 13 s, corresponding to nearly 100% GFM replacement. From consumer side prespective, another contributing factor to this large gap is the decrease in the percentage of resistive loads from LC_3 to LC_6. Resistive loads exhibit a grid-friendly characteristic by reducing active power consumption

during voltage disruptions, aiding system restoration during IM startup. As this percentage diminishes from LC_4 to LC_6, voltage and frequency recovery increasingly depend on the participation of generation fleet, specifically GFM units.

Beyond LC_6, none of the remaining load classes were able to handle the startup of M_2, even with the maximum time constant of ($T_N = 13$ s), which corresponds to 100% GFM of the total generation in this scenario. As illustrated in Figure 5.22, the trends for M_1 and M_2 begin to diverge starting from LC_2 and LC_3. This discrepancy arises because the initial testing points for M_1, derived from the test cases in Chapter 5.2.1, were optimistic for LC_1 to LC_3. The lower time constant values from these initial tests were insufficient to maintain stable operation under a ±24% generation loss scenario, and thus, lower values are not further tested.

Lastly, as shown in Figure 5.22, the initial time constant values for all load classes failed to have sufficient system support during M_3 startup. Increasing the time constant by raising the share of GFM units to 100% only allowed the scenario with purely resistive loads (LC_1) to handle this disturbance. However, since a purely resistive grid is not a realistic representation of a power system with diverse consumer sectors, it is concluded that even with 100% GFM units, the startup of such a large motor cannot be managed in this isolated power system.

- **What distinguishes the performance of LC_1 compared to the other load classes during M_3 startup?**

  For the startup of M_3, the only passing test with an inertia time constant of 13 s (equivalent to 100% GFM to the total generation) is LC_1, whose performance is compared with residential, industrial, tertiary, and mixed sectors in Figure 5.23. The simulation results indicate that, with a purely resistive grid, the severe voltage violation and following that, the voltage-dependent active power reduction, helps the system to handle the inrush of M_3 while keeping all stability criteria within limits. Table 5.2 compares the performance of LC_1 with LC_3-LC_6 regarding stability criteria.

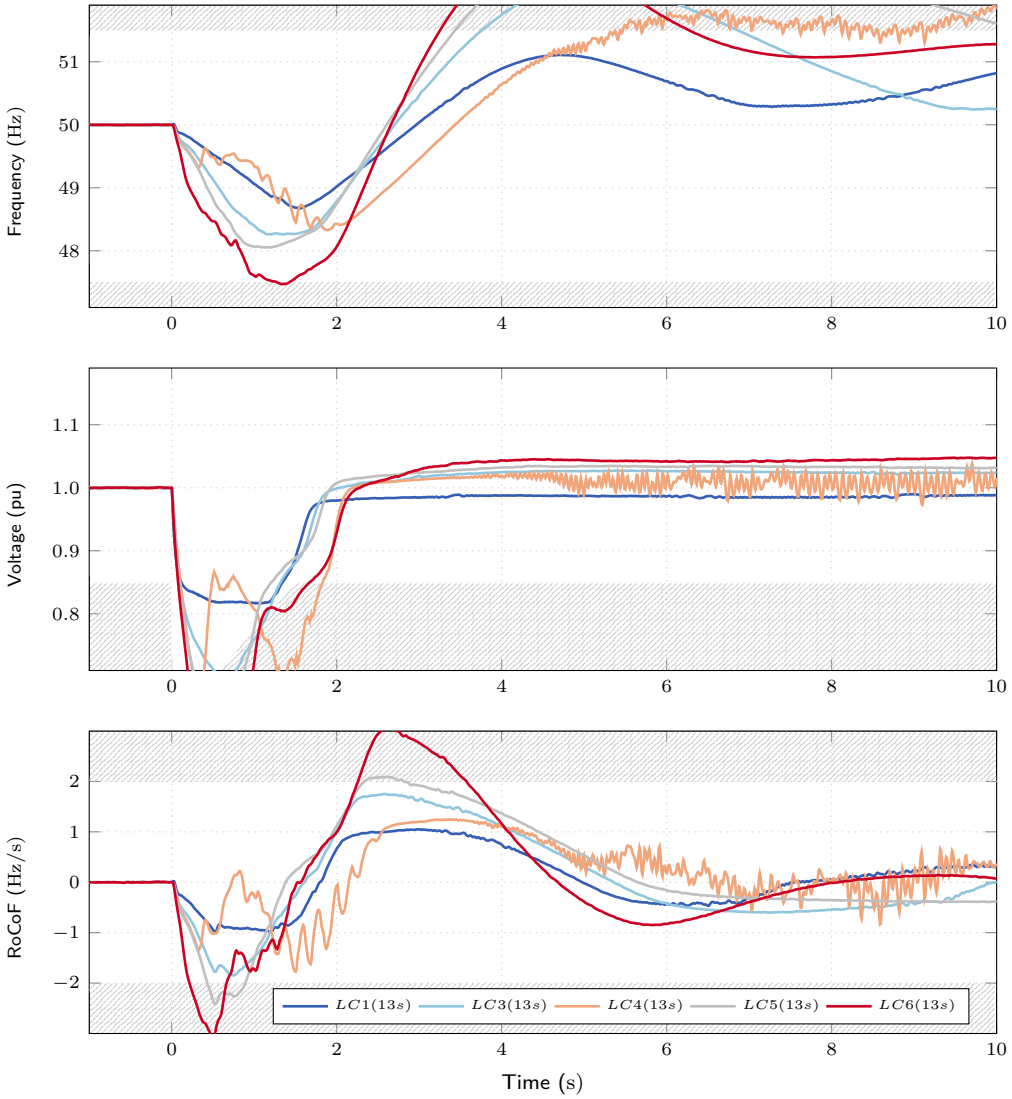

Figure 5.23: Comparison of LC_1 and LC_3-LC_6 performance under the inrush current of M_3 (10% S_G)

The test result for the residential area (LC_3) is also shown in Figure 5.23. As seen, the RoCoF magnitude increases to nearly -2 Hz/s, and a voltage violation at the load bus does not significantly affect the motor consumption, under QT loading (see Chapter 4.2.5). As a result, the system experiences a higher power imbalance compared to LC_1, leading to a greater frequency deviation and a steeper RoCoF. This high RoCoF triggers eight steps of load

shedding (twice as many as in LC_1), occurring by 1.6 s after the onset of the event. Consequently, due to over-production, the frequency rises above 51.5 Hz before the system defense mechanisms can respond.

In the industrial area (LC_4), the initial voltage deviation is significantly larger compared to LC_1 and LC_3. However, within 500 ms, the voltage begins to recover. This phase coincides with the motor (M_3) accelerating, as the peak demand for reactive current transitions to a higher active current demand. During this time, as the power factor of M_3 increases, the network frequency drops, causing other neighboring motors to decelerate. This results in a reduction in slip and, eventually, a decrease in the power factor of these motors (see Chapter 4.2.5). As a consequence, the reactive power demand rises again, which causes the voltage at the load bus to fall below 0.63 pu, leading to the test failing due to voltage violation.

In the mixed load sector (LC_5), the voltage initially drops following the onset of the event, as depicted in Figure 5.23. The initial RoCoF reaches -2.3 Hz/s, and the frequency drops to approximately 48 Hz, triggering ten load-shedding steps. During the subsequent phase, as M_3 accelerates and its power factor improves, the voltage recovers within the allowable FRT band of the generation units. However, with 50% of the island's load disconnected, the frequency rises to 53 Hz, resulting in test failure for LC_5 due to violations of both frequency and RoCoF limits.

The results for the tertiary sector (LC_6) with 100% GFM units reveal that voltage violations is significantly more severe compared to all other sectors, as illustrated in Figure 5.23. In LC_6, the voltage drops to a minimum of 0.48 pu and fails to recover into the FRT continuous operation range. This voltage level risks causing the disconnection of generation units [52]. Additionally, within 500 ms after the onset of the event, the measured RoCoF exceeds -3 Hz/s. Such a steep RoCoF would activate protection mechanisms not only for conventional units but also for RENs, which are unable to manage the resulting high torque gradients and the associated mechanical stress on their turbines. Consequently, under the startup of M_3, the loss of generation in

LC_6 becomes inevitable.

As illustrated in Figure 5.23, the frequency rises beyond 51.5 Hz approximately 3.2 seconds after the event onset, following the disconnection of 50% of the total load in the network. Since the simulation does not include the disconnection of generation units due to protection device activation, the frequency continues to rise beyond this point, exceeding 53 Hz, which is outside the permissible band. The violation of all three stability criteria, along with the loss of a significant portion or potentially all of the loads and generation, significantly increases the likelihood of the system transitioning from an emergency state to a complete blackout.

Table 5.2: Comparison of LC_1 against LC_3-LC_6 under M_3 inrush with 100% GFM units

Load Sector	Grid Forming (%)	Frequency Boundary	Voltage Boundary	RoCoF
LC_1	100%	✓	✓	✓
LC_3	100%	✗	✓	✓
LC_4	100%	✓	✗	✓
LC_5	100%	✗	✓	✗
LC_6	100%	✗	✗	✗

5.5 Summary

This chapter has investigated the minimum required GFM units necessary to maintain stability under various load classes within an exemplary power system. The focus of the islanding study includes the following aspects:

- Analyzing the required time constant for different power imbalances following islanding events, according to ENTSO-E recommended incident
- Evaluating the influence of pre-event operating conditions of GFM units on system performance

- Assessing the impact of wind turbine control in GFM units and aerodynamic behavior on stability of the island
- Investigating the necessity of studying motor inrush currents and their effects during islanding scenarios

The key contributions of Chapter 5 are summarized in the following:

In Chapter 5.2.1, the required network time constant, maintained through increasing the share of GFM-WT units is investigated to stabilize grid voltage and frequency following islanding and a subsequent generation loss of ±24%. In both scenarios, the WTs operate below their rated wind speed, at approximately 76% of their rated power. The results has demonstrated how varying the share of GFM units helps establish the stability threshold for each load sector. This investigation has built on the findings from Chapter 4.4, where certain load classes failed to meet stability criteria with the specified time constant. The analysis has highlighted the variation in results across different load sectors under ±24% power loss. The required time constant is shown to be asymmetrical between import and export cases, attributed to the operational limitations of GFM units and the characteristic of PE loads.

In Chapter 5.2.2, the focus has shifted to investigating the required time constant based on the ENTSO-E standard for system strength studies during the transition to 100% inverter-dominant systems. A power imbalance of ±40% is analyzed following the loss of the main AC grid. The results has highlighted the influence of GFM unit control design on power system stability, particularly during a 40% export loss. Increasing the time constant beyond a certain percentage of GFM units leads to violations of the frequency boundary. The primary cause of these oscillations was identified as the interference between the LFSM-O controller and the dynamics of the WT controller. Two boundaries were observed in the case of a 40% export loss; the lower boundary corresponds to the required time constant for each load class, while the upper boundary is determined by the GFM unit. The test results for a 40% import loss has shown that islanding of this magnitude is unmanageable in many load classes, including LC_1, even when 100% of the generation is composed of GFM units. The results emphasized the influence of load characteristics, particularly during incidents with high imbalance. It was observed

that the resistive load (LC_1) does not provide meaningful insight into the required time constant in the system, with its performance inversely affected by increasing time constant.

In Chapter 5.3, the impact of the operation point of RENs prior to the islanding event on the required time constant is investigated and compared with the findings from the Chapter 5.2.1. A similar scenario with a ±24% power loss is conducted, but in this case, the WTs operate at their nominal wind speed. The investigation aimed to highlight the effect of limited headroom from converter hardware concerning over-current by comparing the results with those of the Chapter 5.2.1. The simulation results has shown that, to compensate for the converter limitations, the proportion of GFM units had to be significantly increased by approximately 50%. Additionally, it was observed that, even with the same power imbalance, 50% of the load classes could not maintain stable operation. For a 24% export loss, operating at rated power did not show a significant difference compared to the results from operating below rated power. In the worst case, it required an increase of approximately 24% in the percentage of GFM units to maintain stability in the network.

From the perspective of the GFM units, an enhanced inertia emulation was observed, operating at rated speed. An improvement in the RoCoF was noted after islanding compared to operation below-rated speed. However, voltage instability, which occurred during operation at rated speed, was identified as the primary reason for failure in this scenario.

The summary of the required percentage of GFM in relation to the total generation is presented in Figure 5.24. This figure displays the results from the six case studies discussed in Chapters 5.2.1 to 5.3, illustrating the overlapping region for the required GFM percentage to maintain stability in the power system across various load sectors. For each load class, the figure shows the percentage of GFM units necessary to stabilize the system under different disturbances. Figure 5.24 shows a wider overlapping area in most test scenarios, except for the cases with 24% import loss at rated power and 40% import loss, where the overlap is noticeably reduced. In these two scenarios, even 100% GFM is only sufficient to ensure stable operation in specific load classes.

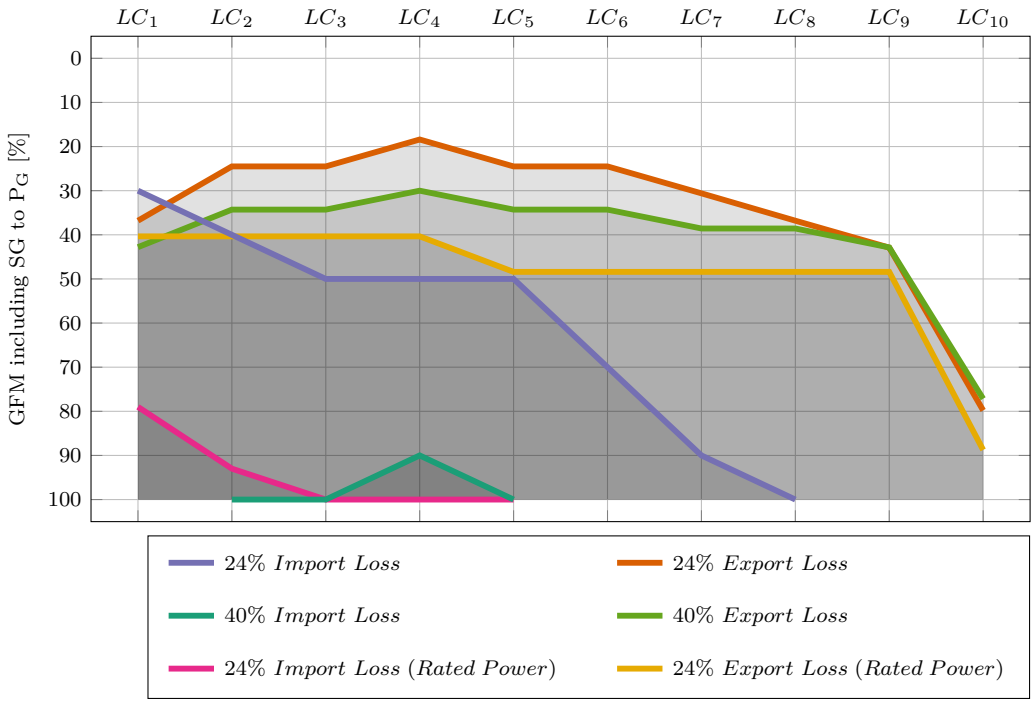

Figure 5.24: Trendline graph of minimum required GFM units based on load characteristics under various disturbances

Chapter 5.4 has focused on disturbances occur in a weak power system dominated by RENs. For these test cases, the time constants obtained in Chapter 5.2.1 are retained as the initial test conditions. The inrush current of IM of three different sizes is analyzed to evaluate system vulnerability in terms of strength and voltage stability, considering the initial percentage of GFM units.

It was observed that the initial time constant level was sufficient to maintain stability for motors rated at $5\%S_G$. However, larger motors require a reassessment of the GFM proportion to ensure system stability. It was observed that an increased share of GFM units enhances the system's ability to achieve stable operation and resilience against voltage disturbances. Some scenarios demonstrated stability when GFM was increased to 100% of the total generation. Additionally, it was noted that the characteristics of adjacent loads significantly influence the percentage of GFM required to manage similar disturbances. This variability in results ranged from 40% to 100% GFM.

6 SUMMARY

The main objective of this work has been to investigate power system stability following the islanding of an AC grid. A detailed study was conducted to establish requirements for the composition of the islanded grid, considering various types of consumer and generation. Particular attention was given to determining the necessary proportion of GFM units to manage the loss of a heavily loaded transmission line, especially when the local grid is dominated by power-electronic loads on the consumer side. For the islanding scenario, a two-node network was developed, incorporating emergency grid functions operating on timescales ranging from milliseconds to several seconds.

Chapter 2 of this thesis focused on identifying the control requirements necessary for RENs to replicate the performance of conventional synchronous generator units in power systems. A detailed investigation was conducted to establish these requirements, leading to the identification of key terminology and the definition of "Grid Forming" according to ENTSO-E standards. A comprehensive literature review in Chapter 2 evaluated recent publications on control concepts designed to stabilize AC grids. Chapter 2 subsequently provided a detailed overview of a conventional generation unit with a synchronous generator, its control mechanisms, and system-level functions, including LFSM-O. Additionally, a grid-following control for wind turbines was introduced, along with extensions to enhance their support for the AC grid. These generation unit models were employed in subsequent chapters to analyze islanding scenarios.

Chapter 3 introduced the modified-RVVC control, designed for application in wind turbine units categorized under grid-forming concepts. The design process focused on achieving the right balance of dynamics, stability, and robustness, while ensuring compliance with grid code requirements. A trade-off was made in selecting control

parameters to address conflicting performance expectations. The design procedure began with the selection of the inertia constant and virtual impedance parameters, followed by the use of the system's linear model to determine parameters for other controller parameters. For over-current protection, a voltage-based scheme was implemented through a nonlinear virtual impedance. The controller's performance was validated by testing the designed unit under various grid conditions, ranging from highly inductive to purely resistive networks with different grid short-circuit ratios. The designed modified-RVVC successfully maintained stability and adequate damping across these scenarios.

Following in Chapter 3, the full control architecture for the wind turbine was designed to utilize the turbine's rotating mass for providing instantaneous reserves in both directions. This included modifications to the MSC and DC-link controllers, enabling grid support while maintaining operational constraints. Additionally, the MPPT controller in the GSC was modified to minimize the negative impact of it on inertia emulation at below-rated speeds. The chapter concludes with the verification of the grid-forming functionality of the fully designed GFM-WT unit. A series of test cases based on the FNN scenarios demonstrated the performance, both at the unit level and in comparison with the generation units introduced in the previous chapter.

Chapter 4 focused on load dynamics in power systems and their influence on potential islanding scenarios. Accordingly, Chapter 4 introduced an aggregated load model, dividing it into various load sectors and components. For each sector, the load components and predominant load categories were identified based on existing literature. For each sector, the load components and predominant load categories were identified based on existing literature. The three main load categories, namely resistive loads, induction machines, and power electronic loads, were modeled to represent the primary consumers in each sector. Based on these load categories, ten load sectors were introduced in Chapter 4, including a base sector (fully resistive), residential, industrial, tertiary, and other configurations used as case studies to identify potential dynamics. The case studies accounted for variations in the proportion of induction machines relative to resistive components and migration toward higher share of power-electronic loads and their impact on the minimum

required system strength, which is further explored in the next chapter.

The following part of Chapter 4 presented the islanded network configuration, consisting of three generation units with system-level controls and the load buses equipped with load-shedding schemes. Stability criteria for islanding studies were also introduced, ensuring continuous operation of the units in compliance with grid codes. Subsequently, ten load classes have been tested in two case studies, each subjected to a ±24% power imbalance following a system split. The islanding results in Chapter 4 highlighted the differing performance of load sectors compared to the base load class (pure resistive) and demonstrated how load dynamics influence overall system performance following islanding with a similar power imbalance magnitude. The findings confirmed that pure resistive loads, as a simplified load representation in islanding studies, do not provide a realistic evaluation of the power system, neither from the perspective of consumer representation nor for assessing the performance of generation units. Chapter 4 also revealed increased voltage sensitivity in industrial areas, the impact of transitioning from load class one to ten on the RoCoF, and relieving the burden on the generation fleet due to voltage-based power reduction in residential feeders. Additionally, Chapter 4 confirmed the system's vulnerability arising from the limitations associated with PE loads during high power imbalances, particularly regarding the modulation index and current limitations.

Chapter 5 investigated the minimum required time constant via varying the share of GFM units for all load classes. Special focus has been given to the factors involved in determining the time constant, as well as the load characteristics. In the first step, the initial time constant from the previous chapter was used as the starting point. If the network's performance after islanding with a ±24% power imbalance in the specific load class was acceptable, the time constant was reduced in a step-wise manner. Conversely, if the network's time constant was insufficient, it was increased until the border for stable operation was achieved in each load sector. Since the time constant was increased by varying the percentage of the modified-RVVC based GFM unit, this chapter also addresses the question of how much the GFM percentage shall increase to ensure stable operation during significant disturbances following islanding. The disturbances studied included

a ±24% power imbalance with generation below rated/rated power and a ±40% power imbalance. The results confirmed that, in addition to the load dynamics in each sector, there was a significant dependency on the unit's operating point prior to the disturbance, the GFM control structure for the wind turbine (due to the interaction between the LFSM-O and the MPPT controller), and the magnitude of the imbalance. Furthermore, the findings showed that operating the GFM unit at rated wind speed still improved system stability after a generation imbalance in terms of system strength, though a higher share was required compared to operation at below-rated wind speed to manage a similar power imbalance. This led to a wide range of time constant values that cannot be summarized by a single value obtained only from considering the imbalance magnitude or the results of studies with the purely resistive load. Chapter 5 highlights a range of GFM penetration levels, identifying an overlap region where the system can withstand severe contingencies, such as the loss of a heavily loaded line carrying up to 40% of the network load. This overlap indicates the minimum GFM percentage required to maintain stability under all considered scenarios.

Further in Chapter 5, the system strength was analyzed in response to the inrush current from an induction machine in a stable islanded network with various load classes. The startup of three induction machines with different rated powers was tested, revealing that a reassessment of the GFM proportion is necessary to manage the inrush current of larger IMs. Additionally, it was observed that in some load classes, a GFM share of up to 100% is required, depending on the IM's rating. Furthermore, the results indicated that many cases failed, particularly with the largest size of the IM. The chapter also highlighted that the characteristics of adjacent loads significantly influence the required GFM percentage to handle similar disturbances, with the range varying from 40% to 100% GFM.

In summary, this thesis has demonstrated the necessity of replacing GFL with GFM-WT units to improve network strength. Additionally, it emphasized the importance of considering load dynamics and the provision of inertia from a finite available energy source in islanding scenarios. Therefore, this thesis achieved aforementioned objectives by:

- Conducting a thorough conceptual investigation to identify the main requirements for GFM control, which later in this thesis serves as a benchmark for evaluating the modified-RVVC control implemented in this work.
- Developing a comprehensive GFM scheme (modified-RVVC) by using a validated small-signal model to select the control parameters for the controllers in a GSC of WT.
- Developing a damping scheme to enhance control robustness across varying grid strengths; implementing an over-current scheme to maintain the voltage source characteristics of the unit.
- Adopting the control of a full Type 4 wind turbine with a full-scale converter to enable complete GFM functionality, provide bidirectional instantaneous support, and dynamic voltage support.
- Benchmarking the performance of the developed GFM unit against other generation units using FNN test cases.
- Conducting an in-depth investigation into load dynamics, the characteristics of each load sector, and the impact of the migration towards a higher share of power electronic loads on the islanding stability.
- Identifying multiple load classes to evaluate their performance relative to each other in a single islanding scenario with a similar generation fleet.
- A comprehensive investigation to determine the minimum system strength in the power system across various system split scenarios. Varying the share of the GFM unit to achieve stable operation in each load class.
- Assessing the adequacy of the system strength in response to the inrush current from a large motor during islanding.

The findings of this thesis demonstrated that the developed modified-RVVC based GFM-WT unit significantly enhanced grid stability, regardless of operation at below rated or rated power. The results highlighted that the dynamics of wind turbines influence the required system strength, with MPPT operation affecting the outcomes. This underscores the importance of modeling wind turbines in detail, rather than

assuming an infinite power source, to obtain more precise results. Furthermore, EMT simulations revealed the impact of control interactions and limitations on the stability of the islanded system and showed that constant impedance loads do not adequately represent island loads for inertia-related investigations. Therefore, it is concluded that understanding the nature and dynamics of loads allows for a more precise determination of the power system's strength in potential system split scenarios, thereby reducing the risk of system collapse during islanding events.

7 APPENDIX

7.1 Synchronous Generator Parameters

In the two-node network used for islanding studies, a synchronous generator is directly connected to the grid to represent a minimum 10% contribution of conventional generation to the total system generation. The generator's rating is scaled to conduct tests under varying network time constants and load conditions. However, the base model of the round-rotor synchronous generator in MATLAB/Simulink is initially configured for a 3.8 MVA unit. The generator parameters, expressed in standard per-unit values, are summarized in Table 7.1 [42], [126]:

Table 7.1: Synchronous generator parameters

Generator Parameters	Values
Rated Power (MVA)	3.8
Rated line to line voltage (kV-rms)	0.69
Pole pairs	2
Armature resistance (pu)	0.003
Unsaturated reactance X_d (pu)	1
Unsaturated transient reactance X'_d (pu)	0.25
Unsaturated transient time constant (open) T'_d (s)	3
Unsaturated sub-transient time constant (open) T''_d (s)	0.05
Unsaturated sub-transient reactance X''_d (pu)	0.2
Unsaturated reactance X_q (pu)	1
Unsaturated transient reactance X'_q (pu)	0.25
Unsaturated sub-transient reactance X''_q (pu)	0.2
Inertia constant H (s)	5

7.2 Dynamic Equations for Active and Reactive Powers

Figure 7.1 illustrates a three-phase voltage-source converter connected to the grid through an R-L circuit. Traditionally, power transfer between two voltage sources is described using quasi-stationary power-angle equations [127]. However, when a VSC is connected to the network, electromagnetic transients significantly influence control performance, necessitating more rigorous transfer functions. In this section, active and reactive power transfer functions are derived as a function of load angle and voltage magnitude, based on Kirchhoff's Voltage Law in the Laplace domain [127].

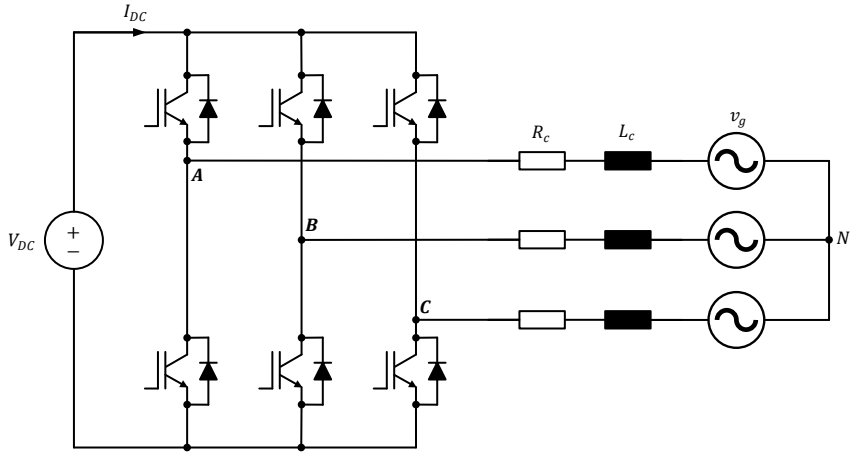

Figure 7.1: VSC connected to an AC system through R-L circuit

In a synchronous dq frame with the d-axis aligned with the AC source voltage ($V_{gd} = V_g$ and $V_{gq} = 0$), the dynamic equations of the main circuit in Figure 7.1 can be written as [30]:

$$\frac{L}{\omega_0}\frac{di_{gd}}{dt} = V_{cd} - V_{gd} - Ri_{gd} + \omega_g L i_{gq} \tag{7.1}$$

$$\frac{L}{\omega_0}\frac{di_{gq}}{dt} = V_{cq} - V_{gq} - Ri_{gq} - \omega_g L i_{gd} \tag{7.2}$$

$$V_{cd} = V_c \cos(\delta), \quad V_{cq} = V_c \sin(\delta) \tag{7.3}$$

In above equations $L = L_c$ and $R = R_c$. The nonlinear terms $V_c \cos(\delta)$ and $V_c \sin(\delta)$ are then linearized around the operating point δ_0 and substituted into 7.1 & 7.2 equations [30].

$$\frac{L}{\omega_0}\frac{d\Delta i_{gd}}{dt} = -V_{c0}\sin(\delta_0)\Delta\delta + \Delta V_c \cos(\delta_0) - R\Delta i_{gd} + \omega_g L \Delta i_{gq} \tag{7.4}$$

$$\frac{L}{\omega_0}\frac{d\Delta i_{gq}}{dt} = V_{c0}\cos(\delta_0)\Delta\delta + \Delta V_c \sin(\delta_0) - R\Delta i_{gq} - \omega_g L \Delta i_{gd} \tag{7.5}$$

Applying the Laplace transformation to equations 7.4 and 7.5 yields expressions for Δi_{gd} and Δi_{gq} as:

$$\Delta i_{gd} = \frac{-V_{c0}\sin(\delta_0)\Delta\delta + \Delta V_c \cos(\delta_0) + \omega_g L \Delta i_{gq}}{\frac{L}{\omega_0}s + R} \tag{7.6}$$

$$\Delta i_{gq} = \frac{V_{c0}\cos(\delta_0)\Delta\delta + \Delta V_c \sin(\delta_0) - \omega_g L \Delta i_{gd}}{\frac{L}{\omega_0}s + R} \tag{7.7}$$

Substituting equation 7.6 into 7.7 and equation 7.7 into 7.6 yields:

$$\begin{aligned}\Delta i_{gd} = &\frac{-V_{c0}\sin(\delta_0)\left(\frac{L}{\omega_0}s + R\right) + \omega_g L V_{c0}\cos(\delta_0)}{\left(\frac{L}{\omega_0}s + R\right)^2 + (\omega_g L)^2}\Delta\delta \\ &+ \frac{\omega_g L \sin(\delta_0) + \cos(\delta_0)\left(\frac{L}{\omega_0}s + R\right)}{\left(\frac{L}{\omega_0}s + R\right)^2 + (\omega_g L)^2}\Delta V_c\end{aligned} \tag{7.8}$$

$$\Delta i_{gq} = \frac{V_{c0}\cos(\delta_0)\left(\frac{L}{\omega_0}s + R\right) + V_{c0}\sin(\delta_0)\omega_g L}{\left(\frac{L}{\omega_0}s + R\right)^2 + (\omega_g L)^2}\Delta\delta - \frac{\cos(\delta_0)\omega_g L - \sin(\delta_0)\left(\frac{L}{\omega_0}s + R\right)}{\left(\frac{L}{\omega_0}s + R\right)^2 + (\omega_g L)^2}\Delta V_c \tag{7.9}$$

Equations 7.4, 7.5, 7.8, and 7.9 are also employed to compute the initial values of the grid currents and voltages:

$$I_{gd_0} = \frac{V_{c0}\sin(\delta_0)\omega_g L + RV_{c0}\cos(\delta_0) - RV_g}{R^2 + (\omega_g L)^2} \tag{7.10}$$

$$I_{gq_0} = \frac{-V_{c0}\cos(\delta_0)\omega_g L + RV_{c0}\sin(\delta_0) + V_g\omega_g L}{R^2 + (\omega_g L)^2} \tag{7.11}$$

$$V_{cd_0} = V_{c0}\cos(\delta_0) \tag{7.12}$$

$$V_{cq_0} = V_{c0}\sin(\delta_0) \tag{7.13}$$

$$\Delta V_{cd} = \frac{L}{\omega_0}\Delta i_{gd}s - \omega_g L\Delta i_{gq} + R\Delta i_{gd} \tag{7.14}$$

$$\Delta V_{cq} = \frac{L}{\omega_0}\Delta i_{gq}s + \omega_g L\Delta i_{gd} + R\Delta i_{gq} \tag{7.15}$$

$$\Delta V_{cd} = \frac{\left[\cos(\delta_0)\left(\frac{L}{\omega_0}\right)^2 s^2 + 2R\frac{L}{\omega_0}\cos(\delta_0)s + \cos(\delta_0)\left(R^2 + (\omega_g L)^2\right)\right]\Delta V_c}{\left(\frac{L}{\omega_0}s + R\right)^2 + (\omega_g L)^2} \tag{7.16}$$

$$\Delta V_{cq} = \frac{\left[\sin(\delta_0)\left(\frac{L}{\omega_0}\right)^2 s^2 + 2R\frac{L}{\omega_0}\sin(\delta_0)s + \sin(\delta_0)\left(R^2 + (\omega_g L)^2\right)\right]\Delta V_c}{\left(\frac{L}{\omega_0}s + R\right)^2 + (\omega_g L)^2} \tag{7.17}$$

The expressions for active and reactive power can then be written as follows:

$$\Delta P_{ac} = \Delta V_{cd} I_{gd_0} + \Delta V_{cq} I_{gq_0} + \Delta i_{gd} V_{cd_0} + \Delta i_{gq} V_{cq_0} \tag{7.18}$$

$$\Delta Q_{ac} = -\Delta V_{cd} I_{gq_0} + \Delta V_{cq} I_{gd_0} + \Delta i_{gd} V_{cq_0} - \Delta i_{gq} V_{cd_0} \tag{7.19}$$

To account for the influence of the transient virtual impedance (TVI) introduced in Chapter 3.2.5, the resistance and inductance in the above equations are replaced by:

$$\omega_g L = \left(X_c + X_v \cdot \frac{s}{s + \omega_{c,hpf}}\right) \tag{7.20}$$

$$R = \left(R_c + R_v \cdot \frac{s}{s + \omega_{c,hpf}}\right) \tag{7.21}$$

Considering these substitutions and based on equations 7.8, 7.9 and 7.10 - 7.17, the power matrix expression is derived as follows:

$$\begin{bmatrix} \Delta P_{ac} \\ \Delta Q_{ac} \end{bmatrix} = \begin{bmatrix} T_{p\delta} & T_{pV_c} \\ T_{q\delta} & T_{qV_c} \end{bmatrix} \begin{bmatrix} \Delta\delta \\ \Delta V_c \end{bmatrix} \tag{7.22}$$

$$\begin{cases} T_{p\delta} = \dfrac{a_1 s^4 + b_1 s^3 + c_1 s^2 + d_1 s + e_1}{g s^4 + h s^3 + j s^2 + k s + l}, \\ T_{pV_c} = \dfrac{a_2 s^4 + b_2 s^3 + c_2 s^2 + d_2 s + e_2}{g s^4 + h s^3 + j s^2 + k s + l}, \\ T_{q\delta} = \dfrac{a_3 s^4 + b_3 s^3 + c_3 s^2 + d_3 s + e_3}{g s^4 + h s^3 + j s^2 + k s + l}, \\ T_{qV_c} = \dfrac{a_4 s^4 + b_4 s^3 + c_4 s^2 + d_4 s + e_4}{g s^4 + h s^3 + j s^2 + k s + l}. \end{cases} \tag{7.23}$$

The denominator is similar in all four transfer functions which is expressed as follows:

$$\begin{aligned} g &= L_c^2 \\ h &= 2\omega_{c,hpf} L_c^2 + 2L_c R_c + 2L_c R_v \\ j &= (\omega_{c,hpf})^2 L_c^2 + 4\omega_{c,hpf} L_c R_c + 2\omega_{c,hpf} L_c R_v + R_c^2 + 2R_c R_v + R_v^2 + X_c^2 + 2X_c X_v + X_v^2 \\ k &= 2(\omega_{c,hpf})^2 L_c R_c + 2\omega_{c,hpf} R_c^2 + 2\omega_{c,hpf} R_c R_v + 2\omega_{c,hpf} X_c^2 + 2\omega_{c,hpf} X_c X_v \\ l &= (\omega_{c,hpf})^2 R_c^2 + (\omega_{c,hpf})^2 X_c^2 \end{aligned}$$

The numerators of the transfer functions primarily depend on the operating point of the converter. The expressions for the numerators of all four transfer functions are given below:

For $\mathbf{T_{p\delta}}$:

$$\begin{aligned} a_1 = {} & \cos(\delta_0)L_c^2X_cV_cV_g + \cos(\delta_0)L_c^2X_vV_cV_g + L_c^2R_c\sin(\delta_0)V_cV_g \\ & + L_c^2R_v\sin(\delta_0)V_cV_g - L_c^2V_cX_c - L_c^2V_cX_v \end{aligned}$$

$$\begin{aligned} b_1 = {} & 2\omega_{c,hpf}\cos(\delta_0)L_c^2X_cV_cV_g + \omega_{c,hpf}\cos(\delta_0)L_c^2X_vV_cV_g + 2\omega_{c,hpf}L_c^2R_c\sin(\delta_0)_cV_g \\ & + \omega_{c,hpf}L_c^2R_v\sin(\delta_0)V_cV_g - 2\omega_{c,hpf}L_c^2V_cX_c - \omega_{c,hpf}L_c^2V_cX_v - L_c\sin(\delta_0)V_cV_g \end{aligned}$$

$$\begin{aligned} c_1 = {} & \omega_{c,hpf}^2\cos(\delta_0)L_c^2X_cV_cV_g + \cos(\delta_0)X_cV_cV_g + \cos(\delta_0)X_vV_cV_g \\ & + \omega_{c,hpf}^2L_c^2R_c\sin(\delta_0)V_cV_g - \omega_{c,hpf}^2L_c^2V_cX_c - 2\omega_{c,hpf}L_c\sin(\delta_0)V_cV_g \\ & - R_c\sin(\delta_0)V_cV_g - R_v\sin(\delta_0)V_cV_g \end{aligned}$$

$$\begin{aligned} d_1 = {} & 2\omega_{c,hpf}\cos(\delta_0)X_cV_cV_g + \omega_{c,hpf}\cos(\delta_0)X_vV_cV_g - \omega_{c,hpf}^2L_c\sin(\delta_0)V_cV_g \\ & - 2\omega_{c,hpf}R_c\sin(\delta_0)V_cV_g - \omega_{c,hpf}R_v\sin(\delta_0)V_cV_g \end{aligned}$$

$$e_1 = \omega_{c,hpf}^2\cos(\delta_0)X_cV_cV_g - \omega_{c,hpf}^2R_c\sin(\delta_0)V_cV_g$$

For $\mathbf{T_{pV_c}}$:

$$\begin{aligned}
a_2 = &- \cos(\delta_0) L_c^2 R_c V_c V_g - \cos(\delta_0) L_c^2 R_v V_c V_g + L_c^2 R_c V_c + L_c^2 X_v V_c \\
&+ L_c^2 \sin(\delta_0) X_c V_c V_g + L_c^2 \sin(\delta_0) X_v V_c V_g
\end{aligned}$$

$$\begin{aligned}
b_2 = &-2\omega_{c,\mathrm{hpf}} \cos(\delta_0) L_c^2 R_c V_c V_g - \omega_{c,\mathrm{hpf}} \cos(\delta_0) L_c^2 R_v V_c V_g + \cos(\delta_0) L_c V_g \\
&+ 2\omega_{c,\mathrm{hpf}} L_c^2 R_c V_c + \omega_{c,\mathrm{hpf}} L_c^2 R_v V_c \\
&+ 2\omega_{c,\mathrm{hpf}} L_c^2 \sin(\delta_0) X_c V_c V_g + \omega_{c,\mathrm{hpf}} L_c^2 \sin(\delta_0) X_v V_c V_g
\end{aligned}$$

$$\begin{aligned}
c_2 = &-\omega_{c,\mathrm{hpf}}^2 \cos(\delta_0) L_c^2 R_c V_c V_g + 2\omega_{c,\mathrm{hpf}} \cos(\delta_0) L_c V_g + 2\cos(\delta_0) R_c V_g \\
&+ \omega_{c,\mathrm{hpf}}^2 L_c^2 R_c V_c + \omega_{c,\mathrm{hpf}}^2 L_c^2 \sin(\delta_0) X_c V_c V_g \\
&+ \sin(\delta_0) V_g X_c + \sin(\delta_0) V_g X_v
\end{aligned}$$

$$\begin{aligned}
d_2 = &\omega_{c,\mathrm{hpf}}^2 \cos(\delta_0) L_c V_g + 2\omega_{c,\mathrm{hpf}} \cos(\delta_0) R_c V_g + \omega_{c,\mathrm{hpf}} \cos(\delta_0) R_v V_g \\
&+ 2\omega_{c,\mathrm{hpf}} \sin(\delta_0) V_g X_c + \omega_{c,\mathrm{hpf}} \sin(\delta_0) V_g X_v
\end{aligned}$$

$$e_2 = \omega_{c,\mathrm{hpf}}^2 \cos(\delta_0) R_c V_g + \omega_{c,\mathrm{hpf}}^2 \sin(\delta_0) V_g X_c$$

For $\mathbf{T_{q\delta}}$:

$$\begin{aligned}
a_3 = &-\cos(\delta_0)L_c^2R_cV_cV_g - \cos(\delta_0)L_c^2R_vV_cV_g + L_c^2R_cV_cV_g + L_c^2R_vV_cV_g \\
&+ L_c^2\sin(\delta_0)X_cV_cV_g + L_c^2\sin(\delta_0)X_vV_cV_g
\end{aligned}$$

$$\begin{aligned}
b_3 = &-2\omega_{c,\mathrm{hpf}}\cos(\delta_0)L_c^2R_cV_cV_g - \omega_{c,\mathrm{hpf}}\cos(\delta_0)L_c^2R_vV_cV_g - \cos(\delta_0)L_cV_cV_g \\
&+ 2\omega_{c,\mathrm{hpf}}L_c^2R_cV_cV_g + \omega_{c,\mathrm{hpf}}L_c^2R_vV_cV_g \\
&+ 2\omega_{c,\mathrm{hpf}}L_c^2\sin(\delta_0)X_cV_cV_g + \omega_{c,\mathrm{hpf}}L_c^2\sin(\delta_0)X_vV_cV_g
\end{aligned}$$

$$\begin{aligned}
c_3 = &-\omega_{c,\mathrm{hpf}}^2\cos(\delta_0)L_c^2R_cV_cV_g - 2\omega_{c,\mathrm{hpf}}\cos(\delta_0)L_cV_cV_g - \cos(\delta_0)R_cV_cV_g \\
&- \cos(\delta_0)R_vV_cV_g + \omega_{c,\mathrm{hpf}}^2L_c^2R_cV_cV_g + \omega_{c,\mathrm{hpf}}^2L_c^2\sin(\delta_0)X_cV_cV_g \\
&- \sin(\delta_0)X_cV_cV_g - \sin(\delta_0)X_vV_cV_g
\end{aligned}$$

$$\begin{aligned}
d_3 = &-\omega_{c,\mathrm{hpf}}^2\cos(\delta_0)L_cV_cV_g - 2\omega_{c,\mathrm{hpf}}\cos(\delta_0)R_cV_cV_g - \omega_{c,\mathrm{hpf}}\cos(\delta_0)R_vV_cV_g \\
&- 2\omega_{c,\mathrm{hpf}}\sin(\delta_0)X_cV_cV_g - \omega_{c,\mathrm{hpf}}\sin(\delta_0)X_vV_cV_g
\end{aligned}$$

$$e_3 = -\omega_{c,\mathrm{hpf}}^2\cos(\delta_0)R_cV_cV_g - \omega_{c,\mathrm{hpf}}^2\sin(\delta_0)X_cV_cV_g$$

For $\mathbf{T_{qV_c}}$:

$$\begin{aligned} a_4 = &- \cos(\delta_0) L_c^2 V_g X_c - \cos(\delta_0) L_c^2 V_g X_v - L_c^2 R_c \sin(\delta_0) V_g + L_c^2 R_c V_c \\ &- L_c^2 R_v \sin(\delta_0) V_g + L_c^2 R_v V_c \end{aligned}$$

$$\begin{aligned} b_4 = &-2\omega_{c,\mathrm{hpf}} \cos(\delta_0) L_c^2 V_g X_c - \omega_{c,\mathrm{hpf}} \cos(\delta_0) L_c^2 V_g X_v - 2\omega_{c,\mathrm{hpf}} L_c^2 R_c \sin(\delta_0) V_g \\ &+ 2\omega_{c,\mathrm{hpf}} L_c^2 R_c V_c - \omega_{c,\mathrm{hpf}} L_c^2 R_v \sin(\delta_0) V_g + \omega_{c,\mathrm{hpf}} L_c^2 R_v V_c \\ &- L_c \sin(\delta_0) V_g \end{aligned}$$

$$\begin{aligned} c_4 = &-\omega_{c,\mathrm{hpf}}^2 \cos(\delta_0) L_c^2 V_g X_c + \cos(\delta_0) V_g X_c + \cos(\delta_0) V_g X_v \\ &- \omega_{c,\mathrm{hpf}}^2 L_c^2 R_c \sin(\delta_0) V_g + \omega_{c,\mathrm{hpf}}^2 L_c^2 R_c V_c - 2\omega_{c,\mathrm{hpf}} L_c \sin(\delta_0) V_g \\ &- R_c \sin(\delta_0) V_g - R_v \sin(\delta_0) V_g \end{aligned}$$

$$\begin{aligned} d_4 = &\, 2\omega_{c,\mathrm{hpf}} \cos(\delta_0) V_g X_c + \omega_{c,\mathrm{hpf}} \cos(\delta_0) V_g X_v - \omega_{c,\mathrm{hpf}}^2 L_c \sin(\delta_0) V_g \\ &- 2\omega_{c,\mathrm{hpf}} R_c \sin(\delta_0) V_g - \omega_{c,\mathrm{hpf}} R_v \sin(\delta_0) V_g \end{aligned}$$

$$e_4 = \omega_{c,\mathrm{hpf}}^2 \cos(\delta_0) V_g X_c - \omega_{c,\mathrm{hpf}}^2 R_c \sin(\delta_0) V_g$$

The above transfer functions are used for frequency-domain analysis and control design, which are shown and discussed in detail in Chapter 3.2.5.

7.3 Islanding Study Cases

This section provides a more detailed presentation of the study cases discussed in Chapter 5. The test scenarios are summarized in Table 7.2, indicating the post-islanding unbalance percentages and the corresponding WTG loading conditions under which islanding was initiated.

Table 7.2: Islanding test scenarios and descriptions

Scenario	Islanding condition	Test description
S1	24% import loss	WTGs operating in curtailed mode due to below-rated wind speed
S2	24% export loss	WTGs operating in curtailed mode due to below-rated wind speed
S3	40% import loss	WTGs operating in curtailed mode due to below-rated wind speed
S4	40% export loss	WTGs operating in curtailed mode due to below-rated wind speed
S5	24% import loss	WTGs operating at nominal power due to rated wind speed
S6	24% export loss	WTGs operating at nominal power due to rated wind speed

Test cases and Test Matrix for Scenario 1 (S1)

As the test cases are defined individually for each scenario, Table 7.3 provides a summary outlining the corresponding test cases. This includes each unit's contribution, the generation time constant (scaled according to total generation capacity), and the network time constant, which is defined in Chapter 4.3.1 (see Equation 4.4). According to Table 7.3, ten scenarios are considered for a 24% import loss (S1), with the network time constant varying from 1 to 10 seconds.

Table 7.3: Test configurations with varying generation and network time constant for S1

Test No.	GFM-WTG (%)	GFL-WTG (%)	SG (%)	Generation Time Constant T_G (s)	Network Time Constant T_N (s)
T1	0%	90%	10%	1	1
T2	10%	80%	10%	2	2
T3	20%	70%	10%	3	3
T4	30%	60%	10%	4	4
T5	40%	50%	10%	5	5
T6	50%	40%	10%	6	6
T7	60%	30%	10%	7	7
T8	70%	20%	10%	8	8
T9	80%	10%	10%	9	9
T10	90%	0%	10%	10	10

Table 7.4 presents the test matrix used for this scenario. The tests marked with an 'X' indicate which simulations were performed; however, they do not necessarily result in a successful islanding. No marking in the table indicates that, based on the test result from the previous step $(T_N - 1)$ or $(T_N + 1)$, no additional test was required.

Table 7.4: Overview of the test matrix for S1

Test No.	LC_1	LC_2	LC_3	LC_4	LC_5	LC_6	LC_7	LC_8	LC_9	LC_{10}
T1										
T2	X									
T3	X	X								
T4	X	X	X	X	X					
T5	X	X	X	X	X					
T6	X	X	X	X	X	X				
T7	X	X	X	X	X	X				
T8	X	X	X	X	X	X	X	X	X	X
T9							X	X	X	X
T10								X	X	X

Test Cases and Test Matrix for Scenario 2 (S2)

Table 7.5 provides a summary outlining the corresponding test cases for islanding scenario (S2). The symbol "—" in Table 7.5 indicates that the corresponding case is not meaningful. This is because the SG share is fixed across all test cases; therefore, this scenario is not applicable, as it would require changing the percentage of SG.

Table 7.5: Test configurations with varying generation and network time constant for S2

Test No.	GFM-WTG (%)	GFL-WTG (%)	SG (%)	Generation Time Constant T_G (s)	Network Time Constant T_N (s)
T11	—	—	—	—	—
T12	2.3%	87.7%	10.0%	1.2	2
T13	8.4%	81.6%	10.0%	1.8	3
T14	14.5%	75.5%	10.0%	2.5	4
T15	20.7%	69.3%	10.0%	3.1	5
T16	26.8%	63.2%	10.0%	3.7	6
T17	32.9%	57.1%	10.0%	4.3	7
T18	39.0%	51.0%	10.0%	4.9	8
T19	45.2%	44.8%	10.0%	5.5	9
T20	51.3%	38.7%	10.0%	6.1	10
T21	57.5%	32.5%	10.0%	6.8	11
T22	63.6%	26.4%	10.0%	7.4	12
T23	69.7%	20.3%	10.0%	8.0	13
T24	75.8%	14.2%	10.0%	8.6	14
T25	81.9%	8.1%	10.0%	9.2	15
T26	88.1%	1.9%	10.0%	9.8	16

Table 7.6: Overview of the test matrix for S2

Test No.	LC_1	LC_2	LC_3	LC_4	LC_5	LC_6	LC_7	LC_8	LC_9	LC_{10}
T11										
T12				X						
T13		X	X	X	X	X				
T14		X	X	X	X	X	X			
T15	X	X	X	X	X	X	X	X		
T16	X	X	X	X	X	X	X	X	X	
T17	X	X	X	X	X	X	X	X	X	
T18	X	X	X	X	X	X	X	X	X	X
T19								X	X	X
T20								X	X	X
T21										X
T22										X
T23										X
T24	X*	X*	X*	X*	X*	X*	X*	X*	X*	
T25	X*	X*	X*	X*	X*	X*	X*	X*	X*	X*
T26	X*	X*	X*	X*	X*	X*	X*	X*	X*	X*

Note: Cells marked with an asterisk (X*) are additional tests conducted to asses whether an upper boundary also emerges in this scenario.

Test Cases and Test Matrix for Scenario 3 (S3)

Table 7.7 provides a summary outlining the corresponding test cases for islanding scenario S3.

Table 7.7: Test configurations with varying generation and network time constant for S3

Test No.	GFM-WTG (%)	GFL-WTG (%)	SG (%)	Generation Time Constant T_G (s)	Network Time Constant T_N (s)
T27	0%	90.0%	10.0%	1	1
T28	10.0%	80.0%	10.0%	2	2
T29	20.0%	70.0%	10.0%	3	3
T30	30.0%	60.0%	10.0%	4	4
T31	40.0%	50.0%	10.0%	5	5
T32	50.0%	40.0%	10.0%	6	6
T33	60.0%	30.0%	10.0%	7	7
T34	70.0%	20.0%	10.0%	8	8
T35	80.0%	10.0%	10.0%	9	9
T36	90.0%	0%	10.0%	10	10

Table 7.8: Overview of the test matrix for S3

Test No.	LC_1	LC_2	LC_3	LC_4	LC_5	LC_6	LC_7	LC_8	LC_9	LC_{10}
T27										
T28										
T29										
T30										
T31										
T32										
T33										
T34	X	X	X	X	X	X	X	X	X	X
T35	X	X	X	X	X	X	X	X	X	X
T36	X	X	X		X	X	X	X	X	X

Test Cases and Test Matrix for Scenario 4 (S4)

Table 7.9 summarizes the corresponding test cases for islanding scenario S4.

Table 7.9: Test configurations with varying generation and network time constant for S4

Test No.	GFM-WTG (%)	GFL-WTG (%)	SG (%)	Generation Time Constant T_G (s)	Network Time Constant T_N (s)
T37	—	—	—	—	—
T38	—	—	—	—	—
T39	3.2%	86.8%	10.0%	1.3	3
T40	7.1%	82.9%	10.0%	1.7	4
T41	11.5%	78.5%	10.0%	2.1	5
T42	15.7%	74.3%	10.0%	2.6	6
T43	20.0%	70.0%	10.0%	3.0	7
T44	24.3%	65.7%	10.0%	3.4	8
T45	28.6%	61.4%	10.0%	3.9	9
T46	32.9%	57.1%	10.0%	4.3	10
T47	37.2%	52.8%	10.0%	4.7	11
T48	41.4%	48.6%	10.0%	5.1	12
T49	45.8%	44.2%	10.0%	5.6	13
T50	50.0%	40.0%	10.0%	6.0	14
T51	54.3%	35.7%	10.0%	6.4	15
T52	58.6%	31.4%	10.0%	6.9	16
T53	62.9%	27.1%	10.0%	7.3	17
T54	67.2%	22.8%	10.0%	7.7	18
T55	71.5%	18.5%	10.0%	8.1	19
T56	75.7%	14.3%	10.0%	8.6	20
T57	80.0%	10.0%	10.0%	9.0	21
T58	84.3%	5.7%	10.0%	9.4	22
T59	88.6%	1.4%	10.0%	9.9	23

Table 7.10: Overview of the test matrix for S4

Test No.	LC_1	LC_2	LC_3	LC_4	LC_5	LC_6	LC_7	LC_8	LC_9	LC_{10}
T37										
T38										
T39										
T40										
T41										
T42				X						
T43		X	X	X	X	X				
T44		X	X	X	X	X	X	X		
T45	X	X	X	X	X	X	X	X	X	
T46	X	X	X	**X**	X	X	X	X	X	
T47	X	X	X	X	X	X	X	X	X	
T48	X	X	X	X	X	X	X	X	X	
T49	X	X	X	X	X	X	X	X	X	
T50	X	X	X	X	X	X	X	X	X	
T51	X	X	X	X	X	X	X	X	X	
T52	X	X	X	X	X	X	X	X	X	
T53	X	X	X	X	X	X	X	X	X	X
T54	X	X	X	X	X	X	X	X	X	X
T55	X	X	X	X	X	X	X	X	X	X
T56	X	X	X	X	X	X	X	X	X	X
T57	X	X	X	X	X	X	X	X	X	X
T58	X	X	X	X	X	X	X	X	X	X
T59	X	X	X	X	X	X	X	X	X	X

Test Cases and Test Matrix for Scenario 5 (S5)

Table 7.11 provides a summary outlining the corresponding test cases for islanding scenario S5.

Table 7.11: Test configurations with varying generation and network time constant for S5

Test No.	GFM-WTG (%)	GFL-WTG (%)	SG (%)	Generation Time Constant T_G (s)	Network Time Constant T_N (s)
T60	3.3%	86.7%	10.0%	1.3	1.0
T61	16.4%	73.6%	10.0%	2.6	2.0
T62	29.6%	60.4%	10.0%	4.0	3.0
T63	42.7%	47.3%	10.0%	5.3	4.0
T64	55.8%	34.2%	10.0%	6.6	5.0
T65	68.9%	21.1%	10.0%	7.9	6.0
T66	82.1%	7.9%	10.0%	9.2	7.0
T67	90.0%	0%	10.0%	10.0	7.6

Table 7.12: Overview of the test matrix for S5

Test No.	LC_1	LC_2	LC_3	LC_4	LC_5	LC_6	LC_7	LC_8	LC_9	LC_{10}
T60										
T61										
T62	X									
T63	X	X								
T64	X	X	X	X	X					
T65	X	X	X	X	X					
T66		X	X	X	X	X	X	X	X	X
T67			X	X	X	X	X	X	X	X

Test Cases and Test Matrix for Scenario 6 (S6)

Table 7.13 provides a summary outlining the corresponding test cases for islanding scenario S6.

Table 7.13: Test configurations with varying generation and network time constant for S6

Test No.	GFM-WTG (%)	GFL-WTG (%)	SG (%)	Generation Time Constant T_G (s)	Network Time Constant T_N (s)
T68	—	—	—	—	—
T69	6.1%	83.9%	10.0%	1.6	2.0
T70	14.2%	75.8%	10.0%	2.4	3.0
T71	22.3%	67.7%	10.0%	3.2	4.0
T72	30.4%	59.6%	10.0%	4.0	5.0
T73	38.4%	51.6%	10.0%	4.8	6.0
T74	46.5%	43.5%	10.0%	5.6	7.0
T75	54.5%	35.5%	10.0%	6.5	8.0
T76	62.6%	27.4%	10.0%	7.3	9.0
T77	70.7%	19.3%	10.0%	8.1	10.0
T78	78.8%	11.2%	10.0%	9.9	11.0
T79	86.8%	3.2%	10.0%	9.7	12.0

Table 7.14: Overview of the test matrix for S6

Test No.	LC_1	LC_2	LC_3	LC_4	LC_5	LC_6	LC_7	LC_8	LC_9	LC_10
T68										
T69										
T70				X						
T71	X	X	X	X	X	X				
T72	X	X	X	X	X	X	X			
T73	X				X	X	X	X	X	
T74									X	
T75									X	
T76										
T77										X
T78										X
T79										X

BIBLIOGRAPHY

[1] *Technical requirements for the connection and operation of customer installations to the extra high voltage network (TCR extra high voltage) English translation of VDE-AR-N 4130*. Tech. rep. November. VDE-AR-N 4130, 2018.

[2] R. Musca and H. Just: "Damping-enhanced schemes and wide-synchronization control for grid-forming converters". In *22nd Wind and Solar Integration Workshop (WIW 2023)*. 2023.

[3] T. Sauer, N. Schulz, and B. Engel: "Control strategies of electrolyzers to contribute inertia and fast frequency reserve in context of a megawatt-scale hydrogen living-lab". In *22nd Wind and Solar Integration Workshop (WIW 2023)*. Copenhagen, Denmark: IET, 2023.

[4] M. Nuschke: "Frequenzstabilität im umrichterdominierten Verbundnetz". PhD thesis. Technischen Universität Braunschweig, 2022. ISBN: 9783839618035.

[5] *Bundesnetzagentur für Elektrizität, Gas, Telekommunikation, Post und Eisenbahnen, Hrsg. SMARD: Strommarktdaten. 2023*. URL: https://www.smard.de/home.

[6] M. Ndreko, S. Rüberg, and W. Winter: "Grid Forming Control for Stable Power Systems with up to 100 % Inverter Based Generation: A Paradigm Scenario Using the IEEE 118-Bus System". In *17th wind Integration workshop*. October. Stockholm, Sweden, 2018.

[7] K. Vennemann, T. Hennig, W. Winter, G. Deiml, J. Lehner, H. Abele, and J. Weidner: "Systemic Issues of Converter-based Generation and Transmission Equipment in Power Systems". In *17th Int'l Wind Integration Workshop*. October. Stockholm, Sweden, 2018.

[8] ENTSO-E: *High Penetration of Power Electronic Interfaced Power Sources and the Potential Contribution of Grid Forming Converters*. Tech. rep. Brussels, Belgium: ENTSO-E, 2020. URL: https://euagenda.eu/upload/publications/untitled-292051-ea.pdf.

[9] J. Z. Zhou, H. Ding, S. Fan, Y. Zhang, and A. M. Gole: "Impact of short-circuit ratio and phase-locked-loop parameters on the small-signal behavior? of a VSC-HVDC converter". In *IEEE Transactions on Power Delivery* 5 (2014), pp. 2287–2296. ISSN: 08858977. DOI: 10.1109/TPWRD.2014.2330518.

[10] T. Breithaupt, D. Herwig, L. H. A. Mertens, and R. Meyer: *Report on systemic issues*. Tech. rep. 2016. URL: www.h2020-migrate.eu.

[11] T. Ackermann, T. Prevost, V. Vittal, A. J. Roscoe, J. Matevosyan, and N. Miller: "Paving the Way: A Future Without Inertia Is Closer Than You Think". In *IEEE Power and Energy Magazine* 6 (2017), pp. 61–69. ISSN: 1540-7977. DOI: 10.1109/MPE.2017.2729138. URL: http://ieeexplore.ieee.org/document/8070502/.

[12] NEP: *Bewertung der Systemstabilität Netzentwicklungsplan Strom 2037 mit Ausblick 2045, Version 2023, zweiter Entwurf*. Tech. rep. URL: https://www.netzentwicklungsplan.de/sites/default/files/2023-09/NEP%7B%5C_%7D2037%7B%5C_%7D2045%7B%5C_%7DV2023%7B%5C_%7D2%7B%5C_%7DEntwurf%7B%5C_%7DSystemstabilitaet.pdf.

[13] D. Howard and S. Achilles: "Design Considerations and Test Results of a Grid-Forming Dual-Fed WTG". In *21st Wind & Solar Integration Workshop*. The Hague, Netherlands, 2022.

[14] P. Tielens, P. Henneaux, and S. Cole: *Penetration of renewables and reduction of synchronous inertia in the European power system—Analysis and solutions*. Tech. rep. 2018. URL: https://asset-ec.eu/.

[15] S. Gierschner, N. Fazli, and H.-G. Eckel: "Contribution of Converter-fed Loads to Grid Frequency Control in Islanding Scenarios". In *2020 IEEE 11th International Symposium on Power Electronics for Distributed Generation Systems (PEDG)*. 2020, pp. 403–408. DOI: 10.1109/PEDG48541.2020.9244370.

[16] R. Chishiki, H. Haga, K. Arimatsu, and Y. Ito: "Potential for New Energy Management by Variable Distribution Voltage Based on Electricity Consumption within Consumers". In *2023 25th European Conference on Power Electronics and Applications (EPE'23 ECCE Europe)*. Aalborg, Denmark, 2023, pp. 1–8. ISBN: 9789075815412. DOI: 10.23919/EPE23ECCEEurope58414.2023.10264417.

[17] T. Rump, H.-g. Eckel, D. Duckwitz, and C. Glöckler: "Emergency Islanding Scenario with df/dt-based Inertia Emulation, different Load Types and additional

Load Control". In *16th Wind Integration Workshop*. Berlin, Germany, 2017, pp. 2–8.

[18] B. Saleh, M. Garmabad, T. Wohlfahrt, I. Paloja, and F. Turki: "A comparative study of different PLL techniques for synchronization of grid-connected converters under unbalanced and distorted grid conditions". In *2023 25th European Conference on Power Electronics and Applications (EPE'23 ECCE Europe)*. Aalborg, Denmark, 2023, pp. 1–10. ISBN: 9789075815412. DOI: 10.23919/EPE23ECCEEurope58414.2023.10264598.

[19] ENTSO-E: *Inertia and Rate of Change of Frequency (RoCoF)*. Tech. rep. Brussels, Belgium, 2020. URL: https://eepublicdownloads.azureedge.net/clean-documents/SOC%20documents/Inertia%20and%20RoCoF%7B%5C_%7Dv17%7B%5C_%7Dclean.pdf.

[20] J. Rocabert, A. Luna, F. Blaabjerg, and P. Rodríguez: "Control of Power Converters in AC Microgrids". In *IEEE Transactions on Power Electronics* 11 (2012), pp. 4734–4749. DOI: 10.1109/TPEL.2012.2199334.

[21] B. Weise, A. Korai, and A. Constantin: "Comparison of Selected Grid-Forming Converter Control Strategies for Use in Power Electronic Dominated Power Systems". In *18th Int'l Wind Integration Workshop*. Dublin, Ireland, 2019.

[22] Ramasubramanian, D. and Zhang, Q. and Paz, B. and Wang, W. and Pabat-Stroe, R.: "Performance specification and evaluation criteria for grid forming simulation models". In *22nd Wind and Solar Integration Workshop (WIW 2023)*. Copenhagen, Denmark: IET, 2023.

[23] C. Heising, D. Meyer, T. Hennig, K. Vennemann, G. Deiml, W. Winter, and H. Wrede: "Need for Grid-Forming Converter-Control in Future System-Split Scenarios". In *18th Wind Integration Workshop*. Dublin, Ireland, 2019.

[24] T. Qoria, T. Prevost, G. Denis, F. Gruson, F. Colas, and X. Guillaud: "Power Converters Classification and Characterization in Power Transmission Systems". In *2019 21st European Conference on Power Electronics and Applications (EPE '19 ECCE Europe)*. Genova, 2019, pp. 1–9. DOI: 10.23919/EPE.2019.8914783.

[25] ENTSOE: "Performance Aspects of Grid Forming Converters". In *18th Wind Integration Workshop*. Dublin, Ireland: ENTSOE, 2019.

[26] D. Guillaume: "From grid-following to grid-forming: The new strategy to build 100 % power-electronics interfaced transmission system with enhanced transient behavior". In November 2017 (2018). URL: https://tel.archives-ouvertes.fr/tel-01905827.

[27] S. D'Arco and J. A. Suul: "Virtual synchronous machines—Classification of implementations and analysis of equivalence to droop controllers for microgrids". In *2013 IEEE Grenoble Conference*. Grenoble, France: IEEE, 2013, pp. 1–7. DOI: 10.1109/PTC.2013.6652456.

[28] E. Rokrok, T. Qoria, A. Bruyere, B. Francois, and X. Guillaud: "Transient Stability Assessment and Enhancement of Grid-Forming Converters Embedding Current Reference Saturation as Current Limiting Strategy". In *IEEE Transactions on Power Systems* 2 (2022), pp. 1519–1531. DOI: 10.1109/TPWRS.2021.3107959.

[29] Y. Chen, R. Hesse, D. Turschner, and H.-P. Beck: "Comparison of methods for implementing virtual synchronous machine on inverters". In *International Conference on Renewable Energies and Power Quality (ICREPQ'12)*. Santiago de Compostela, Spain, 2012. URL: https://doi.org/10.24084/repqj10.453.

[30] T. Qoria: "Grid-forming control to achieve a 100% power electronics interfaced power transmission systems". PhD thesis. HESAM Université, 2020. URL: https://pastel.archives-ouvertes.fr.

[31] A. W. Korai: "Dynamic Performance of Electrical Power Systems with High Penetration of Power Electronic Converters: Analysis and New Control Methods for Mitigation of Instability Threats and Restoration". PhD thesis. Universität Duisburg-Essen, 2019, p. 139.

[32] Daniel Duckwitz: "Power System Inertia Derivation of Requirements and Comparison of Inertia Emulation Methods for Converter-based Power Plants". PhD thesis. University of Kassel, 2019, p. 197. URL: https://doi.org/10.17170/kobra-20190510451.

[33] A. Tarraso, N.-b. Lai, G. N. Baltas, and P. Rodriguez: "Power Quality Services Provided by Virtually Synchronous FACTS". In 17 (2019), pp. 1996–1073. DOI: 10.3390/en12173292.

[34] W. Zhang: "Control of grid connected power converters with grid support functionalities". PhD thesis. Universitat Politècnica de Catalunya, 2017.

[35] M. Abdollahi, J. I. Candela, J. Rocabert, R. S. Munoz Aguilar, and J. R. Hermoso: "Synchronous power controller merits for dynamic stability improvement in long line by renewables". In *2016 IEEE International Conference on Renewable Energy Research and Applications (ICRERA)*. 2016, pp. 760–765. DOI: 10.1109/ICRERA.2016.7884438.

[36] Zhong, Qing-Chang and Nguyen, Phi-Long and Ma, Zhenyu and Sheng, Wanxing: "Self-Synchronized Synchronverters: Inverters Without a Dedicated Synchronization Unit". In *IEEE Transactions on Power Electronics* 2 (2014), pp. 617–630. DOI: 10.1109/TPEL.2013.2258684.

[37] N. Fazli, S. Gierschner, M. Gierschner, L. Cai, and H.-G. Eckel: "Rotating-Voltage-Vector Control for Wind Energy Plants Providing Possibility for Ancillary Services". In *2018 20th European Conference on Power Electronics and Applications (EPE'18 ECCE Europe)*. Riga, Latvia: IEEE, 2018, pp. 1–10.

[38] N. Fazli, S. Gierschner, H.-G. Eckel, and L. Cai: "Island Mode Operation of Rotating-Voltage-Vector Control for Wind Power Plants". In *2019 21st European Conference on Power Electronics and Applications (EPE '19 ECCE Europe)*. 2019, P.1–P.10. DOI: 10.23919/EPE.2019.8915556.

[39] N. Fazli, D. Hammes, S. Gierschner, and H.-G. Eckel: "Stability analysis in an inverter-dominant microgrid facing in-rush current of an induction machine". In *2022 24th European Conference on Power Electronics and Applications (EPE'22 ECCE Europe)*. 2022, pp. 1–11.

[40] M. Gilsenan, D. Mcmullin, and S. Engelken: "System Services By Wind Power Plants Supporting 75% Wind Penetration in Ireland". In *17th International Wind Integration Workshop*. October. Stockholm, Sweden, 2018.

[41] S. Dong, X. Fang, J. Tan, N. Gao, X. Cui, and A. Hoke: "A Unified Analytical Method to Quantify Three Types of Fast Frequency Response from Inverter-based Resources". In *22nd Wind & Solar Integration Workshop*. Copenhagen, Denmark, 2023.

[42] I. Boldea: *Synchronous Generators*. 2nd Editio. CRC Press Taylor & Francis Group, 2016, p. 498. ISBN: 9781315214184. DOI: https://doi.org/10.1201/b19310.

[43] "IEEE Recommended Practice for Excitation System Models for Power System Stability Studies". In *IEEE Std 421.5-2016 (Revision of IEEE Std 421.5-2005)* (2016), pp. 1–207. DOI: 10.1109/IEEESTD.2016.7553421.

[44] Prabha Kundur: *Power System Stability and Control*. 1st. Toronto, Canada: McGraw-Hill Education Ltd, 1994, p. 1200. ISBN: 007035958X.

[45] O. Homaee and S. Jadid: "Investigation of synchronous generator in reactive power market–an accurate view". In *IET Generation, Transmission & Distribution* 11 (2014), pp. 1881–1890. DOI: https://doi.org/10.1049/iet-gtd.2013.0901. eprint: https://ietresearch.onlinelibrary.wiley.com/doi/pdf/10.1049/iet-gtd.2013.0901. URL: https://ietresearch.onlinelibrary.wiley.com/doi/abs/10.1049/iet-gtd.2013.0901.

[46] J. Machowski, J. W. Bialek, and J. R. Bumby: *Power system dynamics and stability*. Chichester, New York: John Wiley & Sons Ltd, 1997. ISBN: 0 471 97174 X (PPC).

[47] ENTSO-E: *Frequency Sensitive Mode ENTSO-E guidance document for national implementation for network codes on grid connection*. Tech. rep. January. Brussels, Belgium: ENTSO-E, 2018. URL: https://eepublicdownloads.entsoe.eu/clean-documents/Network%20codes%20documents/NC%20RfG/IGD%7B%5C_%7DFSM%7B%5C_%7Dfinal.pdf.

[48] ENTSO-E: *P1–Policy 1: Load-Frequency Control and Performance [C]*. Tech. rep. Brussels, Belgium: ENTSO-E, 2009. URL: https://eepublicdownloads.entsoe.eu/clean-documents/pre2015/publications/ce/oh/Policy1%7B%5C_%7Dfinal.pdf.

[49] ENTSO-E: *Limited frequency sensitive mode ENTSO-E guidance document for national implementation for network codes on grid connection*. Tech. rep. January. 2018. URL: https://eepublicdownloads.entsoe.eu/clean-documents/Network%20codes%20documents/NC%20RfG/IGD%7B%5C_%7DLFSM-O-U%7B%5C_%7Dfinal.pdf.

[50] J. Lehner: "Necessary Time Response of LFSM-O to Ensure Frequency Stability in the ENTSO-E Continental Europe Synchronous Area". In *15th Wind Integration Workshop*. Vienna, 2016. URL: www.windintegrationworkshop.org%7B%5C%%7D09%20%7B%5C%%7D09.

[51] *Technical requirements for the connection and operation of customer installations to the medium voltage network (TAR medium voltage) English translation of VDE-AR-N 4110*. Tech. rep. March. VDE-AR-N 4110, 2017.

[52] *Technical requirements for grid connection of high voltage direct current systems and direct current-connected power park modules (TCR HVDC) English translation of VDE-AR-N 4131*. Tech. rep. March. VDE-AR-N 4131, 2019.

[53] Tarrasó, Andres and Candela, Jose Ignacio and Rocabert, Joan and Rodriguez, Pedro: "Grid voltage harmonic damping method for SPC based power converters with multiple virtual admittance control". In *2017 IEEE Energy Conversion Congress and Exposition (ECCE)*. IEEE, 2017, pp. 64–68. ISBN: 9781509029983. DOI: 10.1109/ECCE.2017.8095762.

[54] ENTSO-E: *High Penetration of Power Electronic Interfaced Power Sources (HPoPEIPS)*. Tech. rep. March. Brussels, Belgium, 2017, p. 37. URL: https://consultations.entsoe.eu/system-development/entso-e-connection-codes-implementation-guidance-d-3/user%7B%5C_%7Duploads/igd-high-penetration-of-power-electronic-interfaced-power-sources.pdf.

[55] R. Teodorescu, M. Liserre, and P. Rodríguez: *Grid Converters for Photovoltaic and Wind Power Systems*. John Wiley & Sons, Ltd, 2011, p. 416. ISBN: 9780470057513. DOI: 10.1002/9780470667057.

[56] M. Nasiri and R. Mohammadi: "Peak Current Limitation for Grid Side Inverter by Limited Active Power in PMSG-Based Wind Turbines During Different Grid Faults". In 1 (2017), pp. 3–12. DOI: 10.1109/TSTE.2016.2578042.

[57] A. Yazdani and R. Iravani: *Voltage-Sourced Converters in Power Systems: Modeling, Control, and Applications*. 2010. John Wiley & Sons Ltd, 2010, p. 541. ISBN: 9780470551578.

[58] R. Ottersten: "On Control of Back-to-Back Converters and Sensorless Induction Machine Drives". PhD thesis. Chalmers University of Technology, 2003.

[59] R. Miceli, C. Nevoloso, G. Scaglione, G. Schettino, G. Sorrentino, and F. Viola: "Comparison between Voltage Oriented Control and Synchronous Power Control for Grid-Connected Inverter Applications". In *2023 International Conference on Clean Electrical Power (ICCEP)*. 2023, pp. 708–714. DOI: 10.1109/ICCEP57914.2023.10247455.

[60] M. Nasiri, J. Milimonfared, and S. Fathi: "A review of low-voltage ride-through enhancement methods for permanent magnet synchronous generator based wind turbines". In *Renewable and Sustainable Energy Reviews* 2015 (2015), pp. 399–415. ISSN: 1364-0321. DOI: https://doi.org/10.1016/j.rser.2015.03.079.

[61] V. Yaramasu, B. Wu, P. C. Sen, S. Kouro, and M. Narimani: "High-power wind energy conversion systems: State-of-the-art and emerging technologies". In *Proceedings of the IEEE* 5 (2015), pp. 740–788. ISSN: 15582256. DOI: 10.1109/JPROC.2014.2378692.

[62] I. Erlich, A. Korai, and F. Shewarega: "Study on the minimum share of conventional generation units required for stable operation of future converter-dominated grids". In *2018 IEEE Power & Energy Society General Meeting (PESGM)*. 2018, pp. 1–5. DOI: 10.1109/PESGM.2018.8585943.

[63] J. Fortmann: *Modeling of Wind Turbines with Doubly Fed Generator System*. 1. Springer Vieweg Wiesbaden, 2014, pp. XXIII, 183. ISBN: 978-3-658-06881-3. DOI: https://doi.org/10.1007/978-3-658-06882-0.

[64] S. Laudahn, J. Seidel, B. Engel, T. Bülo, and D. Premm: "Substitution of synchronous generator based instantaneous frequency control utilizing inverter-coupled DER". In *2016 IEEE 7th International Symposium on Power Electronics for Distributed Generation Systems (PEDG)*. 2016, pp. 1–8. DOI: 10.1109/PEDG.2016.7527020.

[65] P. Weber, W. Schulze, P. Pawlowski, M. Suriyah, and T. Leibfried: "Grid-forming synchronverter-based control method with current limiting method for grid-side converters of type 4 wind power plants". In *22nd Wind and Solar Integration Workshop (WIW 2023)*. Copenhagen, Denmark, 2023.

[66] T. Qoria, F. Gruson, F. Colas, G. Denis, T. Prevost, and X. Guillaud: "Inertia effect and load sharing capability of grid forming converters connected to a transmission grid". In *15th IET International Conference on AC and DC Power Transmission (ACDC 2019)*. 2019, pp. 1–6. DOI: 10.1049/cp.2019.0079.

[67] Ghimire, S. and Kkuni, K. V. and Jakobsen, S. C. and Knueppel, T. and Jensen, K. H. and Guest, E. and Rasmussen, T. W. and Yang: "Grid-forming control methods for weakly connected offshore WPPs". In *22nd Wind and Solar Integration Workshop (WIW 2023)*. Copenhagen, Denmark: IET, 2023.

[68] T. Qoria, F. Gruson, F. Colas, X. Guillaud, M.-S. Debry, and T. Prevost: "Tuning of Cascaded Controllers for Robust Grid-Forming Voltage Source Converter". In *2018 Power Systems Computation Conference (PSCC)*. 2018, pp. 1–7. DOI: 10.23919/PSCC.2018.8443018.

[69] T. Qoria, F. Gruson, F. Colas, G. Denis, T. Prevost, and X. Guillaud: "Critical Clearing Time Determination and Enhancement of Grid-Forming Converters Embedding Virtual Impedance as Current Limitation Algorithm". In *IEEE Journal of Emerging and Selected Topics in Power Electronics* 2 (2020), pp. 1050–1061. DOI: 10.1109/JESTPE.2019.2959085.

[70] J. Van de Vyver, J. D. M. De Kooning, B. Meersman, L. Vandevelde, and T. L. Vandoorn: "Droop Control as an Alternative Inertial Response Strategy for the Synthetic Inertia on Wind Turbines". In *IEEE Transactions on Power Systems* 2 (2016), pp. 1129–1138. DOI: 10.1109/TPWRS.2015.2417758.

[71] P. Unruh, M. Nuschke, P. Strauss, and F. Welck: "Overview on Grid-Forming Inverter Control Methods". In *Energies* (May 2020), p. 2589. DOI: 10.3390/en13102589.

[72] D. Duckwitz, M. Shan, and B. Fischer: "Synchronous Inertia Control for Wind Turbines". In *13th Wind Integration Workshop*. November. Berlin, Germany, 2014.

[73] L. Zhang, L. Harnefors, and H.-P. Nee: "Interconnection of Two Very Weak AC Systems by VSC-HVDC Links Using Power-Synchronization Control". In *IEEE Transactions on Power Systems* 1 (2011), pp. 344–355. DOI: 10.1109/TPWRS.2010.2047875.

[74] J. Wang, Y. Wang, Y. Gu, W. Li, and X. He: "Synchronous frequency resonance of virtual synchronous generators and damping control". In *2015 9th International Conference on Power Electronics and ECCE Asia (ICPE-ECCE Asia)*. 2015, pp. 1011–1016. DOI: 10.1109/ICPE.2015.7167905.

[75] X. Li, Y. Hu, Y. Shao, and G. Chen: "Mechanism analysis and suppression strategies of power oscillation for virtual synchronous generator". In *IECON 2017 - 43rd Annual Conference of the IEEE Industrial Electronics Society*. 2017, pp. 4955–4960. DOI: 10.1109/IECON.2017.8216855.

[76] C. Glöckler, D. Duckwitz, and F. Welck: "Virtual Synchronous Machine Control with Virtual Resistor for Enhanced Short Circuit Capability". In *2017 IEEE PES Innovative Smart Grid Technologies Conference Europe, ISGT-Europe 2017 - Proceedings*. IEEE, 2017, pp. 1–6. DOI: 10.1109/ISGTEurope.2017.8260278.

[77] D. Yang, H. Wu, X. Wang, and F. Blaabjerg: "Suppression of synchronous resonance for VSGs". In *The Journal of Engineering* (13 2017), 2574–2579(5). URL: https://digital-library.theiet.org/content/journals/10.1049/joe.2017.0792.

[78] A. D. Paquette and D. M. Divan: "Virtual Impedance Current Limiting for Inverters in Microgrids With Synchronous Generators". In *IEEE Transactions on Industry Applications* 2 (2015), pp. 1630–1638. DOI: 10.1109/TIA.2014.2345877.

[79] I. Erlich, F. Shewarega, and W. Winter: "A method for incorporating VSC-HVDC into the overall grid voltage-reactive power control task". In *2016 Power Systems Computation Conference (PSCC)*. 2016, pp. 1–7. DOI: 10.1109/PSCC.2016.7540895.

[80] *FNN Guideline: Grid forming behaviour of HVDC systems and DC-connected PPMs*. Tech. rep. March. VDE FNN Guideline, 2020.

[81] M. G. Taul, X. Wang, P. Davari, and F. Blaabjerg: "Current Limiting Control With Enhanced Dynamics of Grid-Forming Converters During Fault Conditions". In *IEEE Journal of Emerging and Selected Topics in Power Electronics* 2 (2020), pp. 1062–1073. DOI: 10.1109/JESTPE.2019.2931477.

[82] J. Struwe, P. Hackl, H. Wrede, and R. Schürhuber: "Comparison of Current-Limitation Approaches for Grid- Forming Converters enabling Fault-Right-Through Operation in Converter-Driven Power Grids". In *21st Wind & Solar Integration Workshop*. The Hague, Netherlands, 2022.

[83] F. Gerini, Y. Zuo, R. Gupta, A. Zecchino, Z. Yuan, E. Vagnoni, R. Cherkaoui, and M. Paolone: "Optimal grid-forming control of battery energy storage systems providing multiple services: Modeling and experimental validation". In *Electric Power Systems Research* (2022), p. 108567. ISSN: 0378-7796. DOI: https://doi.org/10.1016/j.epsr.2022.108567.

[84] N. S. Hasan, N. Rosmin, N. M. Nordin, and M. Y. Hassan: "Virtual inertial support extraction using a super-capacitor for a wind-PMSG application". In *IET Renewable Power Generation* 10 (2019), pp. 1802–1808. ISSN: 1752-1416. DOI: 10.1049/iet-rpg.2018.5655.

[85] N. Fazli, S. Gierschner, and H.-G. Eckel: "Two-step inertia provision with consideration of load type in an islanded wind turbine with grid-supporting voltage control". In *2020 IEEE 11th International Symposium on Power Electronics for Distributed Generation Systems (PEDG)*. 2020, pp. 136–142. DOI: 10.1109/PEDG48541.2020.9244400.

[86] G. Michalke: "Variable Speed Wind Turbines - Modelling, Control, and Impact on Power Systems". PhD thesis. der Technischen Universität Darmstadt, 2008, pp. 1349–1358.

[87] S. Liu, H. Wu, X. Wang, A. Avazov, X. Guillaud, and T. Bosma: "Torsional Vibration Analysis of Grid-Forming PMSG Wind Turbine". In *22nd Wind & Solar Integration Workshop*. Copenhagen, Denmark, 2023.

[88] H. Meng, T. Yang, J.-z. Liu, and Z. Lin: "A Flexible Maximum Power Point Tracking Control Strategy Considering Both Conversion Efficiency and Power Fluctuation for Large-inertia Wind Turbines". In *Energies* (July 2017), p. 939. DOI: 10.3390/en10070939.

[89] C. Neumann and H.-G. Eckel: "Grid-forming control and operational strategies for offshore wind turbines incorporating electrical and mechanical modelling". In *23rd Wind & Solar Integration Workshop (WIW 2024)*. 2024, pp. 477–484. DOI: 10.1049/icp.2024.3834.

[90] I. Erlich: "Aspekte der Umrichterregelung in AC-Offshore-Netzen". In *Energiewende in der Stromversorgung—Systemstabilität und Systemsicherheit–12. ETG/GMA-Tagung Netzregelung und Systemführung*. Berlin, Germany: VDE, 2017, pp. 41–47.

[91] H. Holttinen, M. O'Malley, F. R. Najafabadi, and N. Cutululis: "Grand challenges Grid-research needs for future grid support of wind power plants". In *22nd Wind & Solar Integration Workshop*. Copenhagen, Denmark.

[92] VDE / FNN: *Technical requirements for the connection and operation of customer installations to the high voltage network (TCR high voltage) English translation of VDE-AR-N 4120*. Tech. rep. November. VDE / FNN, 2018, p. 215.

[93] "Wind Energy Power Plants". In *Grid Integration of Wind Energy*. John Wiley & Sons, Ltd, 2014. Chap. 1, pp. 1–30. ISBN: 9781118703274. DOI: https://doi.org/10.1002/9781118703274.ch1. eprint: https://onlinelibrary.wiley.com/doi/pdf/10.1002/9781118703274.ch1. URL: https://onlinelibrary.wiley.com/doi/abs/10.1002/9781118703274.ch1.

[94] L. Zeni, A. J. Rudolph, J. Münster-Swendsen, I. Margaris, and A. D. Hansen: "Virtual inertia for variable speed wind turbines". In *Wind Energy* 8 (2013), pp. 1–20. DOI: https://doi.org/10.1002/we.1549. URL: https://doi.org/10.1002/we.1549.

[95] *Modelling and Aggregation of Loads in Flexible Power Networks*. Tech. rep. February. CIGRE Brochure 566, 2014.

[96] N. Schäfer, S. S. Kulkarni, G. Arnold, and V. V. B. Mahtani: "Towards Standardised Testing Procedures for Inertia Provision of Grid Forming Inverters". In *21st Wind & Solar Integration Workshop*. The Hague, Netherlands, 2022.

[97] L. M. Korunovi, J. V. MilanoviÂ´, S. Z. Djokic, K. Yamashita, S. M. Villanueva, and S. Sterpu: "Recommended Parameter Values and Ranges of Most Frequently Used Static Load Models". In *IEEE Transactions on Power Systems* 6 (2018), pp. 5923–5934. DOI: 10.1109/TPWRS.2018.2834725.

[98] A. W. Korai and I. Erlich: "Frequency dependent voltage control by DER units to improve power system frequency stability". In *2015 IEEE Eindhoven PowerTech*. IEEE, 2015, pp. 1–6. DOI: 10.1109/PTC.2015.7232349.

[99] Tsemekidi Tzeiranak S and Bertoldi P and Castellazzi L and Gonzalez Torres M and Clementi E and Paci D: *Energy Consumption and Energy Efficiency trends in the EU, 2000-2020*. Tech. rep. Joint Research Centre, Institute for Energy and Transport, 2022. DOI: 10.2760/727548(online).

[100] A. P. TELLEZ: "Modelling aggregate loads in power systems". PhD thesis. KTH Royal Institute of Technology, 2017.

[101] A. J. Collin, J. L. Acosta, B. P. Hayes, and S. Z. Djokic: "Component-based Aggregate Load Models for Combined Power Flow and Harmonic Analysis". In *7th Mediterranean Conference and Exhibition on Power Generation, Transmission, Distribution and Energy Conversion*. Agia Napa, 2010.

[102] ITRE: *Overview of Energy Efficiency measures of European industry*. Tech. rep. 2010.

[103] Gemeinsame Forschungsstelle and Institut für Energie und Verkehr and Bertoldi, P and Hirl, B and Labanca, N: *Energy efficiency status report 2012: electricity consumption and efficiency trends in the EU -27*. Tech. rep. Joint Research Centre, Institute for Energy and Transport, 2012. DOI: doi/10.2788/3763.

[104] "Load representation for dynamic performance analysis (of power systems)". In *IEEE Transactions on Power Systems* 2 (1993), pp. 472–482. DOI: 10.1109/59.260837.

[105] ENTSO-E: *Future system inertia*. Tech. rep. URL: https://docstore.entsoe.eu/Documents/Publications/SOC/Nordic/Nordic%7B%5C_%7Dreport%7B%5C_%7DFuture%7B%5C_%7DSystem%7B%5C_%7DInertia.pdf.

[106] ENTSO-E: *Frequency Stability Evaluation Criteria for the Synchronous Zone of Continental Europe*. Tech. rep. Brussels, Belgium, 2016. URL: https://eepublicdownloads.entsoe.eu/clean-documents/SOC%20documents/RGCE%7B%5C_%7DSPD%7B%5C_%7Dfrequency%7B%5C_%7Dstability%7B%5C_%7Dcriteria%7B%5C_%7Dv10.pdf.

[107] N. Fazli, S. Gierschner, and H.-G. Eckel: "Evaluating frequency stability with consideration of load type in different share of renewables and emulated inertia in case of system split". In *2020 22nd European Conference on Power Electronics and Applications (EPE'20 ECCE Europe)*. 2020, P.1–P.9. DOI: 10.23919/EPE20ECCEEurope43536.2020.9215611.

[108] ENTSO-E: *Technical background for the Low Frequency Demand Disconnection requirements*. Tech. rep. Brussels, Belgium: ENTSO-E, 2014, p. 20. URL: https://eepublicdownloads.entsoe.eu/clean-documents/Network%20codes%20documents/NC%20ER/141215%7B%5C_%7DTechnical%7B%5C_%7Dbackground%7B%5C_%7Dfor%7B%5C_%7DLFDD.pdf.

[109] ENTSO-E: *Frequency Measurement Requirements and Usage*. Tech. rep. Brussels, Belgium, 2018. URL: https://docstore.entsoe.eu/Documents/SOC%20documents/Regional%7B%5C_%7DGroups%7B%5C_%7DContinental%7B%5C_%7DEurope/2018/TF%7B%5C_%7DFreq%7B%5C_%7DMeas%7B%5C_%7Dv7.pdf.

[110] J. Barrios-Gomez, F. Sanchez, F. Gonzalez-Longatt, M. Acosta, and D. Topic: "RoCoF Calculation Using Low-Cost Hardware in the Loop: Multi-area Nordic Power System". In *International Conference on Smart Systems and Technologies (SST)*. Osijek, 2020. ISBN: 9781728197593. DOI: 10.1109/SST49455.2020.9264119.

[111] F. Gonzalez-Longatt, J. M. Roldan-Fernandez, H. R. Chamorro, S. Arnaltes, and J. L. Rodriguez-Amenedo: "Investigation of Inertia Response and Rate of Change of Frequency in Low Rotational Inertial Scenario of Synchronous Dominated System". In *Electronics* 18 (2021). DOI: 10.3390/electronics10182288.

[112] RG-CE System Protection & Dynamics Sub Group: *Task Force Overfrequency Control Schemes - Recommendations for the Synchronous Area of Continental Europe*. Tech. rep. September. Brussels, Belgium: ENTSO-E, 2017, pp. 1–8. URL: https://eepublicdownloads.entsoe.eu/clean-documents/SOC%20documents/Regional%7B%5C_%7DGroups%7B%5C_%7DContinental%7B%5C_%7DEurope/2017/170926%7B%5C_%7DRG%7B%5C_%7DCE%7B%

5C_%7DTOP%7B%5C_%7D08.1%7B%5C_%7DD.2%7B%5C_%7DSPD%7B%5C_%7DCodes%7B%5C_%7DTF%7B%5C_%7Dv6%7B%5C_%7DOverfrequency%7B%5C_%7DControl%7B%5C_%7DSchemes.pdf.

[113] ENTSO-E: *Rate of Change of Frequency (RoCoF) withstand capability*. Tech. rep. Brussels, Belgium, 2018. URL: https://eepublicdownloads.entsoe.eu/clean-documents/Network%20codes%20documents/NC%20RfG/IGD%7B%5C_%7DRoCoF%7B%5C_%7Dwithstand%7B%5C_%7Dcapability%7B%5C_%7Dfinal.pdf.

[114] J. Steinkohl: "Testing grid forming requirements OEM perspective on grid modeling for existing and upcoming grid connection requirements". In *22nd Wind and Solar Integration Workshop (WIW 2023)*. Copenhagen, Denmark: IET.

[115] H. Thiesen and C. Jauch: "Determining the Load Inertia Contribution from Different Power Consumer Groups". In *Energies 2020* 1588 (2020). DOI: 10.3390/en13071588.

[116] ENTSO-E: *System Defence Plan*. Tech. rep. Brussels, Belgium: ENTSO-E, 2022. URL: https://eepublicdownloads.entsoe.eu/clean-documents/SOC%20documents/Regional%7B%5C_%7DGroups%7B%5C_%7DContinental%7B%5C_%7DEurope/2022/220215%7B%5C_%7DRGCE%7B%5C_%7DTOP%7B%5C_%7D03.2%7B%5C_%7DD.1%7B%5C_%7DSystem%20Defence%20Plan%7B%5C_%7Dv8%7B%5C_%7Dfinal.pdf.

[117] 50Hertz, Amprion, TenneT, and Transnet BW: *Auswirkungen reduzierter Schwungmasse auf einen stabilen Netzbetrieb*. Tech. rep. 2014. URL: https://www.netzentwicklungsplan.de/sites/default/files/media/documents/Minimale%20Schwungmasse.pdf.

[118] R. Eriksson, N. Modig, and K. Elkington: "Synthetic inertia versus fast frequency response: a definition". In *IET Renewable Power Generation* 5 (2018), pp. 507–514. eprint: https://ietresearch.onlinelibrary.wiley.com/doi/pdf/10.1049/iet-rpg.2017.0370.

[119] Netztransparenz: *Financial impact of imbalance price modules*. 2024. URL: https://www.netztransparenz.de/en/Balancing-Capacity/Imbalance-price/Financial-impact-of-IP-modules.

[120] "IEEE Guide for Planning DC Links Terminating at AC Locations Having Low Short-Circuit Capacities". In *IEEE Std 1204-1997* (1997), pp. 1–216. DOI: 10.1109/IEEESTD.1997.85949.

[121] S. Grunau and F. W. Fuchs: "Effect of wind-energy power injection into weak grids". In *European Wind Energy Conference and Exhibition 2012, EWEC 2012*. 2012, pp. 1150–1156. ISBN: 9781627482912.

[122] ENTSO-E: *System protection behavior and settings during system disturbances*. Tech. rep. Brussels, Belgium: ENTSO-E, 2018.

[123] T. Erckrath, C. Bendfeld, R. Brandl, and M. Jung: "Power Hardware-in-the-Loop Validation of Grid-Forming Control and Current Limitation for Start up of Induction Motors in Microgrids". In *2023 25th European Conference on Power Electronics and Applications (EPE'23 ECCE Europe)*. 2023, pp. 1–9. DOI: 10.23919/EPE23ECCEEurope58414.2023.10264509.

[124] *IEEE Recommended Practice for Industrial and Commercial Power Systems Analysis (Brown Book)*. IEEE, pp. 1–488. ISBN: 1559379685.

[125] M. Falahi, K. L. Butler-Purry, and M. Ehsani: "Induction Motor Starting in Islanded Microgrids". In *IEEE Transactions on Smart Grid* 3 (), pp. 1323–1331. ISSN: 19493053. DOI: 10.1109/TSG.2013.2271261.

[126] "IEEE Guide for Synchronous Generator Modeling Practices and Parameter Verification with Applications in Power System Stability Analyses". In *IEEE Std 1110-2019 (Revision of IEEE Std 1110-2002)* (2020), pp. 1–92. DOI: 10.1109/IEEESTD.2020.9020274.

[127] L. Zhang, L. Harnefors, and H.-p. Nee: "Power-Synchronization Control of Grid-Connected Voltage-Source Converters". In *IEEE Transactions on Power Systems* 2 (2010), pp. 809–820. DOI: 10.1109/TPWRS.2009.2032231.

DECLARATION IN LIEU OF OATH

Ich versichere hiermit durch eigenhändige Unterschrift, dass ich die vorliegende Arbeit selbstständig und ohne die Nutzung anderer als der angegebenen Hilfsmittel angefertigt habe. Alle Stellen, die wörtlich oder sinngemäß aus Veröffentlichungen entnommen wurden, habe ich als solche kenntlich gemacht.

I hereby certify with my personal signature that I have written this thesis independently and without the use of any aids other than those specified. I have marked all passages taken verbatim or in spirit from publications as such.

Place, Date	Signature
Stein, 08.03.2026	signed Nastaran Hammes